UNIVERSIDADE DE LISBOA
FACULDADE DE CIÊNCIAS
DEPARTAMENTO DE QUÍMICA E BIOQUÍMICA

Synthesis and characterisation of luminescent spin crossover iron(III) compounds

Rafaela Farelo Silva Tenera Marques

Mestrado em Química
Especialização em Química

Dissertação orientada por:
Dr. Paulo Nuno Martinho

2020

Agradecimentos

Em primeiro lugar, gostaria de agradecer ao Dr. Paulo Nuno Martinho, pela oportunidade de me orientar em mais um projeto, por todo o apoio, ajuda e motivação ao longo deste ano, pela experiência partilhada e, principalmente, pela amizade. Agradecer, em especial, por me dar a oportunidade de crescer enquanto pessoa e cientista, podendo partilhar a orientação da Ana Rita Reis que foi sempre uma excelente companhia em laboratório e um muito obrigado pelo trabalho na síntese das moléculas luminescentes.

Gostaria também de agradecer à Dra. Liliana Ferreira e à Dra. Clara Gomes por todo o tempo e trabalho dedicado para que a minha investigação pudesse prosseguir. Também uma palavra de agradecimento para o Dr. Artur Mouro pelo auxílio nas medições de luminescência.

Quero também agradecer a todo o grupo do laboratório, em particular ao Marcos Bento pela companhia e boa disposição sempre no laboratório e à Dra. Marta Saraiva por toda a ajuda e partilha de conhecimentos.

I need to also thank COST Action E-COST for the scientific opportunity that I had during this year and to the amazing group I found in Bordeaux, in particular to Dr. Guillaume Chastanet, Dr. Patrick Rosa and Dr. Matheau Gonidec, who made sure my stay was rich in new experiences.

Por fim, à minha família e aos meus amigos, quero agradecer às pessoas que me apoiam incondicionalmente, em especial ao meu irmão, à minha mãe e ao meu namorado, por todo o amor e paciência para me ouvirem falar da área que tenho o gosto de trabalhar.

Abstract

This work was dedicated to the study of Fe(III) complexes displaying the spin crossover phenomenon that ultimately can be used in spintronic devices and sensors, and to the study of Fe(III) complexes with multifunctional properties, combining both spin crossover and luminescence, as a door to create a spin crossover-based magneto-optical switch.

The ligands used to prepare the complexes were tridentate and pentadentate Schiff base compounds. These ligands were synthesized by condensation reactions between different salicylaldehydes and amines. The tridentate ligands were of the family X_2-salEen and the pentadentate ligands were either X-salpet or X_2-salpet compounds.

The Fe(III) complexes displaying the spin crossover phenomenon were formed using the X_2-salEen ligands and different iron salts. These complexes were obtained as salts where the Fe(III) cation needed one anion to balance the charges and, for that, perchlorate, hexafluorophosphate, tetraphenylborate, tetrafluoroborate and nitrate were used as counter-ions.

A total of thirty-one new Fe(III) complexes were synthesized and characterized by FTIR and UV-vis spectroscopy, single crystal and powder X-ray diffraction and SQUID magnetometry. Although the majority of the compounds were obtained as crystals, some of them did not diffract with good enough quality, making it impossible to solve and present their structure.

The Fe(III) complexes prepared using the tridentate ligands revealed that the same samples at the same temperature presented different spin states while being in either solid state (by SQUID magnetometry) or in solution (by UV-vis).

For the Fe(III) complexes prepared with tridentate ligands it was also found that when using the same anions, the compounds display different SCO behaviors. One complex in particular crystallized in different solvate forms and revealed different SCO curves, thus indicating that the solvent also influences the SCO phenomenon. In general, changing the ligand, influenced the magnetic behavior, however some exceptions were observed. Three complexes using different halogen substituents prepared with the same anion and solvent displayed identical SCO curves with hysteresis.

Additionally, twelve Fe(III) complexes were synthesized aiming at producing multifunctional compounds with spin crossover and luminesce properties. The complexes were prepared with different X_2-salpet ligands and a luminescent dye. While the synthesis of the organic dye proved to be unsuccessful, the synthesis of the inorganic dye, a Ru(II) complex, was successful and presented a quantum yield of 10%.

For the multifunctional group of complexes, FTIR and UV-vis showed evidence that the complexes might have been synthesized with the projected structure, even though further testing is needed to confirm it. SQUID magnetometry showed similar magnetic profiles in compounds with different salpets.

Keywords: Iron; Spin crossover; Schiff bases; Luminescence; Ruthenium.

Resumo

A transição de spin é um fenómeno estudado na área da química de coordenação. Esta propriedade é característica de complexos octaédricos de metais de transição do grupo 3*d*, entre d^4 e d^7, uma vez que são os únicos que conseguem apresentar diferentes distribuições eletrónicas para o mesmo número de eletrões nas orbitais *d*. Esta transição é caraterizada pela troca entre os dois estados de spin, spin-alto e spin-baixo, e ocorre apenas quando as energias de emparelhamento e do campo de ligandos têm a mesma ordem de grandeza. Esta propriedade apresenta um grande potencial no desenvolvimento de diversos tipos de aparelhos, sendo, deste modo, cada vez mais apelativa para investigadores. Diferentes curvas de transições de spin são aplicadas em aparelhos distintos. De um modo geral, as transições abruptas são utilizadas para interruptores moleculares, as graduais para sensores e as com histereses para dispositivos de armazenamento de informação. Uma transição de spin pode ocorrer quando o sistema em estudo sofre diversas perturbações externas (temperatura, pressão, luz, tec.), sendo que nesta dissertação a perturbação usada para induzir a transição de spin foi a variação de temperatura. Os complexos de Ferro(III) foram escolhidos pela quantidade de estudos já realizados com diversos ligandos, pelas suas características eletrónicas, complexo d^5, e pela sua abundância na Terra.

Este trabalho teve como objetivo a síntese de complexos de Fe(III) com transição de spin para serem utilizados para as propriedades anteriormente referidas, e complexos de Fe(III) multifuncionais, combinando a transição de spin com luminescência para criar interruptores magneto-óticos baseados em transição de spin.

Neste trabalho, os ligandos utilizados para a formação de complexos de Fe(III) foram bases de Schiff tridentadas e pentadentadas, sendo preparadas através de reações de condensação entre salicilaldeídos com diferentes substituintes e aminas, tendo gerado ligandos tridentados X_2-salEen e ligandos pentadentados X-salpet e X_2-salpet.

Para os complexos de Ferro(III) com transição de spin, os ligandos utilizados foram diferentes X_2-salEen divididos em dois grupos por substituintes, os homonucleares e os heteronucleares. No grupo dos homonucleares os ligandos foram 3,5-F-salEen, 3,5-Cl-salEen e 3,5-I-salEen e no grupo dos heteronucleares os ligandos foram 3-Br-5-Cl-salEen, 5-Cl-3-I-salEen e 5-Cl-3-NO_2-salEen. Estes complexos precisam de um contra-ião para contrabalançarem a carga positiva dos catiões e os cinco aniões selecionados foram: perclorato, hexafluorofosfato, tetrafenilborato, tetrafluorborato e nitrato.

No primeiro grupo foram sintetizados trinta e um complexos novos de Ferro(III) e estes foram caracterizados e estudados através de espectroscopia de infravermelho com transformada de Fourier (FTIR) e de Ultra Violeta-visível (UV-vis), difração de raios-X de pós e de cristal único e também através de magnetometria de SQUID. No que diz respeito à difração de raios-X de cristal único, alguns compostos não apresentaram níveis de qualidade suficiente para serem considerados válidos ou não chegaram mesmo a difratar, pelo que só foram analisados alguns resultados desta técnica específica para alguns dos complexos. Apenas um complexo não apresentou a troca de anião, sendo comprovada através de espectroscopia de FTIR e de estudos de difração de raios-X de cristal único. Os restantes 31 complexos foram sintetizados com sucesso.

Numa primeira fase, os compostos foram divididos por grupos do mesmo ligando e analisados individualmente através das técnicas anteriores. Os grupos correspondentes aos ligandos com substituintes homonucleares foram $[Fe(3,5\text{-}Br\text{-}salEen)_2]Y$, $[Fe(3,5\text{-}Cl\text{-}salEen)_2]Y$, $[Fe(3,5\text{-}F\text{-}salEen)_2]Y$ e $[Fe(3,5\text{-}I\text{-}salEen)_2]Y$ e os grupos dos ligandos com substituintes heteronucleares foram $[Fe(3\text{-}Br\text{-}5\text{-}Cl\text{-}salEen)_2]Y$, $[Fe(5\text{-}Cl\text{-}3\text{-}I\text{-}salEen)_2]Y$ e $[Fe(5\text{-}Br\text{-}3\text{-}NO_2\text{-}salEen)_2]Y$.

Após a análise individual, procuraram-se padrões na magnetometria de SQUID para os mesmos grupos de ligandos, mas que, de modo geral, não foram encontrados, uma vez que os complexos do mesmo grupo apresentaram resultados de transição de spin diferentes, podendo isto pressupor que o ligando influencia a transição de spin.

Fizeram-se as mesmas comparações, mas neste caso dividindo os complexos por diferentes grupos de aniões. Através dos resultados da magnetometria de SQUID, não foram encontradas similaridades uma vez que os complexos pertencentes ao mesmo grupo apresentaram resultados de transição de spin diferentes, provando assim que aniões são importantes para alcançar transições de spin. No entanto, o grupo contendo o anião perclorato foi exceção à regra. Dos seis complexos com este anião, quatro apresentaram maioritariamente um estado de spin-baixo entre os 10 e os 370 K, com os restantes a conterem solvente na estrutura, impossibilitando uma comparação direta.

O estudo do solvente na estrutura do cristal também permitiu aferir que influencia as curvas de transição de spin, com duas implicações diferentes. Num dos estudos o solvente na estrutura é o mesmo e no outro os solventes na estrutura são diferentes. No primeiro estudo, os ligandos são diferentes, o anião (tetrafenilborato) e os dois solventes na estrutura cristalina são os mesmos. Os três complexos sintetizados em comparação apresentaram comportamentos magnéticos semelhantes, sendo caracterizados por um aumento no $\chi_M T$ com o aumento do número de ciclos e pelo aparecimento de janelas de histerese entre 200 e 355 K em todos os ciclos realizados. Para um destes complexos foi realizada difração de raios-X de cristal único, para se entender as diferenças na estrutura após a realização dos ciclos e observou-se que houve perda dos solventes e que as diferenças no perfil magnético são consequência de rearranjos na sua estrutura. Para os outros dois complexos é necessário aplicar a mesma técnica para se confirmar o rearranjo das moléculas com a perda do solvente. No entanto, foi possível realizar raios-X de pós antes e depois dos estudos de magnetometria de SQUID para os três complexos e que permitiu compreender que a estrutura é diferente, já que nem todos os picos de difração nos difratogramas são correspondentes.

No segundo estudo analisaram-se dois solvatos, com o mesmo ligando e anião, mas que diferem no tipo de solventes na estrutura, o que teve consequência no comportamento magnético dos complexos. Um dos solvatos mostrou-se estável no intervalo entre 10 e 370 K, com cerca de 50% de centros em alto spin e 50% em baixo spin. No entanto o outro solvato, no mesmo intervalo, apresentou um perfil interessante com uma curva gradual/abrupta e com uma transição praticamente completa, a 200 K, passando de um estado spin-baixo para um estado de spin correspondendo a 90% de spin-alto.

Outro resultado interessante foi o obtido para o complexo $[Fe(5\text{-}Br\text{-}3\text{-}NO_2\text{-}salEen)_2]PF_6$ que apresentou um perfil de transição de spin praticamente completo, a 300 K, e com uma histerese térmica de pequenas dimensões.

A luminescência é um fenómeno que permite às moléculas emitir radiação de forma espontânea, e pode ser estimulada através de diversas formas. Esta propriedade pode ser aplicada em aparelhos óticos, sensores, interruptores de fotões, entre outros. A luminescência pode ocorrer tanto em compostos orgânicos como inorgânicos.

Compostos que emitam na região próxima do infravermelho permitem que quando ligados ao Fe(III) a sua luminescência não seja extinta devido às bandas de absorção do Fe(III). Desta forma tentou sintetizar-se um composto orgânico e um inorgânico com propriedades luminescentes. Infelizmente, a síntese da molécula orgânica não foi bem-sucedida. No entanto a síntese da molécula inorgânica, complexo de Ru(II) foi conseguida e o complexo apresentou luminescência com um rendimento quântico de 10%.

Para este objetivo foram sintetizados doze compostos de Fe(III) com o complexo luminescente de Ru(II) e diferentes ligandos X-salpet e X_2-salpet. Estes complexos foram caraterizados por espetroscopia de NMR (ressonância magnética nuclear), de FTIR (infravermelho com transformada de Fourrier) e de UV-vis (ultravioleta-visível) e por magnetometria de SQUID (dispositivo supercondutor de interferência quântica). Infelizmente, os resultados conseguidos através das espectroscopias são insuficientes para concluir se os complexos projetados foram corretamente sintetizados.

Através de magnetometria de SQUID os perfis magnéticos são todos semelhantes, com uma variação mais acentuada entre 10 K e 100 K, e após essa temperatura as curvas tendem a estabilizar até 370 K.

No entanto, alguns complexos apresentam um valor de $\chi_M T$ superior ao teórico para este tipo de complexos. Estes resultados sugerem que os complexos têm uma massa molar superior à esperada.

Palavras-chave: Ferro; Transição de spin; bases de Schiff; Luminescência; Ruténio.

Contents

1. Introduction 1
  1.1. Spin crossover (SCO) and its relevance 1
  1.2. Spin states in spin crossover 1
    1.2.1. Spin crossover curves 2
    1.2.2. Magnetic Moment and Magnetic Susceptibility 2
    1.2.3. (Photo)Magnetic measurements 3
  1.3. Spin crossover in Fe(III) 3
  1.4. Ligands for spin crossover in Fe(III) complexes 4
    1.4.1. Impact of the solvent, anion and halogen substituent in spin crossover 4
  1.5. Luminescence and its importance 4
    1.5.1. Near Infrared region 5
      1.5.1.1. Organic molecule – Keio Fluors 6
      1.5.1.2. Coordination compounds – Ruthenium complexes 6
  1.6. Spin crossover luminescent complexes (multifunctional materials) 7
2. Results and discussion 8
  2.1. Ligands 8
  2.2. SCO complexes 9
    2.2.1. Homo-substituent compounds 9
      $[Fe(3,5\text{-}Br\text{-}salEen)_2]Y$ 9
        FTIR and UV-vis spectroscopy 9
        Structural characterization 12
        SQUID magnetometry 15
      $[Fe(3,5\text{-}Cl\text{-}salEen)_2]Y$ 17
        FTIR and UV-vis spectroscopy 18
        Structural characterization 19
        SQUID magnetometry 21
      $[Fe(3,5\text{-}F\text{-}salEen)_2]Y$ 23
        FTIR and UV-vis Spectroscopy 23
        Structural characterization 26
        SQUID magnetometry 28
      $[Fe(3,5\text{-}I\text{-}salEen)_2]Y$ 30
        FTIR and UV-vis Spectroscopy 30
        Structural characterization 33
        SQUID magnetometry 34
    2.2.2. Hetero-substituent compounds 35
      $[Fe(3\text{-}Br\text{-}5\text{-}Cl\text{-}salEen)_2]Y$ 35
        FTIR and UV-vis Spectroscopy 36
        Structural characterization 38

SQUID magnetometry 39
[Fe(5-Cl-3-I-salEen)$_2$]Y 43
FTIR and UV-vis Spectroscopy 43
Structural characterization 46
SQUID magnetometry 47
[Fe(5-Br-3-NO$_2$-salEen)$_2$]Y 48
FTIR and UV-vis Spectroscopy 49
Structural characterization 50
SQUID magnetometry 51
2.3. Correlations 53
Complexes with different anions 53
Complexes with different solvents in the crystal lattice 53
Complexes with different substituents 54
Distortion parameters and packing effects 55
2.4. Multifunctional complexes: SCO and luminescence 58
2.4.1. Salpet ligands and an organic luminescent dye 58
2.4.2. Salpet ligands and an inorganic luminescent dye 59
Quantum yield φ_F 60
NMR Spectroscopy 61
FTIR and UV-vis spectroscopy 62
SQUID magnetometry 65
3. Conclusions 66
4. Experimental 67
4.1. Synthesis 67
4.2. Characterization 75
5. Bibliography 76
A. Annex section 80

List of figures, schemes and tables

Figure 1.1 Energy levels splitting in an octahedron geometry, $3d_{xy}$, $3d_{xz}$ and $3d_{yz}$ in the t_{2g} level and the $3dz2$ and $3dx2 - y2$ in the e_g^* level.[30] 1
Figure 1.2 Most common SCO curves: (a) gradual, (b) abrupt, (c) abrupt with thermal hysteresis, (d) stepped and (e) incomplete.[32] 2
Figure 1.3 Iron(III) electron distribution to octahedron LS, IS and HS. 3
Figure 1.4 Schiff base tridentate ligand: H_2-X-salEen. 4
Figure 1.5 Schiff base pentadentate ligand: H_2-X-salpet 4
Figure 1.6 Fluorescence and phosphorescence mechanisms (Jablonski diagram).[55] 5
Figure 1.7 BODIPY, fluorescent organic dyes. 6
Figure 1.8 Keio Fluors, fluorescent organic dye. 6
Figure 1.9 Ruthenium complex, luminescent inorganic dye 7
Figure 2.1 FTIR spectrum of **C1**. 10
Figure 2.2 UV-vis spectra of **C1-C5** in acetonitrile 11
Figure 2.3 X-ray crystal structure of **C3•H_2O•CH_3CN**, at 296 K: (a) asymmetric unit; (b) unit cell. 13
Figure 2.4 Hydrogen bonds in the X-ray single crystal structure: (a) **C1** and (b) **C3•H_2O•CH_3CN**. . 13
Figure 2.5 Powder X-ray diffractograms for complexes **C1-C5**. 14
Figure 2.6 Single Crystal and powder X-ray diffractogram of **C1**. 15
Figure 2.7 χ_MT vs T plot for complexes **C1-C5**. 15
Figure 2.8 χ_MT vs T plot for second sample of **C3•H_2O•CH_3CN** 16
Figure 2.9 UV-vis spectra of **C6-C9** in acetonitrile 18
Figure 2.10 Powder X-ray diffractograms for complexes **C6-C9**. 20
Figure 2.11 χ_MT vs T plot for complexes **C6-C9.** 21
Figure 2.12 χ_MT vs T plot for second sample of **C8•H_2O•CH_3CN** 22
Figure 2.13 FTIR spectra of **C11_1** and **C11_2**. 24
Figure 2.14 UV-vis spectra of **C10-C14** in acetonitrile. 25
Figure 2.15 Powder X-ray diffractograms for complexes **C10-C14** 28
Figure 2.16 χ_MT vs T plot for complexes **C10-C14.** 28
Figure 2.17 FTIR spectra of **C19_1** and **C19_2**. 30
Figure 2.18 FTIR spectrum of **C18** 31
Figure 2.19 UV-vis spectra of **C15-C19** in acetonitrile. 32
Figure 2.20 Powder X-ray diffractograms for **C15-C19**. 34
Figure 2.21 χ_MT vs T plot for complexes **C15-C19.** 35
Figure 2.22 UV-vis spectra of **C20-C24** in acetonitrile. 37
Figure 2.23 Powder X-ray diffractograms for **C20-C24**. 39
Figure 2.24 χ_MT vs T plot for complexes **C20•CH_3CN-C24.** 40
Figure 2.25 χ_MT vs T plot for second sample of **C22•H_2O•CH_3CN**, between 355 K and 10 K. 41
Figure 2.26 χ_MT vs T plot for second sample of **C22•H_2O•CH_3CN**, between 370 K and 10 K. 41
Figure 2.27 X-ray crystal structure of **C22**: (a) before SQUID magnetometry **C22•H_2O•CH_3CN** at 293 K and (b) after SQUID magnetometry at 110 K **C22**. 42
Figure 2.28 FTIR spectrum of **C25_1** and **C25_2**. 44
Figure 2.29 UV-vis spectra of **C25-C28** in acetonitrile. 45
Figure 2.30 Powder X-ray diffractograms for complexes **C25-C28** 47
Figure 2.31 χ_MT vs T plot for complexes **C25-C28•2H_2O.** 48
Figure 2.32 UV-vis spectra of **C29** and **C30** 49
Figure 2.33 Powder X-ray diffractograms for complexes **C29** and **C30** 51
Figure 2.34 χ_MT vs T plot for complexes **C29** and **C30.** 52
Figure 2.35 χ_MT vs T plot for complexes **C12_1•H_2O•MeOH** and **C12_2•CH_3CN**. 53
Figure 2.36 χ_MT vs T plot for **C22•H_2O•CH_3CN.** 54
Figure 2.37 χ_MT vs T plot for complexes **C3.H_2O.CH_3CN**, **C8. H_2O.CH_3CN** and **C22. H_2O.CH_3CN.**
.... 55
Figure 2.38 Distortion parameters: (a) local angular distortion; (b) trigonal distortion; (c) Fe-O-C-C torsion; (d) dihedral angle and (d) triangular distortion. 56

Figure 2.39 NMR spectrum of **L1_1** in DMSO. ... 59
Figure 2.40 Fluorescence emission spectrum at 434 nm of **L2** ... 60
Figure 2.41 ^{1}H NMR spectrum of **C31** to **C41** in DMSO. ... 61
Figure 2.42 FTIR spectra of **C37_1** and **C37_2.** ... 62
Figure 2.43 UV-vis spectra of (a) mono-substituents **C31** to **C35**, (b) homo-substituents **C36** to **C38** and (c) hetero-substituents **C40** and **C41**. ... 63
Figure 2.44 $\chi_M T$ vs T plot for complexes **C31-C41** ... 65
Figure A.1 FTIR spectrum of **C2.** ... 80
Figure A.2 FTIR spectrum of **C3.** ... 80
Figure A.3 FTIR spectrum of **C4** ... 81
Figure A.4 FTIR spectrum of **C5** ... 81
Figure A.5 X-ray crystal structure of **C1**, at 296 K: (a) asymmetric unit; (b) unit cell. ... 82
Figure A.6 Single Crystal and powder X-ray diffractogram of **C3•H_2O•CH_3CN** ... 82
Figure A.7 FTIR spectrum of **C6** ... 82
Figure A.8 FTIR spectrum of **C7** ... 83
Figure A.9 FTIR spectrum of **C8** ... 83
Figure A.10 FTIR spectrum of **C9** ... 84
Figure A.11 X-ray crystal structure of **C6**, at 110 K: (a) asymmetric unit; (b) unit cell. ... 84
Figure A.12 X-ray crystal structure of **C8•H_2O•CH_3CN**, at 296 K: (a) asymmetric unit; (b) unit cell. ... 85
Figure A.13 Hydrogen bonds in the X-ray single crystal structure: (a) **C6** and (b) **C8•H_2O•CH_3CN**; C-H···***π*** (c) **C8•H2O•CH3CN**. ... 85
Figure A.14 Single Crystal and powder X-ray diffractogram of **C6** ... 86
Figure A.15 Single Crystal and powder X-ray diffractogram of **C8•H_2O•CH_3CN**. ... 86
Figure A.16 FTIR spectrum of **C10** ... 87
Figure A.17 FTIR spectrum of **C12_1**. ... 87
Figure A.18 FTIR spectrum of **C12_2**. ... 88
Figure A.19 FTIR spectrum of **C13** ... 88
Figure A.20 FTIR spectrum of **C14** ... 89
Figure A.21 X-ray crystal structure of **C10**, at 296 K: (a) asymmetric unit; (b) unit cell. ... 90
Figure A.22 X-ray crystal structure of **C11**, at 296 K: (a) asymmetric unit; (b) unit cell. ... 90
Figure A.23 X-ray crystal structure of **C12_1•H_2O•MeOH** and **C12_2•CH_3CN**, at 296 K: (a) (c) asymmetric unit; (b) (d) unit cell ... 91
Figure A.24 X-ray crystal structure of **C14**, at 296 K: (a) asymmetric unit; (b) unit cell. ... 91
Figure A.25 Hydrogen bonds in the X-ray single crystal structure: (a) **C10;** (b) **C11**; (c) **C12_1•H_2O•MeOH**; (d) **C12_2•CH_3CN** and (e) **C14** ... 92
Figure A.26 Single Crystal and powder X-ray diffractogram of **C10** ... 92
Figure A.27 Single Crystal and powder X-ray diffractogram of **C11** ... 93
Figure A.28 Single Crystal and powder X-ray diffractogram of **C12_1•H_2O•MeOH.** ... 93
Figure A.29 Single Crystal and powder X-ray diffractogram of **C12_2•CH_3CN.** ... 93
Figure A.30 Single Crystal and powder X-ray diffractogram of **C14** ... 94
Figure A.31 FTIR spectrum of **C15.** ... 94
Figure A.32 FTIR spectrum of **C16.** ... 95
Figure A.33 FTIR spectrum of **C17** ... 95
Figure A.34 X-ray crystal structure of **C15**, at 296 K: (a) asymmetric unit; (b) unit cell. ... 96
Figure A.35 X-ray crystal structure of **C18**, at 296 K: (a) asymmetric unit; (b) unit cell. ... 96
Figure A.36 X-ray crystal structure of **C19**, at 296 K: (a) asymmetric unit; (b) unit cell. ... 97
Figure A.37 Hydrogen bonds in the X-ray single crystal structure: (a) **C15;** (b) **C18** and (c) **C19**. ... 97
Figure A.38 Single Crystal and powder X-ray diffractogram of **C15** ... 98
Figure A.39 Single Crystal and powder X-ray diffractogram of **C18** ... 98
Figure A.40 Single Crystal and powder X-ray diffractogram of **C19** ... 98
Figure A.41 FTIR spectrum of **C20** ... 99
Figure A.42 FTIR spectrum of **C21** ... 99
Figure A.43 FTIR spectrum of **C22** ... 100
Figure A.44 FTIR spectrum of **C23** ... 100

Figure A.45 FTIR spectrum of **C24** 101
Figure A.46 X-ray crystal structure of **C20•CH_3CN**, at 296 K: (a) asymmetric unit; (b) unit cell... 102
Figure A.47 X-ray crystal structure of **C21**, at 296 K: (a) asymmetric unit; (b) unit cell. 102
Figure A.48 X-ray crystal structure of **C22•H_2O•CH_3CN**, at 296 K: (a) asymmetric unit; (b) unit cell. 102
Figure A.49 Hydrogen bonds in the X-ray single crystal structure: (a) **C20•CH_3CN;** (b) **C21** and (c) **C22•H_2O•CH_3CN.** 103
Figure A.50 Single Crystal and powder X-ray diffractogram of **C20•CH_3CN.** 103
Figure A.51 Single Crystal and powder X-ray diffractogram of **C21** 104
Figure A.52 Single Crystal and powder X-ray diffractogram of **C22•H_2O•CH_3CN.** 104
Figure A.53 FTIR spectrum of **C26** 104
Figure A.54 FTIR spectrum of **C27** 105
Figure A.55 FTIR spectrum of **C28** 105
Figure A.56 X-ray crystal structure of **C25**, at 296 K: (a) asymmetric unit; (b) unit cell. 106
Figure A.57 X-ray crystal structure of **C26•2H_2O•CH_3CN**, at 296 K: (a) asymmetric unit; (b) unit cell. 107
Figure A.58 X-ray crystal structure of **C27•H_2O•CH_3CN**, at 296 K: (a) asymmetric unit; (b) unit cell. 107
Figure A.59 X-ray crystal structure of **C28•2H_2O**, at 296 K: (a) asymmetric unit; (b) unit cell. 107
Figure A.60: Hydrogen bonds in the X-ray single crystal structure: (a) **C25;** (b) **C26•2H_2O•CH_3CN** and (c) **C27•H_2O•CH_3CN;** C-H$\cdots$**π** (d) **C8•H2O•CH3CN** 108
Figure A.61 Single Crystal and powder X-ray diffractogram of **C25** 108
Figure A.62 Single Crystal and powder X-ray diffractogram of **C26•2H_2O•CH_3CN.** 109
Figure A.63 Single Crystal and powder X-ray diffractogram of **C27•H_2O•CH_3CN.** 109
Figure A.64 Single Crystal and powder X-ray diffractogram of **C28•2H_2O** 109
Figure A.65 FTIR spectrum of **C29** 110
Figure A.66 FTIR spectrum of **C30** 110
Figure A.67: X-ray crystal structure of **C29**, at 296 K: (a) asymmetric unit; (b) unit cell 111
Figure A.68 X-ray crystal structure of **C30**, at 296 K: (a) asymmetric unit; (b) unit cell. 111
Figure A.69 Hydrogen bonds in the X-ray single crystal structure: (a) **C29** and (b) **C30**. 112
Figure A.70 Single Crystal and powder X-ray diffractogram of **C29** 112
Figure A.71 Single Crystal and powder X-ray diffractogram of **C30** 112
Figure A.72 $\chi_M T$ vs T plot for **C29**, at the rate 1 K min^{-1} 113
Figure A.73 Powder X-ray diffractogram before and after SQUID of: (a) **C3•H_2O•CH_3CN;** (b) **C8•H_2O•CH_3CN;** (c) **C22•H_2O•CH_3CN.** 114
Figure A.74 FTIR spectrum of **C31** 115
Figure A.75 FTIR spectrum of **C32** 115
Figure A.76 FTIR spectrum of **C33** 116
Figure A.77 FTIR spectrum of **C34** 116
Figure A.78 FTIR spectrum of **C35** 117
Figure A.79 FTIR spectrum of **C36** 117
Figure A.80 FTIR spectrum of **C38** 118
Figure A.81 FTIR spectrum of **C39** 118
Figure A.82 FTIR spectrum of **C40** 119
Figure A.83 FTIR spectrum of **C41** 119

Scheme 2.1 Reaction mechanism for the synthesis of the tridentate ligands (X_1=F, Cl, Br, I and X_2= F, Cl, Br, I, NO_2). 8
Scheme 2.2. Synthesis of pentadentate ligands (X_1=X_2=H, F, Cl, Br, I). 9
Scheme 2.3 Synthesis of the complexes with the 3,5-Br-salEen ligand with the anions perchlorate, hexafluorophosphate, tetraphenylborate, tetrafluoroborate and nitrate 9
Scheme 2.4 Synthesis of the complexes with the 3,5-Cl-salEen ligand with the anions perchlorate, hexafluorophosphate, tetraphenylborate and nitrate. 17

Scheme 2.5 Synthesis of the complexes with the 3,5-F-salEen ligand, with the anions perchlorate, hexafluorophosphate, tetraphenylborate, tetrafluoroborate and nitrate.......... 23
Scheme 2.6 Synthesis of the complexes with the 3,5-I-salEen ligand, with the anions perchlorate, hexafluorophosphate, tetraphenylborate, tetrafluoroborate and nitrate.......... 30
Scheme 2.7 Synthesis of the complexes with the 3-Br-5-Cl-salEen ligand, with the anions perchlorate, hexafluorophosphate, tetraphenylborate, tetrafluoroborate and nitrate.......... 36
Scheme 2.8 Synthesis of the complexes with the 5-Cl-3-I-salEen ligand, with the anions perchlorate, hexafluorophosphate, tetraphenylborate and tetrafluoroborate.......... 43
Scheme 2.9 Synthesis of the complexes with the 5-Br-3-NO_3-salEen ligand, with the anions hexafluorophosphate and tetraphenylborate. 49
Scheme 2.10 Synthesis of the organic luminescent dye. 58
Scheme 2.11 Synthesis of the inorganic luminescent dye.......... 59
Scheme 2.12 Synthesis of the complexes with the pentadentate ligands (X= F, Cl, I, NO_2) and L2 (Ru complex). 61

Table 2.1 Wavenumbers for the characteristic FTIR spectrum bands, for complexes **C1-C5**.......... 10
Table 2.2 Values for the bands UV-vis, for complexes **C1-C5**.......... 11
Table 2.3 Crystal data and structure refinement of **C1** and **C3•H_2O•CH_3CN**.......... 12
Table 2.4 Representative bond lengths of **C1** and **C3•H_2O•CH_3CN**, at 296 K. 13
Table 2.5 Hydrogen bond lengths and angles for **C1** and **C3•H_2O•CH_3CN**.......... 14
Table 2.6 Wavenumbers for the characteristic FTIR spectrum bands, for complexes **C6-C9**.......... 18
Table 2.7 Values for the bands UV-vis, for complexes **C6-C9**.......... 19
Table 2.8 Representative bond lengths of **C6** and **C8•H_2O•CH_3CN**.......... 20
Table 2.9 Hydrogen bond and C-H···π interaction lengths and angles for **C6** and **C8•H_2O•CH_3CN**. 20
Table 2.10 Wavenumbers for the characteristic FTIR spectrum bands, for complexes **C10-C14**. 24
Table 2.11 Values for the bands UV-vis, for complexes **C10-C14**. 25
Table 2.12 Representative bond lengths of **C10-C12_2•CH_3CN** and **C14** at 296 K.......... 27
Table 2.13 Hydrogen bond lengths and angles for **C10-C12_2.H_2O.CH_3CN** and **C14**. 27
Table 2.14 Representative bond lengths of **C12_2•CH_3CN** at 110 K and 296 K. 29
Table 2.15 Hydrogen bond lengths and angles for **C12_2•CH_3CN** at 110 K and 296 K.......... 29
Table 2.16 Wavenumbers for the characteristic FTIR spectrum bands, for complexes **C15-C19**. 31
Table 2.17 Values for the bands UV-vis, for complexes **C15-C19**. 32
Table 2.18 Representative bond lengths of **C15**, **C18** and **C19** at 296 K.......... 33
Table 2.19 Hydrogen bond lengths and angles for **C15**, **C18** and **C19**.......... 34
Table 2.20 Wavenumbers for the characteristic FTIR spectrum bands, for complexes **C20-C24**. 36
Table 2.21 Values for the bands UV-vis, for complexes **C20-C24**. 37
Table 2.22 Representative bond lengths of **C20•CH_3CN-C22•H_2O•CH_3CN** at 296 K. 38
Table 2.23 Hydrogen bond lengths and angles for **C20•CH3CN-C22•H2O•CH3CN**.......... 39
Table 2.24 Representative bond lengths of **C22•H_2O•CH_3CN** before SQUID magnetometry at 296 K and **C22** after SQUID magnetometry at 110 K. 43
Table 2.25 Wavenumbers for the characteristic FTIR spectrum bands, for complexes **C25-C28**. 44
Table 2.26 Values for the bands UV-vis, for complexes **C25-C28**. 45
Table 2.27 Representative bond lengths of **C25-C28•$2H_2O$** at 296 K.......... 46
Table 2.28 Hydrogen bond and C-H···π interaction lengths and angles for **C25-C27•H_2O•CH_3CN**. 46
Table 2.29 Wavenumbers for the characteristic FTIR spectrum bands, for complexes **C29** and **C30**. 49
Table 2.30 Values for the bands UV-vis, for complex **C29** and **C30**. 50
Table 2.31 Representative bond lengths of **C29** and **C30** at 296 K.......... 50
Table 2.32 Hydrogen bond lengths and angles for **C29** and **C30**.......... 51
Table 2.33 Representative bond lengths of **C29** at 110 K and 296 K. 52
Table 2.34 Hydrogen bond lengths and angles for **C29** at 110 K and 296 K.......... 52
Table 2.35 Σ, Θ, Ω, τ and $\boldsymbol{\alpha}$ for **C1** to **C30**, at 296 K.......... 57
Table 2.36 Wavenumbers for the characteristic FTIR spectrum bands, for complexes **C31** to **C41**... 62
Table 2.37 Values for the bands UV-vis, for complexes **C31** to **C41**.......... 63
Table 2.38 $\chi_M T$ values for the **C31-C41** at 370 K. 65

Table A.1 Crystal data and structure refinement of **C6** and **C8•H_2O•CH_3CN**................................. 84
Table A.2 Crystal data and structure refinement of **C10-C12_2•CH_3CN** and **C14**.......................... 89
Table A.3 Crystal data and structure refinement of **C5, C18** and **C19**.. 96
Table A.4 Crystal data and structure refinement of **C20•CH_3CN-C22•H_2O•CH_3CN**.................... 101
Table A.5 Crystal data and structure refinement of **C25-C28•2H_2O**... 106
Table A.6: Crystal data and structure refinement of **C29** and **C30**... 111

Abbreviations and Symbols

Δ_{oct} – Delta octahedral
γ – Molar fraction
μ – Magnetic moment
χ_M – Molar magnetic susceptibility
Φ_F – Quantum yield
1D – One dimension
Ac – Acid
BODIPY – Borondipyrromethene
DMF – Dimethylformamide
DMSO – Dimethyl sulfoxide
DNA – Deoxyribonucleic acid
dppz - Dipyridophenazine
EtOH – Ethanol
FTIR – Fourier-transform infrared
HS – High-spin
ILCT – Intra-ligand charge-transfer
IS – Intermediate spin state
ISC – Intersystem crossing
k_B – Boltzmann constant
LIESST – Light-induced excited spin state trapping
LLCT – Ligand-to-ligand charge transfer
LMCT – Ligand-to-metal charge transfer
LMMCT – Ligand-to-metal-metal charge transfer
LS – Low-spin
MeOH – Methanol
MLCT – Metal-to-ligand charge transfer
MLLCT – Metal-to-ligand-ligand charge transfer
MMLCT – Metal-to-metal-ligand charge transfer
n – Number of unpaired electrons
NIR – Near infrared
NMR – Nuclear magnetic resonance
OLEDS – Organic light-emitting diodes
phen - phenanthroline
S – Total spin
SalEen – *N*-ethyl-*N*-(2-aminoethyl)salicylaldiminate
Salpet – 2-hydroxybenzylidene)amino)ethyl)amino)propyl)imino)methyl)phenol
SCO – Spin crossover
SQUID – Superconducting quantum interference device
$T_{1/2}$ – Temperature at which half of the metal centers are in the low-spin state and half are in the high-spin state
UV-vis – Ultraviolet-visible

1. Introduction

1.1. Spin crossover (SCO) and its relevance

Spin crossover is a large, interesting and important area of study in coordination chemistry.[1] This phenomenon is known for more than eighty years and with the advances in technology, the study of compounds with this property deserved a renewed attention in recent years, leading to a boom of research in this area.[2]

Researchers working in this field have created a wide range of materials: SCO networks,[3-6] frameworks,[7-9] gels,[10-12] liquid crystals,[13-15] nanoparticles and nanocrystals,[16-19] nanowires,[20] thin films[21-23] and have applied techniques to fabricate SCO devices.[24] SCO compounds present an electronic lability,[25] that allows materials, with some first-row transition metals, to switch their spin state under an external perturbation, making them candidates for processing, display, memory and switching devices and sensors.[26-29]

This electronic lability results in the change of the magnetic moment and the colour of the compounds, either in solution or in the solid state.[26]

1.2. Spin states in spin crossover

SCO can make use of the crystal field theory to explain the lability of the spins observed in octahedral complexes. This theory explains the bonding in complexes of *d*-block metals, and it is an electrostatic model that uses the ligand electrons to generate an electric field around the metal centre. In this model there are no metal-ligand covalent interactions because the ligands are considered as point charges. The crystal field theory predicts that for an octahedral geometry the five *d* orbitals in the metal complex are not degenerated but instead divided in two sets of different energies, the bonding orbitals t_{2g} of lower energy and the anti-bonding orbitals e_g* of higher energy. The split between these two sets depends on the crystal field, determined by the arrangement and type of ligands. In the octahedral geometry, the split occurs as exhibited in **Figure 1.1**. The energy difference between the two levels is named Δ_{oct}.[30]

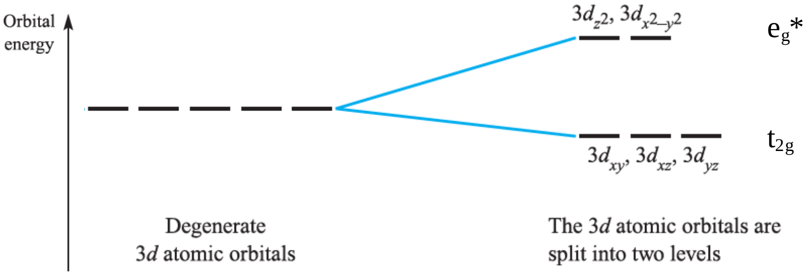

Figure 1.1 Energy levels splitting in an octahedron geometry, $3d_{xy}$, $3d_{xz}$ and $3d_{yz}$ in the t_{2g} level and the $3d_{z^2}$ and $3d_{x^2-y^2}$ in the e_g^* level.[30]

The 3*d* transition metals, between d^4 and d^7, are the only who can present different electron distributions for the same number of electrons in the *d* orbitals. This means that they have the possibility of adopting different electronic configurations, resulting in the high-spin (HS), the low-spin (LS) and rarely in the intermediate spin state (IS).[31] The HS state has the maximum number of unpaired spins and the LS state has the minimum. This electron rearrangement in a complex depends on the ligand field strength and/or pairing energy of the *d* electrons.[32] The HS state is adopted when the ligand field strength is significantly smaller than the pairing energy, which means that the Δ_{oct} is small and the lowest total energy occurs when the electrons are distributed through all the orbitals. In opposition, the LS state occurs when the ligand field strength is significantly larger than the pairing energy, which means that the Δ_{oct} is also large and the lowest total energy happens when the electrons are pairing.[29]

SCO takes place by switching between the two states, HS and LS,[33] which makes this property one of the most spectacular examples of bistability in molecular chemistry.[29] This phenomenon only occurs when the ligand field and the pairing energy of *d* electrons are around the same order of magnitude.[29,32] The switching can be induced by different stimuli, through variation of pressure,[34-36] temperature,[37-38] light irradiation,[39-41] magnetic field,[19] electric field[42] and adsorption/desorption of guest molecules.[31] The most common SCO metals are Fe(II) and Co(II), but in the last few years the Fe(III) and Mn(III) have also seen an increase of reported cases.[43]

1.2.1. Spin crossover curves

SCO curves are very informative and take many forms for systems in the solid state. Below (**Figure 1.2**) is shown the most common SCO profiles that compounds can adopt during spin-state switching.[32] One of the most important information in these curves is the degree of cooperativity associated with the transition, especially the change in metal-donor atom distances. A change in temperature leads to a change in the metal-donor atom distances, therefore, in the lattice properties. A lower temperature represents a smaller bond distance and a lower spin state, while a higher temperature translates to a longer bond distance and, consequently, a higher spin state. When the two states of a spin multiplicity acquire a 1:1 ratio ($\gamma_{HS} = \gamma_{LS} = 0.5$), it is defined as the critical temperature, usually represented as $T_{1/2}$.[44]

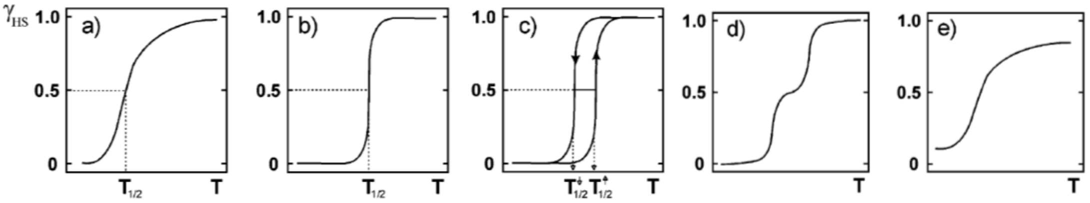

Figure 1.2 Most common SCO curves: (a) gradual, (b) abrupt, (c) abrupt with thermal hysteresis, (d) stepped and (e) incomplete.[32]

The most interesting SCO profile is the one showing an abrupt transition with thermal hysteresis (**Figure 1.2: c**), since it reveals a highly effective cooperativity between metal centers. The bistability associated with the hysteresis allows memory character and highlights potential for systems in memory and display devices. Therefore, the search for a binary system with a well-defined and reasonably broad hysteresis loop at room temperature that can be use in nano-devices continues as one of the main research branches in SCO.[44]

1.2.2. Magnetic Moment and Magnetic Susceptibility

As a consequence of the unpaired electrons in the *d* orbitals, SCO compounds are paramagnetic, and, therefore, present a magnetic moment, which is related with the number of unpaired electrons, n, and total spin, S, calculated by the two following equations, that only consider the spin angular momentum of the electrons, not considering the orbital angular momentum: [30]

$$\mu_{eff} = \sqrt{n(n+2)} \qquad (1.1)$$

$$\mu_{eff} = 2\sqrt{S(S+1)} \quad S = {}^{n}/_{2} \qquad (1.2)$$

In the experimental field of magnetism, the effective magnetic moment (μ_{eff}) can be obtained from the molar magnetic susceptibility (χ_M). To relate $\chi_M T$ and μ_{eff}, expressed in Bohr magnetons (μ_B), equation 1.3 is used, where the 2.828 factor is a result of the Boltzmann constant (k), the Avogadro number (L) and the vacuum permeability (μ_0), in Gaussian units. [44]

$$\mu_{eff} = \sqrt{\frac{3k\chi_M T}{L\mu_0\mu_B^2}} = 2.828\sqrt{\chi_M T} \qquad (1.3)$$

In this dissertation, the samples studied were solids and the apparatus used to measure the magnetisation of our compounds was the SQUID (superconducting quantum interference device) magnetometer. Within the scope of this thesis, a short-term scientific mission took place at the Institut de Chimie de la Matière Condensée de Bordeaux, under the supervision of Dr. Guillaume Chastanet, where it was possible to perform magnetic measurements to study the photoswitching properties in a SQUID magnetometer using light-induced excited spin state trapping (LIESST), but unfortunately none of the samples studied showed this property.

1.2.3. (Photo)Magnetic measurements

Using a SQUID magnetometer, one measures the magnetisation of the sample when exposed to a magnetic field. The magnetisation is then converted (magnetisation/applied magnetic field) in the magnetic susceptibility of the compound. The sample, exposed to a magnetic field, is moved up and down through the loops, which creates an alternating magnetic flux. The potential difference across the magnetometer is examined. These magnetisation measurements are performed as a change of temperature.[45]

The light-induced excited spin state trapping (LIESST) can be used to switch from the LS state to a metastable HS state by exposing the sample to a source of light (laser), usually at low temperatures. The technique traps the systems in the HS state, allowing studies of chemical and physical parameters. In this case, the induced HS state can be transformed in the LS state during warming and the relaxation process can be studied.[32] At cryogenic temperatures, under continuous irradiation, the HS/LS relaxation slows down, which allows to a longer excited metastable state.[39] The LIESST can also give insights on the cooperative effects in crystalline solids.[44,46]

The term T(LIESST) was presented in a way to record the limit temperature above where the photo-induced state ceases to exist.[46] In the group that I had the opportunity to work with in Bordeaux, they used the SQUID magnetometer to perform them, and investigate the relaxation mechanism with kinetics measurements.

1.3. Spin crossover in Fe(III)

The Fe(III) species have five *d* electrons,[44] a d^5 system, where both HS and LS states are paramagnetic (**Figure 1.3**) with one unpaired electron, S=1/2 and $\chi_M T$=0.37 cm^3 mol^{-1} K, in the low-spin state and five unpaired electrons, S=5/2 and $\chi_M T$=4.38 cm^3 mol^{-1} K, in the high-spin state. However, this system can sometimes adopt an intermediate paramagnetic state with S=3/2 and $\chi_M T$=2.19 cm^3 mol^{-1} K.[29,33]

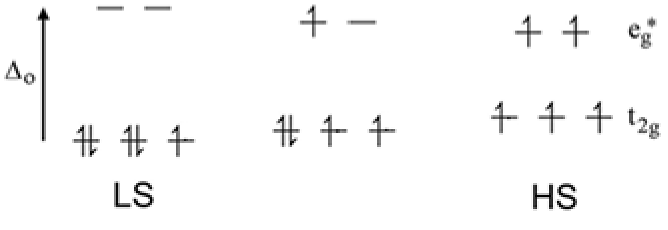

Figure 1.3 Iron(III) electron distribution to octahedron LS, IS and HS.

Fe(III) complexes proved interesting for the development of memory systems and sensors, among others applications, since iron is the most abundant transition metal in the planet. Fe(III) has the capacity to change the magnetic moment and the SCO can be near or at room temperature, so they are ideal candidates for this phenomenon.[33,47,48]

1.4. Ligands for spin crossover in Fe(III) complexes

Several studies proved that ligand design is critical to find a molecule displaying the SCO phenomenon.[43] Monomeric iron(III) SCO compounds can be formed by different ligands: bidentate, tridentate, tetradentate, pentadentate and hexadentate.[48]

For this dissertation, I focused in tridentate and pentadentate Schiff base ligands to synthesize different iron(III) complexes. These types of systems are used in Fe(III) SCO.[48] The ligands are often derived from salicylaldehyde and amines and are very versatile as one can have the starting compounds with different substituents, thus affecting the ligand field strength.[3]

The tridentate ligands with a N2O donor set have been studied in the last few years, where two ligands coordinate to the metal center, adopting a N4O2 donor set. The salEen [*N*-ethyl-*N*-(2-aminoethyl)salicylaldiminate] (**Figure 1.4**) is an example of a N2O tridentate ligand. [47-51]

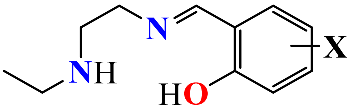

Figure 1.4 Schiff base tridentate ligand: H_2-X-salEen.

The most common pentadentate ligands in Fe(III) SCO are dianionic Schiff bases with N3O2 donor sets.[48] The H_2-X-salpet is one of the ligands in this group (**Figure 1.5**).[52,53] To get Fe(III) complex in an octahedral geometry, a ligand in the final position is needed. When the reaction occurs with the $FeCl_3$, the final position has one chloride ligand. A N-donor ligand can create more stability for the complexes, so a change between chloride ligand and the N-donor ligand can occur.[48] If we have a photoactive ligand with a N-donor ligand (pyridine, per example), it is possible to have a complex with a multifunctional system.[52,53]

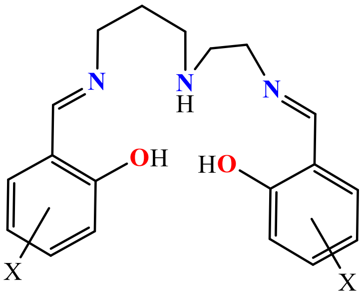

Figure 1.5 Schiff base pentadentate ligand: H_2-X-salpet.

1.4.1. Impact of the solvent, anion and halogen substituent in spin crossover

Inclusions or modifications in the crystal structure, as the solvent, anion or halogen groups, can change dramatically the SCO system.[2,32,33,47]

The existence of a solvent or an anion in the crystal lattice provides an additional defect or positional disorder in the structure.[29] If the complex crystalizes with a solvent in the crystal structure, and the solvent is removed, the crystal lattice is rearranged and, consequently, the magnetic profile is different. Studies also indicate that changing the anion is the reason for the alteration of transition temperature or the type of curve.[44]

1.5. Luminescence and its importance

Luminescence is a very interesting and complex phenomenon that allows some molecules to have a spontaneous emission of radiation. This emission occurs from an excited state, that can be generated in different ways, by photonic excitation, mechanical forces, and chemical/electrochemical reactions, for example.[54]

In terms of mechanism, the luminescence happens as a consequence of the transition of electrons from a ground state to an excited state via absorption of a photon and the return to the ground state accompanied by the emission of a photon. Luminescence can be divided in two types, fluorescence and phosphorescence. Fluorescence is the transition that occurs from a single excited state (S_1) to the ground state (S_0). Phosphorescence is a more complex process, as it happens from the single state (S_1) to the excited triplet state (T_1), creating an intersystem crossing (ISC), and followed by the transition to the ground state (S_0), forbidden by symmetry. These two mechanisms are represented by the Jablonski diagram, **Figure 1.6**.[54]

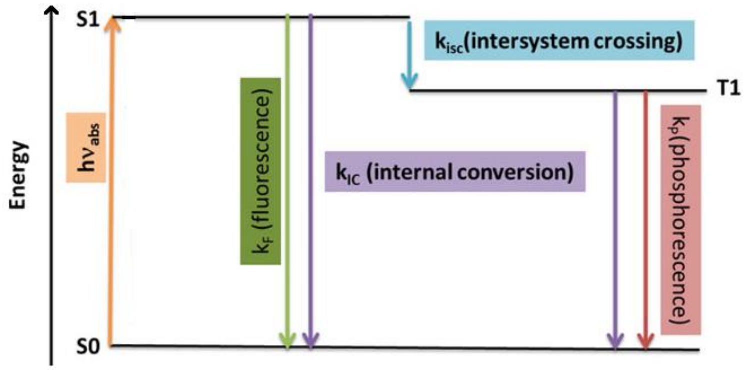

Figure 1.6 Fluorescence and phosphorescence mechanisms (Jablonski diagram).[55]

In fluorescence, the quantum yield φ_F, with absence of external quenches can depend only on kinetic parameters. In phosphorescence, the processes are analogous, but in this case have the competition between the K_P and K_{IC} and the triplet formation, quantum yield φ_{ISC}.[55]

$$\varphi_F = \frac{K_F}{K_F+K_{IC}+K_{ISC}} \tag{1.4}$$

$$\varphi_P = \frac{K_{ISC}}{K_F+K_{IC}+K_{ISC}} * \frac{K_P}{K_p+K_{IC}} \tag{1.5}$$

Fluorescence can have three stage processes, excitation, excited state lifetime and fluorescence emission. As its lifetime is shorter than the phosphorescence, it is the most common used mechanism.[56] In the last few years, the design and synthesis of organic and coordination compounds with luminescence phenomenon, through coordination chemistry, secondary interactions, hydrogen bonding, π interactions or even Van der Waals interactions, led to an increase of chemical and biological research in this area, since it is largely applied in the commercial, the industrial, the technological and the medical fields.[54,57-59] These species have spectroscopic, photophysical and electrochemical properties.[58] The applications are special as trace metal analysis, metal signalling, construction of optical devices and sensor molecules;[57] in bioimaging, sensing, diagnosis and therapy using organic light-emitting diodes (OLEDs);[58,59] hybrid materials and coordination networks;[54] luminescent sensors and photonic switches;[60] for analytical chemistry and clinical biochemistry.[61]

Since luminescence can occur in organic or inorganic molecules, I studied one luminescent molecule of each type. The idea was to coordinate these molecules to the pentadentate Fe(III) complex by metathesis of the labile chloride anion by the luminescent molecules. I focused mainly on molecules emitting in the NIR region far from the strong charge transfer bands in the visible region these Fe(III) complexes possess, therefore avoiding quenching of the luminescence by the Fe(III) absorbance bands.

1.5.1. Near Infrared region

Fluorescent dyes that are bright, and emit in the near infrared (NIR) region, 650 to 2000 nm, [62,63] have been essential in optical engineering, analytical chemistry, biologic chemistry, medicine and photochemistry.[64,65] The most common NIR lights can be found in the technology field, remote controllers for televisions or electronic devices.[63]

This type of dyes show several advantages, as reduction of background signal, because of the lowest auto-absorption and auto-fluorescence of biomolecules, low light scattering and deep penetration of NIR light and low-cost excitation light sources.[63,66] The biggest problem so far for these fluorescent dyes is the insufficient optical characteristics, low fluorescence quantum yields or a lack of photostability.[62]

1.5.1.1. Organic molecule – Keio Fluors

An organic group that have been studied for fluorescent dyes is the BODIPY (borondipyrromethene), **Figure 1.7**, since they have excellent characteristics in intense fluorescence quantum yields, high photo and chemo-stability, sharp absorption and fluorescence emission spectra.[62,65]

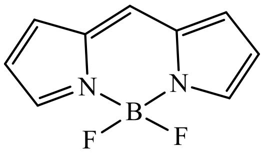

Figure 1.7 BODIPY, fluorescent organic dyes.

To be able to synthetize this type of fluorescent molecules to emit in NIR region, researchers have used different approaches:[62] introduction of electron-donating groups,[67,68] replacement of a C atom with a N atom,[69-71] rigidification of rotatable molecules,[72-74] extension of the π-conjugation by introduction of methylene structures[75,76] and extension of the π-conjugation by the fusion of aryl group.[77-79]
The Keio Fluors are one of the BODIPY subgroup, where with the fusion of an aryl group it is expected that the quantum yield and the extinction coefficient could be increased.[62] In this work, we focused on the Keio Fluor represented in **Figure 1.8**.

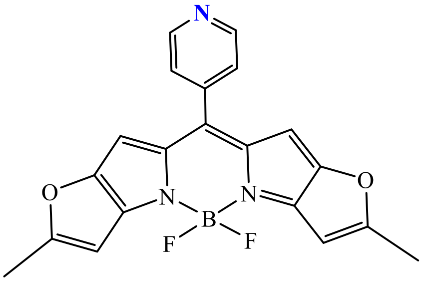

Figure 1.8 Keio Fluors, fluorescent organic dye.

1.5.1.2. Coordination compounds – Ruthenium complexes

Transition metals have been extensively studied for luminescent applications, as they possess rich photophysical properties, particularly the d^6, d^8 and d^{10} electronic configurations. Ruthenium(II), platinum(II), iridium(III), osmium(II), gold(I) and rhenium(I), are examples of these.[80,81]
In comparison to organic molecules, the transition metals can also have metal-to-ligand charge transfer (MLCT), ligand-to-ligand charge transfer (LLCT), intra-ligand charge-transfer (ILCT), ligand-to-metal charge transfer (LMCT), metal–metal-to-ligand charge-transfer (MMLCT), ligand-to-metal–metal charge transfer (LMMCT) and metal-to-ligand–ligand charge-transfer (MLLCT) states. These excited properties are very sensitive to the metal centre, ligands (naphthalene, anthracene and phenanthrene are some examples)[82] and the environment and in that way it is possible to prepare complexes for specific applications, such as anion, cation, amino acids, gas and DNA detection and O_2 sensors.[80]
This specific type of complexes satisfy water solubility, intense luminescence, kinetic inertness, high photo, chemical and optical stability, long lifetimes and low-energy absorption.[83-85]
Such properties allow being specific for photochemistry and photo applications;[80,86] optoelectronics and optical thermometry;[86] luminescent and imaging sensors;[80,86] biological systems, bioimaging for cell imaging;[83-85] medical field, such as antitumor, antibacterial, anti-inflammatory, antimicrobial

properties, DNA foot printing, new drugs for cancer, diabetes, Parkinson and epilepsy disease and restriction enzymes, peptides, proteins receptors;[81,85,87-90] technology and nanotechnology, electronic and nanodevices; colorimetric and chemosensors, for analytical, medical and environmental systems.[85,87]

The ruthenium(II) is especially sensitive for DNA, being useful for new diagnostics based on luminescent DNA probes. The Ru(II) complex that we focused was the one in **Figure 1.9**.[92]

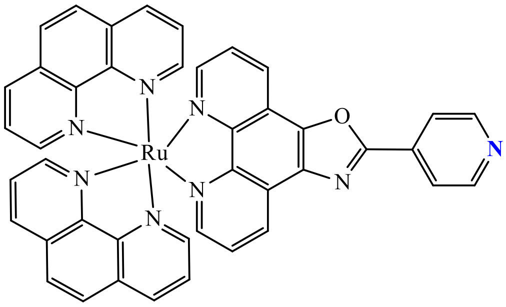

Figure 1.9 Ruthenium complex, luminescent inorganic dye.

1.6. Spin crossover luminescent complexes (multifunctional materials)

The multifunctional materials are one of the main current objectives for SCO research, since these materials have the possibility of combining the switching from SCO with others physical or chemical properties.[2,48] The SCO can be combined with liquid-crystalline behavior, structural arrangements, gel and porous properties, molecular recognition, electrical functionalities (conductivity, magnetism, transport or optic), luminescence, optical activity, electroluminescence, ferroelectricity and redox.[2,49,93,94] Theses functionalities can be applied, for example, in photophysical, electrochemical and catalytic properties, hydrogelation, OLEDs, mix valence chemistry, magneto-optical switches.[90,95]

When SCO is combined with luminescence it is possible to have the two different spin states, LS and HS, and a signaling part with emission that can affect the spin state switching, and that way to create an SCO-based magneto-optical switch. These complexes can be classified in two categories: the first is the complexation of SCO active metal ions with intrinsically luminescent chelating ligands or employing charge balancing luminescent counter anions, but this way has been proven to be difficult, since the complexes exhibited an incomplete or inactive SCO. The second is the covalent-grafting or physical-doping of a luminescent molecule with an SCO active molecular complex, creating a nanocomposite and 1D coordination network.[95]

When these two properties are combined, it is possible to have different applications in nanoscale of hybrid SCO materials,[96] chemosensors and biosensors for nanothermometry and others applications[80,97-99] and fluorescence microscopy.[100,101]

There are potential applications as selective delivery agents in specific iron(III) complexes with a fluorescent ligand, allowing monitoring of the distribution of the fluorophores and iron(III) complexes in cancer cells.[102]

2. Results and discussion

The compounds described in this section were synthesized and characterized by me. Prof. Liliana P. Ferreira was responsible for the collection and treatment of the SQUID raw data. Dr. Clara Gomes was in charge of the collection and treatment of the single crystal X-ray raw data. Dr. Ana Mourato and Prof. Maria Estrela Jorge were responsible for the collection of the powder X-ray raw data.

The main goal of this research project was to synthesize and characterize Fe(III) compounds displaying the SCO phenomenon and Fe(III) multifunctional compounds combining the SCO phenomenon with luminescence.

2.1. Ligands

For the SCO compounds, due to our interest to study the effect of the substituent on the SCO phenomenon, we opted to study different combinations of halogens and in one case we replaced one of the halogens by a strong electron-withdrawing NO_2 group. For convenience purposes we define two classes of ligands: the homo-substituent ligands containing the same halogen in the aromatic ring and the hetero-substituent ligands containing different halogens in the aromatic ring and in one case containing one halogen and a nitro group in the aromatic ring. We chose different salEen ligands, the homo-substituent ligands synthesized were the 3,5-Br-salEen, 3,5-Cl-salEen, 3,5-F-salEen and 3,5-I-salEen and the hetero-substituent were the 3-Br-5-Cl-salEen, 5-Cl-3-I-salEen and 5-Br-3-NO_2-salEen. The ligand preparation was performed in the same fashion by a condensation reaction, **Scheme 2.1**, to a solution of *N*-ethylethylenediamine in methanol the desired aldehyde was added and left stirring for 15 min at room temperature to give a yellow solution, confirming the imine formation.

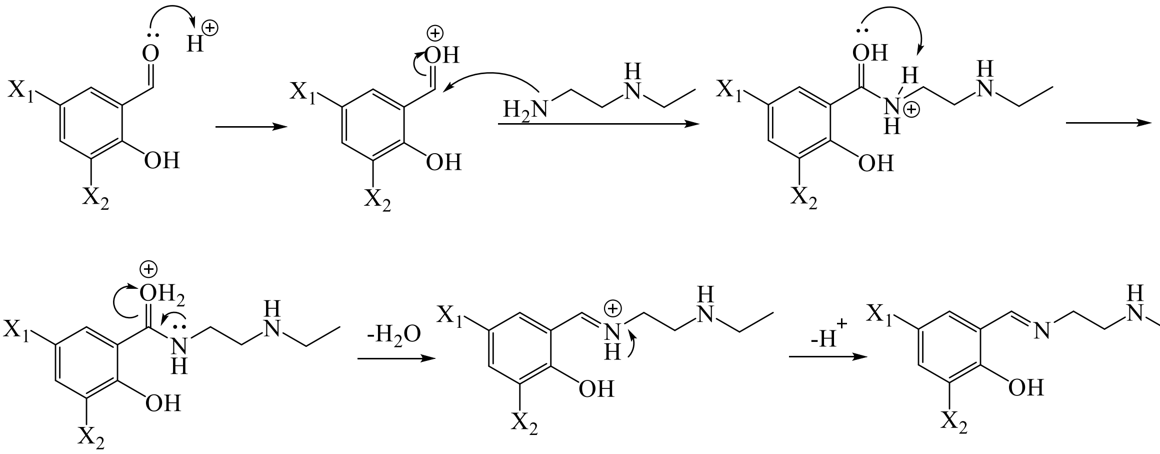

Scheme 2.1 Reaction mechanism for the synthesis of the tridentate ligands (X_1=F, Cl, Br, I and X_2= F, Cl, Br, I, NO_2).

For the multifunctional SCO luminescent compounds, different salpet ligands were synthesized. The preparation of the ligands (**Scheme 2.2**) follows the same reaction mechanism as for the salEen ligands, to a solution of N-(2-aminoethyl)propane-1,3-diamine in methanol the chosen aldehyde was added and left stirring for 45 min at the reflux temperature to give a yellow solution, confirming the imine formation. The mono-substituent salpet ligands synthesized were the H_2salpet, 5-Br-salpet, 5-Cl-salpet, 5-F-salpet and 5-I-salpet. The homo-substituent salpet ligands were 3,5-Br-salpet, 3,5-Cl-salpet, 3,5-F-salpet and 3,5-I-salpet and the hetero-substituents were the 3-Br-5-Cl-salpet and 5-Cl-3-I-salpet.

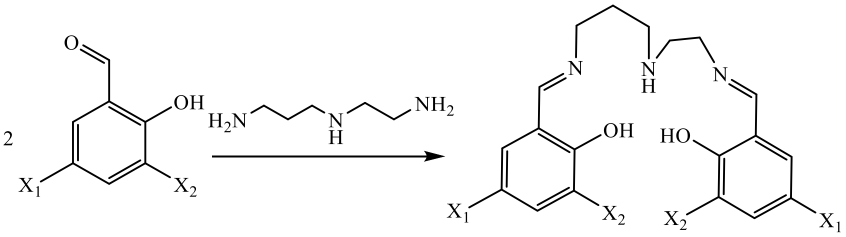

Scheme 2.2. Synthesis of pentadentate ligands (X_1=X_2=H, F, Cl, Br, I).

2.2. SCO complexes

The tridentate ligands discussed in the point above were then reacted with $Fe(NO_3)_3$ or different Fe(II) salts to produce the new Fe(III) salts after air oxidation. We also wanted to study the role of counter-ions in the SCO, so we choose five anions for the synthesis, which were perchlorate, hexafluorophosphate, tetrafluoroborate, tetraphenylborate and nitrate.

2.2.1. Homo-substituent compounds

[Fe(3,5-Br-salEen)$_2$]Y

The reaction of $Fe(NO_3)_3$ and different Fe(II) salts with 3,5-Br-salEen at room temperature resulted in very dark solutions sometimes accompanied by a dark powder, thus confirming the formation of coordination compounds.

In this group, five Fe(III) complexes were synthesized, the **C1** corresponds to [Fe(3,5-Br-salEen)$_2$]ClO_4, **C2** to [Fe(3,5-Br-salEen)$_2$]PF_6, **C3** to [Fe(3,5-Br-salEen)$_2$]BPh_4, **C4** to [Fe(3,5-Br-salEen)$_2$]BF_4 and **C5** to [Fe(3,5-Br-salEen)$_2$]NO_3, as shown in **Scheme 2.3**.

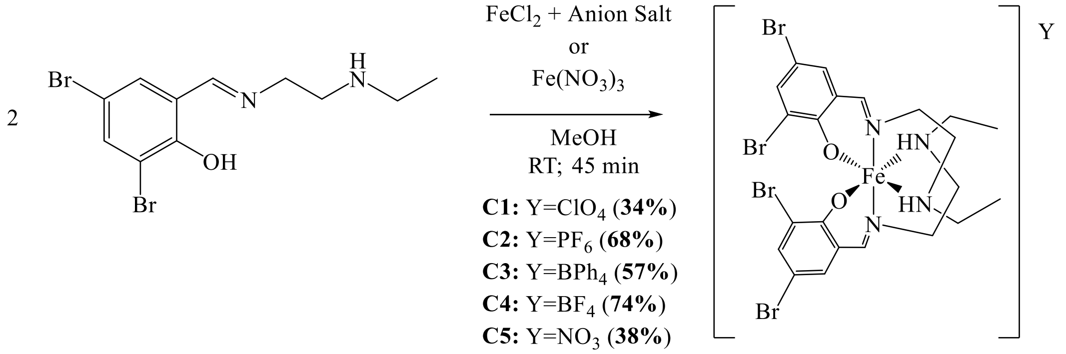

Scheme 2.3 Synthesis of the complexes with the 3,5-Br-salEen ligand with the anions perchlorate, hexafluorophosphate, tetraphenylborate, tetrafluoroborate and nitrate.

The complexes were characterized by Fourier-Transform Infrared (FTIR) spectroscopy, Ultraviolet-visible (UV-vis) spectroscopy, single crystal X-ray diffraction (although crystals were obtained for all complexes, only the **C1** and **C3** showed good quality for single crystal X-ray diffraction), powder X-ray diffraction and Superconducting Quantum Interference Device (SQUID) magnetometry.

FTIR and UV-vis spectroscopy

The FTIR spectroscopy was mainly used to confirm the imine formation through the observation of a strong stretching vibration and the presence of the different anions with the observation of their characteristic vibrational modes. The FTIR spectrum for the **C1** can be observed in **Figure 2.1**, and the assigned vibrations for **C1-C5** are in **Table 2.1.** The FTIR spectrum of the four remaining complexes can be found in the annexes, **Figure A.1**, **Figure A.2**, **Figure A.3** and **Figure A.4**.

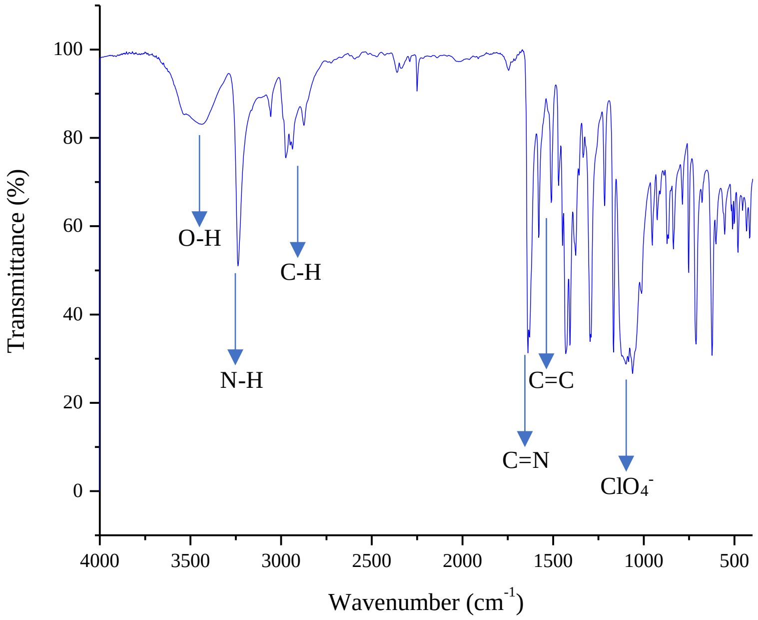

Figure 2.1 FTIR spectrum of **C1**.

Table 2.1 Wavenumbers for the characteristic FTIR spectrum bands, for complexes **C1-C5**.

Complex	**Wavenumber (cm^{-1})**						
	υ(O-H)	**υ(N-H)**	**υ(C-H)**	**υ(C=N)**	**υ(C=C)**	**Anion**	
C1	3439	3238	2974	1639	1576-1475	ClO_4^-	1063, 625
C2	3441	-	2978	1632	1578-1470	PF_6^-	839
C3	3431	3215	2984	1627	1579-1465	BPh_4^-	744-707
C4	3417	-	2972	1619	1578-1429	BF_4^-	1066
C5	3435	3170	2972	1624	1577-1511	NO_3^-	1383

As expected, the vibrations corresponding to O-H bonds are around 3400 cm^{-1}, N-H bonds are around 3200 cm^{-1} (only for **C1**, **C3** and **C5**), C-H bonds are around 2970 cm^{-1}, C=N bonds are around 1600 cm^{-1}, C=C bonds are between 1580-1430 cm^{-1} and the anions vibrations are perchlorate at 625 cm^{-1} and 1063 cm^{-1}, hexafluorophosphate at 839 cm^{-1}, tetraphenylborate at 707 cm^{-1} to 744 cm^{-1}, tetrafluoroborate at 1066 cm^{-1} and nitrate at 1383 cm^{-1}. For **C2** and **C4** the stretching of the N-H bond is not observed because the O-H band is very large and overlaps it. This is possibly related to the higher amount of water present in these two samples. Interesting is the observation of the changes on the imine stretching band which shows at the two edges (1639 cm^{-1} for ClO_4^- and 1619 for BF_4^-) the two anions that are mostly correlated. Both are tetrahedral anions with approximately the same electron density distribution. This possibly indicates that one of them is forming hydrogen bonds with the cation affecting ligand rigidity while the other is not.

The UV-vis spectra for all five complexes were recorded in acetonitrile between 200 and 900 nm and can be observed in **Figure 2.2**.

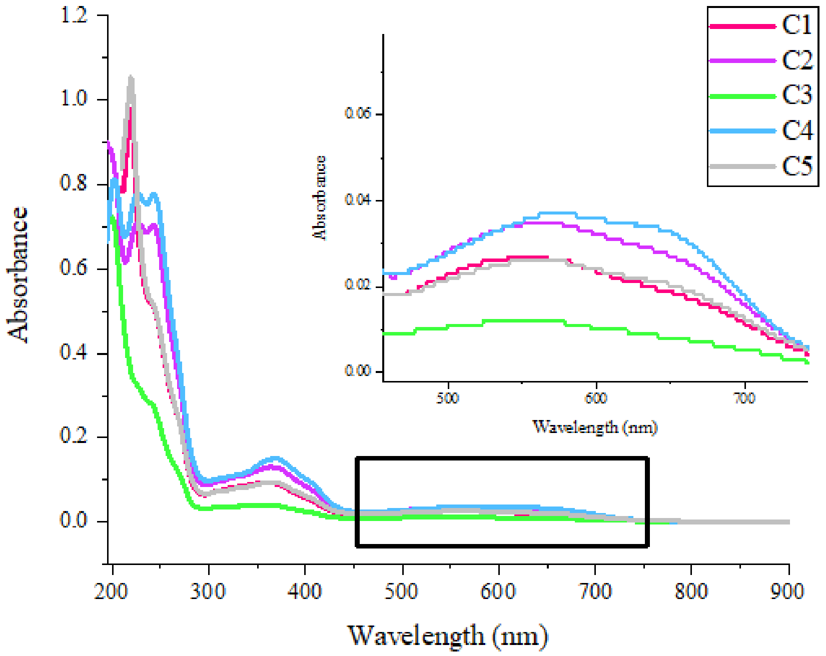

Figure 2.2 UV-vis spectra of **C1-C5** in acetonitrile.

The **C1** and **C3** present four absorption bands, the **C2** and **C5** present five and the **C4** presents six. Details on the bands can be observed in **Table 2.2**.

Table 2.2 Values for the bands UV-vis, for complexes **C1-C5**.

Complex	**Concentration (mol.dm^{-3})**	**Wavelength (nm)**	**Absorbance**	**Molar absorption coefficient (mol.dm^{-3}.cm^{-1})**
C1	10^{-5}	219.0	0.967	96 700
		241.0	0.516	51 600
		360.5	0.094	9 400
		553.0	0.027	2 700
C2	10^{-5}	226.5	0.711	71 100
		242.5	0.703	70 300
		364.0	0.131	13 100
		560.5	0.035	3 500
		635.0	0.028	2 800
C3	10^{-5}	199.0	0.726	72 600
		239.5	0.283	28 300
		356.5	0.041	4 100
		548.5	0.012	1 200
C4	2×10^{-5}	202.0	0.813	40 650
		226.5	0.779	38 950
		243.0	0.777	38 850
		368.5	0.150	7 500
		574.0	0.037	1 850
		649.0	0.033	1 650
C5	10^{-5}	219.5	1.053	105 300
		243.0	0.513	51 300
		364.0	0.095	9 400
		561.0	0.026	2 600
		649.0	0.021	2 100

All complexes in **Table 2.2** present bands at different wavelengths and with different molar absorption coefficients. The bands around 200 nm belong to intraligand interactions, with variations between 105 000 and 28 000 mol.dm^{-3}.cm^{-1}. The higher molar absorption coefficient belongs to **C1** and **C5** and the lower to **C4**. All complexes presented two of this bands except the **C4**, that showed three.

The bands between 300 and 400 nm should be attributed to charge-transfer between the ligands and the iron, or vice-versa, with variations between 9 500 and 3 500 mol.dm^{-3}.cm^{-1}. The bigger molar absorption coefficient belongs to **C1** and **C5** and the smaller to **C2** and **C3**. All complexes presented one of this bands.

Bands between 500 nm and 700 nm also correspond to charge-transfer between the ligands and the iron, or vice-versa, and can be related to the spin states of the metal.[103] The cation has two distinct absorbance bands, one corresponding to the HS state (≈ 500 nm) and the LS state (≈ 650 nm). The **C2, C4** and **C5** present two bands, one around 550 nm and other around 650 nm and the other two show only one band. The 550 nm band variates between 2 700 and 1 200 mol.dm^{-3}.cm^{-1}, the higher molar absorption coefficient belongs to **C1** and **C5** and the smaller to **C2** and **C4**. The 650 nm band varies between 2 800 and 1 650 mol.dm^{-3}.cm^{-1} and the smaller molar absorption coefficient belong to **C4**. In solution at room-temperature, the **C1** and **C3** are essentially low spin and the other three show a mixture between the LS state and the HS state, with more Fe(III) centres in the low spin state. In general, the **C5** presented a higher molar absorption coefficient and the **C4** presented the lower.

Structural characterization

Single Crystal X-ray diffraction

Single crystals with good quality for X-ray diffraction were only obtained for **C1** and **C3**. The remaining compounds were crystalline but presented poor or no diffraction. The single crystal X-ray diffraction allows the prediction of the spin state of the complex at a specific temperature, through the Fe-X bond lengths.

The X-ray data at 296 K revealed that one of the compounds was found in its unsolvated form, **C1**, but the other was crystallized as solvate, **C3•H_2O•CH_3CN**. The crystal data and structure refinement of **C1** and **C3•H_2O•CH_3CN** are listed in **Table 2.3**.

Table 2.3 Crystal data and structure refinement of **C1** and **C3•H_2O•CH_3CN**.

Complex	**C1**		**C3•H_2O•CH_3CN**	
Temperature	296(2) K		296(2) K	
Crystal system	Orthorhombic		Monoclinic	
Space group	P c a 21		P 21/c	
Unit cell dimensions	a = 26.465(6) Å	α = 90°	a = 17.313(2) Å	α = 90°
	b = 11.411(3) Å	β = 90°	b = 15.2753(17) Å	β = 104.706(4)°
	c = 21.698(5) Å	γ = 90°	c = 19.087(2) Å	γ = 90°
Volume	6553(3) Å^3		4882.2(10) Å^3	
Z	4		4	
Goodness-of-fit on F^2	1.056		1.003	
Final R indices [I>2sigma(l)]	R1 = 0.0362	wR2 = 0.0852	R1 = 0.0579	wR2 = 0.1109
R indices (all data)	R1 = 0.0529	wR2 = 0.0906	R1 = 0.1568	wR2 = 0.1346

In **C1**, the asymmetric unit at 296 K comprises two cations and two anions, **Figure A.5 (a)**, in the annexes. The unit cell contains four of this asymmetric units, **Figure A.5 (b)**, in the annexes.

In the case of **C3•H_2O•CH_3CN**, the asymmetric unit at 296 K comprises one cation, one anion, one molecule of acetonitrile and one water molecule, **Figure 2.3 (a)**. The unit cell contains four of these asymmetric units, **Figure 2.3 (b)**.

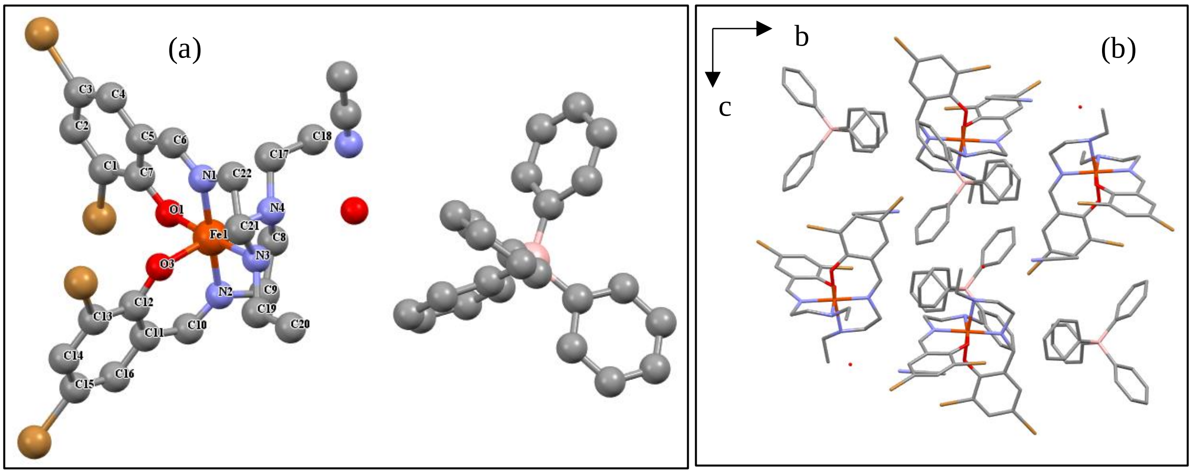

Figure 2.3 X-ray crystal structure of **C3•H$_2$O•CH$_3$CN**, at 296 K: (a) asymmetric unit; (b) unit cell.

Based on the bond lengths reported in the literature, we can assign the spin states based on the lengths around the iron centre. In HS state the Fe-N$_{\text{imine}}$ bond is between 2.10-2.15 Å, the Fe-N$_{\text{amine}}$ bond is between 2.17-2.23 Å and the Fe-O$_{\text{phen}}$ bond between 1.89-1.93 Å. In LS state the Fe-N$_{\text{imine}}$ bond is between 1.93-1.96 Å, the Fe-N$_{\text{amine}}$ bond is between 2.01-2.06 Å and the Fe-O$_{\text{phen}}$ bond between 1.87-1.91 Å. [104] In **Table 2.4** are the representative bond lengths of **C1** and **C3•H$_2$O•CH$_3$CN**, at 296 K, where both complexes show bond lengths corresponding to the LS state.

Table 2.4 Representative bond lengths of **C1** and **C3•H$_2$O•CH$_3$CN**, at 296 K.

Complex	**C1**				**C3•H$_2$O•CH$_3$CN**	
	Molecule 1		**Molecule 2**			
Fe-N$_{\text{imine}}$	Fe-N1	1.916(6)	Fe-N6	1.922(6)	Fe-N1	1.943(4)
	Fe-N3	1.936(6)	Fe-N8	1.924(6)	Fe-N2	1.939(4)
Fe-N$_{\text{amine}}$	Fe-N2	2.033(6)	Fe-N7	2.050(6)	Fe-N3	2.073(5)
	Fe-N4	2.038(6)	Fe-N9	2.037(6)	Fe-N4	2.074(4)
Fe-O$_{\text{phen}}$	Fe-O1	1.885(5)	Fe-O3	1.871(5)	Fe-O1	1.885(3)
	Fe-O2	1.866(5)	Fe-O4	1.875(5)	Fe-O3	1.865(4)
State	LS		LS		LS	

In **Figure 2.4** it is possible to observe the hydrogen bonds for **C1** and **C3•H$_2$O•CH$_3$CN**.

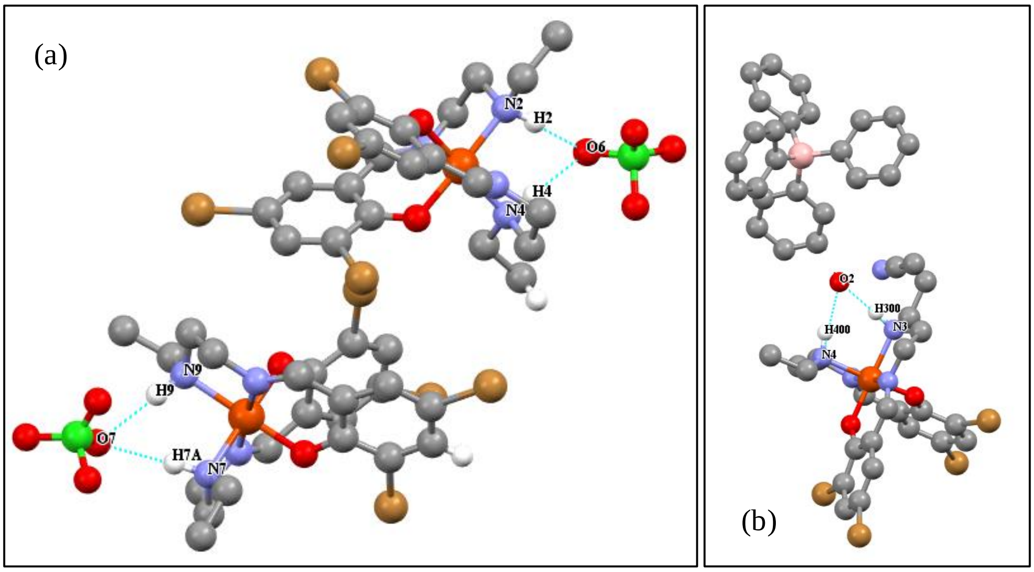

Figure 2.4 Hydrogen bonds in the X-ray single crystal structure: (a) **C1** and (b) **C3•H$_2$O•CH$_3$CN**.

In **Table 2.5** it is possible to observe the hydrogen bonds lengths and the angles for **C1** and $\mathbf{C3{\bullet}H_2O{\bullet}CH_3CN}$. The hydrogen bonds for **C1** are between the nitrogen atoms of the ligand and two oxygen of the anion. In the case of $\mathbf{C3{\bullet}H_2O{\bullet}CH_3CN}$, the hydrogen bonds are between the nitrogen atoms of the ligand and the water.

Table 2.5 Hydrogen bond lengths and angles for **C1** and $\mathbf{C3{\bullet}H_2O{\bullet}CH_3CN}$.

Complex	**D-H···A**	**d(H···A) (Å)**	**d(D···A) (Å)**	**(D-H···A) (°)**
C1	N4-H4···O6	2.122	3.099	175.13
	N2-H2···O6	2.148	3.110	166.16
	N7-H7···O7	2.224	3.163	160.14
	N9-H9···O7	2.100	3.066	168.83
$\mathbf{C3{\bullet}H_2O{\bullet}CH_3CN}$	N3-H3···O2	2.142	3.060	160.23
	N4-H4···O2	2.072	3.027	165.32

Powder X-ray diffraction

Since it was not possible to obtain the single crystal X-ray structures for all compounds, powder X-ray diffraction was used to correlate the diffractograms for all compounds. In **Figure 2.5**, it is possible to observe that **C2**, **C3** and **C5** are more crystalline than the other two complexes, and that all diffractograms have peaks in different angles, so they should correspond to different compounds.

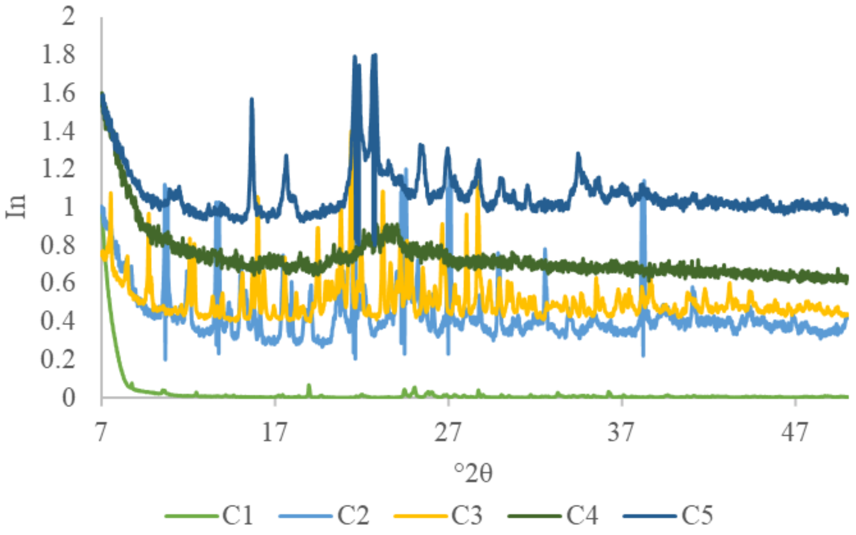

Figure 2.5 Powder X-ray diffractograms for complexes **C1-C5**.

To understand if the single crystal obtained was representative of the entire sample, and since the measurement of powder X-ray diffraction uses a large amount of sample, both diffractograms (powder and pattern generated from the single crystal structure) of **C1** and $\mathbf{C3{\bullet}H_2O{\bullet}CH_3CN}$ were compared.

In **C1**, the powder diffractogram might be influenced by the crystallinity of the sample. As seen in **Figure 2.6**, it is not possible to correlate all peaks in both diffractograms, making it unable to conclude if the crystal represents the whole sample.

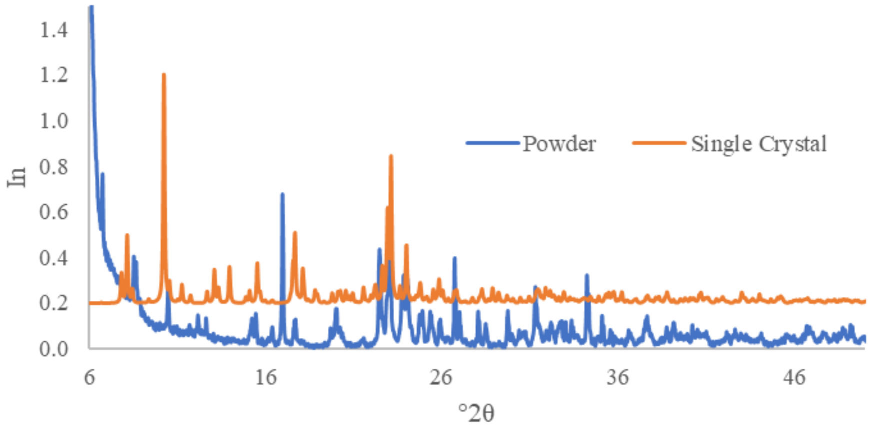

Figure 2.6 Single Crystal and powder X-ray diffractogram of **C1**.

For **C3•H₂O•CH₃CN**, for observation in **Figure A.6**, in the annexes, in the powder and the single crystal diffractograms it is possible to observe that all the powder X-ray peaks had a corresponding peak in the single crystal X-ray. That way, all sample has the same structure.

SQUID magnetometry

The SQUID magnetometry plot for the five complexes can be observe in **Figure 2.7**. The samples were measured with alternating cooling/warming runs at the rate of 5 K min^{-1} between 370 and 10 K, to obtain the molar magnetic susceptibility by the temperature ($\chi_M T$) as a function of the temperature.

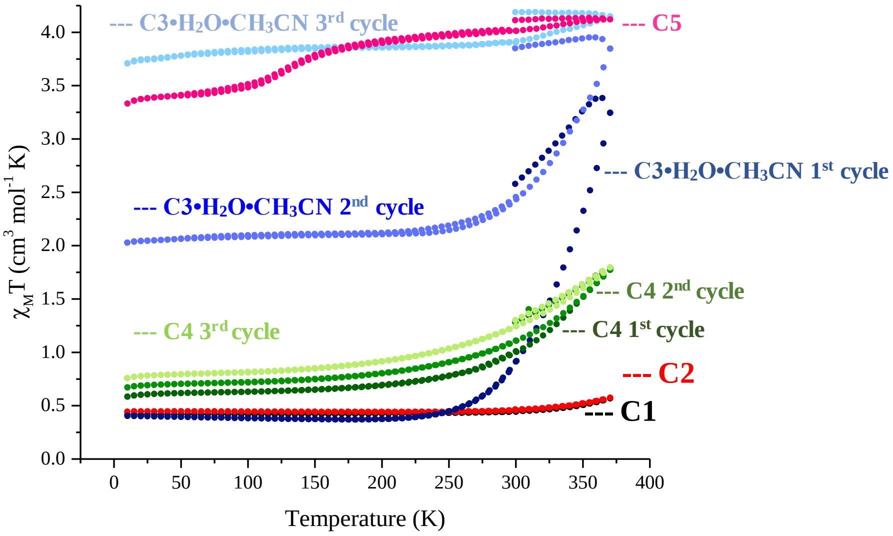

Figure 2.7 χ_MT vs T plot for complexes **C1-C5**.

The **C1** measurement starts at 300 K where a $\chi_M T$ value of 0.44 cm^3 mol^{-1} K was presented. After being cooled to 10 K, it admitted a $\chi_M T$ value of 0.42 cm^3 mol^{-1} K and was then warmed up to 370 K, where the $\chi_M T$ value was 0.57 cm^3 mol^{-1} K. The results indicate that the Fe(III) centers are in the LS state during the analysis.

The **C2** presents a very similar behavior to **C1**. The small increase in $\chi_M T$ at temperatures above 300K suggest that a spin transition might occur at temperatures over 370 K. It would be interesting to perform further studies for this complex. **C1** does not allow such studies, as there are chances that the sample might explode in temperatures above 370 K.

For **C3•H$_2$O•CH$_3$CN**, the sample presented a $\chi_M T$ value of 0.91 cm^3 mol^{-1} K at the initial temperature of 300 K. The sample was cooled to 10 K and admitted a $\chi_M T$ value of 0.40 cm^3 mol^{-1} K. It was then warmed up to 370 K where the $\chi_M T$ value increased to 3.25 cm^3 mol^{-1} K. Between 10 K and 225 K the Fe(III) centers are in the LS state and after that temperature the sample presented a gradual and incomplete SCO curve. At 370 K **C3•H$_2$O•CH$_3$CN** is approximately 70% HS and 30% LS.

When the sample **C3•H$_2$O•CH$_3$CN** was cooled down to 300 K, it admitted a higher $\chi_M T$ value of 2.46 cm^3 mol^{-1} K than the initial value at the same temperature. For that reason, a second cycle was made and at 10 K the sample displayed a $\chi_M T$ value of 2.03 cm^3 mol^{-1} K, corresponding to approximately 45% Fe(III) centers in the HS state and 55% in the LS state. The temperature was then raised again to 370 K and the $\chi_M T$ value increased to 3.85 cm^3 mol^{-1} K, where the sample is approximately 85% HS and 15% LS. When the same sample was cooled one more time to 300 K, it admitted again a higher $\chi_M T$ value of 3.90 cm^3 mol^{-1} K and we decided to execute another cycle. The sample was cooled to 10 K a third time and presented a $\chi_M T$ value of 3.71 cm^3 mol^{-1} K, corresponding to approximately 85% HS and 15% LS. It was then warmed up to 370 K where the $\chi_M T$ value rose to 4.15 cm^3 mol^{-1} K and the centers changed to approximately 95% in the HS and 5% in the LS.

The difference between cycles indicates the loss of the solvent after the first two cycles. Since the sample presented one molecule of acetonitrile and one water molecule in the structure and the second cycle curves in **Figure 2.7** did not present the same values for the same temperature, a new sample was subjected to a new series of cycles, **Figure 2.8**.

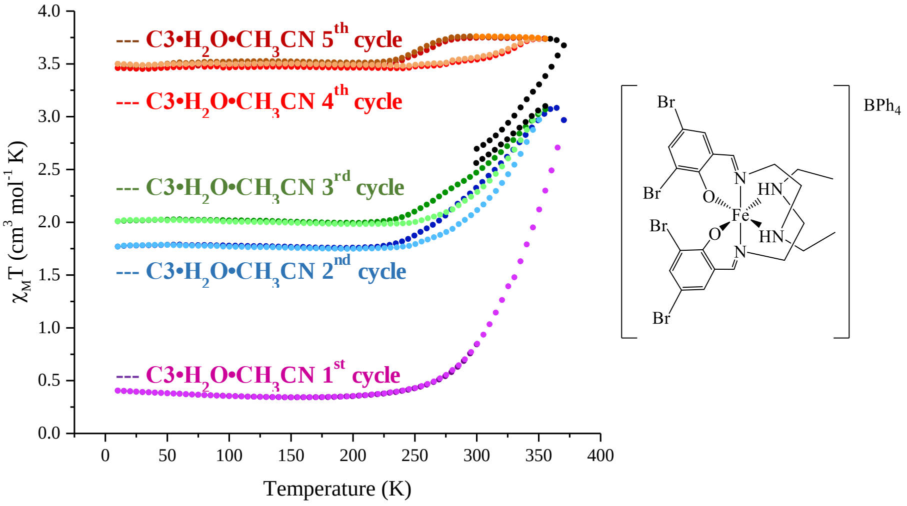

Figure 2.8 $\chi_M T$ vs T plot for second sample of **C3•H$_2$O•CH$_3$CN**.

The first cycle in the new sample revealed a similar behavior as the first cycle in the previous **C3•H$_2$O•CH$_3$CN** sample, but the $\chi_M T$ value at 370 K was higher corresponding approximately 65% in the HS and 35% in the LS.

The second cycle started when the sample was cooled from 300 K to 10 K, where it presented a $\chi_M T$ value of 1.77 cm^3 mol^{-1} K, corresponding to 45% HS and 55% LS. It was then warmed up again to 355 K, the $\chi_M T$ value increased to 3.07 cm^3 mol^{-1} K and the Fe(III) centers were 65% in the HS state and 35% in the LS state. A hysteresis was created in this cycle, between 210 K and 350 K, displaying $\chi_M T$ values of 1.76 and 2.97 cm^3 mol^{-1} K, respectively, with HS and LS values equivalents to 10 K and 355 K.

A third cycle in the same temperature intervals was performed and the $\chi_M T$ value was always higher than the prior cycle, with the hysteresis being maintained, with $\chi_M T$ values between 1.99 and 3.03 cm^3 mol^{-1} K, at 215 K and 350 K, respectively. At 10 K the sample was approximately 45% HS and 55% LS with a $\chi_M T$ value of 2.01 cm^3 mol^{-1} K and at 355 K approximately 65% HS and 35% LS with a $\chi_M T$ value of 3.10 cm^3 mol^{-1} K.

After cycle number three, the sample was warmed up to 370 K where the $\chi_M T$ value was 3.67 cm^3 mol^{-1} K, approximately, 85% HS and 15% LS. Two more cycles between 10 K and 355 K were effectuated. The fourth and fifth cycles presented the same behavior as the cycles before, but with $\chi_M T$ values higher than the prior cycle and with the thermal hysteresis. The two cycles admitted very similar values at 10 K, where it presented a $\chi_M T$ value of 3.46 cm^3 mol^{-1} K (fourth cycle) and 3.50 cm^3 mol^{-1} K (fifth cycle), corresponding to 80% HS and 20% LS. It was then warmed up again to 355 K, the $\chi_M T$ value increased to 3.74 cm^3 mol^{-1} K and the Fe(III) centers were 85% in the HS state and 15% in the LS state. The hysteresis was between 210 K and 255 K with the same $\chi_M T$ values as 10 K and 355 K, respectively. Further analysis of this sample is still needed to better understand these results, such as a comprehensive single crystal X-ray study of the sample after each cycle to find the changes in the structure and the role played by the solvents.

For **C4** three cycles were performed because at the end of every cycle the $\chi_M T$ value was bigger than in the one before. The cycles started at 300 K where $\chi_M T$ values were 1.01 cm^3 mol^{-1} K (first), 1,11 cm^3 mol^{-1} K (second) and 1.25 cm^3 mol^{-1} K (third). The sample was cooled down to 10 K and presented a $\chi_M T$ value of 0.58 cm^3 mol^{-1} K (first cycle), 0.67 cm^3 mol^{-1} K (second cycle) and 0.76 cm^3 mol^{-1} K (third cycle). The sample was then warmed up to 370 K where the $\chi_M T$ value increased to 1.79 cm^3 mol^{-1} K (first cycle), 1.77 cm^3 mol^{-1} K (second cycle) and 1.79 cm^3 mol^{-1} K (third cycle). This difference indicates the loss of the solvent after the cycles. The sample presents a gradual and incomplete SCO curve. In the last cycle at 10 K the sample presented approximately 22% HS and 78% LS and at 370 K approximately 65% HS and 35% LS.

For the **C5** sample a $\chi_M T$ value of 4.01 cm^3 mol^{-1} K was observed at 300 K. When cooled to 10 K it assumes a $\chi_M T$ value of 3.33 cm^3 mol^{-1} K. The sample admitted a $\chi_M T$ value of 4.12 cm^3 mol^{-1} K after warming until 370 K. These results present a gradual and incomplete SCO curve, with a step between 100 and 150 K, and the Fe(III) centers are approximately 75% HS and 25% LS at 10 K and 93% HS and 7% LS at 370 K.

[Fe(3,5-Cl-salEen)$_2$]Y

The reaction of Fe(NO$_3$)$_3$ and different Fe(II) salts with 3,5-Cl-salEen at room temperature resulted in very dark solutions sometimes accompanied by a dark powder, thus confirming the formation of coordination compounds. The reaction with tetrafluoroborate did not occur.

In this group four Fe(III) complexes were synthesized, the **C6** corresponds to [Fe(3,5-Cl-salEen)$_2$]ClO$_4$, **C7** to [Fe(3,5-Cl-salEen)$_2$]PF$_6$, **C8** to [Fe(3,5-Cl-salEen)$_2$]BPh$_4$ and **C9** to [Fe(3,5-Cl-salEen)$_2$]NO$_3$, as displayed in **Scheme 2.4**.

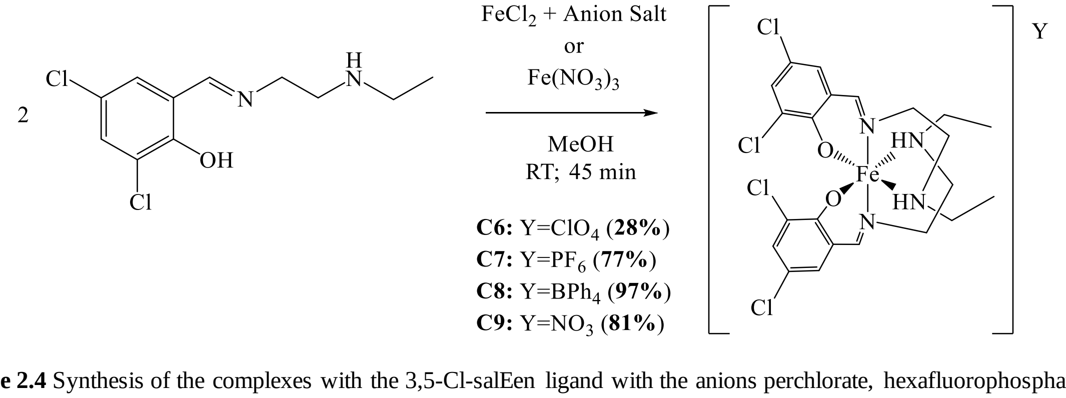

Scheme 2.4 Synthesis of the complexes with the 3,5-Cl-salEen ligand with the anions perchlorate, hexafluorophosphate, tetraphenylborate and nitrate.

FTIR and UV-vis spectroscopy

The FTIR spectroscopy was used to confirm the imine formation through the observation of a strong stretching vibration and the presence of the different anions through the observation of their characteristic vibrational modes. The FTIR assigned vibrations for **C6-C9** are in **Table 2.6**. The FTIR spectrum of the four complexes can be found in the annexes, **Figure A.7, Figure A.8, Figure A.9 and Figure A.10**.

Table 2.6 Wavenumbers for the characteristic FTIR spectrum bands, for complexes **C6-C9**.

Complex	Wavenumber (cm^{-1})						
	υ(O-H)	υ(N-H)	υ(C-H)	υ(C=N)	υ(C=C)	Anion	
C6	3411	3237	2977	1638	1585-1469	ClO_4^-	1062, 624
C7	3414	-	2977	1630	1586-1471	PF_6^-	839
C8	3425	3212	2986	1628	1578-1468	BPh_4^-	742-710
C9	3442	3178	2970	1629	1588-1463	NO_3^-	1385

As expected, the vibrations corresponding to O-H bonds are around 3400 cm^{-1}, N-H bonds are around 3200 cm^{-1} (except the **C7**), C-H bonds are around 2970 cm^{-1}, C=N bonds are around 1600 cm^{-1}, C=C bonds are between 1580-1460 cm^{-1} and the anions vibrations are perchlorate at 624 cm^{-1} and 1062 cm^{-1}, hexafluorophosphate at 839 cm^{-1}, tetraphenylborate at 710 cm^{-1} to 742 cm^{-1} and nitrate at 1385 cm^{-1}. For **C7** the stretching of the N-H bond is not observed because the O-H band is very large and overlaps it. This is possibly related to the higher amount of water present in these two samples.

The UV-vis spectra for all four complexes were recorded in acetonitrile between 190 and 900 nm and can be observed in **Figure 2.9**.

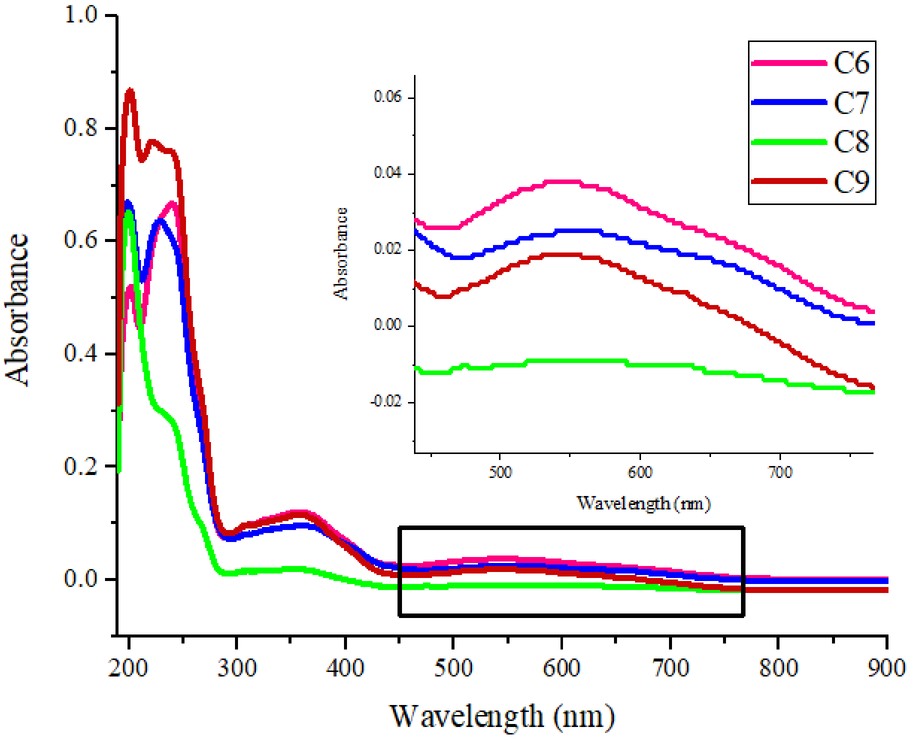

Figure 2.9 UV-vis spectra of **C6-C9** in acetonitrile.

The **C6**, **C7** and **C8** presented five bands and the **C9** presented six. Details on the bands can be observed in **Table 2.7**.

Table 2.7 Values for the bands UV-vis, for complexes **C6-C9**.

Complex	**Concentration ($mol.dm^{-3}$)**	**Wavelength (nm)**	**Absorbance**	**Molar absorption coefficient ($mol.dm^{-3}.cm^{-1}$)**
C6	2 x 10^{-5}	201.5	0.520	26 000
		240.0	0.668	33 400
		358.5	0.120	6 000
		564.0	0.037	1 850
		658.0	0.023	1 150
C7	10^{-5}	198.0	0.669	66 900
		228.5	0.636	63 600
		364.0	0.097	9 700
		555.5	0.025	2 500
		650.0	0.018	1 800
C8	5 x 10^{-6}	199.0	0.649	129 800
		240.0	0.280	56 000
		350.5	0.020	4 000
		550.0*	-	-
C9	2 x 10^{-5}	200.0	0.866	43 300
		221.5	0.777	38 850
		235.5	0.761	38 050
		357.0	0.115	5 750
		542.5	0.019	950
		628.0	0.009	450

* the baseline adjustment was not the best and the absorbance is below 0.

As observed in **Table 2.7**, all complexes present bands at different wavelengths and with different molar absorption coefficients. The bands around 200 nm belong to intraligand interactions, with variations between 129 000 $mol.dm^{-3}.cm^{-1}$, **C8** and 33 400 $mol.dm^{-3}.cm^{-1}$, **C6**. All complexes presented two of this bands except the **C9** that showed three.

The bands between 300 and 400 nm should be attributed to charge-transfer between the ligands and the iron, or vice-versa, with variations between 9 700, **C7** and 4 000 $mol.dm^{-3}.cm^{-1}$, **C8**. All complexes presented one of this bands.

Bands between 500 nm and 700 nm correspond also to charge-transfer between the ligands and the iron, or vice-versa also and can be related to the spin states.[103] The **C6**, **C7** and **C9** present two bands, one around 550 nm and other around 650 nm and the **C8** only one band. The 550 nm band variates between 2 500 and 950 $mol.dm^{-3}.cm^{-1}$ and the 650 nm band variates between 1 800 and 450 $mol.dm^{-3}.cm^{-1}$. At both wavelengths, the higher different molar absorption coefficients belong to **C7** and the smaller belong to **C8** for the first and **C9** for the second. In solution at room-temperature, the **C8** is essentially low spin and the other three show a mixture between the LS state and the HS state, with more Fe(III) centres in the low spin state. In general, the **C7** presented a higher absorbance and the **C8** presented the lower.

Structural characterization

Single Crystal X-ray diffraction

Single crystals with good quality for X-ray diffraction were only obtained for **C6** and **C8**. The remaining compounds were crystalline but presented poor or no diffraction. The spin state of the complex at a specific temperature was predicted, through the Fe-X bond lengths.

The X-ray data at 296 K revealed that one of the compounds was found in its unsolvated form, **C6**, but other was crystallized as solvate, **C8•H_2O•CH_3CN**. The crystal data and structure refinement of **C1** and **C8•H_2O•CH_3CN** are listed in **Table A.1**, in the annexes.

For the **C6**, the asymmetric unit at 110 K comprises one cation and one anion, **Figure A.11 (a)**, in the annexes. The unit cell contains eight asymmetric unit, **Figure A.11 (b),** in the annexes.

In the case of **C8•H₂O•CH₃CN**, the asymmetric unit at 296 K comprises one cation, one anion, one molecule of acetonitrile and one water molecule, **Figure A.12 (a)**, in the annexes. The unit cell contains four asymmetric unit, **Figure A.12 (b)**, in the annexes.

In the **Table 2.8** are the representative bond lengths of **C6** at 110 K and **C8•H₂O•CH₃CN**, at 296 K, where both complexes present bond lengths corresponding to the LS state.

Table 2.8 Representative bond lengths of **C6** and **C8•H₂O•CH₃CN**.

Complex	**C6**		**C8•H₂O•CH₃CN**	
Fe-N$_{imine}$	Fe-N1 Fe-N3	1.928(7) 1.922(7)	Fe-N1 Fe-N4	1.940(2) 1.937(2)
Fe-N$_{amine}$	Fe-N2 Fe-N4	2.040(7) 2.061(7)	Fe-N2 Fe-N3	2.054(3) 2.056(3)
Fe-O$_{phen}$	Fe-O1 Fe-O2	1.870(5) 1.881(6)	Fe-O1 Fe-O2	1.868(2) 1.882(2)
State	LS		LS	

In **Table 2.9** it is possible to observe the hydrogen bonds for the **C6** and **C8•H₂O•CH₃CN**. The hydrogen bonds for **C6** are between the one nitrogen atom of the ligand and one oxygen of the anion. In the case of **C8•H₂O•CH₃CN** the hydrogen bonds are between the nitrogen atoms of the amines of the ligand and the water molecule. Finally, a C-H···π interaction between two aromatic rings of neighboring, between the anion and the cation, **Table 2.9**. In the annexes, in **Figure A.13(a)** and **Figure A.13(b),** it is possible to observe the hydrogen bonds and the C-H···π interaction.

Table 2.9 Hydrogen bond and C-H···π interaction lengths and angles for **C6** and **C8•H₂O•CH₃CN**.

Complex	**D-H···A**	**d(H···A) (Å)**	**d(D···A) (Å)**	**(D-H···A) (º)**
C6	N2-H2···O4	2.107	3.098	170.81
C8•H₂O•CH₃CN	N2-H2···O3	2.133	3.027	155.67
	N3-H3···O3	2.167	3.021	167.41
	C32-H32··· π	2.732	3.109	161.69

Powder X-ray diffraction

Since it was not possible to obtain the single crystal X-ray for all the complexes, the powder X-ray diffraction was used to try to correlate the diffractograms for all the compounds. In **Figure 2.10**, it is possible to observe that the **C7** and **C8** are more crystalline than the other two complexes, and that all the diffractograms have peaks in different angles, so they should correspond to different compound.

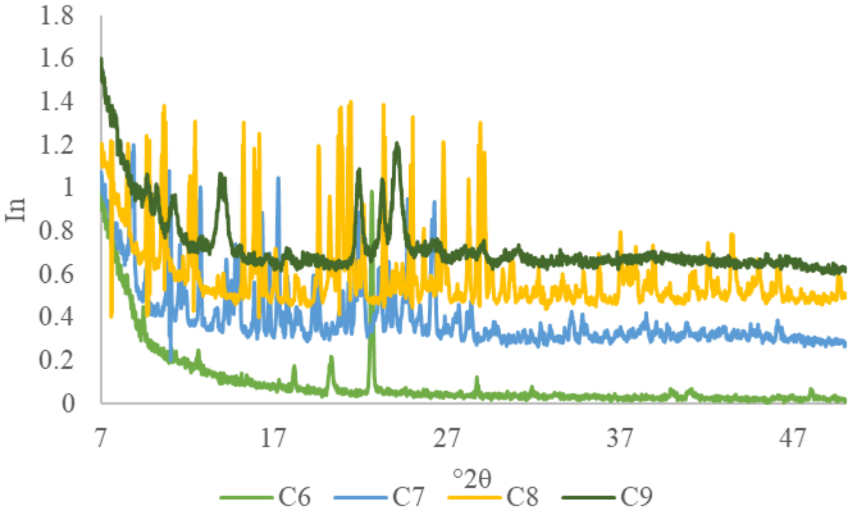

Figure 2.10 Powder X-ray diffractograms for complexes **C6-C9**.

To understand if the single crystal obtained was representative of all the sample and since the measure of powder X-ray diffraction uses a larger amount of sample, powder and pattern generated from the single crystal structure diffractograms of **C6** and **C8•H$_2$O•CH$_3$CN** were compared.

For the **C6**, the powder diffractogram shows less peaks than the single crystal diffractogram, demonstrating less crystallinity, **Figure A.14,** in the annexes. With the data collected it is not possible to confirm if the single crystal is representative of the bulk sample.

In the case of **C8•H$_2$O•CH$_3$CN** by observing **Figure A.15**, in the annexes, the powder and the single crystal diffractograms, it is possible to observe that all the powder X-ray peaks had a corresponding peak in the single crystal X-ray. Therefore, the bulk sample and the single crystal structure are correlated.

<u>SQUID magnetometry</u>

The SQUID magnetometry plot for the four complexes can be observed in **Figure 2.11**. The samples were measured with alternating cooling/warming runs at the rate of 5 K min^{-1} between 370 and 10 K to obtain the molar magnetic susceptibility by the temperature ($\chi_M T$) as function of the temperature.

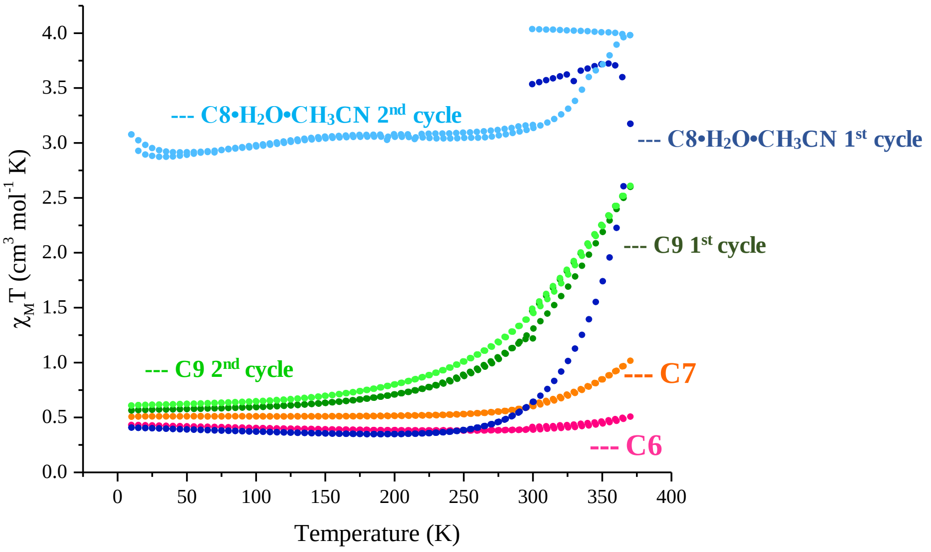

Figure 2.11 χ_MT vs T plot for complexes **C6-C9.**

The **C6** measurement started at 300 K and it was observed a $\chi_M T$ value of 0.39 cm^3 mol^{-1} K. The sample was cooled to 10 K and presented a $\chi_M T$ value of 0.43 cm^3 mol^{-1} K. After it was warmed up to 370 K where the $\chi_M T$ value was 0.51 cm^3 mol^{-1} K. The results indicate that the Fe(III) centers are in the LS state during the analysis.

The **C7** sample at the initial 300 K presented a $\chi_M T$ value of 0.60 cm^3 mol^{-1} K. It was cooled to 10 K and admitted a $\chi_M T$ value of 0.51 cm^3 mol^{-1} K and after was warmed up to 370 K where the $\chi_M T$ value rose to 1.01 cm^3 mol^{-1} K. The sample between 10 K and 300 K is essential in the LS and after that temperature presents a gradual and incomplete SCO curve. At 370 K **C7** is approximately 30% HS and 70% LS. As in the group before small increase in $\chi_M T$ at temperatures above 300K suggest that a spin transition could occur at temperatures over 370 K. It would be interesting to perform further studies for this complex.

For **C8•H$_2$O•CH$_3$CN** a $\chi_M T$ value of 0.64 cm^3 mol^{-1} K was observed at 300 K. The sample was cooled to 10 K and displayed a $\chi_M T$ value of 0.41 cm^3 mol^{-1} K. It was then warmed up to 370 K where the $\chi_M T$ value increased to 3.18 cm^3 mol^{-1} K. Between 10 K and 250 K the Fe(III) centers are in the LS state and after that temperature the sample presented a gradual and incomplete SCO curve. At 370 K **C8•H$_2$O•CH$_3$CN** is approximately 70% in the HS state and 30% in the LS state.

When that sample **C8•H$_2$O•CH$_3$CN** was cooled down to 300 K, it admitted a higher $\chi_M T$ value of 3.16 cm^3 mol^{-1} K than the initial value for the same temperature. The sample was cooled to 10 K again and presented a $\chi_M T$ value of 3.08 cm^3 mol^{-1} K. It was then warmed up to 370 K where the $\chi_M T$ value rose to 3.98 cm^3 mol^{-1} K. At 10 K the sample is approximately 66% HS and 33% LS and at 370 K approximately 90% HS and 10% LS.

When the same sample was cooled to 300 K, it admitted again a higher $\chi_M T$ value of 4.04 cm^3 mol^{-1} K, approximately 92% HS and 8% LS. The sample presented a similar profile to the **C3•H$_2$O•CH$_3$CN**. The difference between cycles indicates the loss of the solvent after the cycles. Since the sample also presented one molecule of acetonitrile and one of water in the structure and the second cycle curves in **Figure 2.11** did not present the same values for the same temperature, a new **C8•H$_2$O•CH$_3$CN** sample was measured with more and different cycles, **Figure 2.12**.

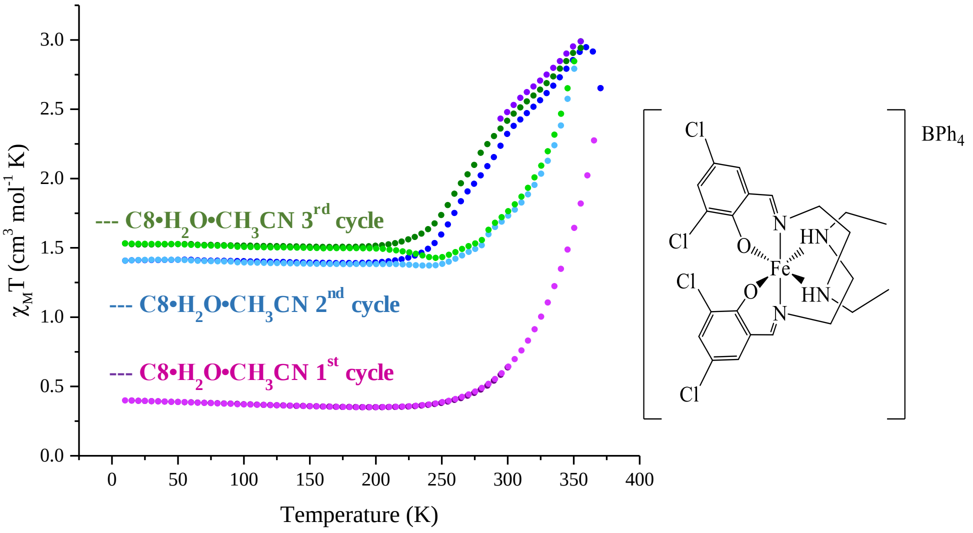

Figure 2.12 χ_MT vs T plot for second sample of **C8•H$_2$O•CH$_3$CN**.

The first cycle in the new sample revealed a similar behavior as the first cycle in the previous **C8•H$_2$O•CH$_3$CN** sample but the $\chi_M T$ value at 370 K was higher, corresponding approximately 55% in the HS and 45% in the LS.

In the second cycle the same sample was cooled to 10 K and admitted a $\chi_M T$ value of 1.41 cm^3 mol^{-1} K, corresponding to 35% HS and 65% LS. It was then warmed up to 355 K where the $\chi_M T$ value increased to 2.94 cm^3 mol^{-1} K and the Fe(III) centers were 65% in the HS and 35% in the LS. The sample presented a hysteresis loop between 185 K and 350 K, displayed $\chi_M T$ values of 1.40 and 2.85 cm^3 mol^{-1} K, respectively. In the hysteresis at 185 K the Fe(III) centers are approximately 35% HS and 65% LS and at 350 K approximately 60% HS and 40% LS.

A third cycle was performed to understand if the hysteresis remained the same and the $\chi_M T$ value was always higher than the prior cycle. The sample was cooled to 10 K and presented a $\chi_M T$ value of 1.53 cm^3 mol^{-1} K, corresponding to 40% HS and 60% LS. Afterwards, it was warmed up to 355 K and admitted a $\chi_M T$ value of 2.99 cm^3 mol^{-1} K, where the Fe(III) centers were approximately 67% in the HS and 33% in the LS. The hysteresis was between 210 K and 255 K presenting the same spin states percentages as for 10 K and 370 K, respectively.

Further studies, such as a comprehensive single crystal X-ray of the sample after each cycle, are needed to understand the changes in the structure as well as the importance of the solvent.

For **C9** two cycles were performed, because the $\chi_M T$ value after and before the first cycle was different at 300 K. At 300 K the first $\chi_M T$ value was of 1.22 cm^3 mol^{-1} K and in the second cycle was 1.46 cm^3 mol^{-1} K. The sample was cooled to 10 K and presented a $\chi_M T$ value of 0.56 cm^3 mol^{-1} K (first cycle) and 0.61 cm^3 mol^{-1} K (second cycle). After it was warmed up to 370 K where the $\chi_M T$ value rose to 2.60 cm^3 mol^{-1} K (first cycle) and 2.61 cm^3 mol^{-1} K (second cycle). The sample presents a gradual and incomplete SCO curve, for the second cycle 10 K is essential LS and at 370 K is approximately 66% HS and 33% LS. The difference between cycles indicates the loss of the solvent after the first cycles.

[Fe(3,5-F-salEen)$_2$]Y

The reaction Fe(NO_3)$_3$ and different Fe(II) salts with 3,5-F-salEen at room temperature resulted in very dark solutions sometimes accompanied by a dark powder, thus confirming the formation of coordination compounds.

In this group five Fe(III) complexes were synthesized, the **C10** corresponds to [Fe(3,5-F-salEen)$_2$]ClO_4, **C11** to [Fe(3,5-F-salEen)$_2$]PF_6, **C12** to [Fe(3,5-F-salEen)$_2$]BPh_4, **C13** to [Fe(3,5-F-salEen)$_2$]BF_4 and **C14** to [Fe(3,5-F-salEen)$_2$]NO_3, **Scheme 2.5**. **C11_1** and **C11_2** are both products of **C11** reaction, and the same applies to **C12_1** and **C12_2**. In these reactions, the solution and the dark powder resulted in crystalline solids after recrystallization. **C11_1** and **C12_1** are the products obtained after slow evaporation of the mother liquor, and **C11_2** and **C12_2** are the powders precipitated during the reaction.

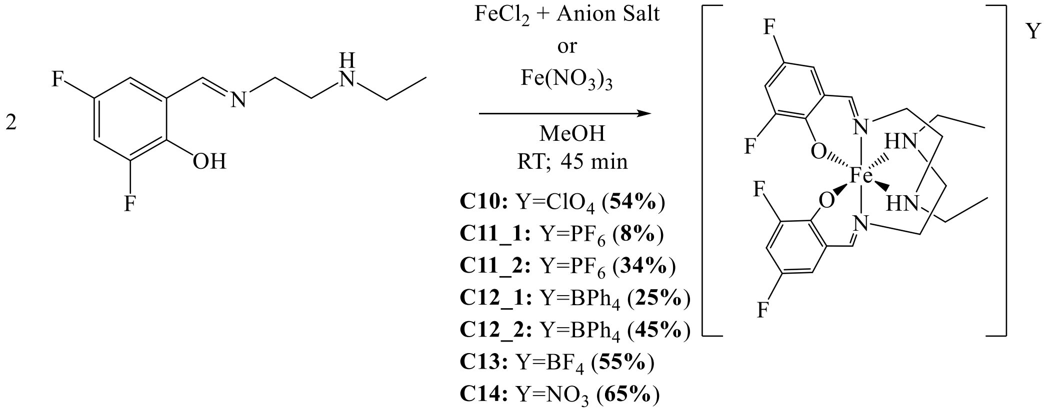

Scheme 2.5 Synthesis of the complexes with the 3,5-F-salEen ligand, with the anions perchlorate, hexafluorophosphate, tetraphenylborate, tetrafluoroborate and nitrate.

FTIR and UV-vis Spectroscopy

The FTIR spectroscopy was used to confirm the imine formation through the observation of a strong stretching vibration and the presence of the different anions through the observation of their characteristic vibrational modes.

The FTIR spectrum for the **C11_1** and **C11_2** perfectly overlaps and therefore they can be considered the same complex, **C11** (**Figure 2.13**). The assigned FTIR vibration for the **C10-C14** are in **Table 2.10**. The FTIR spectrum of the five remaining complexes can be found in the annexes, **Figure A.16, Figure A.17, Figure A.18, Figure A.19 and Figure A.20**.

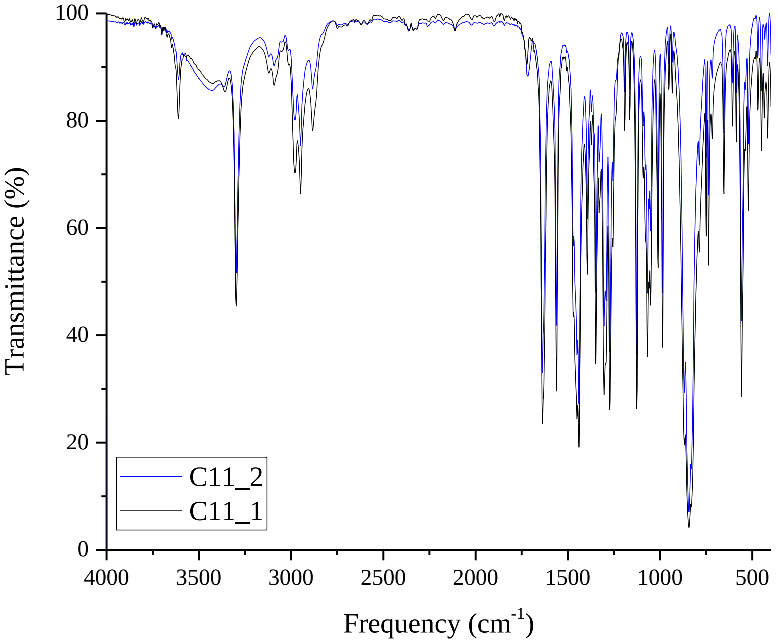

Figure 2.13 FTIR spectra of **C11_1** and **C11_2**.

Table 2.10 Wavenumbers for the characteristic FTIR spectrum bands, for complexes **C10-C14**.

Complex	**Wavenumber (cm^{-1})**						
	υ(O-H)	**υ(N-H)**	**υ(C-H)**	**υ(C=N)**	**υ(C=C)**	**Anion**	
C10	3440	3234	2978	1645	1558-1453	ClO_4^-	1045, 623
C11	3427	3297	2978	1635	1560-1469	PF_6^-	844
C12_1	3442	-	2982	1629	1580-1477	BPh_4^-	743-708
C12_2	3442	3231	2982	1632	1580-1477	BPh_4^-	743-709
C13	3496	3220	2977	1631	1560-1441	BF_4^-	1069
C14	3443	3299	2979	1637	1556-1455	NO_3^-	1382

As expected, the vibrations corresponding to O-H bonds are around 3400 cm^{-1}, N-H bonds are around 3200 cm^{-1} (except for the **C12_1**), C-H bonds are around 2970 cm^{-1}, C=N bonds are around 1600 cm^{-1}, C=C bonds are between 1580-1440 cm^{-1} and the anions vibrations are perchlorate at 623 cm^{-1} and 1045 cm^{-1}, hexafluorophosphate at 844 cm^{-1}, tetraphenylborate at 708 cm^{-1} to 743 cm^{-1} for **C12_1** and at 709 cm^{-1} to 743 cm^{-1} for **C12_2**, tetrafluoroborate at 1069 cm^{-1} and nitrate at 1382 cm^{-1}. For **C12_1** the stretching of the N-H bond is not observed because the O-H band is very large and overlaps it. This is possibly related to the higher amount of water present in these two samples. This is possibly related to the higher amount of water present in these two samples.

The difference between the **C12_1** and **C12_2** is that the second presents a band at 2251 cm^{-1} that is characteristic of the stretching of the C≡N, which probably indicates that this complex crystalized with acetonitrile in the structure and the **C12_1** did not.

As for the first substituent presented, the two anions that are mostly correlated shows the imine stretching band in the two edges (1645 cm^{-1} for ClO_4^- and 1631 for BF_4^-). This possible indicates that one of them is forming hydrogen bonds with the cation while the other is not.

The UV-vis spectra for all six complexes were recorded in acetonitrile between 190 and 900 nm and can be observed in **Figure 2.14**.

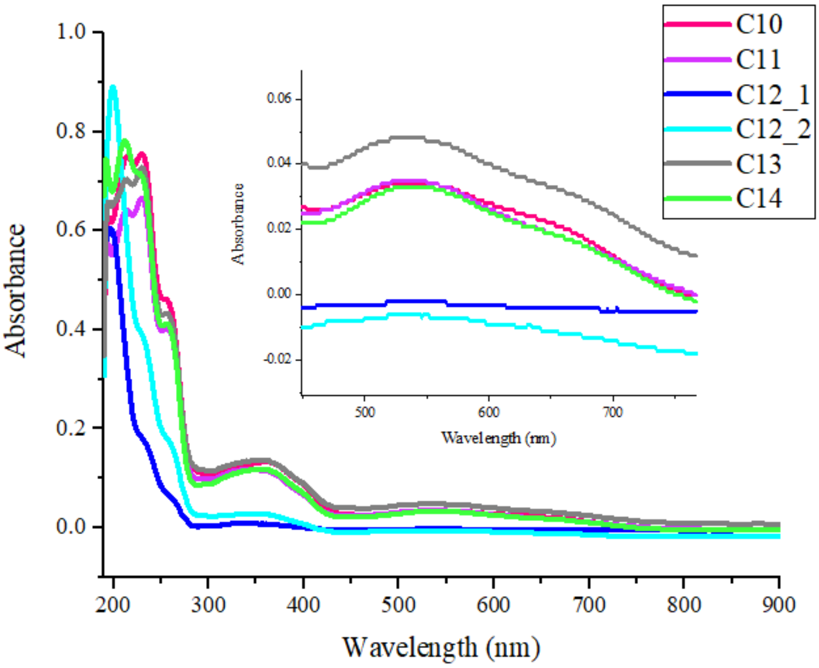

Figure 2.14 UV-vis spectra of **C10-C14** in acetonitrile.

The samples presented seven bands, except the **C12_1** and **C12_2** that presented four. The bands characterization can be observed in **Table 2.11**.

Table 2.11 Values for the bands UV-vis, for complexes **C10-C14**.

Complex	Concentration (mol.dm^{-3})	Wavelength (nm)	Absorbance	Molar absorption coefficient (mol.dm^{-3}.cm^{-1})
C10	10^{-5}	195.0	0.626	62 600
		214.5	0.750	75 000
		230.0	0.755	75 500
		253.5	0.463	46 300
		361.5	0.134	13 400
		539.5	0.034	3 400
		638.5	0.024	2 400
C11	2 x 10^{-5}	196.5	0.757	37 850
		212.0	0.870	43 500
		229.5	0.853	42 650
		256.5	0.521	26 050
		346.0	0.146	7 300
		535.5	0.043	2 150
		632.0	0.021	1 200
C12_1	5 x 10^{-6}	196.5	0.605	121 000
		228.0	0.186	37 200
		265.0	0.052	10 400
		333.5	0.009	1 800
C12_2	7 x 10^{-6}	199.0	0.891	127 285
		228.0	0.397	56 714
		265.0	0.145	20 714
		348.0	0.028	4 000
		550*	-	-

C13	10^{-5}	196.0	0.658	65 800
		214.0	0.704	70 400
		230.0	0.728	72 800
		235.5	0.433	43 300
		353.5	0.136	13 600
		534.0	0.048	4 800
		642.0	0.034	3 400
C14	2 x 10^{-5}	192.0	0.744	37 200
		211.5	0.782	39 100
		224.5	0.718	35 900
		255.5	0.412	20 600
		357.0	0.118	5 900
		538.5	0.033	1 650
		642.0	0.034	1 700

* the baseline adjustment was not the best and the absorbance is below 0.

Table 2.11 shows that all complexes present bands at different wavelengths and with different molar absorption coefficients. The bands around 200 nm correspond to intraligand interactions, with variations between 128 000 and 20 000 mol.dm^{-3}.cm^{-1}. **C12_1** and **C12_2** have the higher molar absorption coefficient and the smaller belongs to **C11** and **C14**. **C12_1** and **C12_2** presented three of this bands and the others four.

The bands between 300 and 400 nm should be attributed to charge-transfer between the ligands and the iron, or vice-versa, with variations between 13 600 and 4 000 mol.dm^{-3}.cm^{-1}. In this bands the opposite happens, as **C11** and **C13** have the higher molar absorption coefficients and the smaller belong to **C12_1** and **C12_2**. All complexes presented one of this bands.

Bands between 500 nm and 700 nm are also charge-transfer between the ligands and the iron, but the cation has two distinct absorbance bands in this region, one corresponding to the HS state (≈ 500 nm) and the LS state (≈ 650 nm).[103] The **C12_1** did not presented bands in this region, the **C12_2** presents one with a below zero value and other complexes present two bands, one around 530 nm and other around 640 nm. The 530 nm band variates between 4 800 and 1 650 mol.dm^{-3}.cm^{-1}. The 640 nm band variates between 3 400 and 1 200 mol.dm^{-3}.cm^{-1} and the smaller molar absorption coefficients belong to **C14**. In solution at room-temperature, the **C12_2** is essentially low spin and the others show a mixture between the LS state and the HS state, with more Fe(III) centres in the low spin state.

Structural characterization

Single Crystal X-ray diffraction

The only compound that was crystalline but presented poor or no diffraction was the **C13**. All the other complexes presented single crystals with good quality for X-ray diffraction. The spin state of the complex at a specific temperature through the Fe-X bond lengths was predicted.

The X-ray data at 296 K revealed that some of the compounds were found in their unsolvated form **C10, C11** and **C14** but others were crystallized as solvates **C12_1•H_2O•MeOH** and **C12_2•CH_3CN**. The crystal data and structure refinement of this complexes is listed in **Table A.2**, in the annexes.

In **C10**, the asymmetric unit at 296 K comprises one cation and one anion, **Figure A.21 (a)**, in the annexes. The unit cell contains eight asymmetric unit, **Figure A.21 (b)**, in the annexes.

For the **C11**, the asymmetric unit at 296 K comprises one cation and one anion, **Figure A.22 (a)**, in the annexes. The unit cell contains eight asymmetric unit, **Figure A.22 (b)**, in the annexes.

In the case of **C12_1•H_2O•MeOH**, the asymmetric unit at 296 K comprises one cation, one anion, one molecule of methanol and one of water, **Figure A.23 (a)**, in the annexes. The unit cell contains four asymmetric unit, **Figure A.23 (b)**, in the annexes.

In the case of **C12_2•CH$_3$CN**, the asymmetric unit at 296 K comprises one cation, one anion and one molecule of acetonitrile, **Figure A.23 (c)**, in the annexes. The unit cell contains four asymmetric unit, **Figure A.23 (d)**, in the annexes.

In **C14**, the asymmetric unit at 296 K comprises one cation and one anion, **Figure A.24 (a)**, in the annexes. The unit cell contains two asymmetric unit, **Figure A.24 (b)**, in the annexes.

In the **Table 2.12** are the representative bond lengths for the complexes, at 296 K, where all the complexes present bond lengths corresponding to the LS state except the **C12_2•CH$_3$CN** that present bond lengths corresponding to the HS state.

Table 2.12 Representative bond lengths of **C10-C12_2•CH$_3$CN** and **C14** at 296 K.

Complex	**C10**		**C11**		**C12_1•H$_2$O• MeOH**		**C12_2•CH$_3$CN**		**C14**	
Fe-N$_{imine}$	Fe-N1	1.919(2)	Fe-N1	1.936(5)	Fe-N1	1.918(7)	Fe-N1	2.093(3)	Fe-N1	1.922(2)
	Fe-N3	1.929(2)	Fe-N3	1.937(5)	Fe-N4	1.904(7)	Fe-N3	2.077(3)	Fe-N3	1.925(2)
Fe-N$_{amine}$	Fe-N2	2.058(3)	Fe-N2	2.045(5)	Fe-N2	2.037(6)	Fe-N2	2.197(3)	Fe-N2	2.048(2)
	Fe-N4	2.045(2)	Fe-N4	2.068(6)	Fe-N3	2.045(6)	Fe-N4	2.203(3)	Fe-N4	2.051(2)
Fe-O$_{phen}$	Fe-O1	1.878(2)	Fe-O1	1.871(4)	Fe-O1	1.862(5)	Fe-O1	1.907(3)	Fe-O1	1.877(17)
	Fe-O2	1.869(19)	Fe-O2	1.876(5)	Fe-O2	1.874(5)	Fe-O2	1.907(3)	Fe-O2	1.879(17)
State	LS		LS		LS		HS		LS	

In **Table 2.13** it is possible to observe the hydrogen bond lengths and angles for the **C10**, **C11**, **C12_1•H$_2$O•MeOH, C12_2•CH$_3$CN** and **C14**. The hydrogen bonds for **C10** are between the nitrogen atoms of the amines of the ligand and one oxygen of the anion. For **C11** they are between the hydrogens of the nitrogen atoms of the amines of the ligand and two fluor of the anion. In the case of **C12_1•H$_2$O•MeOH** the hydrogens of the nitrogen atoms of the ligand are bonded with the oxygen of the methanol and the hydrogen of the methanol bonds with the oxygen of the water. For **C12_2•CH$_3$CN** one hydrogen of nitrogen atom of the amines of the ligand is bonded to one nitrogen of the acetonitrile. The **C14** bond is between one hydrogen of the nitrogen atoms of the amine of the ligand and one oxygen of the anion. The corresponding figures are in the annexes, **Figure A.25**.

Table 2.13 Hydrogen bond lengths and angles for **C10-C12_2.H$_2$O.CH$_3$CN** and **C14**.

Complex	**D-H···A**	**d(H···A) (Å)**	**d(D···A) (Å)**	**(D-H···A) (º)**
C10	N2-H2···O5	2.222	3.081	171.00
	N4-H4···O5	2.215	3.097	165.49
C11	N2-H2···F9	2.500	3.292	149.17
	N2-H2···F6	2.493	3.335	156.16
	N4-H4···F6	2.306	3.169	167.35
C12_1•H$_2$O•MeOH	N2-H2···O4	2.021	3.000	177.20
	N3-H3···O4	2.129	3.060	158.22
	O4-H4···O3	2.255	3.007	152.54
C12_2•CH$_3$CN	N4-H4···N5	2.205	3.096	171.46
C14	N2-H2···O4	2.042	2.923	168.12

Powder X-ray diffraction

Again, it was not possible to obtain the single crystal X-ray for all the compounds, so this technique was used to correlate the diffractograms for all compounds. In **Figure 2.15**, it is possible to observe that all the complexes show crystallinity, but the **C11**, **C12_2** and **C14** show more crystallinity than the **C10**, **C12_1** and **C13**. It is possible to observed that the diffractograms for all complexes have peaks in different angles. That way, the complexes should be different compound.

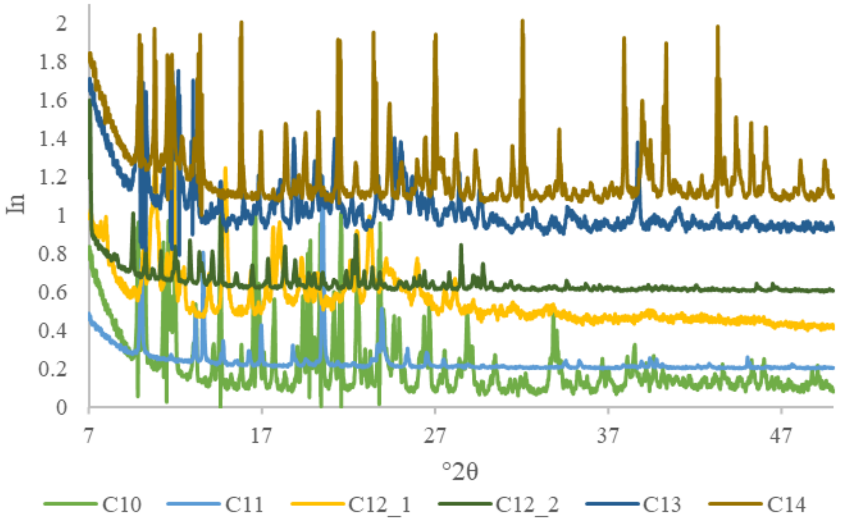

Figure 2.15 Powder X-ray diffractograms for complexes **C10-C14**.

To understand if the single crystal was representative of all the sample, powder and pattern generated from the single crystal structure of **C10**, **C11**, **C12_1•H_2O•MeOH, C12_2•CH_3CN** and **C14** were compared and can be found in the annexes **Figure A.26**, **Figure A.27, Figure A.28, Figure A.29** and **Figure A.30**.

For complexes **C10, C11, C12_2•CH_3CN** and **C14** it is possible to observe that the powder X-ray peaks had a corresponding peak in the single crystal X-ray. Thus, for these complexes the sample has the same structure as the corresponding single crystal.

Although the powder of **C12_1•H_2O•MeOH** has a low crystallinity level, when observing both diffractograms we understand that they do not have the equivalent peaks. In this case, the single crystal was not representative of all sample and it does not have the same structure.

SQUID magnetometry

The SQUID magnetometry plot for the six complexes can be observe in **Figure 2.16**. The samples were measured with alternating cooling/warming runs at the rate of 5 K min^{-1} between 370 and 10 K to obtain the molar magnetic susceptibility by the temperature ($\chi_M T$) as function of the temperature.

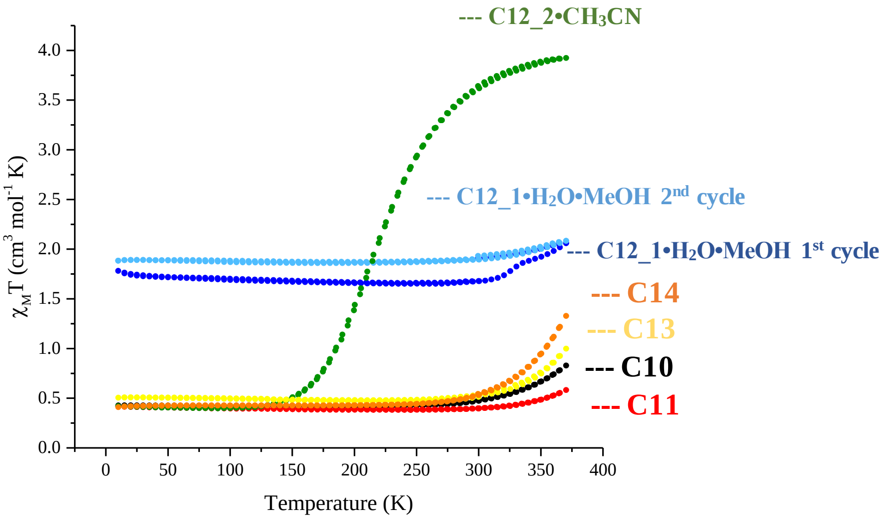

Figure 2.16 χ_MT vs T plot for complexes **C10-C14.**

Complexes **C10**, **C11**, **C13** and **C14** present a similar behavior. Between 10 K and 250 K, Fe(III) centers stay in the LS state and then the $\chi_M T$ value starts to increase at different levels. At 370 K, **C10** has a $\chi_M T$ value of 0.83 cm^3 mol^{-1} K, approximately 20% HS and 80% LS, **C11** had a very small increase, to 0.58 cm^3 mol^{-1} K, maintaining the majority of the centers in the LS state, **C13** $\chi_M T$ value rose to 1.00 cm^3 mol^{-1} K, representing approximately 30% HS and 70% LS and **C14** admitted a $\chi_M T$ value of 1.33 cm^3 mol^{-1} K, with 40% in the HS and 60% in the LS. This small increase in this group of complexes suggest that a spin transition could occur at temperatures over 370 K, making it interesting to perform further studies.

The **C12_1•H$_2$O•MeOH** and **C12_2•CH$_3$CN** displayed different behaviors. In the case of **C12_1•H$_2$O•MeOH** at the initial temperature of 300 K was observed a $\chi_M T$ value of 1.68 cm^3 mol^{-1} K. The sample was cooled to 10 K and presented a $\chi_M T$ value of 1.78 cm^3 mol^{-1} K. It was then warmed up to 370 K where the $\chi_M T$ value was 2.06 cm^3 mol^{-1} K. When the sample was cooled to 300 K, it admitted a slightly higher $\chi_M T$ value of 1.90 cm^3 mol^{-1} K and a second cycle was performed, where the sample was cooled down to 10 K again and presented a $\chi_M T$ value of 1.88 cm^3 mol^{-1} K. It was then warmed up to 370 K where the $\chi_M T$ value was 2.08 cm^3 mol^{-1} K. The difference between cycles indicates the loss of the solvent after the first cycle. The results reveal that the Fe(III) centers are 50% HS and 50% LS state during the analysis.

The measurements of **C12_2•CH$_3$CN** starts at 300 K with a $\chi_M T$ value of 3.63 cm^3 mol^{-1} K. The sample was cooled to 10 K and admitted a $\chi_M T$ value of 0.42 cm^3 mol^{-1} K and after was warmed up to 370 K where the $\chi_M T$ value rose to 3.92 cm^3 mol^{-1} K. The sample presents a gradual/abrupt and incomplete SCO curve. At 10 K the complex was in a LS state and at 370 K was approximately 90% HS and 10% LS. To be able to further understand the magnetic behavior of **C12_2•CH$_3$CN** with the change in the temperature, a second structure at 110 K was determined by single crystal X-ray diffraction. With this we aimed to understand which differences the crystal lattice presented at both temperatures. In the **Table 2.14** we can observe the representative bonds for both complexes, were at 110 K the Fe(III) centers are in LS state and at 296 K are in HS state.

Table 2.14 Representative bond lengths of **C12_2•CH$_3$CN** at 110 K and 296 K.

Temperature	**110 K**		**296 K**	
Fe-N$_{imine}$	Fe-N1 Fe-N3	1.921(5) 1.929(5)	Fe-N1 Fe-N3	2.093(3) 2.077(3)
Fe-N$_{amine}$	Fe-N2 Fe-N4	2.022(5) 2.035(5)	Fe-N2 Fe-N4	2.197(3) 2.203(3)
Fe-O$_{phen}$	Fe-O1 Fe-O2	1.857(4) 1.868(4)	Fe-O1 Fe-O2	1.907(3) 1.907(3)
State	LS		HS	

In **Table 2.15** it is possible to observe the hydrogen bond lengths and angles presented in the crystal lattice at 110 K and 296 K. No new interactions were formed with cooling the sample, however, a shortening of the existing interaction and a flattening of the interaction angle is observable. The bond angle at 110 K is higher than at 296 K and as expected at 110 K the bond lengths are shorter.

Table 2.15 Hydrogen bond lengths and angles for **C12_2•CH$_3$CN** at 110 K and 296 K.

Complex	**D-H···A**	**d(H···A) (Å)**	**d(D···A) (Å)**	**(D-H···A) (º)**
296 K	N4-H4···N5	2.205	3.096	171.46
110 K	N4-H4···N5	2.037	3.035	175.73

[Fe(3,5-I-salEen)$_2$]Y

The reaction of Fe(NO$_3$)$_3$ and different Fe(II) salts with 3,5-I-salEen at room temperature resulted in very dark solutions sometimes accompanied by a dark powder, thus confirming the formation of coordination compounds.

In this group five Fe(III) complexes were synthesized, the **C15** corresponds to [Fe(3,5-I-salEen)$_2$]ClO$_4$, **C16** to [Fe(3,5-I-salEen)$_2$]PF$_6$, **C17** to [Fe(3,5-I-salEen)$_2$]BPh$_4$, **C18** to [Fe(3,5-I-salEen)$_2$]BF$_4$ and **C19** to [Fe(3,5-I-salEen)$_2$]NO$_3$, **Scheme 2.6**. **C19_1** and **C19_2** are both products of **C19** reaction. In this reaction, the solution and the dark powder resulted in crystalline solids after recrystallization. **C19_1** is the products obtained after slow evaporation of the mother liquor, and **C19_2** is the powders precipitated during the reaction.

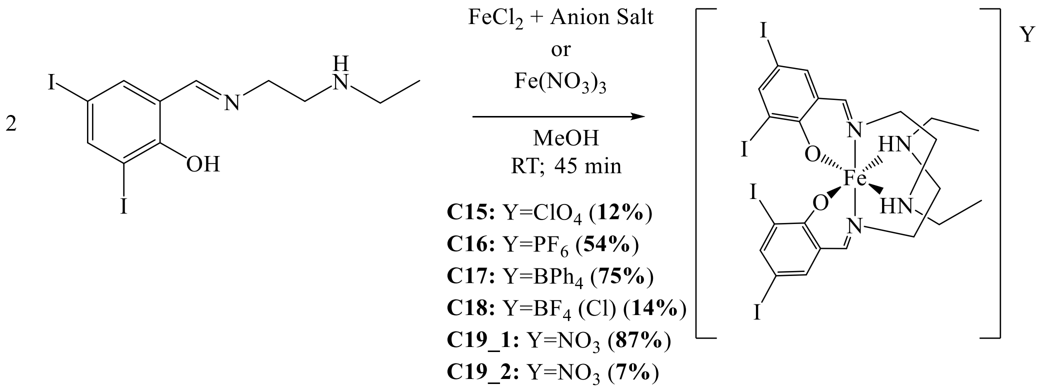

Scheme 2.6 Synthesis of the complexes with the 3,5-I-salEen ligand, with the anions perchlorate, hexafluorophosphate, tetraphenylborate, tetrafluoroborate and nitrate.

FTIR and UV-vis Spectroscopy

The FTIR spectroscopy was used to confirm the imine formation through the observation of a strong stretching vibration and the presence of the different anions through the observation of their characteristic vibrational modes.

The FTIR spectrum for the **C19_1** and **C19_2** can be overlapped, that way we considered that they were the same complex, **C19**, **Figure 2.17**. The FTIR assigned vibrations for **C15-C19** are in **Table 2.16**. The FTIR spectrum of the remaining complexes can be found in in the annexes, **Figure A.31, Figure A.32** and **Figure A.33.**

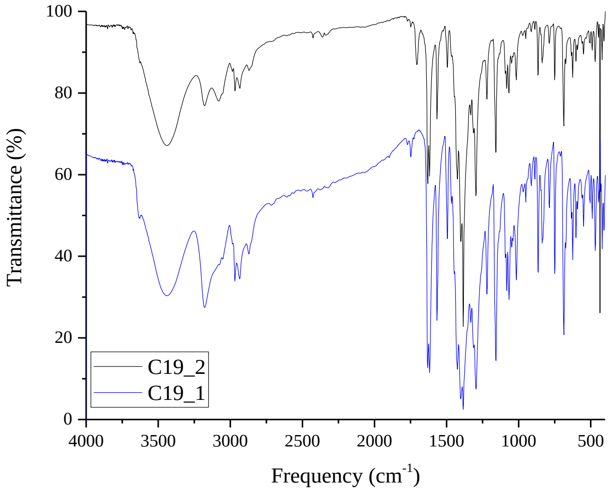

Figure 2.17 FTIR spectra of **C19_1** and **C19_2**.

Table 2.16 Wavenumbers for the characteristic FTIR spectrum bands, for complexes **C15-C19**.

Complex	**Wavenumber (cm^{-1})**						
	υ(O-H)	**υ(N-H)**	**υ(C-H)**	**υ(C=N)**	**υ(C=C)**	**Anion**	
C15	3416	3234	2966	1619	1564-1462	ClO_4^-	1066, 625
C16	3437	3093	2969	1632	1565-1470	PF_6^-	840
C17	3500	3238	2977	1618	1577-1478	BPh_4^-	745-707
C18	3441	3059	2979	1629	1567-1468	BF_4^-	-
C19	3440	3177	2969	1630	1564-1465	NO_3^-	1385

The vibrations corresponding to O-H bonds are around 3400 cm^{-1}, N-H bonds are around 3200 cm^{-1}, C-H bonds are around 2970 cm^{-1}, C=N bonds are around 1600 cm^{-1}, C=C bonds are between 1580-1430 cm^{-1} and the anions vibrations are perchlorate at 625 cm^{-1} and 1066 cm^{-1}, hexafluorophosphate at 840 cm^{-1}, tetrafenilborate at 707 cm^{-1} to 745 cm^{-1} and nitrate at 1385 cm^{-1}. For **C18** the tetrafluoroborate vibration was not observed in the FTIR spectrum, which means that the change of counter-ion did not occur, **Figure 2.18**.

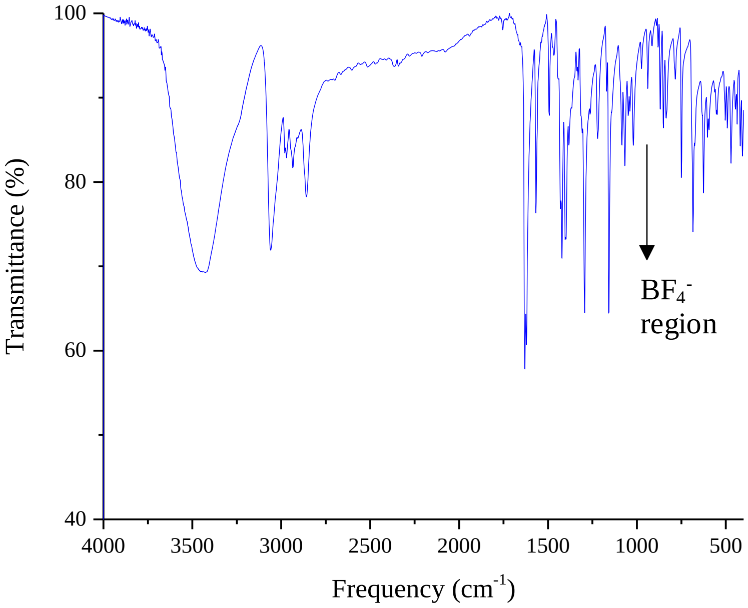

Figure 2.18 FTIR spectrum of **C18**.

The UV-vis spectra for all five complexes were recorded in acetonitrile between 190 and 900 nm and can be observed in **Figure 2.19**.

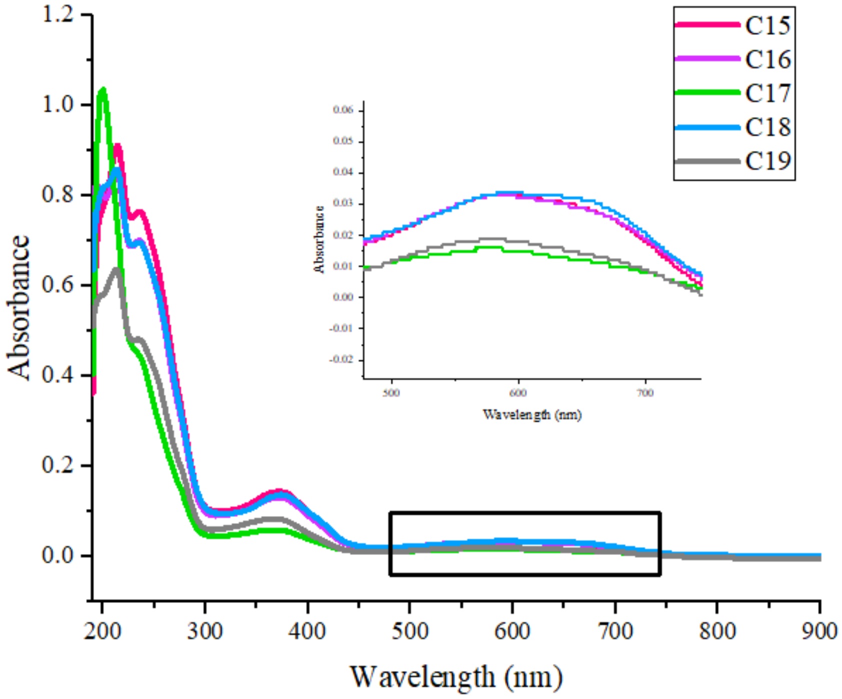

Figure 2.19 UV-vis spectra of **C15-C19** in acetonitrile.

The **C15** and **C17** present four bands, the **C16** and **C19** present five bands and the **C18** presents six bands. Details in the bands can be observed in **Table 2.17**.

Table 2.17 Values for the bands UV-vis, for complexes **C15-C19**.

Complex	Concentration (mol.dm^{-3})	Wavelength (nm)	Absorbance	Molar absorption coefficient (mol.dm^{-3}.cm^{-1})
C15	2 x 10^{-5}	214.0 235.5 371.5 588.0	0.911 0.765 0.143 0.033	45 550 38 250 7 150 1 650
C16	10^{-5}	193.5 214.0 235.5 375.0 585.0	0.825 0.844 0.700 0.130 0.033	82 500 84 400 70 000 13 000 3 300
C17	10^{-5}	200.0 233.5 366.0 576.0	1.035 0.451 0.058 0.016	103 500 45 100 5 800 1 600
C18	10^{-5}	200.5 213.0 234.5 373.5 593.0 620.0	0.817 0.859 0.696 0.137 0.034 0.033	81 700 85 900 69 600 13 700 3 400 3 300
C19	10^{-5}	199.5 212.5 234.0 365.5 579.5	0.580 0.635 0.481 0.083 0.019	58 000 63 500 48 100 8 300 1 900

All complexes in **Table 2.17** present bands at different wavelengths and with different molar absorption coefficients. The bands around 200 nm belong to intraligand interactions, with variations between 103 500 (**C17**) and 38 000 mol.dm^{-3}.cm^{-1} (**C15**). Complexes **C15** and **C17** presented two bands, while the others displayed three.

The bands between 300 and 400 nm should be attributed to charge-transfer between the ligands and the iron, or vice-versa, with variations between 13 700 and 5 800 mol.dm^{-3}.cm^{-1}. The higher molar absorption coefficients belong to **C18** and **C16** and the smaller belong to **C17**. All complexes presented one of this bands.

Bands between 500 nm and 700 nm also correspond to charge-transfer between the ligands and the iron, or vice-versa, and to spin states.[103] The **C18** present two bands, one around 590 nm and other around 620 nm and the other complexes presents only one. All complexes presented one band around 585 nm with variations between 3 400 and 1 600 mol.dm^{-3}.cm^{-1}. In solution at room-temperature, **C18** displays fractions in both HS and LS states, with slightly more Fe(III) centres in the HS state. The other complexes show the LS state. In general, **C15** presented the lowest coefficients.

Structural characterization

Single Crystal X-ray diffraction

Single crystals with good quality for X-ray diffraction were only obtained for **C15**, **C18** and **C19**. The other two compounds were crystalline but presented poor or no diffraction. The single crystal X-ray diffraction allows the prediction of the spin state of the complex at a specific temperature, through the Fe-X bond lengths.

The X-ray data at 296 K revealed that the compounds were found in their unsolvated form **C15**, **C18** and **C19**. The crystal data and structure refinement of this complexes is listed in **Table A.3**, in the annexes.

In **C15**, the asymmetric unit at 296 K comprises two cation and two anions. The unit cell contains eight asymmetric unit, **Figure A.34**, in the annexes.

In the case of **C18**, the asymmetric unit at 296 K comprises one cation and one chloride. The unit cell contains four asymmetric unit, **Figure A.35**, in the annexes. The single crystal data corroborate the FTIR results where no anion exchange occurred.

For **C19**, the asymmetric unit at 296 K comprises one cation and one anion. The unit cell contains eight asymmetric unit, **Figure A.36**, in the annexes.

In **Table 2.18** are the representative bond lengths of **C15**, **C18** and **C19**, at 296 K, where the three complexes reveal bond lengths corresponding to the LS state.

Table 2.18 Representative bond lengths of **C15**, **C18** and **C19** at 296 K.

Complex	C15				C18		C19	
	Molecule 1		Molecule 2					
Fe-N$_{imine}$	Fe-N1 Fe-N3	1.922(9) 1.933(10)	Fe-N5 Fe-N7	1.932(10) 1.940(9)	Fe-N1 Fe-N3	1.930(6) 1.926(6)	Fe-N1 Fe-N3	1.939(7) 1.921(7)
Fe-N$_{amine}$	Fe-N2 Fe-N4	2.059(12) 2.037(10)	Fe-N6 Fe-N8	2.026(13) 2.044(10)	Fe-N2 Fe-N4	2.021(7) 2.033(6)	Fe-N2 Fe-N4	2.021(7) 2.040(7)
Fe-O$_{phen}$	Fe-O1 Fe-O2	1.881(9) 1.864(9)	Fe-O11 Fe-O12	1.860(9) 1.886(8)	Fe-O1 Fe-O2	1.864(6) 1.870(5)	Fe-O1 Fe-O2	1.881(5) 1.860(6)
State	LS		LS		LS		LS	

In **Table 2.19** it is possible to observe the hydrogen bond lengths and angles for the **C15**, **C18** and **C19**. The hydrogen bonds for **C15** and **C19** are between the hydrogens of the nitrogen atoms of the ligand and one oxygen of the anion. In case of **C18** the hydrogen bonds are between one hydrogen of the nitrogen atoms of the amine of the ligand and one chloride anion. The corresponding figures are in the annexes, **Figure A.37**.

Table 2.19 Hydrogen bond lengths and angles for **C15**, **C18** and **C19.**

Complex	D-H···A	d(H···A) (Å)	d(D···A) (Å)	(D-H···A) (°)
C15	N2-H2···O6	2.274	3.228	164.02
	N6-H6···O10	2.088	3.052	167.15
	N8-H8···O10	2.112	3.090	174.54
C18	N4-H4···Cl1	2.319	3.161	163.79
C19	N2-H2···O4	2.107	2.987	148.73
	N4-H4···O3	1.995	2.969	171.94

Powder X-ray diffraction

In **Figure 2.20**, it is possible to observe that the **C16** and **C17** show more crystallinity than **C19**, which has more crystallinity than the **C15** and the **C18**. It is also possible to observe that all the diffractograms have peaks in different angles, so they should be different compound.

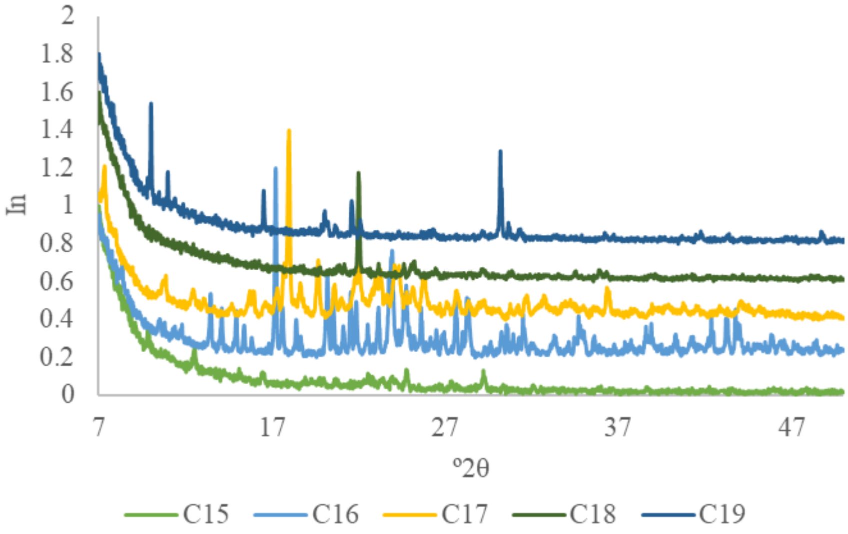

Figure 2.20 Powder X-ray diffractograms for **C15-C19**.

The powder and pattern generated from the single crystal structure of **C15**, **C18** and **C19** were compared to understand if the single crystal observe was representative of all the sample, **Figure A.38**, **Figure A.39** and **Figure A.40**, in the annexes.

For complexes **C15** and **C18**, the powder diffractogram did not showed well-defined peaks, demonstrating less crystallinity than the single crystal diffractogram. With the data collected, it was not possible to guarantee that all the sample has the same structure.

The same happen to **C19** but although the powder diffractogram has a low crystallinity level, when observing both diffractograms we understand that they have equivalent peaks. We conclude that the crystal is representative of all sample.

SQUID magnetometry

The SQUID magnetometry plot for the five complexes can be observe in **Figure 2.21**. The samples were measured with alternating cooling/warming runs at the rate of 5 K min^{-1} between 370 and 10 K to obtain the molar magnetic susceptibility by the temperature ($\chi_M T$) as function of the temperature.

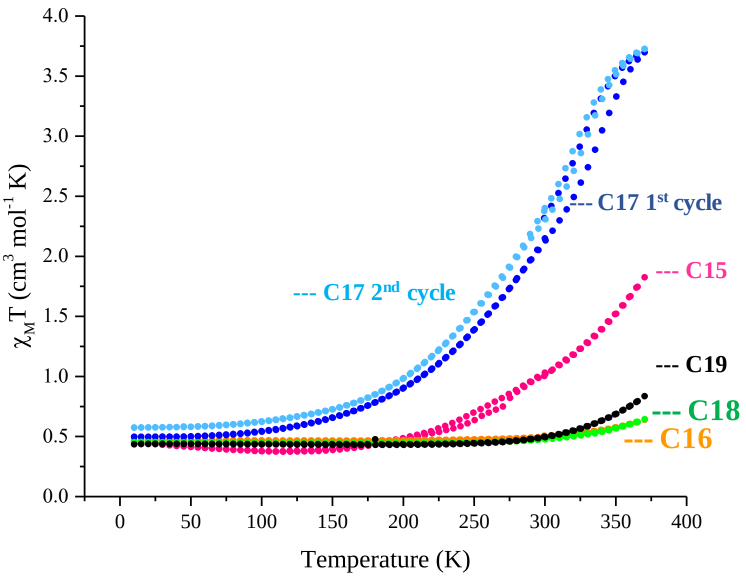

Figure 2.21 χ_MT vs T plot for complexes **C15-C19.**

The **C15** measurement started at 300 K where a $\chi_M T$ value of 1.03 cm^3 mol^{-1} K was observed. The sample was cooled to 10 K and admitted a $\chi_M T$ value of 0.45 cm^3 mol^{-1} K and after was warmed up to 370 K, where the $\chi_M T$ value rose to 1.82 cm^3 mol^{-1} K. Between 10 K and 150 K, the complex is essentially LS and after that temperature presents a gradual and incomplete SCO curve. At 370 K the sample is approximately 50% HS and 50% LS.

Three complexes in this groups displayed similar behavior, **C16**, **C18** and **C19**. After maintaining a stable $\chi_M T$ value between 10 K and 250 K, it started to rose in different proportion. At 370 K, **C16** and **C18** presented a $\chi_M T$ value of 0.64 cm^3 mol^{-1} K, with the majority of Fe(III) centers in the LS state and **C19** $\chi_M T$ increased to 0.84 cm^3 mol^{-1} K, where the sample is approximately 20% HS and 80% LS.

For **C17**, at the initial temperature of 300 K was observed a $\chi_M T$ value of 2.15 cm^3 mol^{-1} K. The sample was cooled to 10 K and presented a $\chi_M T$ value of 0.50 cm^3 mol^{-1} K. It was then warmed up to 370 K where the $\chi_M T$ value increased to 3.70 cm^3 mol^{-1} K. When the sample was cooled to 300 K, it admitted a slightly higher $\chi_M T$ value of 2.40 cm^3 mol^{-1} K, so a second cycle was performed. The **C17** was cooled down to 10 K again and presented a $\chi_M T$ value of 0.57 cm^3 mol^{-1} K. It was then warmed up to 370 K where the $\chi_M T$ value was 3.73 cm^3 mol^{-1} K. This difference indicates the loss of the solvent after the first cycle. The sample presents a gradual and incomplete SCO curve, at 10 K it is in the LS state and at 370 K is approximately 85% HS and 15% LS.

2.2.2.Hetero-substituent compounds

[Fe(3-Br-5-Cl-salEen)$_2$]Y

The reaction of Fe(NO$_3$)$_3$ and different Fe(II) salts with 3-Br-5-Cl-salEen at room temperature resulted in very dark solutions sometimes accompanied by a dark powder, thus confirming the formation of coordination compounds.

In this group five Fe(III) complexes were synthesized, were **C20** corresponds to [Fe(3-Br-5-Cl-salEen)$_2$]ClO$_4$, **C21** to [Fe(3-Br-5-Cl-salEen)$_2$]PF$_6$, **C22** to [Fe(3-Br-5-Cl-salEen)$_2$]BPh$_4$, **C23** to [Fe(3-Br-5-Cl-salEen)$_2$]BF$_4$ and **C24** to [Fe(3-Br-5-Cl-salEen)$_2$]NO$_3$, in **Scheme 2.7**.

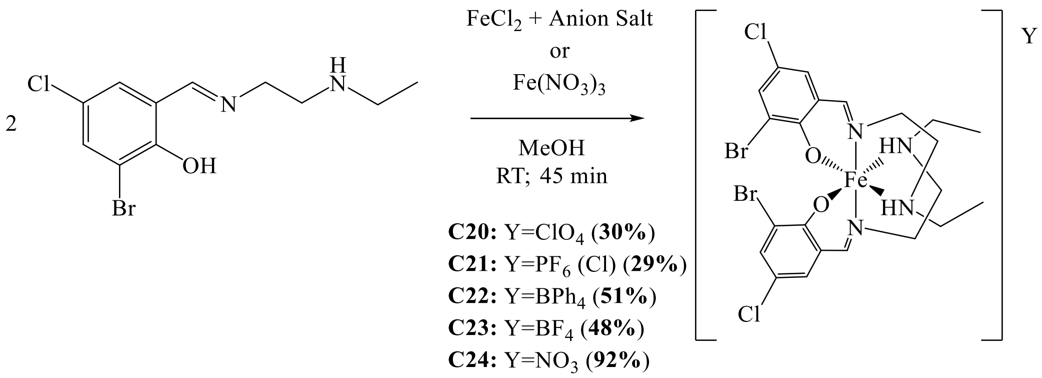

Scheme 2.7 Synthesis of the complexes with the 3-Br-5-Cl-salEen ligand, with the anions perchlorate, hexafluorophosphate, tetraphenylborate, tetrafluoroborate and nitrate.

FTIR and UV-vis Spectroscopy

The FTIR spectroscopy was used to confirm the imine formation through the observation of a strong stretching vibration and the presence of the different anions through the observation of their characteristic vibrational modes. The FTIR assigned vibrations for **C20-C24** can be observed in **Table 2.20**. The FTIR spectrum of the five complexes can be found in the annexes, **Figure A.41, Figure A.42, Figure A.43, Figure A.44 and Figure A.45**.

Table 2.20 Wavenumbers for the characteristic FTIR spectrum bands, for complexes **C20-C24**.

Complex	**Wavenumber (cm^{-1})**						
	υ(O-H)	**υ(N-H)**	**υ(C-H)**	**υ(C=N)**	**υ(C=C)**	**Anion**	
C20	3433	3234	2976	1630	1581-1468	ClO_4^-	1062, 623
C21	3444	-	2970	1632	1583-1464	PF_6^-	839
C22	3438	3219	2982	1625	1579-1478	BPh_4^-	743-708
C23	3417	-	2970	1619	1583-1428	BF_4^-	1069
C24	3440	3171	2977	1628	1586-1514	NO_3^-	1384

As anticipated, the vibrations corresponding to O-H bonds are around 3400 cm^{-1}, N-H bonds are around 3200 cm^{-1} (only for **C20**, **C22** and **C24**), C-H bonds are around 2970 cm^{-1}, C=N bonds are around 1600 cm^{-1}, C=C bonds are between 1590-1460 cm^{-1} and the anions vibrations are perchlorate at 623 cm^{-1} and 1062 cm^{-1}, hexafluorophosphate at 839 cm^{-1}, tetraphenylborate at 708 cm^{-1} to 743 cm^{-1}, tetrafluoroborate at 1069 cm^{-1} and nitrate at 1384 cm^{-1}. For **C21** and **C23** the stretching of the N-H bond is not observed because the O-H band is very large and overlaps it. This is possibly related to the higher amount of water present in these two samples.

As for the two substituents presented before, the perchlorate and the tetrafluoroborate shows the imine stretching band in the two edges, 1645 cm^{-1} and 1631 cm^{-1}, respectively. This could indicate that one of them is forming hydrogen bonds with the cation while the other is not.

The UV-vis spectra for all five complexes was recorded in acetonitrile between 190 and 900 nm and can be observed in **Figure 2.22**.

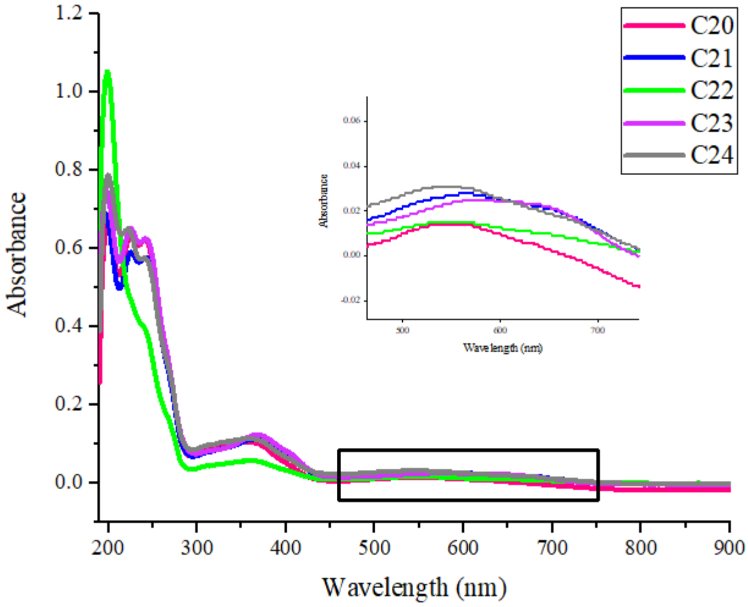

Figure 2.22 UV-vis spectra of **C20-C24** in acetonitrile.

Most of the samples presented six absorption bands except **C22**, that presented four. Details on the bands can be observed in **Table 2.21**.

Table 2.21 Values for the bands UV-vis, for complexes **C20-C24**.

Complex	Concentration (mol.dm^{-3})	Wavelength (nm)	Absorbance	Molar absorption coefficient (mol.dm^{-3}.cm^{-1})
C20	2 x 10^{-5}	199.0 225.5 241.5 357.0 548.5 627.0	0.662 0.639 0.622 0.105 0.014 0.006	33 100 31 950 31 100 5 250 700 300
C21	10^{-5}	194.0 225.5 241.5 364.0 564.5 635.5	0.694 0.591 0.578 0.113 0.028 0.023	69 400 59 100 57 800 11 300 2 800 2 300
C22	10^{-5}	198.5 237.5 360.0 540.5	1.052 0.408 0.056 0.010	105 200 40 800 5 600 1 000
C23	10^{-5}	197.5 225.0 241.5 364.5 576.5 631.0	0.751 0.652 0.625 0.123 0.025 0.023	75 100 65 200 62 500 12 300 2 500 2 300
C24	10^{-5}	199.5 222.0 240.5 357.0 544.0 632.0	0.788 0.650 0.575 0.114 0.031 0.021	78 800 65 000 57 500 11 400 3 100 2 100

All complexes in **Table 2.21** present bands at different wavelengths and with different molar absorption coefficients. The bands around 200 nm correspond to intraligand interactions, with the higher molar absorption coefficient belonging to **C22**, 105 200 mol.dm^{-3}.cm^{-1} and the lower to **C20**, 31 100 mol.dm^{-3}.cm^{-1}. All complexes presented three of this bands except the **C22** that presented two.
The bands between 300 and 400 nm should be attributed to charge-transfer between the ligands and the iron, or vice-versa, with the bigger molar absorption coefficients belonging to **C23**, 12 300 mol.dm^{-3}.cm^{-1} and the smaller to **C20**, 5 250 mol.dm^{-3}.cm^{-1}. All complexes presented one of this bands.
Bands between 500 nm and 700 nm also correspond to charge-transfer between the ligands and the iron, or vice-versa, and to spin states. All complexes present two bands, except the **C22** that only presented one. The **C20**, **C22** and **C24** presented one band around 550 nm and the **C21** and **C23** presented one around 570 nm. The other band was around 635 nm. The bands at 550 and 570 nm has variations between 3 100 (**C24**) and 700 mol.dm^{-3}.cm^{-1} (**C20**). For the bands at 635 nm the higher molar absorption coefficients belong to **C21**, 2 300 mol.dm^{-3}.cm^{-1} and the smaller to **C20**, 300 mol.dm^{-3}.cm^{-1}. The C22 is the only one in the LS state in solution at room-temperature, while the others presents fractions in the HS and LS states, although all have more Fe(III) centres in the LS state, but for the **C23** that is not so clear. The **C20** presented the lowest coefficients.

Structural characterization

Single Crystal X-ray diffraction

Single crystals with good quality for X-ray diffraction were only obtained for **C20, C21** and **C22**. The remaining compounds were crystalline but presented poor or no diffraction. The spin state of the complex at a specific temperature, through the Fe-X bond lengths, was predicted.
The X-ray data at 296 K revealed that one compound was found in their unsolvated form **C21** and the other two were found in the solvated **C20•CH$_3$CN** and **C22•H$_2$O•CH$_3$CN**. The crystal data and structure refinement of this complexes is listed in **Table A.4**, in the annexes.
In **C20•CH$_3$CN**, the asymmetric unit at 296 K comprises one cation, one anion and one molecule of acetonitrile. The unit cell contains eight asymmetric unit, **Figure A.46**, in the annexes.
For the **C21**, at 296 K the asymmetric unit comprises three cations and three anions (one hexafluorophosphate and two chlorides). The unit cell contains eight asymmetric units, **Figure A.47**, in the annexes.
In the case of **C22•H$_2$O•CH$_3$CN**, the asymmetric unit at 296 K comprises one cation, one anion, one molecule of acetonitrile and one water molecule. The unit cell contains four asymmetric unit, **Figure A.48**, in the annexes.
In **Table 2.22** are the representative bond lengths of **C20•CH$_3$CN**, **C21** and **C22•H$_2$O•CH$_3$CN** at 296 K where the **C20•CH$_3$CN** show bond lengths corresponding to the LS state, the **C21** show bond lengths corresponding to the LS state for two molecules and for one molecule show bond lengths corresponding to the HS and **C22•H$_2$O•CH$_3$CN** show bond lengths corresponding to the HS state.

Table 2.22 Representative bond lengths of **C20•CH$_3$CN-C22•H$_2$O•CH$_3$CN** at 296 K.

Complex	**C20•CH$_3$CN**		**C21**						**C22•H$_2$O•CH$_3$CN**	
			Molecule 1		**Molecule 2**		**Molecule 3**			
Fe-N$_{imine}$	Fe-N2	1.920(3)	Fe-N5	2.086(5)	Fe-N1	1.922(5)	Fe-N7	1.925(5)	Fe-N1	1.982(9)
	Fe-N4	1.921(3)	Fe-N5	2.086(5)	Fe-N3	1.926(5)	Fe-N7	1.925(5)	Fe-N3	1.990(19)
Fe-N$_{amine}$	Fe-N1	2.058(3)	Fe-N6	2.171(5)	Fe-N2	2.044(5)	Fe-N8	2.043(6)	Fe-N2	2.119(10)
	Fe-N3	2.040(3)	Fe-N6	2.171(5)	Fe-N4	2.050(5)	Fe-N8	2.043(6)	Fe-N4	2.112(10)
Fe-O$_{phen}$	Fe-O1	1.874(2)	Fe-O3	1.919(4)	Fe-O1	1.885(4)	Fe-O4	1.868(4)	Fe-O1	1.877(10)
	Fe-O2	1.871(3)	Fe-O3	1.919(4)	Fe-O2	1.870(4)	Fe-O4	1.868(4)	Fe-O2	1.897(8)
State	LS		HS		LS		LS		HS	

In **Table 2.23** it is possible to observe the hydrogen bond lengths and angles for **C20•CH$_3$CN**, **C21** and **C22•H$_2$O•CH$_3$CN**. The hydrogen for **C20•CH$_3$CN** is between the hydrogens of the nitrogen atoms of the ligand and one oxygen of the anion. For **C21** the hydrogen bonds are between the hydrogens of the nitrogen atoms of the amine of the ligand and the chlorine anions. In case of **C22•H$_2$O•CH$_3$CN** the hydrogen bonds are between the hydrogen of the nitrogen atoms of the ligand and the water. The hydrogen bonds for the **C20•CH$_3$CN**, **C21** and **C22•H$_2$O•CH$_3$CN** can be observed in **Figure A.49** in the annexes.

Table 2.23 Hydrogen bond lengths and angles for **C20•CH3CN-C22•H2O•CH3CN.**

Complex	**D-H···A**	**d(H···A) (Å)**	**d(D···A) (Å)**	**(D-H···A) (º)**
C20•CH$_3$CN	N1-H1···O4	2.568	3.301	165.01
	N3-H3···O4	2.307	3.104	175.00
C21	N2-H2···Cl5	2.239	3.215	174.19
	N4-H4···Cl5	2.525	3.314	165.56
	N6-H6···Cl6	2.112	3.090	174.54
	N8-H8···Cl6	2.507	3.297	166.30
C22•H$_2$O•CH$_3$CN	N2-H2···O3	2.193	3.107	154.59
	N4-H4···O3	2.081	3.048	168.73

Powder X-ray diffraction

This technique was used to correlate the diffractograms for all compounds. In **Figure 2.23**, it is possible to observe that all the complexes show crystallinity, but the **C23** show less than the other four. Also, all diffractograms have peaks in different angles, so they correspond to different compounds.

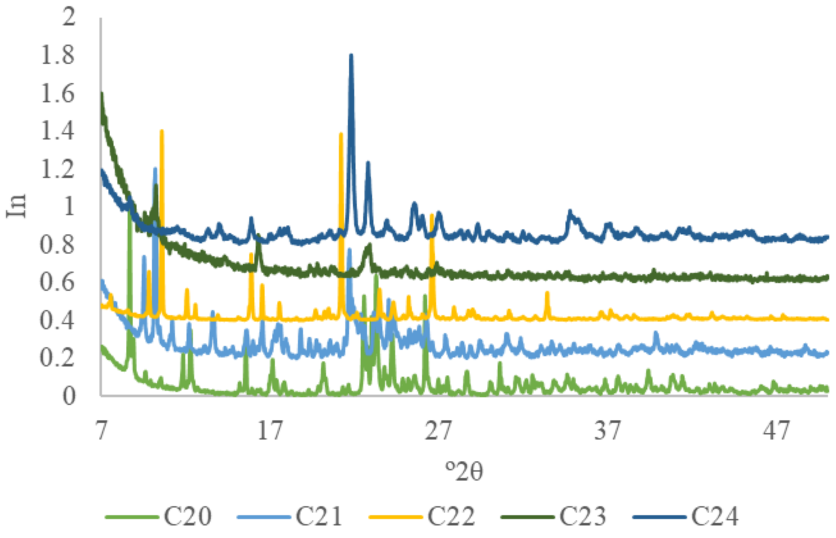

Figure 2.23 Powder X-ray diffractograms for **C20-C24**.

To understand if the single crystal observe was representative of all the sample, both diffractograms (powder and pattern generated from the single crystal structure) of **C20**, **C21** and **C22** were compared. For all complexes it is possible to observe that all the powder X-ray peaks had a corresponding peak in the single crystal X-ray, **Figure A.50**, **Figure A.51** and **Figure A.52**, in the annexes. That way we conclude that all the sample have the same structure.

SQUID magnetometry

The SQUID magnetometry plot for the five complexes can be observe in **Figure 2.24**. The samples were measure with alternating cooling/warming runs at the rate of 5 K min^{-1} between 370 and 10 K to obtain the molar magnetic susceptibility by temperature ($\chi_M T$) as a function of the temperature.

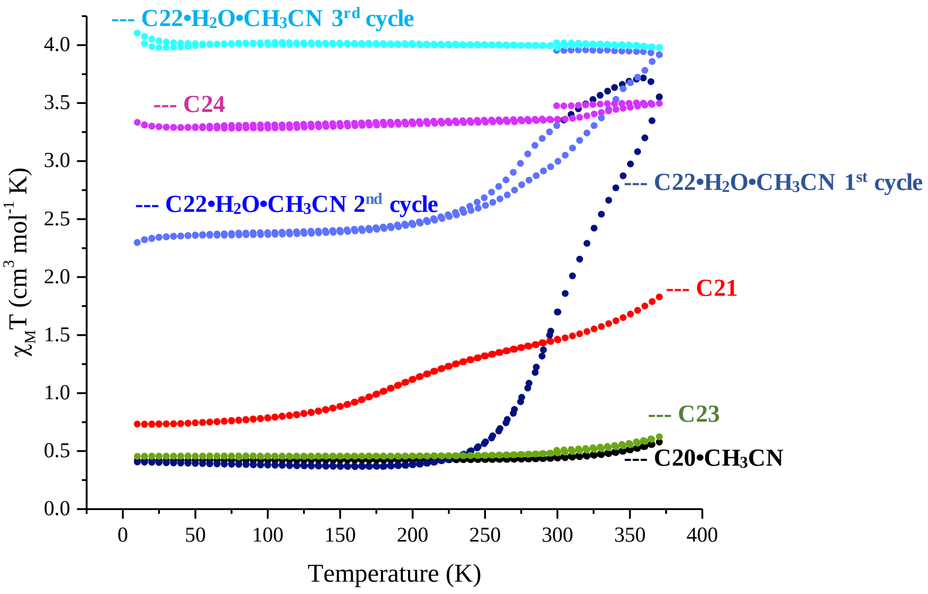

Figure 2.24 χ_MT vs T plot for complexes **C20•CH$_3$CN-C24.**

The **C20•CH$_3$CN** and **C23** displayed similar behaviors and $\chi_M T$ value, maintaining the Fe(III) centres in LS state during the analysis. $\chi_M T$ value was around 0.45 cm^3 mol^{-1} K between 10 and 300 K, with a small rise at 370 K, where it was 0.58 cm^3 mol^{-1} K (**C20•CH$_3$CN**) and 0.62 cm^3 mol^{-1} K (**C23**).

In case of **C21**, at the initial temperature of 300 K it was observed a $\chi_M T$ value of 1.46 cm^3 mol^{-1} K. The sample was cooled to 10 K and presented a $\chi_M T$ value of 0.73 cm^3 mol^{-1} K. It was then warmed up to 370 K where the $\chi_M T$ value rose to 1.83 cm^3 mol^{-1} K. The sample presents a gradual and incomplete SCO curve with a step in the warming and cooling curves between 123 and 275 K. The sample at 10 K is approximately 25% HS and 75% LS and at 370 K is approximately 50% HS and 50% LS. It would be interesting to perform further studies at higher temperatures.

In case of **C22•H$_2$O•CH$_3$CN**, the sample presented a $\chi_M T$ value of 1.70 cm^3 mol^{-1} K at 300 K. The sample was cooled to 10 K and admitted a $\chi_M T$ value of 0.41 cm^3 mol^{-1} K. It was then warmed up to 370 K, where the $\chi_M T$ value increased to 3.55 cm^3 mol^{-1} K. The sample presented a gradual and incomplete SCO curve, at 10 K is LS state and at 370 K is approximately 80% HS and 20% LS. When the sample was cooled to 300 K, it admitted a $\chi_M T$ value of 3.31 cm^3 mol^{-1} K, higher than the initial value at the same temperature and a second cycle was performed. The sample was cooled to 10 K again and presented a $\chi_M T$ value of 2.30 cm^3 mol^{-1} K (50% HS state and 50% LS). It was then warmed up to 370 K where the $\chi_M T$ value was 3.92 cm^3 mol^{-1} K (88% HS state and 12% LS state). In this cycle the sample presented a hysteresis between 225 K and 350 K and displayed $\chi_M T$ values of 2.53 and 3.69 cm^3 mol^{-1} K, respectively. At 225 K the Fe(III) centers are approximately 55% in the HS and 45% in the LS and at 350 K approximately 80% in the HS and 20% in the LS.

When the same sample was cooled down to 300 K, it admitted again a higher $\chi_M T$ value of 3.98 cm^3 mol^{-1} K and a third cycle was executed. The sample was cooled to 10 K and presented a $\chi_M T$ value of 4.10 cm^3 mol^{-1} K and it was warmed up to 370 K where the $\chi_M T$ value was 3.98 cm^3 mol^{-1} K. In this cycle the sample presented at 10 K approximately 93% HS and 7% LS and at 370 K approximately 90% HS and 10% LS. This difference between cycles indicates the loss of the solvent after the first and the second cycles.

Since the sample presented one molecule of acetonitrile and one of water in the structure, and presents a hysteresis, a new sample was measured to perform more and different cycles, to understand if the hysteresis created in the second cycle can be kept.

Three cycles between 355 K and 10 K were executed, **Figure 2.25**, but the hysteresis was lost. Thus, for the hysteresis to appear it is necessary to warm up the sample first to 370 K, for the crystals to lose the necessary solvent.

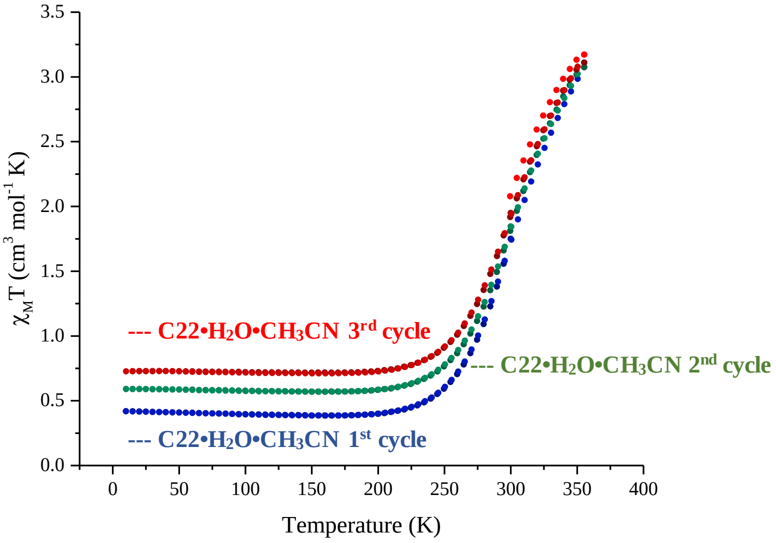

Figure 2.25 χ_MT vs T plot for second sample of **C22•H2O•CH3CN**, between 355 K and 10 K.

The sample was warmed up to 370K where it admitted a $\chi_M T$ value of 3.74 cm^3 mol^{-1} K, approximately 84% HS and 16% LS, and performed four more cycles between 350 K and 10 K, **Figure 2.26**.

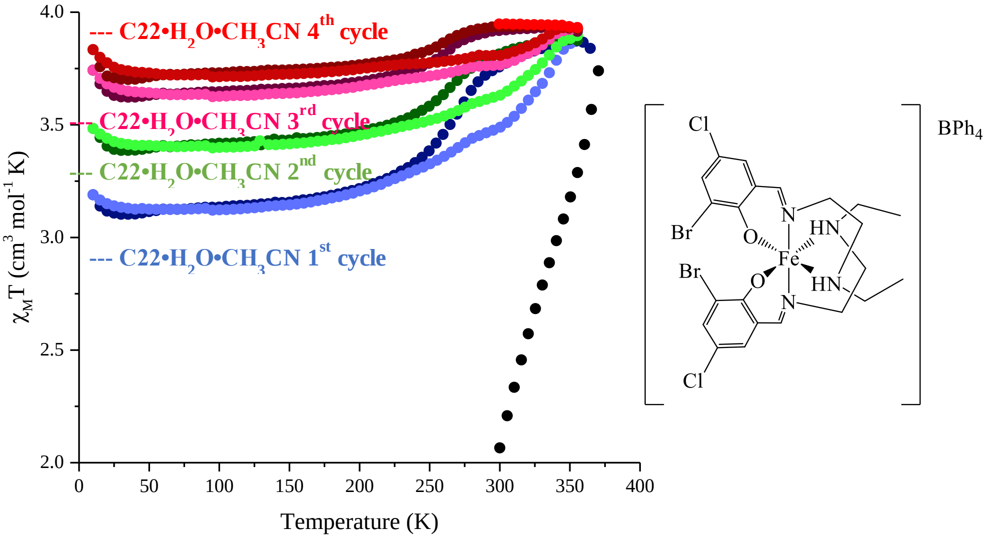

Figure 2.26 χ_MT vs T plot for second sample of **C22•H2O•CH3CN**, between 370 K and 10 K.

During these cycles, there was a significant difference of $\chi_M T$ value at 10 K, with values increasing with the number of cycles, although these differences become smaller from cycle to cycle. In cycle one, the $\chi_M T$ value of the sample was 3.19 cm^3 mol^{-1} K, corresponding to 70% HS and 30% LS, while in cycle two was 3.48 cm^3 mol^{-1} K (Fe(III) centers approximately 78% in the HS and 22% in the LS), thus, a difference of 8%. The **C22•H$_2$O•CH$_3$CN** on cycle number three displayed a $\chi_M T$ value of 3.74 cm^3 mol^{-1} K (approximately 85% HS and 15% LS), an increase of 7%. In the last cycle presented a $\chi_M T$ value of 3.83 cm^3 mol^{-1} K, corresponding to 87% HS and 13% LS, an even smaller increase of 2%. At 355 K, although there were differences, they were not significant, with $\chi_M T$ value of the sample between 3.88 cm^3 mol^{-1} K in cycle one and 3.93 cm^3 mol^{-1} K in cycles three and four, with the Fe(III) centers being approximately 88% in the HS and 12% in the LS through all cycles.

The sample presented a hysteresis in all cycles between 220 K and 350 K. As before, the differences of $\chi_M T$ value at a lower temperature (220 K) are significant, while at higher temperature (350 K) are not. At 220 K, cycle one presented a $\chi_M T$ value of 3.26 cm^3 mol^{-1} K (72% in the HS and 28% in the LS) and in the second cycle a $\chi_M T$ value of 3.49 cm^3 mol^{-1} K (78% in the HS and 22% in the LS), therefore, an increment of 6%. Cycle three displayed a $\chi_M T$ value of 3.70 cm^3 mol^{-1} K (82% in the HS and 18% in the LS), a smaller increase, of 4%, while the last cycle presented a $\chi_M T$ value of 3.76 cm^3 mol^{-1} K (84% in the HS and 16% in the LS), a difference of 2%. At 350 K, $\chi_M T$ value started at 3.86 cm^3 mol^{-1} K in cycle one and was 3.93 cm^3 mol^{-1} K in cycle four, with the Fe(III) centers being approximately 88% in the HS and 12% in the LS.

We were able to recover some crystals after the cycling studies and again data was collected by single crystal X-ray diffraction. The new structure revealed that both solvent molecules are no longer present in the crystalline lattice, however the crystal symmetry is preserved. The difference in the cycles is a consequence of the structure rearrange. The single crystal X-ray diffraction was performed to one of the crystals before (at 296 K) and after all the cycles (110 K), **Figure 2.27**.

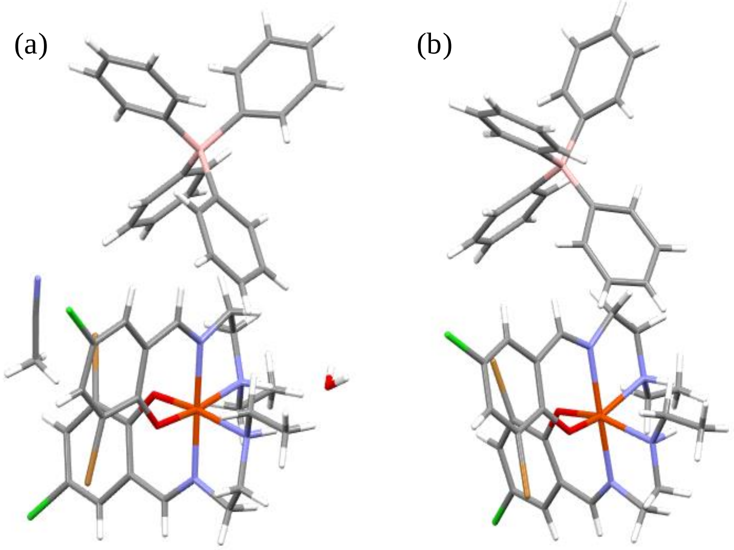

Figure 2.27 X-ray crystal structure of **C22**: (a) before SQUID magnetometry **C22•H$_2$O•CH$_3$CN** at 293 K and (b) after SQUID magnetometry at 110 K **C22**.

In **Table 2.24** are the representative bonds for both complexes before and after the SQUID magnetometry. As expected, the bond lengths are shorter before the SQUID magnetometry, indicating that the samples presented a higher HS character after the SQUID magnetometry, and that the sample after the SQUID magnetometry did not show any hydrogen bonds.

Table 2.24 Representative bond lengths of **C22•H_2O•CH_3CN** before SQUID magnetometry at 296 K and **C22** after SQUID magnetometry at 110 K.

Complex	**Before C22•H_2O•CH_3CN**		**After C22**	
Fe-N_{imine}	Fe-N1	1.982(9)	Fe-N1	2.103(12)
	Fe-N3	1.990(19)	Fe-N3	2.101(12)
Fe-N_{amine}	Fe-N2	2.119(10)	Fe-N2	2.222(13)
	Fe-N4	2.112(10)	Fe-N4	2.208(11)
Fe-O_{phen}	Fe-O1	1.877(10)	Fe-O1	1.875(14)
	Fe-O2	1.897(8)	Fe-O2	1.915(9)
State	LS/HS		HS	

For the **C24** sample a $\chi_M T$ value of 3.36 cm^3 mol^{-1} K was observed at 300 K. When cooled to 10 K it assumes a $\chi_M T$ value of 3.33 cm^3 mol^{-1} K and had a $\chi_M T$ value of 3.50 cm^3 mol^{-1} K after warming until 370 K. The sample at 10 K is approximately 70% HS and 30% LS and at 370 K is approximately 88% HS and 12% LS.

[Fe(5-Cl-3-I-salEen)$_2$]Y

The reaction of $Fe(NO_3)_3$ and different Fe(II) salts with 5-Cl-3-I-salEen at room temperature resulted in very dark solutions sometimes accompanied by a dark powder, thus confirming the formation of coordination compounds. The reaction with nitrate did not occur.

In this group four Fe(III) complexes were synthesized, were **C25** corresponds to [Fe(5-Cl-3-I-salEen)$_2$]ClO_4, **C26** to [Fe(5-Cl-3-I-salEen)$_2$]PF_6, **C27** to [Fe(5-Cl-3-I-salEen)$_2$]BPh_4 and **C28** to [Fe(5-Cl-3-I-salEen)$_2$]BF_4, **Scheme 2.8. C25_1** and **C25_2** are both products of **C25** reaction. In this reaction, the solution and the dark powder resulted in crystalline solids after recrystallization. **C25_1** is the product obtained after slow evaporation of the mother liquor, and **C25_2** is the powder precipitated during the reaction.

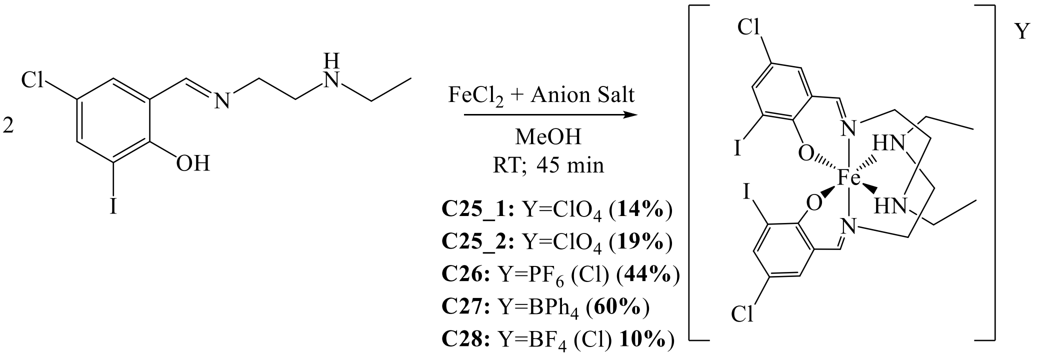

Scheme 2.8 Synthesis of the complexes with the 5-Cl-3-I-salEen ligand, with the anions perchlorate, hexafluorophosphate, tetraphenylborate and tetrafluoroborate.

FTIR and UV-vis Spectroscopy

The FTIR spectroscopy was used to confirm the imine formation through the observation of a strong stretching vibration and the presence of the different anions through the observation of their characteristic vibrational modes.

The FTIR spectrum for the **C25_1** and **C25_2** can be overlapped and that way we considered that they were the same complex, **C25** (**Figure 2.28**). The FTIR assigned vibrations for **C25-C28** are in **Table 2.25**. The FTIR spectrum of the four remaining complexes can be found in the annexes, **Figure A.53, Figure A.54** and **Figure A.55.**

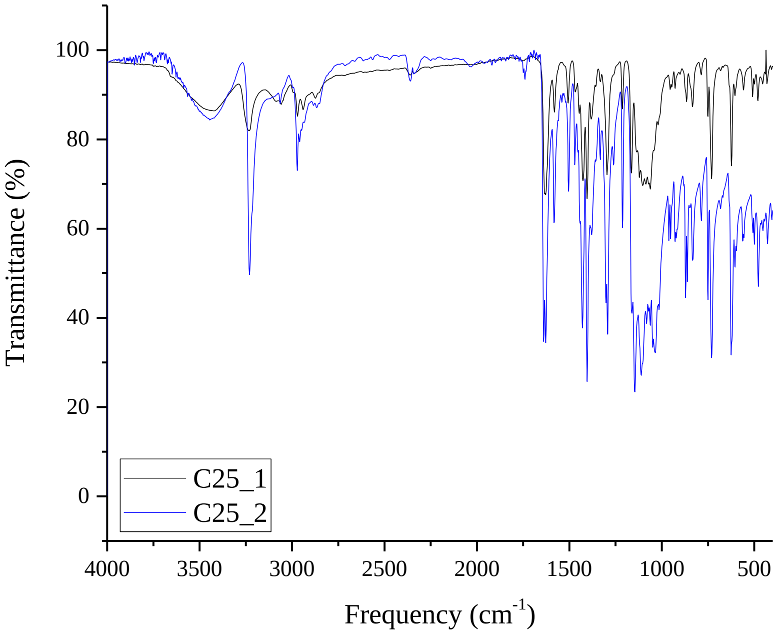

Figure 2.28 FTIR spectrum of **C25_1** and **C25_2**.

Table 2.25 Wavenumbers for the characteristic FTIR spectrum bands, for complexes **C25-C28**.

Complex	**Wavenumber (cm^{-1})**						
	υ(O-H)	**υ(N-H)**	**υ(C-H)**	**υ(C=N)**	**υ(C=C)**	**Anion**	
C25	3448	3234	2971	1627	1581-1448	ClO_4^-	1063, 623
C26	3441	-	2973	1629	1580-1471	PF_6^-	841
C27	3449	3240	2980	1619	1579-1478	BPh_4^-	732-706
C28	3416	-	2968	1633	1580-1462	BF_4^-	1070

The vibrations corresponding to O-H bonds are around 3400 cm^{-1}, N-H bonds are around 3200 cm^{-1} (only for **C25** and **C28**), C-H bonds are around 2970 cm^{-1}, C=N bonds are around 1600 cm^{-1}, C=C bonds are between 1585-1460 cm^{-1} and the anions vibrations are perchlorate at 623 cm^{-1} and 1063 cm^{-1}, hexafluorophosphate at 841 cm^{-1}, tetraphenylborate at 706 cm^{-1} to 732 cm^{-1} and tetrafluoroborate at 1070 cm^{-1}. For **C26** and **C28** the stretching of the N-H bond is not observed, because the O-H bond is very large and overlaps it. This is possibly related to the higher amount of water present in these two samples. The UV-vis spectra for all five complexes were recorded in acetonitrile between 190 and 900 nm and can be observed in **Figure 2.29**.

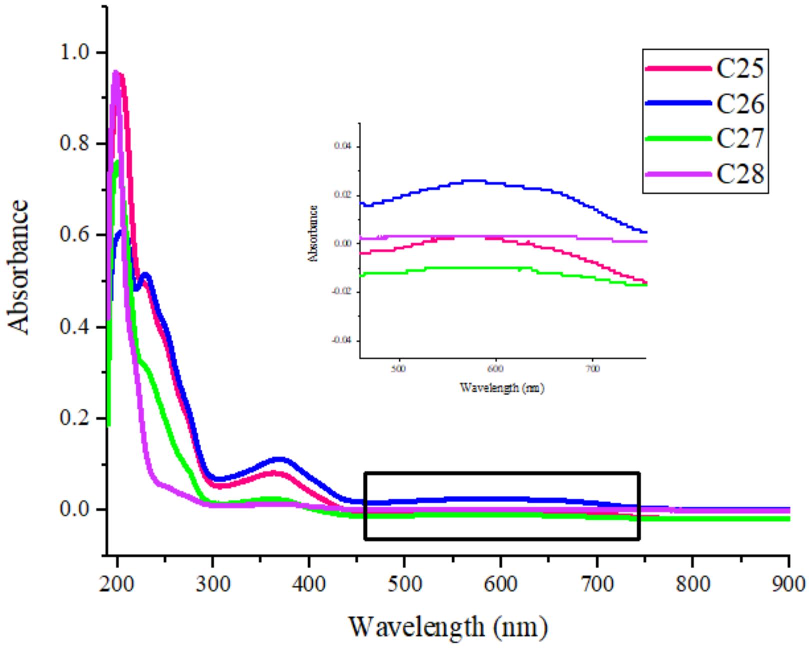

Figure 2.29 UV-vis spectra of **C25-C28** in acetonitrile.

The sample **C28** presented two bands, the **C25** and **C27** presented four bands and the **C26** presented five bands. The bands characterization can be observed in **Table 2.26**.

Table 2.26 Values for the bands UV-vis, for complexes **C25-C28**.

Complex	Concentration (mol.dm^{-3})	Wavelenght (nm)	Absorbance	Molar absoption coeficiente (mol.dm^{-3}.cm^{-1})
C25	10^{-5}	202.5 226.0 363.5 580*	0.952 0.499 0.082 -	95 200 49 900 8 200 -
C26	10^{-5}	206.0 229.0 369.5 577.5 662.5	0.612 0.516 0.112 0.026 0.021	61 200 51 600 11 200 2 600 2 100
C27	8 x 10^{-6}	200.0 228.5 358.5 580*	0.760 0.315 0.025 -	95 000 39 375 3 125 -
C28	8 x 10^{-6}	198.0 216.0	0.957 0.354	119 625 44 250

* the baseline adjustment was not the best and the absorbance is below 0.

In **Table 2.26** are present bands at different wavelengths and with different molar absorption coefficients. The bands around 200 nm corresponded to intraligand interactions, the higher molar absorption coefficients belong to **C28** (119 625 mol.dm^{-3}.cm^{-1}) and the lower to **C26** (61 200 mol.dm^{-3}.cm^{-1}). All complexes presented two of this bands.

The bands between 300 and 400 nm should be attributed to charge-transfer between the ligands and the iron, or vice-versa with variations between 11 200 (**C26**) and 8 200 mol.dm^{-3}.cm^{-1} (**C27**). **C28** did not present bands in this region and the others have one.

Bands between 500 nm and 700 nm also correspond to charge-transfer between the ligands and the iron, or vice-versa, and spin states. The **C28** is the only one that did not present bands in this region. The **C26** have two bands in this region at 577 and 662 nm, while the **C25** and **C27** only admitted one around 580 nm. In solution at room-temperature, the **C25** and **C27** show essentially LS state and the **C26** displays slightly more in the LS but present also a HS state.

Structural characterization

Single Crystal X-ray diffraction

Single crystals with good quality for X-ray diffraction were obtained for all complexes. And we were able to predict the spin state of the complex at a specific temperature through the Fe-X bond lengths. The X-ray data at 296 K revealed that some of the compounds were found in their unsolvated form **C25**, but other were crystallized as solvates **$C26 \bullet 2H_2O \bullet CH_3CN$**, **$C27 \bullet H_2O \bullet CH_3CN$** and **$C28 \bullet 2H_2O$**. The crystal data and structure refinement of this complexes is listed in **Table A.5**, in the annexes.

In **C25**, the asymmetric unit at 296 K comprises one cation and one anion. The unit cell contains four asymmetric units, **Figure A.56**, in the annexes.

In the case of **$C26 \bullet 2H_2O \bullet CH_3CN$**, the asymmetric unit at 296 K comprises one cation, one chloride anion, two molecules of water and one acetonitrile molecule. The unit cell contains eight asymmetric units, **Figure A.57**, in the annexes.

For **$C27 \bullet H_2O \bullet CH_3CN$**, the asymmetric unit at 296 K comprises one cation, one anion, one molecule of acetonitrile and one of water. The unit cell contains four asymmetric units, **Figure A.58**, in the annexes.

The **$C28 \bullet 2H_2O$** asymmetric unit at 296 K comprises one cation, one chloride anion and two molecules of water. The unit cell contains one asymmetric unit, **Figure A.59**, in the annexes.

In the **Table 2.27** are the representative bond lengths of **C25**, **$C26 \bullet 2H_2O \bullet CH_3CN$**, **$C27 \bullet H_2O \bullet CH_3CN$** and **$C28 \bullet 2H_2O$**, at 296 K where **$C26 \bullet 2H_2O \bullet CH_3CN$** show bond lengths corresponding to the HS state, and the other three complexes show bond lengths corresponding to the LS state.

Table 2.27 Representative bond lengths of **C25-$C28 \bullet 2H_2O$** at 296 K.

Complex	**C25**		**$C26 \bullet 2H_2O \bullet CH_3CN$**		**$C27 \bullet H_2O \bullet CH_3CN$**		**$C28 \bullet 2H_2O$**	
$Fe-N_{imine}$	Fe-N1	1.915(3)	Fe-N1	1.931(3)	Fe-N1	2.073(3)	Fe-N1	1.926(13)
	Fe-N3	1.933(3)	Fe-N3	1.934(3)	Fe-N3	2.069(3)	Fe-N3	1.920(13)
$Fe-N_{amine}$	Fe-N2	2.040(4)	Fe-N2	2.032(3)	Fe-N2	2.204(6)	Fe-N2	2.007(15)
	Fe-N4	2.032(4)	Fe-N4	2.036(3)	Fe-N4	2.156(6)	Fe-N4	2.051(15)
$Fe-O_{phen}$	Fe-O1	1.868(3)	Fe-O1	1.873(2)	Fe-O1	1.897(5)	Fe-O1	1.870(11)
	Fe-O2	1.874(3)	Fe-O2	1.875(2)	Fe-O2	1.902(5)	Fe-O2	1.895(12)
State	LS		LS		HS		LS	

In **Table 2.28** it is possible to observe the hydrogen bonds for **C25**, **$C26 \bullet 2H_2O \bullet CH_3CN$** and **$C27 \bullet H_2O \bullet CH_3CN$**. The hydrogen bonds for **C25**, **$C26 \bullet 2H_2O \bullet CH_3CN$** are between the hydrogens of the nitrogen atoms of the amine of the ligand and one oxygen of the anion. In the case of **$C27 \bullet H_2O \bullet CH_3CN$** the hydrogen bonds are between the nitrogen atoms of the ligand and the water. Finally, three C-H···π interaction between two aromatic rings of neighboring, between the anion and the cation, **Table 2.28**. In the annexes, **Figure A.60** it is possible to observe the hydrogen bonds and the C-H···π interaction.

Table 2.28 Hydrogen bond and C-H···π interaction lengths and angles for **C25-$C27 \bullet H_2O \bullet CH_3CN$**.

Complex	**D-H···A**	**d(H···A) (Å)**	**d(D···A) (Å)**	**(D-H···A) (º)**
C25	N2-H2···O3	2.257	3.052	172.85
	N4-H4···O3	2.215	3.039	176.29
$C26 \bullet 2H_2O \bullet CH_3CN$	N4-H4···Cl3	2.492	3.309	175.23
$C27 \bullet H_2O \bullet CH_3CN$	N2-H2···O3	2.269	3.155	149.84
	N4-H4···O3	2.074	3.049	172.55
	$C27_{\pi}$-H46··· π	2.799	3.651	152.68
	$C36_{\pi}$-H37··· π	2.775	3.710	162.23
	$C8_{\pi}$-H3···π	3.301	4.207	165.36

Powder X-ray diffraction

This technique was used to correlate the diffractograms for all compounds. In **Figure 2.30**, it is possible to observe that all the complexes show crystallinity, and all the diffractograms have peaks in different angles, so they are different compounds.

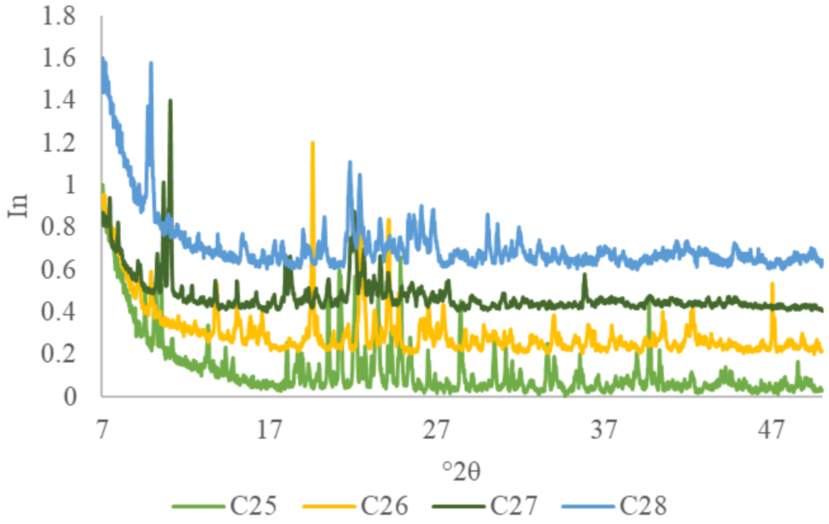

Figure 2.30 Powder X-ray diffractograms for complexes **C25-C28**.

Since the measure of powder X-ray diffraction uses a larger amount of sample than the single crystal, to understand if the single crystal observe was representative of all the sample, both diffractograms of the powder and pattern generated from the single crystal structure of **C25**, **C26•2H$_2$O•CH$_3$CN**, **C27•H$_2$O•CH$_3$CN** and **C28•2H$_2$O** were compared, **Figure A.61**, **Figure A.62**, **Figure A.63** and **Figure A.64**, in the annexes.

In case of **C25**, **C26•2H$_2$O•CH$_3$CN** and **C28•2H$_2$O** it is possible to observe that all the powder X-ray peaks had a corresponding peak in the corresponding single crystal X-ray. All the sample have the same structure.

When observing both diffractograms of **C27•H$_2$O•CH$_3$CN**, we understand that they do not have the equivalent peaks, **Figure A.63**, in the annexes. Thus, all the sample does not have the same structure.

SQUID magnetometry

The SQUID magnetometry plot for the four complexes can be observe in **Figure 2.31**. The samples were measured with alternating cooling/warming runs at the rate of 5 K min^{-1} between 370 and 10 K to obtain the molar magnetic susceptibility by the temperature ($\chi_M T$) as a function of the temperature.

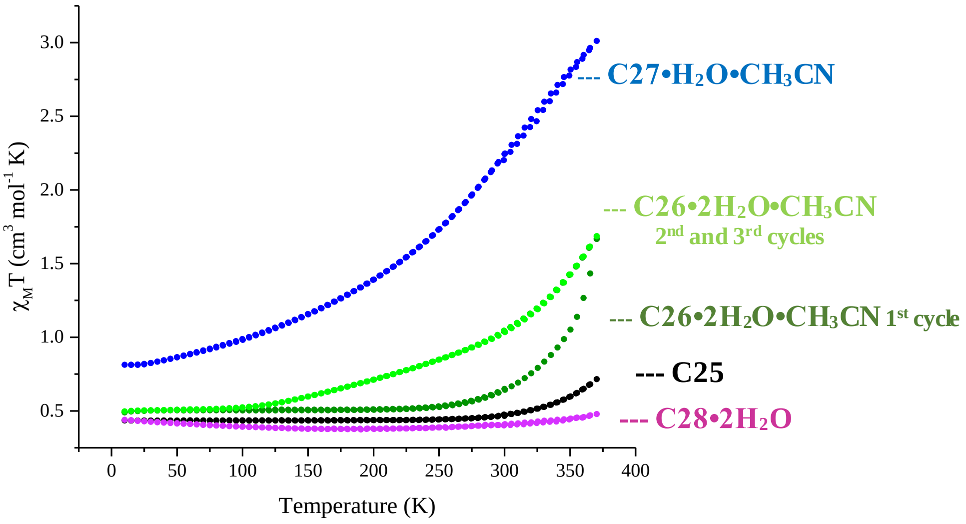

Figure 2.31 $\chi_M T$ vs T plot for complexes **C25-C28•2H$_2$O.**

Complexes **C25** and **C28•2H$_2$O** display a similar behavior. From 10 K to 250 K they maintain the $\chi_M T$ value, 0.41 cm^3 mol^{-1} K for **C28•2H$_2$O** and 0.46 cm^3 mol^{-1} K for **C25**. At 370 K **C28•2H$_2$O** presents a $\chi_M T$ value of 0.48 cm^3 mol^{-1} K while **C25** was 0.56 cm^3 mol^{-1} K. These results indicate that the Fe(III) centers from both samples are in LS state during the analysis.

In **C26•2H$_2$O•CH$_3$CN** sample at the initial temperature of 300 K presented a $\chi_M T$ value of 0.65 cm^3 mol^{-1} K. The sample was cooled to 10 K and displayed a $\chi_M T$ value of 0.49 cm^3 mol^{-1} K and was then warmed up to 370 K where the $\chi_M T$ value increased to 1.67 cm^3 mol^{-1} K. When the sample was cooling to 300 K, it admited a slightly higher $\chi_M T$ value of 1.04 cm^3 mol^{-1} K, than at the initial temperature. The second and third cycle are equal and the $\chi_M T$ values at 10 K and 370 K are the same as the $\chi_M T$ values for the first cycle, although the first cycle presents a different type of increase, slower before 300 K and much faster afterwards. The sample presents a gradual and incomplete SCO curve. Between 10 K and 250 K the sample presented a LS state and at 370 K approximately 65% HS and 35% LS. This difference indicates the loss of the solvent after the first cycle.

For the **C27•H$_2$O•CH$_3$CN** sample a $\chi_M T$ value of 2.24 cm^3 mol^{-1} K was observed at 300 K. The sample was cooled to 10 K and had a $\chi_M T$ value of 0.81 cm^3 mol^{-1} K. It was warmed up to 370 K where the $\chi_M T$ value rose to 3.01 cm^3 mol^{-1} K. The sample presents a gradual and incomplete SCO curve and at 10 K is approximately 11% HS and 89% LS and at 370 K is approximately 66% HS and 33%

[Fe(5-Br-3-NO$_2$-salEen)$_2$]Y

The reaction of Fe(NO$_3$)$_3$ and different Fe(II) salts with 5-Br-3-NO$_3$-salEen at room temperature resulted in very dark solutions sometimes accompanied by a dark powder, thus confirming the formation of coordination compounds.

In this group only two Fe(III) complexes were synthesized, were **C29** corresponds to [Fe(5-Br-3-NO$_3$-salEen)$_2$]PF$_6$ and **C30** to [Fe(5-Br-3-NO$_3$-salEen)$_2$]BPh$_4$, **Scheme 2.9**. There is no explanation for the yield of **C30**.

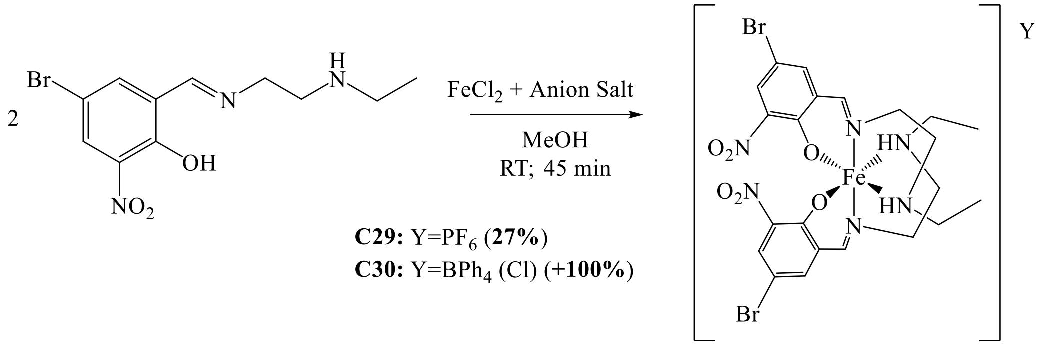

Scheme 2.9 Synthesis of the complexes with the 5-Br-3-NO_3-salEen ligand, with the anions hexafluorophosphate and tetraphenylborate.

FTIR and UV-vis Spectroscopy

The FTIR spectroscopy was used to confirm the imine formation through the observation of a strong stretching vibration and the presence of the different anions through the observation of their characteristic vibrational modes. The FTIR assigned vibrations for **C29** and **C30** are in **Table 2.29**. The FTIR spectrum of the two complexes can be found in the annexes, **Figure A.65** and **Figure A.66**.

Table 2.29 Wavenumbers for the characteristic FTIR spectrum bands, for complexes **C29** and **C30**.

Complex	**Wavenumber (cm^{-1})**						
	υ(O-H)	**υ(N-H)**	**υ(C-H)**	**υ(C=N)**	**υ(C=C)**	**Anion**	
C29	3371	3278	2969	1638	1594-1464	PF_6^-	843
C30	3426	-	2993	1636	1592-1466	BPh_4^-	751-704

Here, the vibrations corresponding to O-H bonds are around 3400 cm^{-1}, N-H bonds are around 3200 cm^{-1} (only for **C29**), C-H bonds are around 2970 cm^{-1}, C=N bonds are around 1600 cm^{-1}, C=C bonds are between 1580-1430 cm^{-1} and the anions vibrations are hexafluorophosphate at 843 cm^{-1} and tetraphenylborate at 706 cm^{-1} to 751. For **C30** the stretching of the N-H bond is not observed because the O-H bond is very large and overlaps it. This is possibly related to the higher amount of water present in these two samples.

The UV-vis spectra for both complexes were recorded in acetonitrile between 200 and 900 nm and can be observed in **Figure 2.32**.

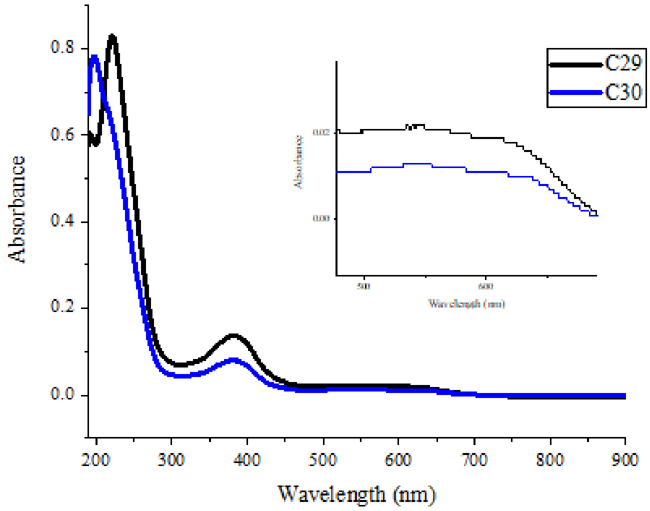

Figure 2.32 UV-vis spectra of **C29** and **C30**.

The samples present three bands. Details on the bands can be observed in **Table 2.30**.

Table 2.30 Values for the bands UV-vis, for complex **C29** and **C30**.

Complex	Concentration (mol.dm^{-3})	Wavelength (nm)	Absorbance	Molar absorption coefficient (mol.dm^{-3}.cm^{-1})
C29	10^{-5}	221.5 381.0 546.0	0.828 0.136 0.022	82 800 13 600 2 200
C30	8 x 10^{-6}	197.5 381.0 543.5	0.782 0.079 0.013	97 750 9 875 1 625

Both complexes in **Table 2.30** present bands at different wavelengths and with different molar absorption coefficients. The bands around 200 nm belong to intraligand interactions, with variations between 97 750 and 82 800 mol.dm^{-3}.cm^{-1}.

The bands between 300 and 400 nm should be attributed to charge-transfer between the ligands and the iron, or vice-versa with variations between 13 600 and 9 875 mol.dm^{-3}.cm^{-1}.

Bands between 500 nm and 700 nm also correspond to charge-transfer between the ligands and the iron, or vice-versa and to spin states. The complexes present a large band, but it is not possible to separate in two. The band around 540 nm have values around 2 000 mol.dm^{-3}.cm^{-1}. For all wavelengths, the higher molar absorption coefficients belong to **C30** and the smaller belong to **C29**. In solution at room-temperature, both complexes show the LS state.

Structural characterization

Single Crystal X-ray diffraction

Single crystals with good quality for X-ray diffraction were obtained for both complexes. The spin state of the complex at a specific temperature was predicted through the Fe-X bond lengths.

The X-ray data at 296 K revealed that the compounds were found in their unsolvated form **C29** and **C30**. The crystal data and structure refinement of this complexes is listed in **Table A.5**, in the annexes.

In **C29**, the asymmetric unit at 296 K comprises one cation and one anion. The unit cell contains four asymmetric units, **Figure A.67** in the annexes.

For the **C30**, at 296 K the first asymmetric unit comprises one cation and one chloride anion. The unit cell contains four asymmetric units, **Figure A.68** in the annexes.

In the **Table 2.31** are the representative bond lengths of **C29** and **C30,** at 296 K, where both complexes present bond lengths corresponding to the LS state.

Table 2.31 Representative bond lengths of **C29** and **C30** at 296 K.

Complex	**C29**		**C30**	
Fe-N$_{imine}$	Fe-N3 Fe-N6	1.926(6) 1.946(6)	Fe-N1 Fe-N3	1.927(7) 1.923(7)
Fe-N$_{amine}$	Fe-N1 Fe-N4	2.064(6) 2.048(6)	Fe-N2 Fe-N4	2.0356(11) 2.0150(11)
Fe-O$_{phen}$	Fe-O2 Fe-O3	1.894(3) 1.902(3)	Fe-O1 Fe-O2	1.892(6) 1.880(5)
State	LS		LS	

In **Table 2.32** it is possible to observe the hydrogen bond lengths and angles for **C29** and **C30**. The hydrogen bonds for **C29** are between the hydrogens of the nitrogen atoms of the ligand and one fluor of the anion. In the case of **C30** the hydrogen bonds are between the hydrogen of the nitrogen atoms of the ligand and the anion. In the annexes, **Figure A.69** it is possible to observe the hydrogen bonds.

Table 2.32 Hydrogen bond lengths and angles for **C29** and **C30**.

Complex	**D-H···A**	**d(H···A) (Å)**	**d(D···A) (Å)**	**(D-H···A) (º)**
C29	N2-H2···F1	2.418	3.160	168.85
	N4-H4···F1	2.311	3.232	156.95
C30	N1-H1···Cl1	2.308	3.288	178.14
	N4-H4···Cl1	2.331	3.310	176.84

Powder X-ray diffraction

This technique was used to correlate the diffractograms for the two compounds. In **Figure 2.33**, it is possible to observe that both show crystallinity and present peaks at different angles.

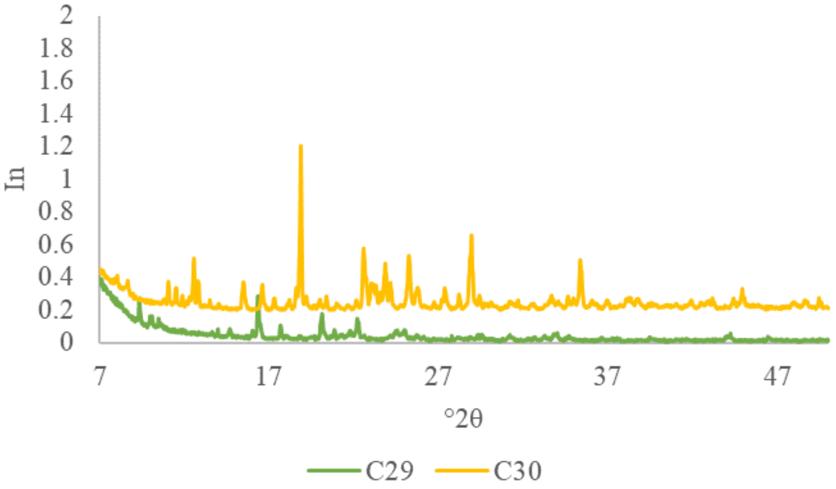

Figure 2.33 Powder X-ray diffractograms for complexes **C29** and **C30**.

The comparison between the powder and pattern generated from the single crystal structure diffractograms was used to understand if the single crystal observe was representative of all the sample. In case of **C29** the powder diffractogram demonstrate less crystallinity than the single crystal diffractogram, **Figure A.70,** in the annexes. But when both diffractograms are observed, they have the equivalent peaks. Thus, the single crystal was representative of all.

For the **C30** the single crystal shows less peaks than the powder diffractogram, **Figure A.71,** in the annexes. Therefore, the single crystal was not representative of all sample and they do not have the same structure.

SQUID magnetometry

The SQUID magnetometry plot for the two complexes can be observe in **Figure 2.34**. The samples were measured with alternating cooling/warming runs at the rate of 5 K min^{-1} between 370 and 10 K to obtain the molar magnetic susceptibility ($\chi_M T$) as function of temperature.

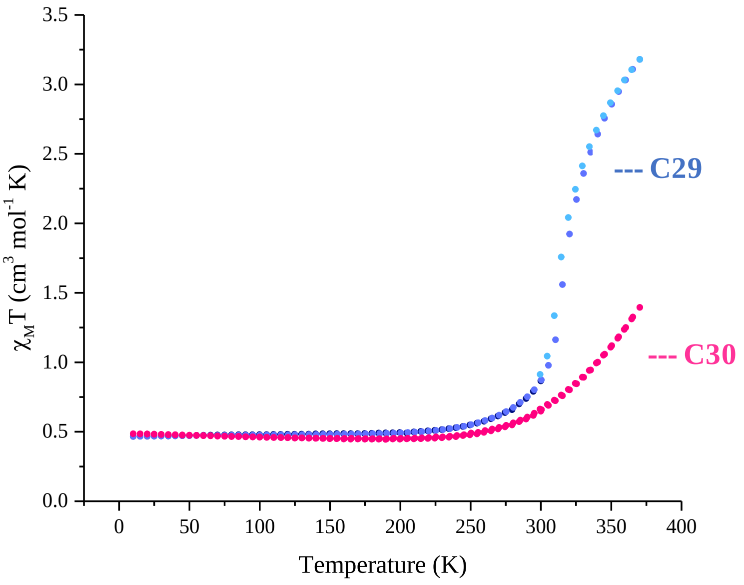

Figure 2.34 χ_MT vs T plot for complexes **C29** and **C30.**

The measurements of **C29** starts at 300 K and presented a $\chi_M T$ value of 0.87 cm^3 mol^{-1} K. The sample was cooled to 10 K and admitted a $\chi_M T$ value of 0.46 cm^3 mol^{-1} K and after was warmed up to 370 K where the $\chi_M T$ value rose to 3.18 cm^3 mol^{-1} K. The cycle presents a hysteresis at 300 K but when we perform cycles at rate of 1 K min^{-1} the hysteresis disappeared, **Figure A.72** in the annexes. The sample presents an abrupt and incomplete SCO curve. The sample at 10 K presented a LS state and at 370 K is approximately 70% HS and 30% LS. A single crystal X-ray diffraction for the same crystal was performed to understand what differences the crystal lattice presents at both temperatures. In the **Table 2.33** is possible to observe the representative bonds for both complexes, were the Fe(III) centers are in LS state but at 110 K the bond lengths are shorter, as expected, and at that temperature have more centers in LS than at 296 K.

Table 2.33 Representative bond lengths of **C29** at 110 K and 296 K.

Temperature	**110 K**		**296 K**	
Fe-N$_{imine}$	Fe-N1	1.923(6)	Fe-N3	1.926(6)
	Fe-N3	1.924(6)	Fe-N6	1.946(6)
Fe-N$_{amine}$	Fe-N2	2.0196(9)	Fe-N1	2.064(6)
	Fe-N4	2.0192(9)	Fe-N4	2.048(6)
Fe-O$_{phen}$	Fe-O2	1.878(5)	Fe-O2	1.894(3)
	Fe-O3	1.889(5)	Fe-O3	1.902(3)
State	LS		LS	

In **Table 2.34** it is possible to observe the hydrogen bonds lengths and angles at 110 K and 296 K. The bond angle at 110 K is higher than at 296 K and as expected at 110 K the bond lengths are shorter.

Table 2.34 Hydrogen bond lengths and angles for **C29** at 110 K and 296 K.

Temperature	**D-H···A**	**d(H···A) (Å)**	**d(D···A) (Å)**	**(D-H···A) (º)**
110 K	N2-H2··F1	2.328	3.178	168.96
	N4-H4··F1	2.353	3.197	163.65
296 K	N2-H2···F1	2.418	3.160	168.85
	N4-H4···F1	2.311	3.232	156.95

Sample **C30** at the initial temperature of 300 K was observed a $\chi_M T$ value of 0.65 cm^3 mol^{-1} K. It was cooled to 10 K and presented a $\chi_M T$ value of 0.49 cm^3 mol^{-1} K and was then warmed up to 370 K where the $\chi_M T$ value increased to 1.39 cm^3 mol^{-1} K. Between 10 K and 250 K the sample presented a LS state and after that admits a gradual and incomplete SCO curve. At 370 K approximately 67% HS and 33% LS.

2.3. Correlations

Complexes with different anions

When we compare complexes with the same ligand, it was only possible to find a clear correlation for the 3,5-F-salEen ligand. For this series of complexes, crystals with good quality for X-ray diffraction were obtained for all five salts, therefore, it was the only one with enough data to compare, except for **C13**. Complexes **C10**, **C11** and **C14** did not present solvent in the structure and the Fe(III) centers until 300 K are in low spin state, and after that temperature the $\chi_M T$ value rose to 40% high spin state and 60% low spin state for **C14**. The others presented lower high spin character, although they all start to raise after 300 K.

Complexes with different solvents in the crystal lattice

The synthesis of **C12** created two different products. Both complexes have the 3,5-F-SalEen ligand and BPh_4 as anion. The difference is in the solvents in the crystal's structures. The first crystalized with water and methanol, **C12_1•H_2O•MeOH**. The second crystalized with acetonitrile, **C12_2•CH_3CN**. This differences in the lattice generates different results in all techniques performed (FTIR, UV-vis spectroscopy and SQUID magnetometry). In the SQUID magnetometry we observed that the **C12_1•H_2O•MeOH** presented a steady $\chi_M T$ value, that corresponds to 50% HS and 50% LS state Fe(III) centres. The **C12_2•CH_3CN** presented a gradual/abrupt and incomplete SCO curve. The sample at 10 K presented a LS state and at 370 K is approximately 90% HS and 10% LS. The different SQUID for these two complexes can be observed in **Figure 2.35**.

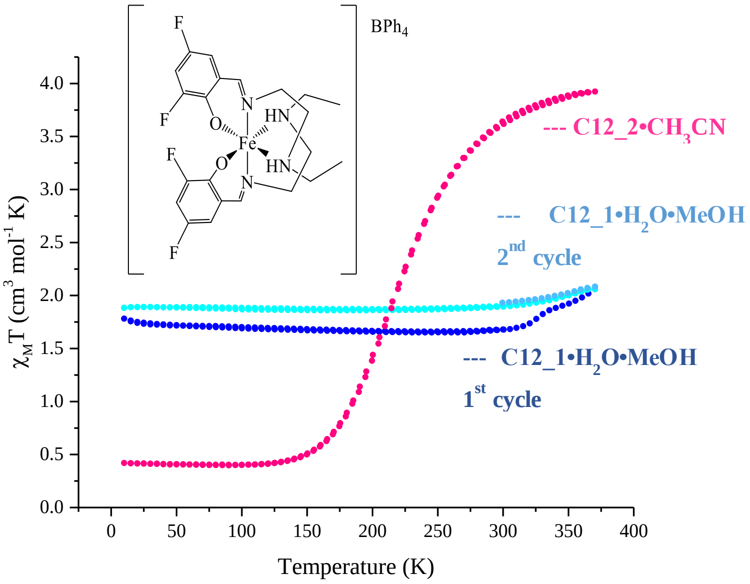

Figure 2.35 $\chi_M T$ vs T plot for complexes **C12_1•H_2O•MeOH** and **C12_2•CH_3CN**.

Complexes with different substituents

When we compare complexes with the same anion, we find a pattern in perchlorate. In all complexes with it, with the exception of **C15**, the Fe(III) centers until 300 K are in low spin state, and in some cases, after that temperature the $\chi_M T$ value rose slightly, maintaining the majority of the centers in low spin state. With hexafluorophosphate and tetrafluoroborate there is not a defined pattern, although there are more complexes with these anions that maintain low spin Fe(III) centers at temperatures higher than 300 K than those complexes who start to have a majority of centers in high spin. Complexes with nitrate defined two almost opposite states. **C5** and **C23** get close to a high spin state during the measurements, while **C13** and **C19** maintained a low spin state. It would be interesting to measure these crystals, but it would need a better quality of diffraction.

Three complexes were synthesized with BPh_4 as anion and water and acetonitrile in the structure, **C3•H_2O•CH_3CN**, **C8•H_2O.CH_3CN**, **C22•H_2O•CH_3CN**. The SQUID magnetometry for these complexes admitted a similar behavior, as a bigger number of cycles translated to an increase in $\chi_M T$ value. The SQUID for **C22•H_2O•CH_3CN** is presented in **Figure 2.36**.

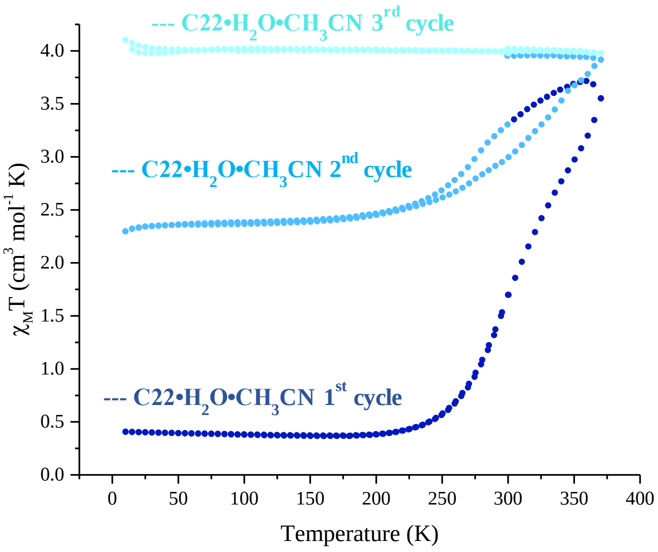

Figure 2.36 $\chi_M T$ vs T plot for **C22•H_2O•CH_3CN.**

Other similarity that we observed in the $\chi_M T$ vs T plot of these three complexes happened when the 1st cycle was between 10 and 370 K and the others only between 10 and 355 K. In this case, all cycles created a hysteresis around 200 to 355 K and a bigger number of cycles translated to an increase in $\chi_M T$ value, as seen in **Figure 2.37**.

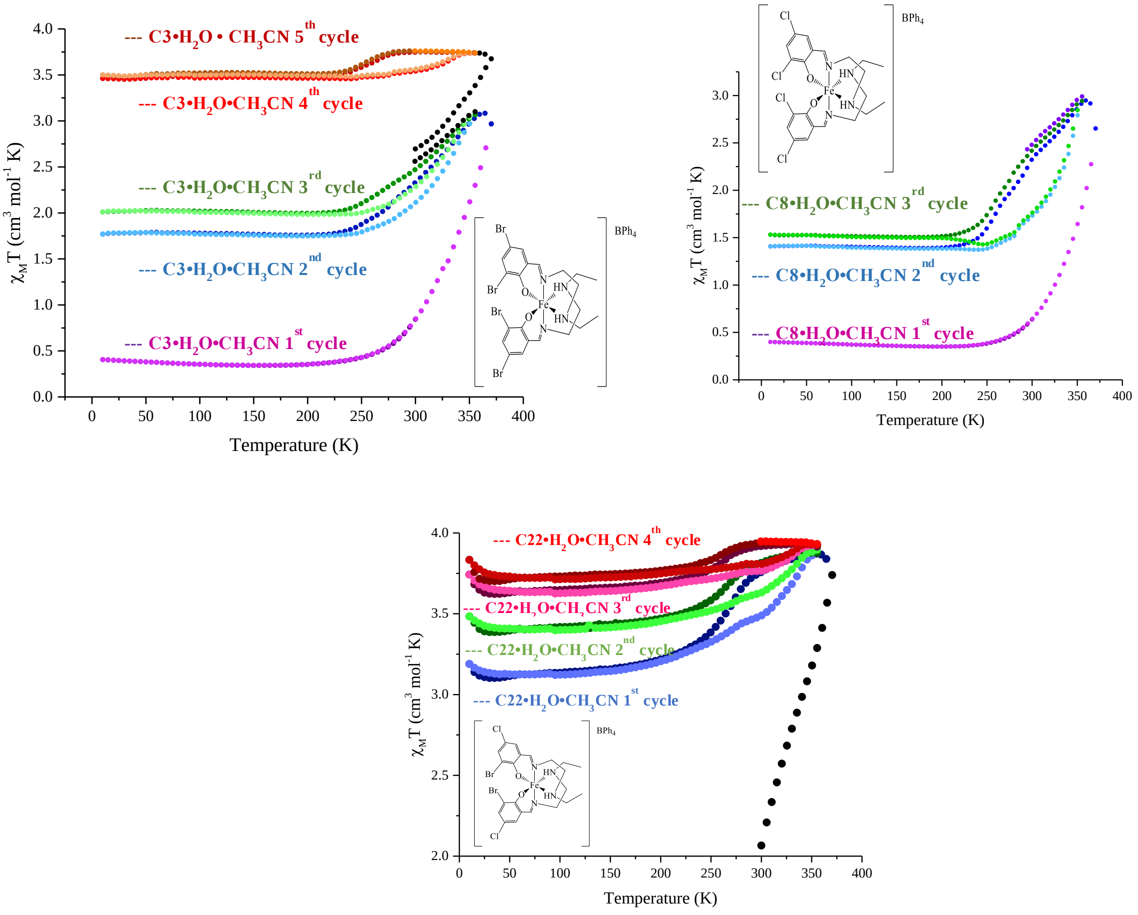

Figure 2.37 $\chi_M T$ vs T plot for complexes **C3.H$_2$O.CH$_3$CN**, **C8. H$_2$O.CH$_3$CN** and **C22. H$_2$O.CH$_3$CN.**

A single crystal X-ray diffraction was performed for the crystal of **C22•H$_2$O•CH$_3$CN** after all this cycles and the solvent and water are no longer in the structure of this crystals. The difference in the cycles is a consequence of the structure rearrange. It is expected that further results show the same response from the other two complexes, but a powder X-ray diffraction was performed and compared with the powder X-ray diffraction for these three complexes after the SQUID, **Figure A.73**. The three complexes show that both diffractometers are different, proving that the sample suffers rearranges in the structure.

Distortion parameters and packing effects

Five different distortion parameters will be considered and calculated. Previous studies of this parameters were made by Halcrow, who studied the magnetic and structural data of solvated and unsolvated salts of [Fe(sal)$_2$trien]$^+$ using the first four parameters that we will discuss. [104] The first parameter was previously shown by Guionneau for the family of [FeL$_n$(NCS)$_2$] of Fe(III) compounds.[105] Paulo Nuno Martinho analyses, in his PhD thesis, the first four parameters for one compound that is similar with compounds discussed in this group. He also defines a new and complementary fifth parameter. [106]

The first parameter, Σ, measures local angular distortions of the octahedral donor, **Figure 2.35 (a)**. The octahedron would have five N-Fe-N, one O-Fe-O and six N-Fe-O angles. In an ideal octahedron, all angles would have 90° and the sum presented in the **equation 2.1** would have a value equal to zero. The Σ increases with degree of deformation.

$$\Sigma = \sum_{i=1}^{12} |90 - \varphi_i| \qquad (2.1)$$

The second parameter, Θ, defines the degree of trigonal distortion of the N and O donor atoms from octahedral geometry towards trigonal prismatic, **Figure 2.35 (b)**. The octahedron would have 24 angles. In an ideal octahedron all angles would have 60° and the sum presented in **equation 2.2** would have a value equal to zero. The Θ increases with the degree deformation.

$$\Theta = \sum_{i=1}^{24} \left|60 - \theta_j\right| \tag{2.2}$$

The third parameter, τ, measures the Fe-O-C-C torsion angles involving the two individual peroxide groups, **Figure 2.6**.

The fourth parameter, α, measures the dihedral angle between the two ligands, **Figure 2.35 (c)**. In an ideal octahedral geometry with τ=0 the value of α would be 90°. In his research Halcrow concludes that it's possible to predicted that HS $[Fe(sal)_2trien]^+$ complexes showing α > 90° shouldn't undergo thermal spin transitions, but the solid lattice can also inhibit SCO through more subtle intermolecular contacts. The fifth parameter, ω, measures the triangular distortion of the eight triangles found in an octahedron, **Figure 2.35 (e)**. The octahedron would have 24 angles. In an ideal octahedral geometry, all the 24 angles would be equal to 60° and the sum presented in **equation 2.3** would have a value equal to zero. The ω increases with the degree deformation.

$$\Omega = \sum_{i=1}^{24} \left|60 - \omega_n\right| \tag{2.3}$$

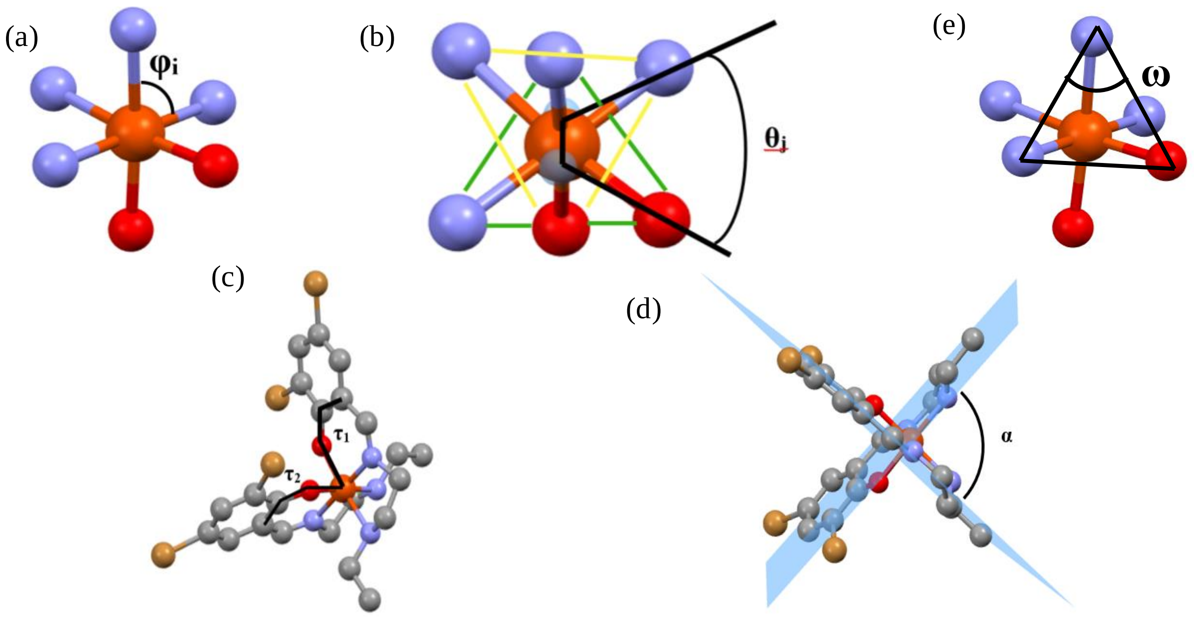

Figure 2.38 Distortion parameters: (a) local angular distortion; (b) trigonal distortion; (c) Fe-O-C-C torsion; (d) dihedral angle and (d) triangular distortion.

The distortion parameters and the spin states of the complexes at 296 K were analysed to find corelations. The distortion parameters for all the complexes can be observed in **Table 2.35**.

For some complexes when the Σ, Θ and Ω are high the τ will be the low. This was observed for the **C12_2•CH_3CN**, **C21_molecule 1**, **C22•H_2O•CH_3CN** and **C27•H_2O•CH_3CN** and these four complexes are in the HS state at 296 K. When the Σ, Θ and Ω are low the τ will be the high. This was observed for the **C1_molecule 1**, **C6**, **C11**, **C15_molecule 2**, **C18**, **C21_molecule 2** and **C25** and these seven complexes are in the LS state at 296 K. In the middle of all parameters is the **C26•H$_2$O•CH$_3$CN** and the **C29** complexes, which can be justified, because at 296 K both are in an intermediate state between the HS and the LS. There are others complexes that have the Σ and Θ low and the τ and Ω high. This was observed for the **C1_molecule 2**, **C10** and **C20•CH$_3$CN** and these three complexes are in the LS state at 296 K. Other exception is the **C30**, that have the Σ and Ω low and the τ and Θ high and this complex at 296 K is in the LS state. For the other eight complexes, **C3•H$_2$O•CH$_3$CN**, **C8•H$_2$O•CH$_3$CN**, **C12_1•H$_2$O•MeOH**, **C14**, **C15_molecule 1**, **C19**, **C21_molecule 3** and **C28•H$_2$O** the distortion parameters and the spin states of the complexes at 296 K could not be correlate.

Table 2.35 Σ, Θ, Ω, τ and **α** for **C1** to **C30**, at 296 K.

Complex		**Σ / º**	**Θ / º**	**Ω / º**	**τ / º**	**α / º**
C1	**Molecule 1**	37.87	69.49	64.84	28.66 29.65	65.96
	Molecule 2	44.30	68.96	75.08	24.79 29.44	67.54
C3•H$_2$O•CH$_3$CN		43.34	84.54	69,19	7.39 14.60	87.89
C6		35,59	58.00	62.03	29.94 32.00	64.45
C8•H$_2$O•CH$_3$CN		44.34	78.13	66,72	9.55 13.93	87.15
C10		41.38	71.37	84.64	20.03 25.95	71.97
C11		42.56	72.90	69.20	22.17 22.17	73.66
C12_1•H$_2$O•MeOH		49.39	77.64	70.78	0.96 14.92	89.94
C12_2•CH$_3$CN		62.23	184.47	102.93	2.30 8.38	84.53
C14		43.04	64.78	64.17	12.12 12.54	82.46
C15	**Molecule 1**	46.34	71.30	71.81	26.69 30.12	67.48
	Molecule 2	40.33	69.17	66.09	27.17 29.85	66.42
C18		45.27	69.55	64,49	20.18 24.18	78.92
C19		51.27	95.38	80.66	16.65 21.60	78.17
C20•CH$_3$CN		37.16	64.63	75.19	30.27 32.24	64.90
C21	**Molecule 1**	69.18	200.69	116.46	0.25 0.25	81.23
	Molecule 2	43.43	72.56	71.71	22.22 26.21	72.28
	Molecule 3	39.05	76.39	71.16	23.39 23.39	71.97
C22•H$_2$O•CH$_3$CN		72.30	124.83	361.18	5.50 10.86	89.91
C25		41.81	65.60	64.70	17.13 33.59	73.45
C26•H$_2$O•CH$_3$CN		46.87	81.25	75.54	21.84 25.53	72.57

C27•H_2O•CH_3CN	69.30	205.39	117.22	6.14 10.18	87,72
C28•H_2O	46.99	79.41	72.20	14.37 20.16	80.57
C29	45.67	76.10	67.13	17.58 22.58	78.59
C30	37.86	74.61	65.42	22.50 23.36	75.23

2.4. Multifunctional complexes: SCO and luminescence

In this chapter we tried to synthesize two different luminescent dyes, defined as good candidates where one was organic (**L1**) and one was inorganic (**L2**), to create different multifunctional complexes.
The reaction of the Fe(III) chloride, the luminescent dye and triethylamine at the reflux temperature resulted in a brown dark solution, thus confirming the complex formation.

2.4.1. Salpet ligands and an organic luminescent dye

The organic luminescent dye needed a reaction in four steps (**Scheme 2.10**).

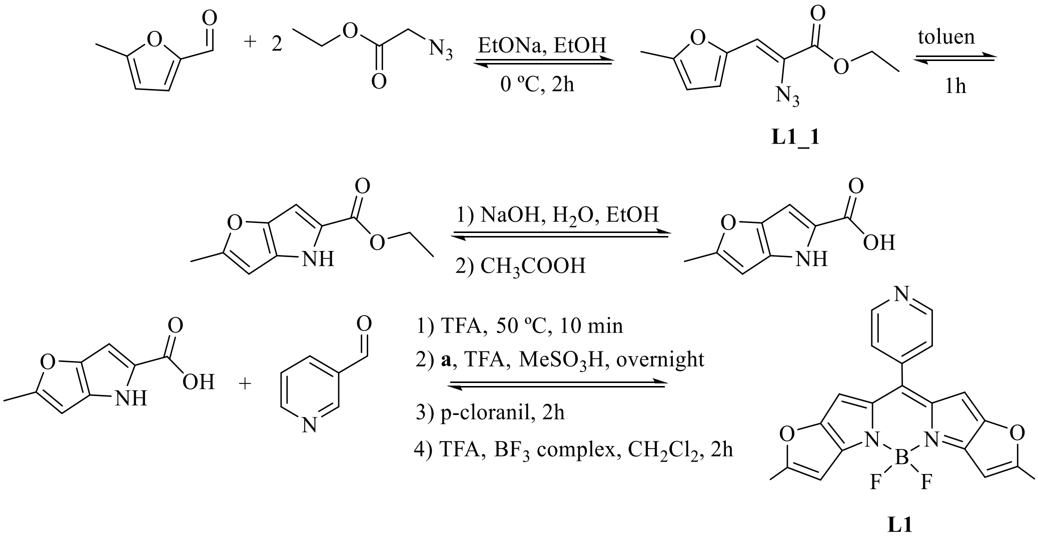

Scheme 2.10 Synthesis of the organic luminescent dye.

Unfortunately, me and BSc. Ana Rita Reis have tried to perform the first step several times, protecting from the light, at low temperature and with inert atmosphere, but we were never able to synthesize the 2-Methyl-4H-furo[3,2-b]pyrrole-5-carboxylic acid ethyl ester (**L1_1**). In the several procedures we should obtain a solution and we always obtained a precipitate and the NMR spectrum just presented the solvent peak (DMSO, 2.50), the water (3.44 and 3.53) and one peak at 7.47 that correspond to one aromatic proton, but for this complex we should observe two aromatic protons, and four aliphatic protons (**Figure 2.39**).

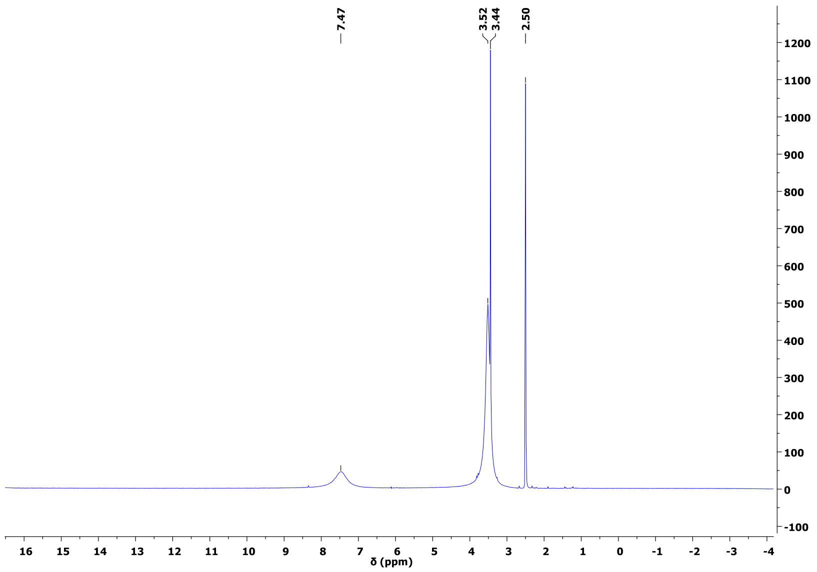

Figure 2.39 NMR spectrum of **L1_1** in DMSO.

2.4.2.Salpet ligands and an inorganic luminescent dye

The inorganic luminescent dye (**L2**) was successfully synthesized by BSc Ana Rita Reis, in a four-step reaction (**Scheme 2.11**). All products were z by FTIR spectroscopy. The first product (**L2_1**) was characterized by ^{1}H NMR spectroscopy and the bidimensional NMR technique, COSY. L2_1 and L2 were also characterized by UV-vis spectroscopy.

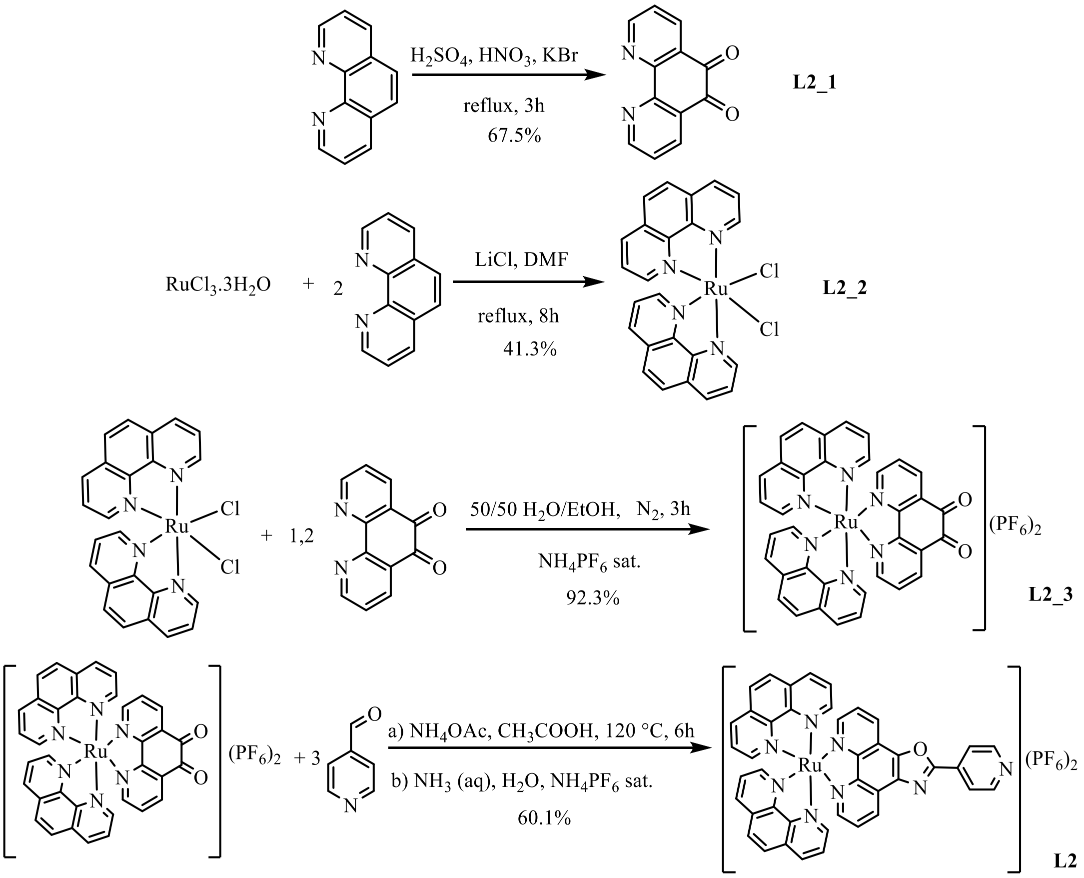

Scheme 2.11 Synthesis of the inorganic luminescent dye.

Quantum yield φ_F

The quantum yield is a parameter that measure the efficiency of the compound, the fraction of emitted photons as a function of absorbed photons. The φ_F was calculated comparing one sample well studied and with values well defined with the one in study, equation (2.4) where Φ is the quantum yield of the sample and the reference, *Grad* is the gradient of the intensity of fluorescence vs absorbance and *n* is the refractive index of the solvent.

$$\Phi_{sample} = \Phi_{\mathrm{ref}} \times \left(\frac{\mathrm{Grad}_{\mathrm{sample}}}{\mathrm{Grad}_{\mathrm{ref}}}\right) \times \left(\frac{n_{sample}}{n_{ref}}\right)^2 \qquad (2.4)$$

I had the opportunity to measure the quantum yield for this Ru(II) complex under the orientation of Dr. Artur Moro, in the Faculty of Science and Technologies of the University Nova of Lisbon. The **L2** present a φ_F of 11%. The fluorescence emission spectrum can be observed in **Figure 2.40**.

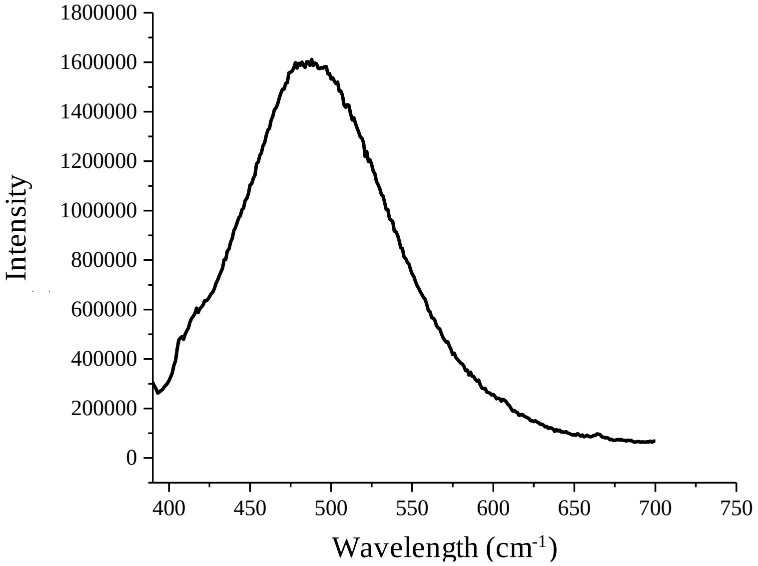

Figure 2.40 Fluorescence emission spectrum at 434 nm of **L2**.

That way, we have tried to synthesize eleven different complexes with eleven different salpet pentadentate ligands and the Ru complex (**L2**), **Scheme 2.12**. Iron(III) chloride, [Ru(phen)2(dppz)] and triethylamine in methanol was added to the different salpet ligand and left stirring and reflux for 45 min to give a dark solution confirming the complex formation. In some cases, the complex gave a dark powder after slow evaporation of the solvent and others were precipitated with addition of ethyl ether when there was few solvent. All eleven complexes were synthesized, the mono-substituents complexes were the **C31** [Fe(H_2salpet)L2], **C32** [Fe(5-Br-salpet)L2], **C33** [Fe(5-Cl-salpet)L2], **C34** [Fe(5-I-salpet)L2], **C35** [Fe(5-F-salpet)L2]. The homo-substituents **C36** [Fe(3,5-Br-salpet)L2], **C37** [Fe(3,5-Cl-salpet)L2], **C38** [Fe(3,5-I-salpet)L2], **C39** [Fe(3,5-F-salpet)L2]. The hetero-substituents complexes with salpet ligands synthesized were the **C40** [Fe(3-Br-5-Cl-salpet)L2], **C41** [Fe(5-Cl-3-I-salpet)L2]. In case of **C37** this complex was precipitated with ethyl ether (**C37_1**) and after the recrystallization of the solution it gave other precipitate (**C37_2**).

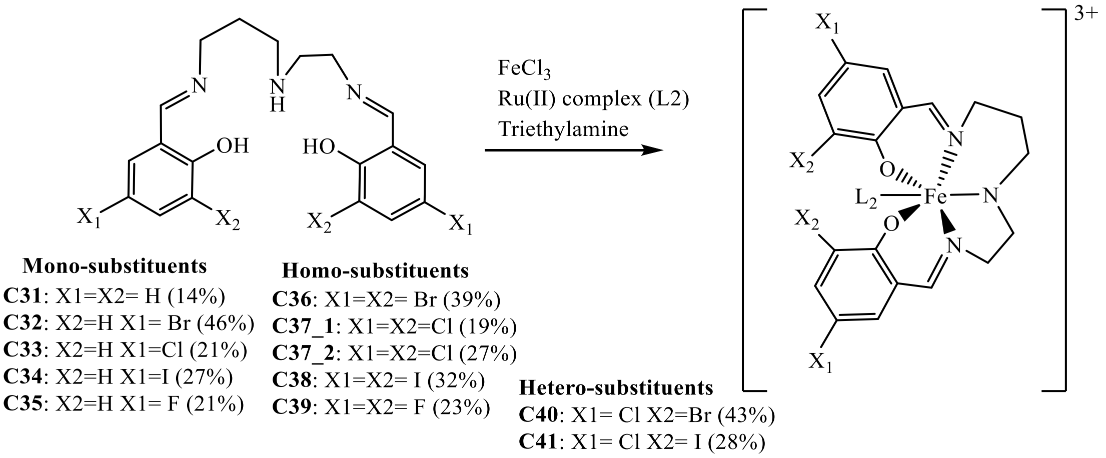

Scheme 2.12 Synthesis of the complexes with the pentadentate ligands (X= F, Cl, I, NO_2) and L2 (Ru complex).

The complexes were characterized by Nuclear Magnetic Resonance (NMR) spectroscopy, Fourier-Transform Infrared (FTIR) spectroscopy, Ultraviolet-Visible (UV-vis) spectroscopy and Superconducting Quantum Interference Device (SQUID) magnetometry.

NMR Spectroscopy

The NMR spectroscopy was performed to understand if the Ru(II) complex had bond to Fe(III) complex. Since the Ru(II) is a diamagnetic complex, the ^{1}H NMR could provide some indications. Nevertheless, this technic did not gave the results expected, because the Fe(III) is paramagnetic and the NMR is more appropriate for diamagnetic compounds. The ^{1}H NMR spectrum for all complexes is presented in **Figure 2.41**, the signals observed are 2.50 (DMSO deuterate) water from the solvent 3.32 and 3.39, a peak at 3.72 that could be water because is a large peak and a signal at 2.08 with no identified correspondence. There was not a signal in the aromatic region.

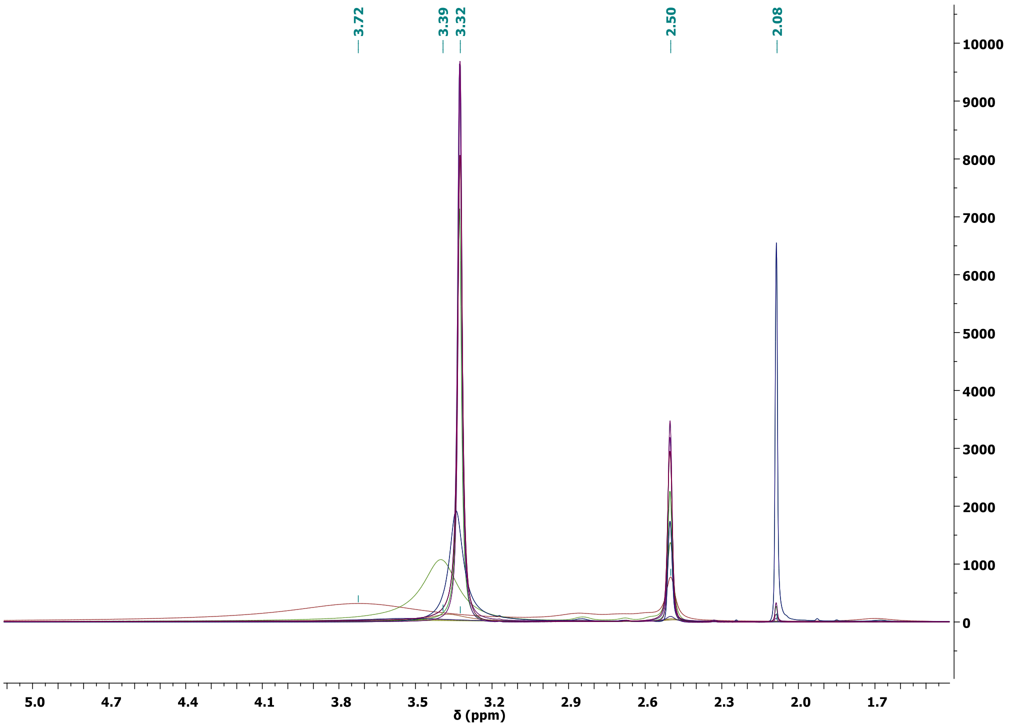

Figure 2.41 ^{1}H NMR spectrum of **C31** to **C41** in DMSO.

FTIR and UV-vis spectroscopy

The FTIR spectroscopy was used to confirm the characteristic vibrational modes for the complexes. The FTIR assigned vibrations for **C31** to **C41** can be observed in **Table 2.36.** The FTIR spectrum for the **C37_1** and **C37_2** cannot be overlap and that way we considered that they were not the same complex (**Figure 2.42**). The FTIR spectrum for the remaining complexes is in the annexes, **Figure A.74, Figure A.75, Figure A.76, Figure A.77, Figure A.78, Figure A.79, Figure A.80, Figure A.81, Figure A.82** and **Figure A.83.**

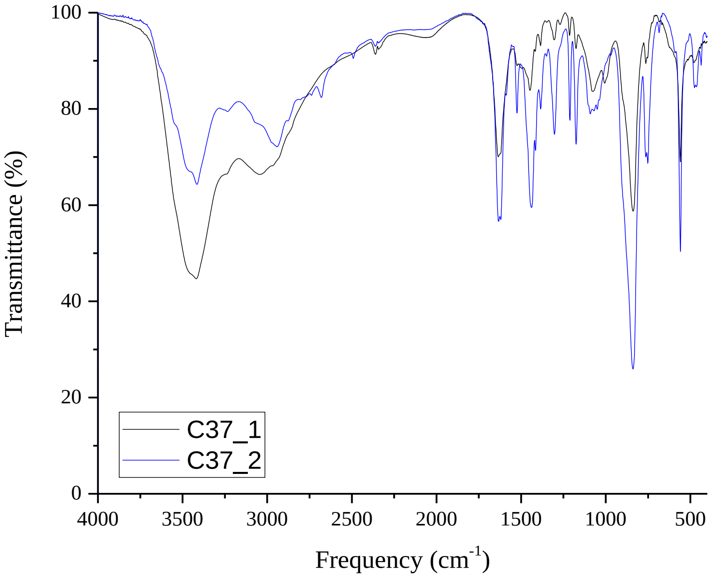

Figure 2.42 FTIR spectra of **C37_1** and **C37_2.**

Table 2.36 Wavenumbers for the characteristic FTIR spectrum bands, for complexes **C31** to **C41.**

Complex	**Wavenumber (cm^{-1})**					
	υ(O-H)	**υ(N-H)**	**υ(C-H)**	**υ(C=N)**	**υ(C=C)**	**PF_6^-**
C31	3436	-	2940	1633	1543-1310	839
C32	3430	3234	2941	1628	1529-1389	844
C33	3437	3227	2947	1629	1522-1383	846
C34	3416	3226	2919	1627	1523-1302	843
C35	3422	3234	2926	1634	1552-1386	838
C36	3415	3241	2926	1621	1578-1301	843
C37_1	3422	3234	3059	1631	1524-1305	839
C37_2	3408	3226	2947	1635	1526-1303	839
C38	3422	-	2919	1621	1563-1374	838
C39	3415	3235	2954	1634	1563-1301	832
C40	3415	3234	2919	1627	1514-1302	846
C41	3436	-	2934	1621	1508-1383	840

The vibrations corresponding to O-H bonds are around 3400 cm^{-1}, N-H bonds are around 3200 cm^{-1} (except for **C31**, **C38** and **C41**), C-H bonds are around 2970 cm^{-1}, C=N bonds are around 1600 cm^{-1}, C=C bonds are between 1580-1430 cm^{-1} and the anions vibrations is hexafluorophosphate around 840 cm^{-1}. For **C31**, **C38** and **C41** the stretching of the N-H bond is not observed because the O-H band is very large and overlaps it. This is possibly related to the higher amount of water present in these two samples.

The UV-vis spectra for all five complexes was recorded in acetonitrile between 205 and 900 nm and can be observed in **Figure 2.43**.

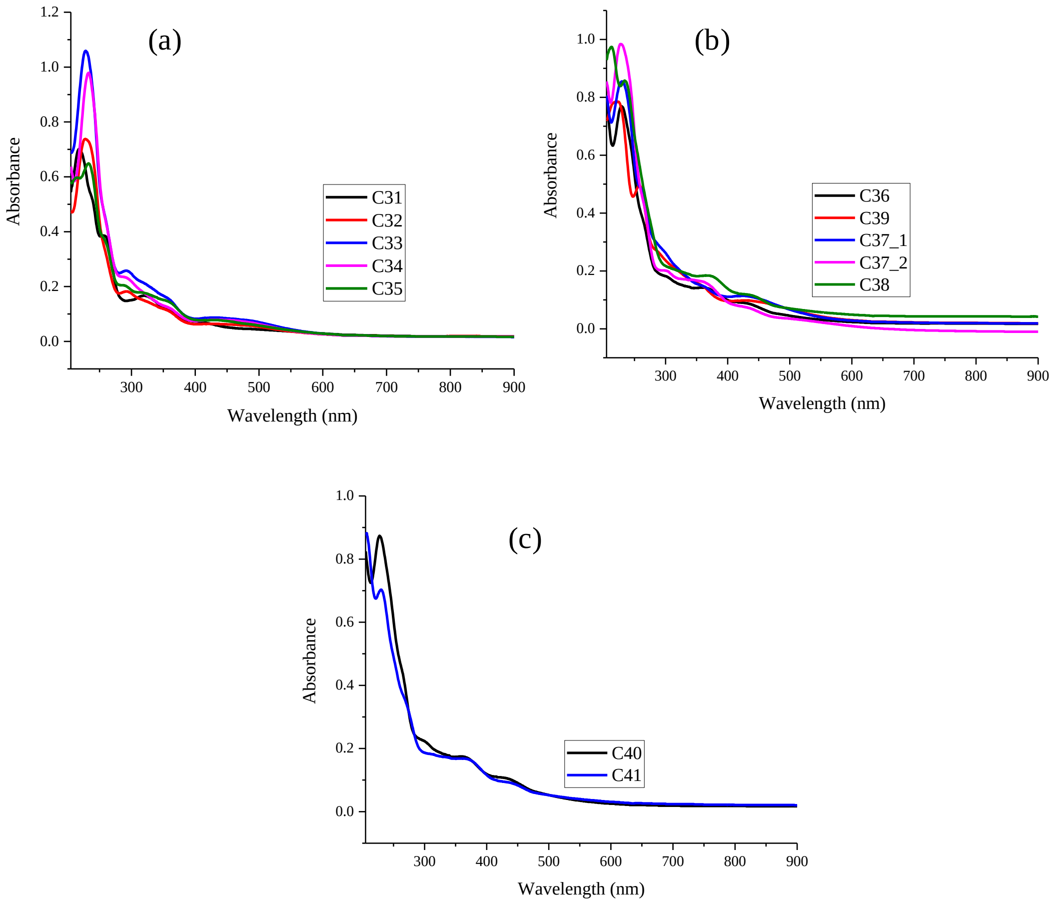

Figure 2.43 UV-vis spectra of (a) mono-substituents **C31** to **C35**, (b) homo-substituents **C36** to **C38** and (c) hetero-substituents **C40** and **C41**.

The sample **C31** presented three bands, the **C32, C33, C34, C36** and **C40** presented four bands, the **C37_1, C37_2, C38** and **C41** presented five bands and the **C35** and **C39** presented six bands. The bands characterization can be observed in **Table 2.37**.

Table 2.37 Values for the bands UV-vis, for complexes **C31** to **C41**.

Complex	Concentration (mol.dm^{-3})	Wavelength (nm)	Absorbance	Molar absorption coefficient (mol.dm^{-3}.cm^{-1})
C31	10^{-5}	218.0	0.702	70 200
		256.0	0.386	38 600
		320.0	0.167	16 700
		409.0	0.07	700
C32	2×10^{-5}	227.5	0.738	36 900
		292.5	0.182	9 100

		356.0	0.114	5 700
		462.5	0.061	3 050
C33	3 x 10^{-5}	228.0	1.059	35 300
		291.5	0.258	8 600
		360.0	0.152	5 067
		430.0	0.087	2 900
C34	10^{-5}	232.5	0.979	97 900
		288.5	0.235	23 500
		354.5	0.127	12 700
		449.0	0.078	7 800
C35	10^{-5}	214.5	0.597	59 700
		233.0	0.649	64 900
		290.5	0.203	20 300
		317.0	0.178	17 800
		356.5	0.147	14 700
		440.0	0.077	7 700
C36	10^{-5}	229.5	0.769	76 900
		292.0	0.188	18 800
		360.0	0.143	14 300
		428.0	0.089	8 900
C37_1	2 x 10^{-5}	230.0	0.855	42 750
		261.0	0.484	24 200
		299.5	0.264	13 200
		355.5	0.151	7 550
		425.0	0.114	5 700
C37_2	3 x 10^{-5}	228.0	0.984	32 800
		295.5	0.202	6 733
		350.5	0.167	5 566
		431.0	0.074	2 466
		509.0	0.033	1 100
C38	2 x 10^{-5}	213.0	0.974	48 700
		234.0	0.858	42 900
		328.0	0.196	9 800
		364.5	0.185	9 250
		429.5	0.119	5 950
C39	2 x 10^{-5}	219.0	0.784	39 200
		223.0	0.785	39 250
		257.5	0.495	24 750
		305.0	0.225	11 250
		348.5	0.160	8 000
		427.5	0.098	4 900
C40	10^{-5}	227.5	0.874	87 400
		293.5	0.229	22 900
		356.5	0.175	17 500
		426	0.108	10 800
C41	10^{-5}	230.0	0.703	70 300
		267.5	0.359	35 900
		326.0	0.175	17 500
		361.5	0.169	16 900
		427.5	0.095	9 500

The Ru(II) dye before coordinated present two bands, at 445 nm (4 220 mol.dm^{-3}.cm^{-1}), corresponding to charge-transfer between the ligands and the metal and 265 nm (18 380 mol.dm^{-3}.cm^{-1}), belonging to intraligand interactions.

At 200 nm bands are correlated to intraligand interactions of ligands belonging to Ru(II) and Fe(III) complexes, the **C35**, **C37_1** and **C39** presented three bands in this region and the others have two. The molar absorption coefficient variates between 97 900 mol.dm^{-3}.cm^{-1} (**C34**) and 6 733 mol.dm^{-3}.cm^{-1} (**C37_2**).

The bands at 300 nm corresponds to charge-transfer between the ligands and the iron, or vice-versa, the **C35**, **C38**, **C39**, and **C41** presented two bands in this region and the others have one. The higher molar absorption coefficient belonging to **C35** (17 800 mol.dm^{-3}.cm^{-1}) and the lower to **C33** (5.067 mol.dm^{-3}.cm^{-1}).

The bands at 400 nm corresponds to charge-transfer between the ligands and the ruthenium, all complexes presented one of this bands, between 10 800 mol.dm^{-3}.cm^{-1} (**C40**) and 700 mol.dm^{-3}.cm^{-1} (**C31**). Comparing to the band of the ruthenium before coordinated all presented a lower wavelength around 425 nm, the ones with a wavelength around 445 are the **C34** and **C35**, the one higher than that that value is the are the **C32** at 362 nm. The fact that this band appears in these spectrums indicates that the desired complex was synthesized.

SQUID magnetometry

The SQUID magnetometry plot for the two complexes can be observe in **Figure 2.44**. The samples were measured with alternating cooling/warming runs at the rate of 5 K min^{-1} between 370 and 10 K to obtain the molar magnetic susceptibility ($\chi_M T$) as function of temperature.

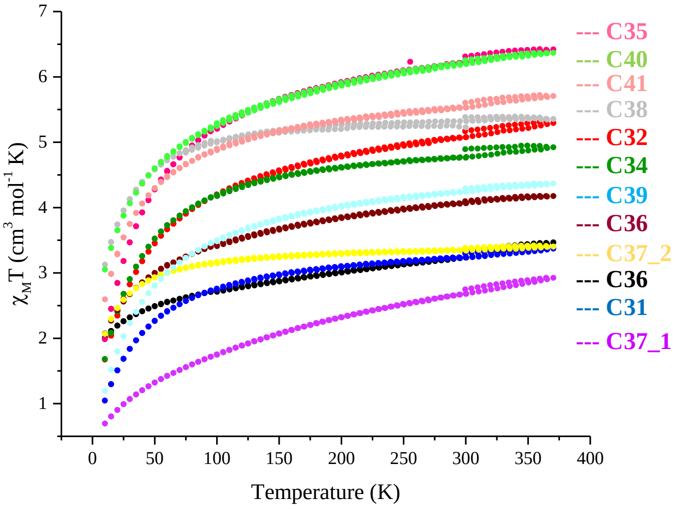

Figure 2.44 χ_MT vs T plot for complexes **C31-C41**.

All the complexes presented similar magnetic profiles, the curve grow between 10 K and 100 K and after that value tends to stabilize. At 370 K all complexes present a higher HS gradient, some complexes presented higher χ_MT value than expected, the molecules should have a higher molecular mass than we were considering. The values at 370 K are presented in **Table 2.38**.

Table 2.38 χ_MT values for the **C31-C41** at 370 K.

Complex	**C31**	**C32**	**C33**	**C34**	**C35**	**C36**	**C37_1**	**C37_2**	**C38**	**C39**	**C40**	**C41**
χ_MT	3.46	5.29	3.37	4.92	6.42	4.18	2.92	3.40	5.36	4.37	6.36	5.70
State (LS:HS)	25:75	HS	25:75	HS	HS	HS	35:65	20:80	HS	HS	HS	HS

3. Conclusions

As planned for this work, two groups of new Fe(III) complexes were synthesized. The first was characterized by changes in anions and halogens in the aromatic ring of the salEen, a tridentate ligand, to understand how these differences affect the spin crossover phenomenon. The second was characterized by changes of the halogens in the aromatic ring of the salpet, a pentadentate ligand, with the addition of a luminescence molecule.

Thirty-one new Fe(III) complexes with different X_2-salEen ligands were synthesized for group one, all being characterized and studied through FTIR and UV-vis spectroscopy, powder X-ray diffractometry and SQUID magnetometry. Almost all complexes were obtain as crystals but not all showed good quality of diffraction in single crystal X-ray studies, which means that it was not possible to solve them and know their structure. The crystals of the complexes with BF_4^- did not present good quality of diffraction in single crystal X-ray diffraction, while the ones with good enough quality did not show the exchange of the Cl^-. Consequently, we were not able to conclude the difference between the stretching N=C bands of the perchlorate and the tetrafluoroborate. The unsuccessful anion exchange only occurred for one of the complexes.

UV-vis spectroscopy allowed us to understand the spin state of the complexes in solution at room temperature and the SQUID magnetometry was used to understand the spin state of samples in the solid state at temperatures between 10 K and 370 K. These techniques allowed to conclude that some complexes did not present the same spin state in solution and solid state at the same temperature.

Also, with SQUID magnetometry it was possible to conclude that the anion influences the SCO phenomenon. Complexes with the same anions displayed different behaviors.

The magnetic profiles of complex **C12** allowed to understand that solvents also influence SCO curves. It crystallized with different solvate forms, as some crystals had water and methanol and the others acetonitrile. A SQUID magnetometry revealed that the solvate with acetonitrile present a gradual/abrupt SCO curve and the other presented a stable 1:1 (HS:LS) state.

Most complexes revealed that changing the ligand influences SCO behavior, although a group of three complexes with the same anion and solvent displayed identical SCO curves. This result was interesting, because the compounds created a hysteresis at temperatures in a period around 200 K and 350 K. All hysteresis increased the magnetic character with the increase in the number of cycles. A powder X-ray diffractometry was performed for the three complexes, showing differences in the structure before and after the SQUID. In one case, a single crystal X-ray diffractometry was performed for the same crystals after the SQUID and we observed that the changes are explained with structure rearrangements.

Most compounds at temperatures near 370 K had an increase in the magnetic character and thus would be interesting to perform more studies at higher temperatures to observe if the transition could occur after that temperature.

For the multifunction group, twelve complexes with different X_2-salpet ligands and the addition of a luminescence molecule were synthesized. The organic dye reaction was unsuccessful, but the inorganic dye synthesizes were successful. The inorganic dye presented luminesce with a quantum yield of 10%. NMR, FTIR and UV-vis spectroscopy and SQUID magnetometry were used to characterize and study the complexes, although the NMR analysis did not present conclusive results, which can be explain by the fact that the Fe(III) is paramagnetic and this technique is more appropriate for diamagnetic compounds. In FTIR we found the characteristic vibration for these complexes, and in the UV-vis we observed the bands corresponding to the iron and the ruthenium. SQUID magnetometry was performed and we conclude that different salpet ligands did not changed the magnetic profile. All complexes presented an abrupt curve between 10 and 100 K and after that temperature tended to stabilize. It is noticeable that in several of these complexes, when temperatures of 370 K are reached, the $\chi_M T$ value is higher than the theorical one. It is, therefore, not possible to assure that we synthesized the projected structure and further testing, like mass spectroscopy, is needed.

4. Experimental

4.1. Synthesis

All reagents and solvents were purchased either from Sigma-Aldrich or Acros and used without further purification.

Synthesis of complex 1 [Fe(3,5-Br-salEen)$_2$]ClO$_4$ - To a solution of *N*-ethylethylenediamine (0.11 mL, 1 mmol) in methanol (20 mL) 3,5-dibromosalicylaldehyde (280 mg, 1 mmol) was added and left stirring for 15 min to give a yellow solution. A solution of iron(II) chloride (64 mg, 0.5 mmol) and sodium perchlorate (70 mg, 0.5 mmol) in methanol was added to the mixture and left stirring for 1 h. The solution was filtered and a dark solid was obtained after slow evaporation of the solvent. The crude solid was recrystallised from an acetonitrile/ethanol mixture (25:75) yielding a crystalline solid after slow evaporation of the solvent (145 mg, 34%). Elemental analysis calculated (%) for $C_{22}H_{26}Br_4ClFeN_4O_6$•MeOH: C 31.24, H 3.31, N 6.34; found: C 31.76, H 3.32, N 6.59. FTIR analysis: υ(O-H) = 3439 cm^{-1}, υ(N-H) = 3238 cm^{-1}, υ(C-H) = 2974 cm^{-1}, υ(C=N) = 1639 cm^{-1}, υ(C=C) = 1576-1475 cm^{-1}, υ(ClO_4^-) = 1063 cm^{-1} and 625 cm^{-1}.

Synthesis of complex 2 [Fe(3,5-Br-salEen)$_2$]PF$_6$ - To a solution of N-ethylethylenediamine (0.11 mL, 1 mmol) in methanol (20 mL) 3,5-dibromosalicylaldehyde (280 mg, 1 mmol) was added and left stirring for 15 min to give a yellow solution. A solution of iron(II) chloride (64 mg, 0.5 mmol) and potassium hexafluorophosphate (92 mg, 0.5 mmol) in methanol was added to the mixture and left stirring for 1 h. The solution was filtered and a crystalline solid was obtained after slow evaporation of the solvent (304 mg, 68%). Elemental analysis calculated (%) for $C_{22}H_{26}Br_4F_6FeN_4O_2P$•MeOH: C 29.71, H 3.14, N 6.02; found: C 31.07, H 3.15, N 6.12. FTIR analysis: υ(O-H) = 3441 cm^{-1}, υ(C-H) = 2978 cm^{-1}, υ(C=N) = 1632 cm^{-1}, υ(C=C) = 1578-1470 cm^{-1}, υ(PF_6^-) = 839 cm^{-1}.

Synthesis of complex 3 [Fe(3,5-Br-salEen)$_2$]BPh$_4$•CH$_3$CN•H$_2$O - To a solution of N-ethylethylenediamine (0.11 mL, 1 mmol) in methanol (20 mL) 3,5-dibromosalicylaldehyde (280 mg, 1 mmol) was added and left stirring for 15 min to give a yellow solution. A solution of iron(II) chloride (64 mg, 0.5 mmol) and ammonium tetraphenylborate (169 mg, 0.5 mmol) in methanol was added to the mixture and left stirring for 1 h. The solution was filtered and a dark solid was obtained. The crude solid was recrystallised from an acetonitrile yielding a crystalline solid after slow evaporation of the solvent (319 mg, 57%). Elemental analysis calculated (%) for $C_{46}H_{46}BBr_4FeN_4O_2$•$H_2O$: C 50.63, H 4.43, N 5.13; found: C 50.31, H 4.27, N 5.60. FTIR analysis: υ(O-H) = 3431 cm^{-1}, υ(N-H) = 3215 cm^{-1}, υ(C-H) = 2984 cm^{-1}, υ(C=N) = 1627 cm^{-1}, υ(C=C) = 1579-1465 cm^{-1}, υ(BPh_4^-) = 744-707 cm^{-1}.

Synthesis of complex 4 [Fe(3,5-Br-salEen)$_2$]BF$_4$ - To a solution of N-ethylethylenediamine (0.11 mL, 1 mmol) in methanol (20 mL) 3,5-dibromosalicylaldehyde (280 mg, 1 mmol) was added and left stirring for 15 min to give a yellow solution. A solution of iron(II) chloride (127 mg, 1 mmol) and sodium tetrafluoroborate (110 mg, 1 mmol) in methanol was added to the mixture and left stirring for 1 h. The solution was filtered and a crystalline solid was obtained after slow evaporation of the solvent (301 mg, 74%). Elemental analysis calculated (%) for $C_{22}H_{26}BBr_4F_4FeN_4O_2$: C 31.43, H 3.12, N 6.66; found: C 31.63, H 3.40, N 6.62. FTIR analysis: υ(O-H) = 3417 cm^{-1}, υ(C-H) = 2972 cm^{-1}, υ(C=N) = 1619 cm^{-1}, υ(C=C) = 1578-1429 cm^{-1}, υ(BF_4^-) = 1066 cm^{-1}.

Synthesis of complex 5 [Fe(3,5-Br-salEen)$_2$]NO$_3$ - To a solution of N-ethylethylenediamine (0.11 mL, 1 mmol) in methanol (20 mL) 3,5-dibromosalicylaldehyde (280 mg, 1 mmol) was added and left stirring for 15 min to give a yellow solution. Iron(III) nitrate (202 mg, 0.5 mmol) in methanol was added to the mixture and left stirring for 1 h. The solution was filtered and a crystalline solid was obtained after slow evaporation of the solvent (144 mg, 38%). Elemental analysis calculated (%) for $C_{22}H_{26}Br_4FeN_5O_5$•H_2O•CH_3CN: C 32.38, H 3.21, N 8.58; found: C 32.18, H 3.36, N 7.91. FTIR analysis: υ(O-H) = 3435 cm^{-1}, υ(N-H) = 3170 cm^{-1}, υ(C-H) = 2972 cm^{-1}, υ(C=N) = 1624 cm^{-1}, υ(C=C) = 1577-1511 cm^{-1}, υ(NO_3^-) = 1383 cm^{-1}.

Synthesis of complex 6 [Fe(3,5-Cl-salEen)$_2$]ClO$_4$ - To a solution of N-ethylethylenediamine (0.11 mL, 1 mmol) in methanol (20 mL) 3,5-dichlorosalicylaldehyde (191 mg, 1 mmol) was added and left stirring for 15 min to give a yellow solution. A solution of iron(II) chloride (64 mg, 0.5 mmol) and sodium perchlorate (70 mg, 0.5 mmol) in methanol was added to the mixture and left stirring for 1 h. The solution was filtered and a dark solid was obtained after slow evaporation of the solvent. The crude solid was recrystallised from an acetonitrile/ethanol mixture (25:75) yielding a crystalline solid after slow evaporation of the solvent (123 mg, 28%). %). FTIR analysis: υ(O-H) = 3411 cm^{-1}, υ(N-H) = 3237 cm^{-1}, υ(C-H) = 2977 cm^{-1}, υ(C=N) = 1638 cm^{-1}, υ(C=C) = 1585-1469 cm^{-1}, υ(ClO$_4^-$) = 1062 cm^{-1} and 624 cm^{-1}.

Synthesis of complex 7 [Fe(3,5-Cl-salEen)$_2$]PF$_6$ - To a solution of N-ethylethylenediamine (0.11 mL, 1 mmol) in methanol (20 mL) 3,5-dichlorosalicylaldehyde (191 mg, 1 mmol) was added and left stirring for 15 min to give a yellow solution. A solution of iron(II) chloride (64 mg, 0.5 mmol) and potassium hexafluorophosphate (92 mg, 0.5 mmol) in methanol was added to the mixture and left stirring for 1 h. The solution was filtered and a crystalline solid was obtained after slow evaporation of the solvent (276 mg, 77%). FTIR analysis: υ(O-H) = 3414 cm^{-1}, υ(C-H) = 2977 cm^{-1}, υ(C=N) = 1630 cm^{-1}, υ(C=C) = 1586-1471 cm^{-1}, υ(PF$_6^-$) = 839 cm^{-1}.

Synthesis of complex 8 [Fe(3,5-Cl-salEen)$_2$]BPh$_4$•H$_2$O•CH$_3$CN - To a solution of N-ethylethylenediamine (0.11 mL, 1 mmol) in methanol (20 mL) 3,5-dichlorosalicylaldehyde (191 mg, 1 mmol) was added and left stirring for 15 min to give a yellow solution. A solution of iron(II) chloride (64 mg, 0.5 mmol) and ammonium tetraphenylborate (169 mg, 0.5 mmol) in methanol was added to the mixture and left stirring for 1 h. The solution was filtered and a dark solid was obtained. The crude solid was recrystallised from an acetonitrile/ethanol mixture (75:25) yielding a crystalline solid after slow evaporation of the solvent (463 mg, 97%). FTIR analysis: υ(O-H) = 3425 cm^{-1}, υ(N-H) = 3212 cm^{-1}, υ(C-H) = 2986 cm^{-1}, υ(C=N) = 1628 cm^{-1}, υ(C=C) = 1578-1468 cm^{-1}, υ(BPh$_4^-$) = 742-710 cm^{-1}.

Synthesis of complex 9 [Fe(3,5-Cl-salEen)$_2$]NO$_3$ - To a solution of N-ethylethylenediamine (0.11 mL, 1 mmol) in methanol (20 mL) 3,5-dichlorosalicylaldehyde (191 mg, 1 mmol) was added and left stirring for 15 min to give a yellow solution. Iron(III) nitrate (202 mg, 0.5 mmol) in methanol was added to the mixture and left stirring for 1 h. The solution was filtered and a crystalline solid was obtained after slow evaporation of the solvent (331 mg, 81%). FTIR analysis: υ(O-H) = 3442 cm^{-1}, υ(N-H) = 3278 cm^{-1}, υ(C-H) = 2970 cm^{-1}, υ(C=N) = 1629 cm^{-1}, υ(C=C) = 1578-1468 cm^{-1}, υ(NO$_3^-$) = 1385 cm^{-1}.

Synthesis of complex 10 [Fe(3,5-F-salEen)$_2$]ClO$_4$ - To a solution of N-ethylethylenediamine (0.11 mL, 1 mmol) in methanol (20 mL) 3,5-difluorosalicylaldehyde (158 mg, 1 mmol) was added and left stirring for 15 min to give a yellow solution. A solution of iron(II) chloride (64 mg, 0.5 mmol) and sodium perchlorate (70 mg, 0.5 mmol) in methanol was added to the mixture and left stirring for 1 h. The solution was filtered and a dark solid was obtained after slow evaporation of the solvent. The crude solid was recrystallised from acetonitrile yielding a crystalline solid after slow evaporation of the solvent (165 mg, 54%). FTIR analysis: υ(O-H) = 3440 cm^{-1}, υ(N-H) = 3234 cm^{-1}, υ(C-H) = 2978 cm^{-1}, υ(C=N) = 1645 cm^{-1}, υ(C=C) = 1558-1453 cm^{-1}, υ(ClO$_4^-$) = 1045 cm^{-1} and 623 cm^{-1}.

Synthesis of complex 11 [Fe(3,5-F-salEen)$_2$]PF$_6$ - To a solution of N-ethylethylenediamine (0.11 mL, 1 mmol) in methanol (20 mL) 3,5-difluorosalicylaldehyde (158 mg, 1 mmol) was added and left stirring for 15 min to give a yellow solution. A solution of iron(II) chloride (64 mg, 0.5 mmol) and potassium hexafluorophosphate (92 mg, 0.5 mmol) in methanol was added to the mixture and left stirring for 1 h. The solution was filtered and a dark solid and a solution was obtained. The solution as evaporate and was recrystallised from an acetonitrile/ethanol mixture (25:75) yielding a crystalline solid after slow evaporation of the solvent (27 mg, 8%). The crude solid was recrystallised from an acetonitrile/ethanol mixture (25:75) yielding a crystalline solid after slow evaporation of the solvent (113 mg, 34%). FTIR analysis: υ(O-H) = 3427 cm^{-1}, υ(N-H) = 3297 cm^{-1}, υ(C-H) = 2978 cm^{-1}, υ(C=N) = 1635 cm^{-1}, υ(C=C) = 1560-1469 cm^{-1}, υ(PF$_6^-$) = 844 cm^{-1}.

Synthesis of complex 12 [Fe(3,5-F-salEen)$_2$]BPh$_4$ - To a solution of N-ethylethylenediamine (0.11 mL, 1 mmol) in methanol (20 mL) 3,5-difluorosalicylaldehyde (158 mg, 1 mmol) was added and left stirring for 15 min to give a yellow solution. A solution of iron(II) chloride (64 mg, 0.5 mmol) and ammonium tetraphenylborate (169 mg, 0.5 mmol) in methanol was added to the mixture and left stirring for 1 h. The solution was filtered and a dark solid and a solution was obtained. To the solution a crystalline solid [Fe(3,5-F-salEen)$_2$]BPh$_4$•MeOH•H$_2$O was obtained after slow evaporation of the solvent (108 mg, 25%). Elemental analysis calculated (%) for $C_{46}H_{46}BF_4FeN_4O_2$: C 66.60, H 6.75, N 10.42; found: C 68.24, H 4.86, N 7.51. FTIR analysis: υ(O-H) = 3442 cm^{-1}, υ(C-H) = 2982 cm^{-1}, υ(C=N) = 1629 cm^{-1}, υ(C=C) = 1580-1477 cm^{-1}, υ(BPh$_4^-$) = 743-708 cm^{-1}. The crude solid was recrystallised from acetonitrile yielding a crystalline solid [Fe(3,5-F-salEen)$_2$]BPh$_4$•CH$_3$CN after slow evaporation of the solvent (194 mg, 45%). Elemental analysis calculated (%) for $C_{46}H_{46}BF_4FeN_4O_2$•CH$_3$CN: C 66.31, H 5.67, N 8.04; found: C 66.31, H 5.44, N 8.02. FTIR analysis: υ(O-H) = 3442 cm^{-1}, υ(N-H) = 3231 cm^{-1}, υ(C-H) = 2982 cm^{-1}, υ(C=N) = 1632 cm^{-1}, υ(C=C) = 1580-1477 cm^{-1}, υ(BPh$_4^-$) = 743-709 cm^{-1}.

Synthesis of complex 13 [Fe(3,5-F-salEen)$_2$]BF$_4$ - To a solution of N-ethylethylenediamine (0.11 mL, 1 mmol) in methanol (20 mL) 3,5-difluorosalicylaldehyde (158 mg, 1 mmol) was added and left stirring for 15 min to give a yellow solution. A solution of iron(II) chloride (127 mg, 1 mmol) and sodium tetrafluoroborate (110 mg, 1 mmol) in methanol was added to the mixture and left stirring for 1 h. The solution was filtered and a crystalline solid was obtained after slow evaporation of the solvent (163 mg, 55%). FTIR analysis: υ(O-H) = 3496 cm^{-1}, υ(N-H) = 3220 cm^{-1}, υ(C-H) = 2977 cm^{-1}, υ(C=N) = 1631 cm^{-1}, υ(C=C) = 1560-1441 cm^{-1}, υ(BF$_4^-$) = 1069 cm^{-1}.

Synthesis of complex 14 [Fe(3,5-F-salEen)$_2$]NO$_3$ - To a solution of N-ethylethylenediamine (0.11 mL, 1 mmol) in methanol (20 mL) 3,5-difluorosalicylaldehyde (158 mg, 1 mmol) was added and left stirring for 15 min to give a yellow solution. Iron(III) nitrate (202 mg, 0.5 mmol) in methanol was added to the mixture and left stirring for 1 h. The solution was filtered and a dark solid was obtained after slow evaporation of the solvent. The crude solid was recrystallised from methanol yielding a crystalline solid after slow evaporation of the solvent (186 mg, 65%). FTIR analysis: υ(O-H) = 3443 cm^{-1}, υ(N-H) = 3299 cm^{-1}, υ(C-H) = 2979 cm^{-1}, υ(C=N) = 1637 cm^{-1}, υ(C=C) = 1556-1455 cm^{-1}, υ(NO$_3^-$) = 1382 cm^{-1}.

Synthesis of complex 15 [Fe(3,5-I-salEen)$_2$]ClO$_4$ - To a solution of N-ethylethylenediamine (0.11 mL, 1 mmol) in methanol (20 mL) 3,5-diiodosalicylaldehyde (374 mg, 1 mmol) was added and left stirring for 15 min to give a yellow solution. A solution of iron(II) chloride (64 mg, 0.5 mmol) and sodium perchlorate (70 mg, 0.5 mmol) in methanol was added to the mixture and left stirring for 1 h. The solution was filtered and a dark solid was obtained. The crude solid was recrystallised from an acetonitrile/ethanol mixture (25:75) yielding a crystalline solid after slow evaporation of the solvent (71 mg, 12%). FTIR analysis: υ(O-H) = 3416 cm^{-1}, υ(N-H) = 3234 cm^{-1}, υ(C-H) = 2966 cm^{-1}, υ(C=N) = 1619 cm^{-1}, υ(C=C) = 1564-1462 cm^{-1}, υ(ClO$_4^-$) = 1066 cm^{-1} and 625 cm^{-1}.

Synthesis of complex 16 [Fe(3,5-I-salEen)$_2$]PF$_6$ - To a solution of N-ethylethylenediamine (0.11 mL, 1 mmol) in methanol (20 mL) 3,5-diiodosalicylaldehyde (158 mg, 1 mmol) was added and left stirring for 15 min to give a yellow solution. A solution of iron(II) chloride (64 mg, 0.5 mmol) and potassium hexafluorophosphate (92 mg, 0.5 mmol) in methanol was added to the mixture and left stirring for 1 h. The solution was filtered and a dark solid was obtained. The crude solid was recrystallised from an acetonitrile/ethanol mixture (75:25) yielding a crystalline solid after slow evaporation of the solvent (296 mg, 54%). FTIR analysis: υ(O-H) = 3416 cm^{-1}, υ(N-H) = 3093 cm^{-1}, υ(C-H) = 2966 cm^{-1}, υ(C=N) = 1619 cm^{-1}, υ(C=C) = 1565-1470 cm^{-1}, υ(PF$_6^-$) = 840 cm^{-1}.

Synthesis of complex 17 [Fe(3,5-I-salEen)$_2$]BPh$_4$ - To a solution of N-ethylethylenediamine (0.11 mL, 1 mmol) in methanol (20 mL) 3,5-diiodosalicylaldehyde (158 mg, 1 mmol) was added and left stirring for 15 min to give a yellow solution. A solution of iron(II) chloride (64 mg, 0.5 mmol) and ammonium tetraphenylborate (169 mg, 0.5 mmol) in methanol was added to the mixture and left stirring for 1 h. The solution was filtered and a dark solid was obtained. The crude solid was recrystallised from acetonitrile yielding a crystalline solid after slow evaporation of the solvent (476 mg, 75%). FTIR analysis: υ(O-H) = 3500 cm^{-1}, υ(N-H) = 3238 cm^{-1}, υ(C-H) = 2977 cm^{-1}, υ(C=N) = 1618 cm^{-1}, υ(C=C) = 1577-1478 cm^{-1}, υ(BPh_4^-) = 745-707 cm^{-1}.

Synthesis of complex 18 [Fe(3,5-I-salEen)$_2$]BF_4 - To a solution of N-ethylethylenediamine (0.11 mL, 1 mmol) in methanol (20 mL) 3,5-diiodosalicylaldehyde (158 mg, 1 mmol) was added and left stirring for 15 min to give a yellow solution. A solution of iron(II) chloride (127 mg, 1 mmol) and sodium tetrafluoroborate (110 mg, 1 mmol) in methanol was added to the mixture and left stirring for 1 h. The solution was filtered and a dark solid was obtained after slow evaporation of the solvent. The crude solid was recrystallised from acetonitrile yielding a crystalline solid after slow evaporation of the solvent (70 mg, 14%). FTIR analysis: υ(O-H) = 3441 cm^{-1}, υ(N-H) = 3059 cm^{-1}, υ(C-H) = 2979 cm^{-1}, υ(C=N) = 1629 cm^{-1}, υ(C=C) = 1567-1468 cm^{-1}.

Synthesis of complex 19 [Fe(3,5-I-salEen)$_2$]NO_3 - To a solution of N-ethylethylenediamine (0.11 mL, 1 mmol) in methanol (20 mL) 3,5-diiodosalicylaldehyde (158 mg, 1 mmol) was added and left stirring for 15 min to give a yellow solution. Iron(III) nitrate (202 mg, 0.5 mmol) in methanol was added to the mixture and left stirring for 1 h. The solution was filtered and a dark solid and a solution was obtained. The crude solid was recrystallised from acetonitrile yielding a crystalline solid after slow evaporation of the solvent (36 mg, 7%). To the solution a crystalline solid was obtained after slow evaporation of the solvent (436 mg, 87%). The two crystalline solids are the same. FTIR analysis: υ(O-H) = 3440 cm^{-1}, υ(N-H) = 3177 cm^{-1}, υ(C-H) = 2969 cm^{-1}, υ(C=N) = 1630 cm^{-1}, υ(C=C) = 1564-1465 cm^{-1}, υ(NO_3^-) = 1385 cm^{-1}.

Synthesis of complex 20 [Fe(3-Br-5-Cl-salEen)$_2$]ClO_4•CH_3CN - To a solution of N-ethylethylenediamine (0.11 mL, 1 mmol) in methanol (20 mL) 3-bromo-5-chlorosalicylaldehyde (235 mg, 1 mmol) was added and left stirring for 15 min to give a yellow solution. A solution of iron(II) chloride (64 mg, 0.5 mmol) and sodium perchlorate (70 mg, 0.5 mmol) in methanol was added to the mixture and left stirring for 1 h. The solution was filtered and a dark solid was obtained after slow evaporation of the solvent. The crude solid was recrystallised from acetonitrile yielding a crystalline solid after slow evaporation of the solvent (120 mg, 30%). FTIR analysis: υ(O-H) = 3433 cm^{-1}, υ(N-H) = 3234 cm^{-1}, υ(C-H) = 2976 cm^{-1}, υ(C=N) = 1625 cm^{-1}, υ(C=C) = 1581-1468 cm^{-1}, υ(ClO_4^-) = 1062 cm^{-1} and 623 cm^{-1}.

Synthesis of complex 21 [Fe(3-Br-5Cl-salEen)$_2$]PF6 - To a solution of N-ethylethylenediamine (0.11 mL, 1 mmol) in methanol (20 mL) 3-bromo-5-chlorosalicylaldehyde (235 mg, 1 mmol) was added and left stirring for 15 min to give a yellow solution. A solution of iron(II) chloride (64 mg, 0.5 mmol) and potassium hexafluorophosphate (92 mg, 0.5 mmol) in methanol was added to the mixture and left stirring for 1 h. The solution was filtered and a dark solid was obtained. The crude solid was recrystallised from an acetonitrile/ethanol mixture (75:25) yielding a crystalline solid after slow evaporation of the solvent (117 mg, 29%). FTIR analysis: υ(O-H) = 3444 cm^{-1}, υ(C-H) = 2970 cm^{-1}, υ(C=N) = 1632 cm^{-1}, υ(C=C) = 1583-1464 cm^{-1}, υ(PF_6^-) = 839 cm^{-1}.

Synthesis of complex 22 [Fe(3-Br-5-Cl-salEen)$_2$]BPh_4•H_2O•CH_3CN - To a solution of N-ethylethylenediamine (0.11 mL, 1 mmol) in methanol (20 mL) 3-bromo-5-chlorosalicylaldehyde (235 mg, 1 mmol) was added and left stirring for 15 min to give a yellow solution. A solution of iron(II) chloride (64 mg, 0.5 mmol) and ammonium tetraphenylborate (169 mg, 0.5 mmol) in methanol was added to the mixture and left stirring for 1 h. The solution was filtered and a dark solid was obtained. The crude solid was recrystallised from an acetonitrile/ethanol mixture (75:25) yielding a crystalline solid after slow evaporation of the solvent (266 mg, 51%). Elemental analysis calculated (%) for $C_{30}H_{35}BBr_2Cl_2FeN_5O_4$•$H_2O$•$CH_3CN$: C 55.26, H 4.97, N 6.71; found: C 55.17, H 4.50, N 6.71. FTIR analysis: υ(O-H) = 3438 cm^{-1}, υ(N-H) = 3219 cm^{-1}, υ(C-H) = 2982 cm^{-1}, υ(C=N) = 1625 cm^{-1}, υ(C=C) = 1579-1478 cm^{-1}, υ(BPh_4^-) = 743-708 cm^{-1}.

Synthesis of complex 23 $[Fe(3\text{-}Br\text{-}5\text{-}Cl\text{-}salEen)_2]BF_4$ - To a solution of N-ethylethylenediamine (0.11 mL, 1 mmol) in methanol (20 mL) 3-bromo-5-chlorosalicylaldehyde (235 mg, 1 mmol) was added and left stirring for 15 min to give a yellow solution. A solution of iron(II) chloride (127 mg, 1 mmol) and sodium tetrafluoroborate (110 mg, 1 mmol) in methanol was added to the mixture and left stirring for 1 h. The solution was filtered and a crystalline solid was obtained after slow evaporation of the solvent (185 mg, 48%). FTIR analysis: υ(O-H) = 3417 cm^{-1}, υ(C-H) = 2970 cm^{-1}, υ(C=N) = 1619 cm^{-1}, υ(C=C) = 1583-1428 cm^{-1}, υ(BF_4^-) = 1069 cm^{-1}.

Synthesis of complex 24 $[Fe(3\text{-}Br\text{-}5\text{-}Cl\text{-}salEen)_2]NO_3$ - To a solution of N-ethylethylenediamine (0.11 mL, 1 mmol) in methanol (20 mL) 3-bromo-5-chlorosalicylaldehyde (235 mg, 1 mmol) was added and left stirring for 15 min to give a yellow solution. Iron(III) nitrate (202 mg, 0.5 mmol) in methanol was added to the mixture and left stirring for 1 h. The solution was filtered and a crystalline solid was obtained after slow evaporation of the solvent (335 mg, 92%). FTIR analysis: υ(O-H) = 3440 cm^{-1}, υ(N-H) = 3171 cm^{-1}, υ(C-H) = 2977 cm^{-1}, υ(C=N) = 1628 cm^{-1}, υ(C=C) = 1586-1514 cm^{-1}, υ(NO_3^-) = 1384 cm^{-1}.

Synthesis of complex 25 $[Fe(5\text{-}Cl\text{-}3\text{-}I\text{-}salEen)_2]ClO_4$ - To a solution of N-ethylethylenediamine (0.11 mL, 1 mmol) in methanol (20 mL) 5-chloro-3-iodosalicylaldehyde (282 mg, 1 mmol) was added and left stirring for 15 min to give a yellow solution. A solution of iron(II) chloride (64 mg, 0.5 mmol) and sodium perchlorate (70 mg, 0.5 mmol) in methanol was added to the mixture and left stirring for 1 h. The solution was filtered and a dark solid and a solution was obtained. To the solution a crystalline solid was obtained after slow evaporation of the solvent (60 mg, 14%). The crude solid was recrystallised from acetonitrile yielding a crystalline solid after slow evaporation of the solvent (80 mg, 19%). FTIR analysis: υ(O-H) = 3448 cm^{-1}, υ(N-H) = 3234 cm^{-1}, υ(C-H) = 2971 cm^{-1}, υ(C=N) = 1627 cm^{-1}, υ(C=C) = 1581-1448 cm^{-1}, υ(ClO_4^-) = 1063 cm^{-1} and 623 cm^{-1}.

Synthesis of complex 26 $[Fe(5\text{-}Cl\text{-}3\text{-}I\text{-}salEen)_2]PF_6\cdot 2H_2O\bullet CH_3CN$ - To a solution of N-ethylethylenediamine (0.11 mL, 1 mmol) in methanol (20 mL) 5-chloro-3-iodosalicylaldehyde (282 mg, 1 mmol) was added and left stirring for 15 min to give a yellow solution. A solution of iron(II) chloride (64 mg, 0.5 mmol) and potassium hexafluorophosphate (92 mg, 0.5 mmol) in methanol was added to the mixture and left stirring for 1 h. The solution was filtered and a dark solid was obtained. The crude solid was recrystallised from acetonitrile yielding a crystalline solid after slow evaporation of the solvent (217 mg, 44%). FTIR analysis: υ(O-H) = 3441 cm^{-1}, υ(C-H) = 2973 cm^{-1}, υ(C=N) = 1629 cm^{-1}, υ(C=C) = 1580-1471 cm^{-1}, υ(PF_6^-) = 841 cm^{-1}.

Synthesis of complex 27 $[Fe(5\text{-}Cl\text{-}3\text{-}I\text{-}salEen)_2]BPh_4\cdot H_2O\bullet CH_3CN$ - To a solution of N-ethylethylenediamine (0.11 mL, 1 mmol) in methanol (20 mL) 5-chloro-3-iodosalicylaldehyde (282 mg, 1 mmol) was added and left stirring for 15 min to give a yellow solution. A solution of iron(II) chloride (64 mg, 0.5 mmol) and ammonium tetraphenylborate (169 mg, 0.5 mmol) in methanol was added to the mixture and left stirring for 1 h. The solution was filtered and a dark solid was obtained after slow evaporation of the solvent. The crude solid was recrystallised from acetonitrile yielding a crystalline solid after slow evaporation of the solvent (342 mg, 60%). FTIR analysis: υ(O-H) = 3449 cm^{-1}, υ(N-H) = 3240 cm^{-1}, υ(C-H) = 2980 cm^{-1}, υ(C=N) = 1619 cm^{-1}, υ(C=C) = 1579-1478 cm^{-1}, υ(BPh_4^-) = 732-706 cm^{-1}.

Synthesis of complex 28 $[Fe(5\text{-}Cl\text{-}3\text{-}I\text{-}salEen)_2]BF_4\cdot 2H_2O$ - To a solution of N-ethylethylenediamine (0.11 mL, 1 mmol) in methanol (20 mL) 5-chloro-3-iodosalicylaldehyde (282 mg, 1 mmol) was added and left stirring for 15 min to give a yellow solution. A solution of iron(II) chloride (127 mg, 1 mmol) and sodium tetrafluoroborate (110 mg, 1 mmol) in methanol was added to the mixture and left stirring for 1 h. The solution was filtered and a crystalline solid was obtained after slow evaporation of the solvent (44 mg, 10%). FTIR analysis: υ(O-H) = 3416 cm^{-1}, υ(C-H) = 2968 cm^{-1}, υ(C=N) = 1633 cm^{-1}, υ(C=C) = 1580-1462 cm^{-1}, υ(BF_4^-) = 1070 cm^{-1}.

Synthesis of complex 29 [Fe(5-Br-3-NO$_2$-salEen)$_2$]PF$_6$ - To a solution of N-ethylethylenediamine (0.11 mL, 1 mmol) in methanol (20 mL) 5-bromo-3-nitrosalicylaldehyde (246 mg, 1 mmol) was added and left stirring for 15 min to give a yellow solution. A solution of iron(II) chloride (64 mg, 0.5 mmol) and potassium hexafluorophosphate (92 mg, 0.5 mmol) in methanol was added to the mixture and left stirring for 1 h. The solution was filtered and a dark solid was obtained. The crude solid was recrystallised from an acetonitrile/ethanol mixture (75:25) yielding a crystalline solid after slow evaporation of the solvent (112 mg, 27%). Elemental analysis calculated (%) for $C_{22}H_{26}Br_2F_6FeN_6O_6P$•EtOH: C 32.86, H 3.68, N 9.58; found: C 32.90, H 3.44, N 9.80. FTIR analysis: υ(O-H) = 3371 cm^{-1}, υ(N-H) = 3278 cm^{-1}, υ(C-H) = 2969 cm^{-1}, υ(C=N) = 1638 cm^{-1}, υ(C=C) = 1594-1464 cm^{-1}, υ(PF_6^-) = 843 cm^{-1}.

Synthesis of complex 30 [Fe(5-Br-3-NO$_2$-salEen)$_2$]BPh$_4$ - To a solution of N-ethylethylenediamine (0.11 mL, 1 mmol) in methanol (20 mL) 5-bromo-3-nitrosalicylaldehyde (246 mg, 1 mmol) was added and left stirring for 15 min to give a yellow solution. A solution of iron(II) chloride (64 mg, 0.5 mmol) and ammonium tetraphenylborate (169 mg, 0.5 mmol) in methanol was added to the mixture and left stirring for 1 h. The solution was filtered and a dark solid was obtained. The crude solid was recrystallised from an acetonitrile yielding a crystalline solid after slow evaporation of the solvent (1.107 mg, +100%). %). FTIR analysis: υ(O-H) = 3426 cm^{-1}, υ(C-H) = 2993 cm^{-1}, υ(C=N) = 1636 cm^{-1}, υ(C=C) = 1592-1466 cm^{-1}, υ(BPh_4^-) = 751-702 cm^{-1}.

Synthesis of complex 31 [Fe(salpet)Ru(phen)$_2$(dppz)]•Cl•2PF$_6$ - To a solution of N-(2-aminoethyl)-1,3-propanediamine (0.025 mL, 0.2 mmol) in methanol (20 mL) salicylaldehyde (0.04 mL, 0.4 mmol) was added and left stirring and reflux for 45 min to give a yellow solution. Iron(III) chloride (32 mg, 0.2 mmol), [Ru(phen)2(dppz)] (151 mg, 0.2 mmol) and triethylamine (56 mg, 0.4 mmol) in methanol was added to the mixture and left stirring and reflux for 45 min. The solution was filtered left for evaporation of the solvent. When the solution had few amount of solvent (5 mL) add ethyl ether a dark brown powder had precipitated (33 mg, 14%). FTIR analysis: υ(O-H) = 3436 cm^{-1}, υ(C-H) = 2940 cm^{-1}, υ(C=N) = 1633 cm^{-1}, υ(C=C) = 1543-1310 cm^{-1}, υ(PF_6^-) = 839 cm^{-1}.

Synthesis of complex 32 [Fe(5-Br-salpet)Ru(phen)$_2$(dppz)]•Cl•2PF$_6$ - To a solution of N-(2-aminoethyl)-1,3-propanediamine (0.025 mL, 0.2 mmol) in methanol (20 mL) 5-bromosalicylaldehyde (80 mg, 0.4 mmol) was added and left stirring and reflux for 45 min to give a yellow solution. Iron(III) chloride (32 mg, 0.2 mmol), [Ru(phen)2(dppz)] (151 mg, 0.2 mmol) and triethylamine (56 mg, 0.4 mmol) in methanol was added to the mixture and left stirring and reflux for 45 min. The solution was filtered left for evaporation of the solvent. When the solution had few amount of solvent (5 mL) add ethyl ether a dark brown powder had precipitated (120 mg, 46%). A solution in methanol is still evaporating. FTIR analysis: υ(O-H) = 3430 cm^{-1}, υ(N-H) = 3234 cm^{-1}, υ(C-H) = 2941 cm^{-1}, υ(C=N) = 1628 cm^{-1}, υ(C=C) = 1529-1389 cm^{-1}, υ(PF_6^-) = 844 cm^{-1}.

Synthesis of complex 33 [Fe(5-Cl-salpet)Ru(phen)$_2$(dppz)]•Cl•2PF$_6$ - To a solution of N-(2-aminoethyl)-1,3-propanediamine (0.025 mL, 0.2 mmol) in methanol (20 mL) 5-chlorosalicylaldehyde (63 mg, 0.4 mmol) was added and left stirring and reflux for 45 min to give a yellow solution. Iron(III) chloride (32 mg, 0.2 mmol), [Ru(phen)2(dppz)] (151 mg, 0.2 mmol) and triethylamine (56 mg, 0.4 mmol) in methanol was added to the mixture and left stirring and reflux for 45 min. The solution was filtered left for evaporation of the solvent. When the solution had few amount of solvent (5 mL) add ethyl ether a dark brown powder had precipitated (51 mg, 21%). A solution in methanol is still evaporating. FTIR analysis: υ(O-H) = 3437 cm^{-1}, υ(N-H) = 3227 cm^{-1}, υ(C-H) = 2947 cm^{-1}, υ(C=N) = 1629 cm^{-1}, υ(C=C) = 1522-1383 cm^{-1}, υ(PF_6^-) = 846 cm^{-1}.

Synthesis of complex 34 [Fe(5-I-salpet)Ru(phen)$_2$(dppz)]•Cl•2PF$_6$ - To a solution of N-(2-aminoethyl)-1,3-propanediamine (0.025 mL, 0.2 mmol) in methanol (20 mL) 5-iodosalicylaldehyde (99 mg, 0.4 mmol) was added and left stirring and reflux for 45 min to give a yellow solution. Iron(III) chloride (32 mg, 0.2 mmol), [Ru(phen)2(dppz)] (151 mg, 0.2 mmol) and triethylamine (56 mg, 0.4

mmol) in methanol was added to the mixture and left stirring and reflux for 45 min. The solution was filtered left for evaporation of the solvent. When the solution had few amount of solvent (5 mL) add ethyl ether a dark brown powder had precipitated (75 mg, 27%). FTIR analysis: υ(O-H) = 3416 cm^{-1}, υ(N-H) = 3226 cm^{-1}, υ(C-H) = 2919 cm^{-1}, υ(C=N) = 1627 cm^{-1}, υ(C=C) = 1523-1302 cm^{-1}, υ(PF$_6^-$) = 843 cm^{-1}.

Synthesis of complex 35 [Fe(5-F-salpet)Ru(phen)$_2$(dppz)]•Cl•2PF$_6$ – To a solution of N-(2-aminoethyl)-1,3-propanediamine (0.025 mL, 0.2 mmol) in methanol (20 mL) 5-fluorosalicylaldehyde (56 mg, 0.4 mmol) was added and left stirring and reflux for 45 min to give a yellow solution. Iron(III) chloride (32 mg, 0.2 mmol), [Ru(phen)2(dppz)] (151 mg, 0.2 mmol) and triethylamine (56 mg, 0.4 mmol) in methanol was added to the mixture and left stirring and reflux for 45 min. The solution was filtered left for evaporation of the solvent. When the solution had few amount of solvent (5 mL) add ethyl ether a dark brown powder had precipitated (51 mg, 21%). FTIR analysis: υ(O-H) = 3422 cm^{-1}, υ(N-H) = 3234 cm^{-1}, υ(C-H) = 2926 cm^{-1}, υ(C=N) = 1634 cm^{-1}, υ(C=C) = 1552-1386 cm^{-1}, υ(PF$_6^-$) = 838 cm^{-1}.

Synthesis of complex 36 [Fe(3,5-Br-salpet)Ru(phen)$_2$(dppz)]•Cl•2PF$_6$ – To a solution of N-(2-aminoethyl)-1,3-propanediamine (0.025 mL, 0.2 mmol) in methanol (20 mL) 3,5-bromosalicylaldehyde (112 mg, 0.4 mmol) was added and left stirring and reflux for 45 min to give a yellow solution. Iron(III) chloride (32 mg, 0.2 mmol), [Ru(phen)2(dppz)] (151 mg, 0.2 mmol) and triethylamine (56 mg, 0.4 mmol) in methanol was added to the mixture and left stirring and reflux for 45 min. The solution was filtered left for evaporation and a brown powder was obtained (115 mg, 39%). A solution in methanol is still evaporating. FTIR analysis: υ(O-H) = 3415 cm^{-1}, υ(N-H) = 3241 cm^{-1}, υ(C-H) = 2926 cm^{-1}, υ(C=N) = 1621 cm^{-1}, υ(C=C) = 1578-1301 cm^{-1}, υ(PF$_6^-$) = 843 cm^{-1}.

Synthesis of complex 37 [Fe(3,5-Cl-salpet)Ru(phen)$_2$(dppz)]•Cl•2PF$_6$ – To a solution of N-(2-aminoethyl)-1,3-propanediamine (0.025 mL, 0.2 mmol) in methanol (20 mL) 3,5-chlorosalicylaldehyde (76 mg, 0.4 mmol) was added and left stirring and reflux for 45 min to give a yellow solution. Iron(III) chloride (32 mg, 0.2 mmol), [Ru(phen)2(dppz)] (151 mg, 0.2 mmol) and triethylamine (56 mg, 0.4 mmol) in methanol was added to the mixture and left stirring and reflux for 45 min. The solution was filtered left for evaporation of the solvent. When the solution had few amount of solvent (5 mL) add ethyl ether a dark brown powder had precipitated **C37_1** (50 mg, 19%). FTIR analysis: υ(O-H) = 3422 cm^{-1}, υ(N-H) = 3234 cm^{-1}, υ(C-H) = 3059 cm^{-1}, υ(C=N) = 1631 cm^{-1}, υ(C=C) = 1524-1305 cm^{-1}, υ(PF$_6^-$) = 839 cm^{-1}. After the ether evaporate, dissolve in methanol, a brown powder was obtained **C37_2** (70 mg, 27%). FTIR analysis: υ(O-H) = 3408 cm^{-1}, υ(N-H) = 3226 cm^{-1}, υ(C-H) = 2947 cm^{-1}, υ(C=N) = 1635 cm^{-1}, υ(C=C) = 1526-1303 cm^{-1}, υ(PF$_6^-$) = 839 cm^{-1}.

Synthesis of complex 38 [Fe(3,5-I-salpet)Ru(phen)$_2$(dppz)]•Cl•2PF$_6$ – To a solution of N-(2-aminoethyl)-1,3-propanediamine (0.025 mL, 0.2 mmol) in methanol (20 mL) 3,5-iodosalicylaldehyde (150 mg, 0.4 mmol) was added and left stirring and reflux for 45 min to give a yellow solution. Iron(III) chloride (32 mg, 0.2 mmol), [Ru(phen)2(dppz)] (151 mg, 0.2 mmol) and triethylamine (56 mg, 0.4 mmol) in methanol was added to the mixture and left stirring and reflux for 45 min. The solution was filtered left for evaporation and a brown powder was obtained (104 mg, 32%). FTIR analysis: υ(O-H) = 3422 cm^{-1}, υ(C-H) = 2919 cm^{-1}, υ(C=N) = 1621 cm^{-1}, υ(C=C) = 1563-1374 cm^{-1}, υ(PF$_6^-$) = 838 cm^{-1}.

Synthesis of complex 39 [Fe(3,5-F-salpet)Ru(phen)$_2$(dppz)]•Cl•2PF$_6$ – To a solution of N-(2-aminoethyl)-1,3-propanediamine (0.025 mL, 0.2 mmol) in methanol (20 mL) 3,5-fluorosalicylaldehyde (63 mg, 0.4 mmol) was added and left stirring and reflux for 45 min to give a yellow solution. Iron(III) chloride (32 mg, 0.2 mmol), [Ru(phen)2(dppz)] (151 mg, 0.2 mmol) and triethylamine (56 mg, 0.4 mmol) in methanol was added to the mixture and left stirring and reflux for 45 min. The solution was filtered left for evaporation of the solvent. When the solution had few amount of solvent (5 mL) add ethyl ether a dark brown powder had precipitated (57 mg, 23%). A solution in methanol is still evaporating. FTIR analysis: υ(O-H) = 3415 cm^{-1}, υ(N-H) = 3235 cm^{-1}, υ(C-H) = 2954 cm^{-1}, υ(C=N) = 1634 cm^{-1}, υ(C=C) = 1563-1301 cm^{-1}, υ(PF_6^-) = 832 cm^{-1}.

Synthesis of complex 40 [Fe(3-Br-5-Cl-salpet)Ru(phen)$_2$(dppz)]•Cl•2PF$_6$ – To a solution of N-(2-aminoethyl)-1,3-propanediamine (0.025 mL, 0.2 mmol) in methanol (20 mL) 3-bromo-5-chlorosalicylaldehyde (101 mg, 0.4 mmol) was added and left stirring and reflux for 45 min to give a yellow solution. Iron(III) chloride (32 mg, 0.2 mmol), [Ru(phen)2(dppz)] (151 mg, 0.2 mmol) and triethylamine (56 mg, 0.4 mmol) in methanol was added to the mixture and left stirring and reflux for 45 min. The solution was filtered left for evaporation and a brown powder was obtained (118 mg, 43%). A solution in methanol is still evaporating. FTIR analysis: υ(O-H) = 3415 cm^{-1}, υ(N-H) = 3234 cm^{-1}, υ(C-H) = 2919 cm^{-1}, υ(C=N) = 1627 cm^{-1}, υ(C=C) = 1514-1302 cm^{-1}, υ(PF_6^-) = 846 cm^{-1}.

Synthesis of complex 41 [Fe(5-Cl-3-I-salpet)Ru(phen)$_2$(dppz)]•Cl•2PF$_6$ – To a solution of N-(2-aminoethyl)-1,3-propanediamine (0.025 mL, 0.2 mmol) in methanol (20 mL) 5-chloro-3-iodosalicylaldehyde (113 mg, 0.4 mmol) was added and left stirring and reflux for 45 min to give a yellow solution. Iron(III) chloride (32 mg, 0.2 mmol), [Ru(phen)2(dppz)] (151 mg, 0.2 mmol) and triethylamine (56 mg, 0.4 mmol) in methanol was added to the mixture and left stirring and reflux for 45 min. The solution was filtered left for evaporation and a brown powder was obtained (82 mg, 28%). A solution in methanol is still evaporating. FTIR analysis: υ(O-H) = 3436 cm^{-1}, υ(C-H) =2934 cm^{-1}, υ(C=N) = 1621 cm^{-1}, υ(C=C) = 1508-1383 cm^{-1}, υ(PF_6^-) = 840 cm^{-1}.

4.2. Characterization

The Elemental Analyses were conducted at Faculty of Farmacy of University of Lisbon.

Balance: The balances were classic *Mettler Toledo* and analytic *Mettler Toledo* AE 100.
Fourier-transform infrared spectroscopy: Infrared spectra were obtained from KBr pellets using a *Nicolet FTIR* with 1 cm^{-1} resolution, between 400 cm^{-1} and 4000 cm^{-1}.
UV-vis spectroscopy: UV-vis spectra were collected in a *UV-1601-Visible spectrophotometer* from Shimadzer between 900-190 nm.
Crystal X-ray diffraction: Crystals suitable for single-crystal X-ray analysis were grown as described in the synthetic procedure. Selected crystals were covered with Fomblin (polyfluoroether oil) and mounted on a nylon loop. The data was collected at 296 K and 110 K on a *Bruker D8 Venture diffractometer* equipped with a Photon 100 detector and an Oxford Cryostem Cooler, using graphite monochromated Mo-Kα radiation (λ = 0.71073 Å). The data was processed using the APEX3 suite software package, which includes integration and scaling (SAINT), absorption corrections (SADABS) and space group determination (XPREP). Structure solution and refinement were done using direct methods with the programs SHELXS-14 inbuilt in APEX and WinGX-Version 2014.1 software packages. All nonhydrogen atoms were refined anisotropically and the hydrogen atoms were inserted in idealized positions and allowed to refine riding on the parent carbon atom. Amine hydrogen atoms were in difference Fourier peak and refined isotropically. The molecular diagrams were drawn with Mercury, included in the software package.
Powder X-ray diffraction: The measurements were performed using a *Philips Analytical Xray diffractometer* (PW 1730) with automatic data acquisition (APD Philips v3.6B), using Cu Kα radiation (λ = 0.15406 nm) and working at 40 kV/30 mA, in a continuous scan from 7.0080 to 59.9970 (2Θ°), with each step taking 80.0100 s and widening 0.0170 (2Θ°), at 298.15 K.
SQUID magnetometry: Magnetization measurements as a function of temperature were performed using a SQUID magnetometer (Quantum Design MPMS). The curves were obtained at 1000 Oe for temperatures ranging between 10 and 370 K, on cooling and heating modes, using a 5 K min^{-1} and 1 K min^{-1} scan rate. Settle mode was used for all temperatures stabilization. The collected data were corrected for diamagnetic contributions.
Nuclear Magnetic Resonance spectroscopy: RMN spectra were collected in *Bruker Advance* 400 MHz spectrometer in chloroform and DMSO.
Luminescence spectrometry: Fluorescence spectra were collected in *Horiba–Jobin–Yvon SPEX Fluorolog* 3.22 *spectrofluorometer*.

5. Bibliography

[1] D. J. Harding, W. Phonsri, P. Harding, I. A. Gass, K. S. Murray, B. Moubaraki, J. D. Cashion, L. Liu, S. G. Telfer, Chem. Commun.49 (**2013**) 6340-6342.

[2] P. Gütlich, A. B. Gaspar, Y. Garcia, Beilstein J. Org. Chem. 9 (**2013**) 342–391.

[3] P. N. Martinho, A. I. Vicente, S. Realista M. S. Saraiva, A. I. Melato, P. Brandão, L. P. Ferreira, M. D. Carvalho, J. Organomet. Chem. 760 (**2014**) 48-54.

[4] S.B. Erenburg, N.V. Bausk, L.G. Lavrenova, V.A. Varnek, L.N. Mazalov, Solid State Ionics 101 (**1997**) 571-577.

[5] Y. Garcia, P.J. van Koningsbruggen, R. Lapouyade, L. Fournes, L. Rabardel, O. Kahn, V. Ksenofontov, G. Levchenko, P. Gutlich, Chem. Mater. 10 (**1998**) 2426-2433.

[6] Y. Garcia, V. Niel, M.C. Munoz, J.A. Real, Top. Curr. Chem. 233 (**2004**) 229-257.

[7] M. Ruben, U. Ziener, J.M. Lehn, V. Ksenofontov, P. Gutlich, G.B.M. Vaughan, Chem. Eur. J. 11 (**2004**) 94-100.

[8] T. Kitazawa, Y. Gomi, M. Takahashi, M. Takeda, M. Enomoto, A. Miyazaki, T. Enoki, J. Mater. Chem. 6 (**1996**) 119-121.

[9] V. Niel, J.M. Martinez-Agudo, M.C. Munoz, A.B. Gaspar, J.A. Real, Inorg. Chem. 40 (**2001**) 3838.

[10] O. Roubeau, A. Colin, W. Schmitt, R. Clerac, Angew. Chem. Int. Ed. 43 (**2004**) 3283-3286.

[11] P. Grondin, O. Roubeau, M. Castro, H. Saadaoui, A. Colin, R. Clerac, Langmuir 26 (**2010**) 5184-5195.

[12] T. Fujigaya, D.L. Jiang, T. Aida, Chem. Asian J. 2 (**2007**) 106-113.

[13] Y. Galyametdinov, V. Ksenofontov, A. Prosvirin, I. Ovchinnikov, G. Ivanova, P. Gütlich, W. Haase, Angew. Chem. Int. Ed. 40 (**2001**) 4269-4271.

[14] Y. Bodenthin, G. Schwarz, Z. Tomkowicz, M. Lommel, T. Geue, W. Haase, H. Mohwald, U. Pietsch, D.G. Kurth, Coord. Chem. Rev. 253 (**2009**) 2414-2422.

[15] A.B. Gaspar, M. Seredyuk, R. Gutlich, Coord. Chem. Rev. 253 (**2009**) 2399-2413.

[16] E. Coronado, J.R. Galan-Mascaros, M. Monrabal-Capilla, J. Garcia-Martinez, P. Pardo-Ibanez, Adv. Mater. 19 (**2007**) 1359.

[17] T. Forestier, S. Mornet, N. Daro, T. Nishihara, S. Mouri, K. Tanaka, O. Fouche, E. Freysz, J.F. Letard, Chem. Commun. (**2008**) 4327-4329.

[18] F. Volatron, L. Catala, E. Riviere, A. Gloter, O. Stephan, T. Mallah, Inorg. Chem. 47 (**2008)** 6584-6586.

[19] I. Boldog, A.B. Gaspar, V. Martinez, P. Pardo-Ibanez, V. Ksenofontov, A. Bhattacharjee, P. Gutlich, J.A. Real, Angew. Chem. Int. Ed. 47 (**2008**) 6433-6437.

[20] P.N. Martinho, T. Lemma, B. Gildea, G. Picardi, H. Muller-Bunz, R.J. Forster, T.E. Keyes, G. Redmond, G.G. Morgan, Angew. Chem. Int. Ed. 51 (**2012**) 11995-11999.

[21] A. Ruaudelteixier, A. Barraud, P. Coronel, O. Kahn, Thin Solid Films 160 (**1988**) 107-115.

[22] P. Coronel, A. Barraud, R. Claude, O. Kahn, A. Ruaudelteixier, J. Zarembowitch, Journal of Chemical Society, Chem. Commun. (**1989**) 193-194.

[23] S. Cobo, G. Molnar, J.A. Real, A. Bousseksou, Angew. Chem. Int. Ed. 45 (**2006**) 5786-5789.

[24] M. Cavallini, I. Bergenti, S. Milita, G. Ruani, I. Salitros, Z.R. Qu, R. Chandrasekar, M. Ruben, Angew. Chem. Int. Ed. 47 (**2008**) 8596-8600.

[25] S. Floquet, S. Salunke, M. L. Boillot, R. Clément, K. Boukheddaden, E. Rivière, Chem. Mater. 14 (**2002**) 4164-4171.

[26] I. Nemec, R. Herchel, Z. Trávníček, Dalton Trans. 44 (**2015**) 4474–4484.

[27] M. A. Halcrow, Chem. Lett. 43 (**2014**) 1178-1188.

[28] Z. Y Li, J. W. Dai, Y. Shiota, K. Yoshizawa, S. Kanegawa, O. Sato, Chem. Eur. J. 19 (**2013**) 12948 – 12952.

[29] I. Šalitroš, N. T. Madhu, R. Boča, J. Pavlik, M. Ruben, Monatsh. Chem. 140 (**2009**) 695–733.

[30] C. E. Housecroft, A. G. Sharpe, Inorganic chemistry, Second Edition (**2005**), Pearson Education Limited, Essex (England).

[31] C. F. Sheu, S. M. Chen, G. H. Lee, Y. H. Liu, Y. S. Wen, J. J. Lee, Y. C. Chuang, Y. Wang, Eur. J. of Inorg. Chem. 5-6 (**2013**) 894-901.

[32] S. Brooker, Chem. Soc. Rev. 44 (**2015**) 2880—2892

[33] K. Dankhoff, B. Weber, Dalton Trans. 48 (**2019**) 15376–15380

[34] J. A. Real, A. B. Gaspar, M. C. Muñoz, Dalton Trans. 12 (**2005**) 2062-2079.

[35] M. G. Cowan, J. Olguën, S. Narayanaswamy, J. L. Tallon, S. Booker, J. Am. Chem. Soc. 134 (**2012**) 2892-2894.

[36] B. A. Warner, P. Sainctavit, M. Mannini, G. Poneti, R. Sessoli, P. Rosa, J. Phys. Chem. Lett. 4 (**2013**) 1546-1552.

[37] R. C. Stoufer, D. Busch, W. B. Hadley, J. Am. Chem. Soc. 83 (**1961**) 3732-3734.

[38] W. Klaeui, W. Eberspach, P. Guetlich, Inorg. Chem. 26 (**1987**) 3277-3982.

[39] A. Cannizzo, C. J. Milne, C. Consani, W. Gawelda, C. Bressler, F. V.Mourik, M. Chergui, Coord. Chem. Rev. 254 (**2010**) 2677-2686.

[40] O. Sato, Acc. Chem. Res. 36 (**2003**) 692-700.

[41] S. Decurtins, P. Gutlich, C. P. Kuhler, H. Spiering, A. Hauser, Chem. Phys. Lett. 105 (**1984**) 1-4.

[42] F.Prins, M. Monrabal-Capilla, E. A. Osorio, E. Coronado, H. S. J. V. D. Zant, Adv. Mater. 23 (**2011**) 1545-1549.

[43] C. Krüger, P. Augustín, L. Dlháň, J. Pavlik, J. Moncol', I. Nemec, R. Boča, F. Renz, Polyhedron 87 (**2015**) 194–201.

[44] Gütlich, P.; Goodwin, H. A., Top. Curr. Chem. 233 (**2004**) 1–47.

[45] P. Atkins, T. Overton, J. Rourke, M. Weller, F. Armstrong, M. Hagerman Shriver & Atkins' Inorganic Chemistry, Fifth Edition (**2010**) Oxford University Press, Great Britain.

[46] G. Chastanet, C. Desplanches, C. Baldé, P. Rosa, M. Marchivie, P. Guionneau, Chem2 2 (**2018**) 1-18

[47] F. F. Martins, A. Joseph, H. P. Diogo, M. E. M. Piedade, L. P. Ferreira, M. D. Carvalho, S. Barroso, M. J. Romão, M. J. Calhorda, P. N. Martinho, Eur. J. Inorg. Chem.(**2018**) 2976-2983

[48] D. J. Harding, P. Harding, and W. Phonsri, Coord. Chem. Rev. 313 (**2016**) 38-61

[49] M. L. Boillot, B. Weber, C. R. Chim. 21 (**2018**) 1-13

[50] D. J. Harding, D. Sertphon, P. Harding, K. S. Murray, B. Moubaraki, J. D. Cashion, H. Adams, Chem. Eur. J. 19 (**2013**) 1082-1090.

[51] A. Hensa, K. K. Rajak, RSC Adv. 5 (**2015**) 4219.

[52] P. Masárová, P. Zoufalý, J. Moncol, I. Nemec, J. Pavlik, M. Gembický, Z. Trávníček, R. Bočad, I. Šalitroš, New J. Chem. 39 (**2015**) 508.

[53] L. Pogány, B. Brachňaková, P. Masárová, J. Moncol, J. Pavlik, M. Gál, M. Mazúr, R. Herchel, I. Nemec, I. Šalitroš, Chem. Eur. J. 24 (**2018**) 5191 – 5203.

[54] J. Q. Liu, Z. D. Luo, Y. Pan, A. K. Singh, M. Trivedi, A. Kumar, Coord. Chem. Rev. 406 (**2020**) 213145.

[55] A. J. Moro , J. C. Lima, Radiation in Bioanalisys: Fluorescence Spectroscopy (Chapter 3), 8th volume (**2019**), Springer Nature Switzerland AG, Cham (Switzerland).

[56] C.J. Daly, J.C. McGrath, Pharmacol. Ther. 100 (**2003**) 101–118.

[57] C. Basu, S. Chowdhury, R. Banerjee, H. S. Evans, S. Mukherjee, Polyhedron 26 (**2007**) 3617–3624.

[58] J. C. B. Reyes, C.C. Vidyasagar, B. M. M. Flores, V. M. J. Pérez, J. Lumin. 195 (**2018**) 290–313.

[59] K. H. Chang, C. C. Huang, Y. H. Liu, Y. H. Hu, P. T. Chou, Y. C. Lin, Dalton Trans., 11 (**2004**) 1731–1738.

[60] A. P. Silva, D. B. Fox, T. S. Moody, S. M. Weir, Pure Appl. Chem. 73 (**2001**) 503–511.

[61] A.J. Parola, J. C. Lima, F. Pina, J. S. Melo, C. Soriano, E. G. España, R. Aucejo, J. Alvacón, Inorg. Chim. Acta 360 (**2007**) 1200–1208.

[62] K. Umezawa, Y. Nakamura, H. Makino, D. Citterio, K. Suzuki, J. Am. Chem. Soc. 130 (**2008**) 1550-1551.

[63] H. J. Kim, Supramol. Chem. II 8 (**2017**) 107-127.

[64] A. Loupy, B. Tchoubar, D. Astruc, Chem. Rev. 92 (**1992**) 1141-1165.

[65] K. Umezawa, A. Matsui, Y. Nakamura, D. Citterio, K. Suzuki, Chem. Eur. J. 15 (**2009**) 1096 – 1106.

[66] R. Weissleder, Nat. Biotechnol. 19 (**2001**) 316-317.

[67] A. Burghart, H. J. Kim, M. B. Welch, L. H. Thoresen, J. Reibenspies, K. Burgess, F. Bergstrom, L.B. A. Johansson, J. Org. Chem. 64 (**1999**) 7813-7819.

[68] K. Yamada, T. Toyota, K. Takakura, M. Ishimaru, T. Sugawara, New J. Chem. 25 (**2001**) 667-669.

[69] G. Sathyamoorthi, M. L. Soong, T. W. Ross, J. H. Boyer, Heteroat. Chem. 4 (**1993**) 603-608.

[70] J. Killoran, L. Allen, J. F. Gallagher, W. M. Gallagher, D. F. O'Shea, Chem. Commun. (**2002**) 1862-1863.

[71] A. Gorman, J. Killoran, C. O'Shea, T. Kenna, W. M. Gallagher, D. F. O'Shea, J. Am. Chem. Soc. 126 (**2004**) 10619-10631.

[72] J. Chen, A. Burghart, A. D. Kovacs, K. J. Burgess, J. Org. Chem. 65 (**2000**) 2900-2906.

[73] W. L. Zhao, E. M. Carreira, Angew. Chem. Int. Ed. 44 (**2005**) 1677-1679.

[74] W. L. Zhao, E. M. Carreira, Chem. Eur. J. 12 (**2006**) 7254-7263.

[75] K. Rurack, M. Kollmannsberger, J. Daub, Angew. Chem. Int. Ed. 40 (**2001**) 385-387.

[76] S. Atilgan, Z. Ekmekci, A. L. Dogan, D. Guc, E. U. Akkaya, Chem. Commun. (**2006**) 4398-4400.

[77] M. Wada, S. Ito, H. Uno, T. Murashima, N. Ono, T. Urano, Y. Urano, Tetrahedron Lett. 42 (**2001**) 6711-6713.

[78] Z. Shen, H. Rohr, K. Rurack, H. Uno, M. Spieles, B. Schulz, G. Reck,N. Ono, Chem. Eur. J. 10 (**2004**) 4853-4871.

[79] S. Goeb, R. Ziessel, Org. Lett. 9 (**2007**) 737-740.

[80] D. L. Ma, V. P. Y. Ma, D. S. H. Chan, K. H. Leung, H. Z. He, C. H. Leung, Coord. Chem. Rev. 256 (**2012**) 3087– 3113

[81] K. K. W. Lo, S. P. Y. Li, RSC Adv. 4 (**2014**) 10560–10585

[82] O. Penon, A. J. Moro, D. Santucci, D. B. Amabilino, J. C. Lima, L. P. García, L. Rodríguez, Inorg. Chim. Acta 417 (**2014**) 222–229

[83] V. Balzani, G. Bergamini, F. Marchioni, P. Ceroni, Coord. Chem. Rev. 250 (**2006**) 1254-1266.

[84] M. Hardy, D. Konetski, C. Bowman, N. Devaraj, Org. Biomol. Chem. 14 (**2016**) 5555-5558.

[85] V. W. W. Yam, K. M. C. Wong, Chem. Commun. 47 (**2011**) 11579–11592.

[86] R. Huang, J. S. Ward, N. A. Kukhta, J. Avó, J. Gibson, T. Penfold, J. C. Lima, A. S. Batsanov, M. N. Berberan-Santos, M. R. Bryce, F. B. Dias, J. Mater. Chem. C 6 (**2018**) 9238—9247

[87] C. R. Mayer, E. Dumas, F. Secheresse, Chem. Commun. (**2005**) 345–347

[88] S. Arounaguiri, D. Easwaramoorthy, A. Ashokkumar, A. Dattagupta, B. G. Maiya, Indian Acad. Sci. 112 (**2000**) 1–17.

[89] S. T. Zhang, P. Li, C. Liao, T. Luo, X. Kou, D. Xiao, Spectrochim. Acta Part A 201 (**2018**) 161–169.

[90] N.W. Kreofsky, M. D. Dillenburg, E. M. Villa, J. T. Fletcher, Polyhedron 177 (**2020**) 114259.

[91] T. J. Younts, J. Undergraduate Mater. Res. (**2008**).

[92] R. M. Hartshorn, J. K. Barton, J. Am. Chem. Soc. 114 (**1992**) 5919-5925.

[93] C.M. Quintero, G. Félix, I. Suleimanov, J. Sánchez Costa, G. Molnár, L. Salmon, W. Nicolazzi, A. Bousseksou, Beilstein J. Nanotechnol. 5 (**2014**) 2230–2239.

[94] I.cA. Guraliskiy, V. A. Reshetnikov, A. Szebesczyk, E. Gumienna-Kontecka, A. I. Marynin, S. I. Shylin, V. Ksenofontov, I. O. Fritsky, J. Mater. Chem. C 3 (**2015**) 4737–4741.

[95] K. S. Kumar, M. Ruben, Coord. Chem. Rev. 346 (**2017**) 176–205

[96] H.J. Shepherd, C.M. Quintero, G. Moln_ar, L. Salmon, A. Bousseksou, Spin-crossover Materials (**2013**) M.A. Halcrow (Editor) John Wiley & Sons, Chichester, 347-373.

[97] C. D. S. Brites, P. P. Lima, N. J. O. Silva, A. Millan, V. S. Amaral, F. Palacio, L. D. Carlos, Nanoscale 4 (**2012**) 4799-4829.

[98] O. Kraieva, C. M. Quintero, I. Suleimanov, E. M. Hernandez, D. Lagrange, L. Salmon, W. Nicolazzi, G. Molnar, C. Bergaud, A. Bousseksou, Small 12 (**2016**) 6325-6331.

[99] L. Salmon, G. Molnar, D. Zitouni, C. Quintero, C. Bergaud, J. C. Micheau, A. Bousseksou, J. Mater. Chem. 20 (**2010**) 5499.

[100] U. R. Genger, M. Grabolle, S. C. Jaricot, R. Nitschke, T. Nann, Nat. Methods 5 (**2008**) 763-775.

[101] A. Mayer, S. Neuenhofer, Angew. Chem. Int. Ed. England 33 (**1994**) 1044-1072.

[102] M. S. Gruzdev, V. E. Vorobeva, E. M. Zueva, U. V. Chervonova, M. M. Petrova, N. E. Domrachev, Polyhedron 155 (**2018**) 415–424.

[103] A. I. Vicente, X. Wu, Y. Ortin, L. P. Ferreira, M. D. Carvalho, S. Realista, A. Barker, G. G. Morgan, N. Galamba, P. J. Costa, M. J. Calhorda, P. N. Martinho, Dalton Trans. 13 (**2019**) 4239-4247.

[104] R. Pritchard, S. A. Barrett, C. A. Kilne, M. A. Halcrow, Dalton Trans. 24 (**2008**) 3159-3168.

[105] Guionneau, P.; Marchivie, M.; Bravic, G.; Letard, J. F.; Chasseau, D., Top. Curr. Chem. 234 (**2004**) 97-128.

[106] P. N. Martinho, Cooperatively operating hierarchically organized materials for spintronics, PhD thesis (**2010**).

A. Annex section

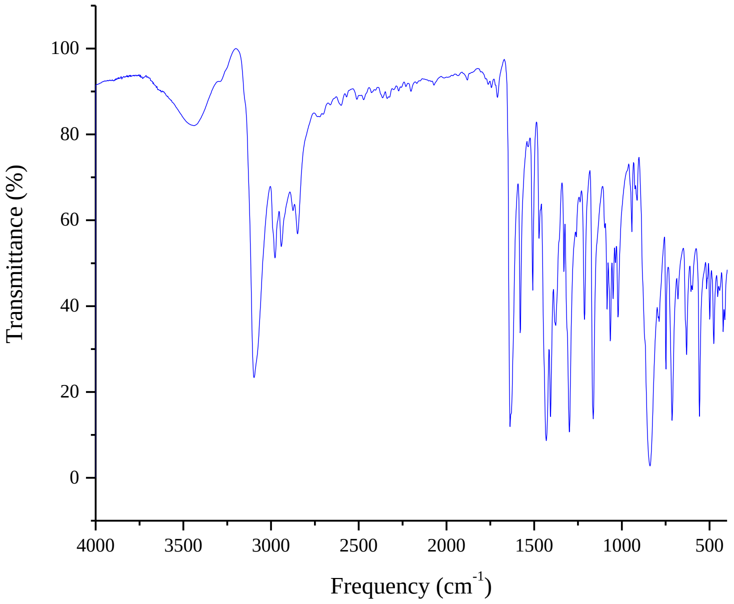

Figure A.1 FTIR spectrum of **C2.**

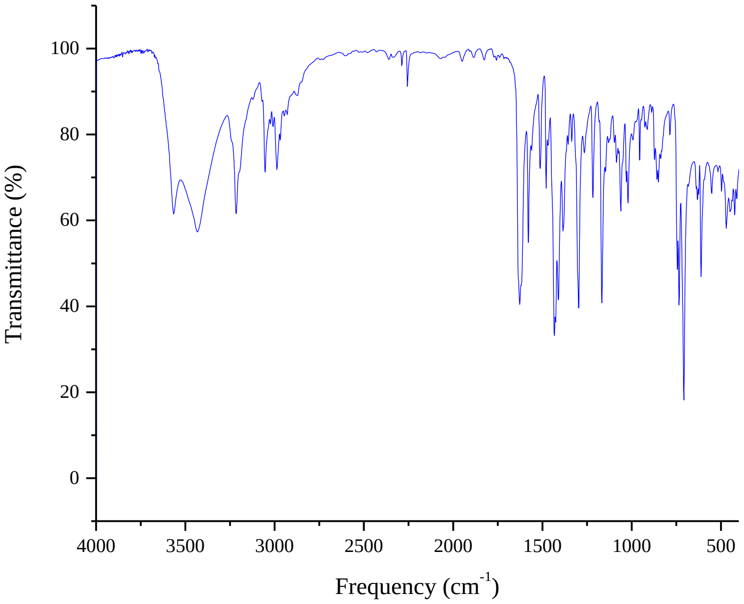

Figure A.2 FTIR spectrum of **C3.**

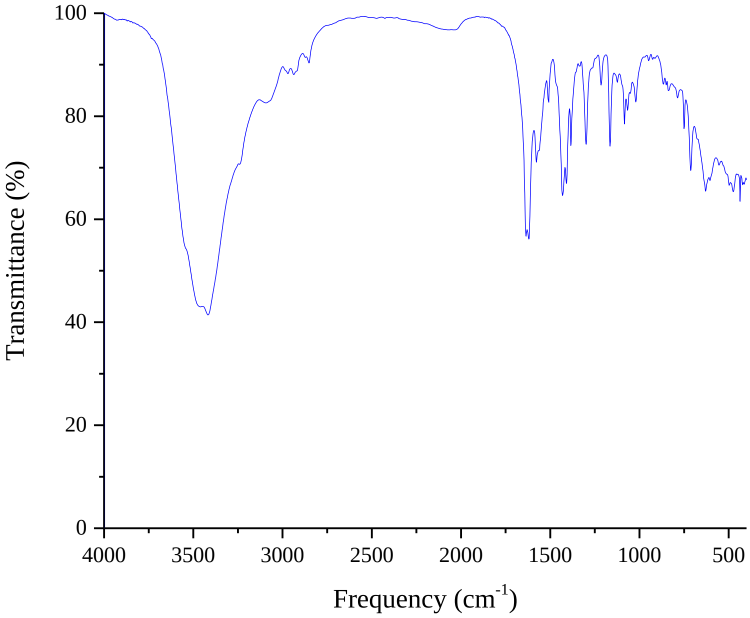

Figure A.3 FTIR spectrum of **C4**.

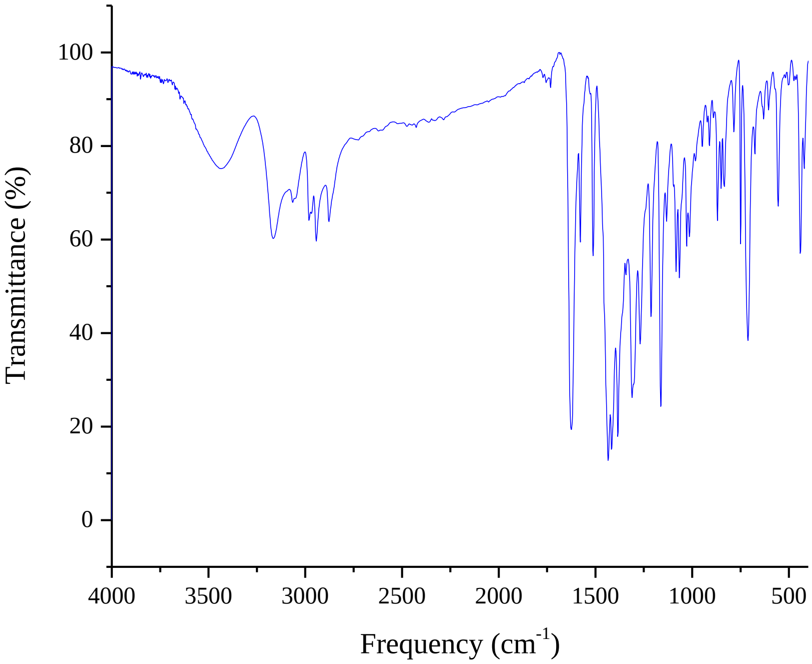

Figure A.4 FTIR spectrum of **C5**.

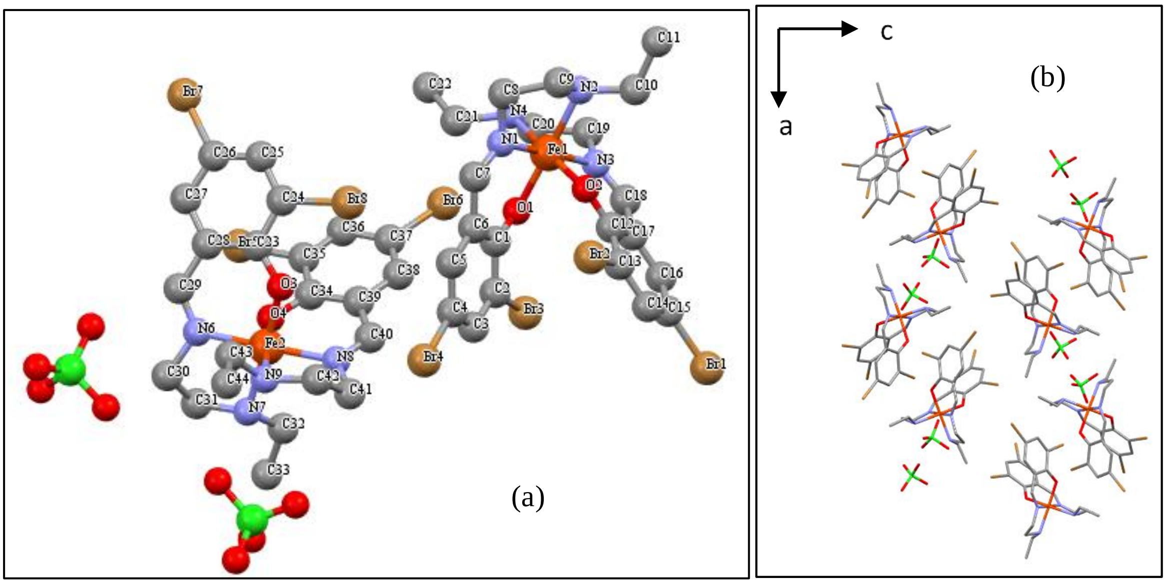

Figure A.5 X-ray crystal structure of **C1**, at 296 K: (a) asymmetric unit; (b) unit cell.

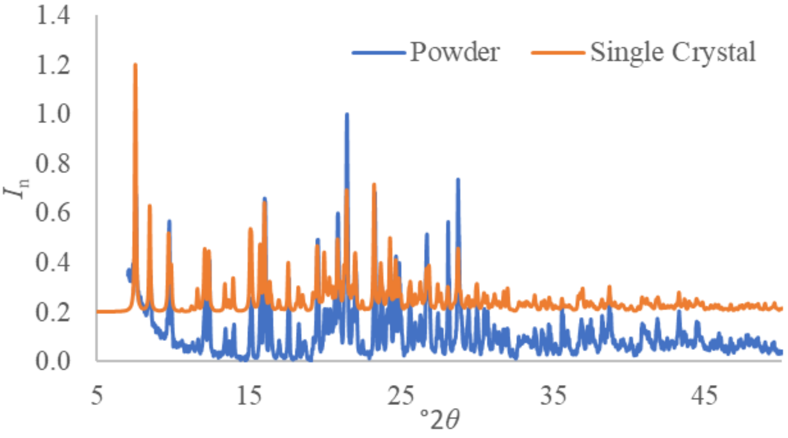

Figure A.6 Single Crystal and powder X-ray diffractogram of **C3•H$_2$O•CH$_3$CN**.

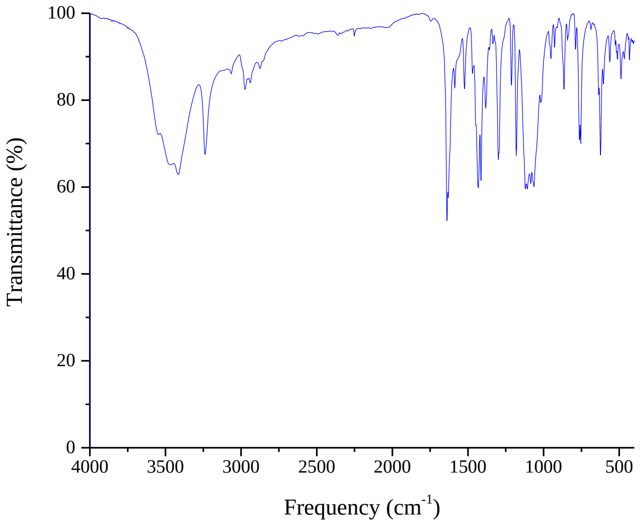

Figure A.7 FTIR spectrum of **C6**.

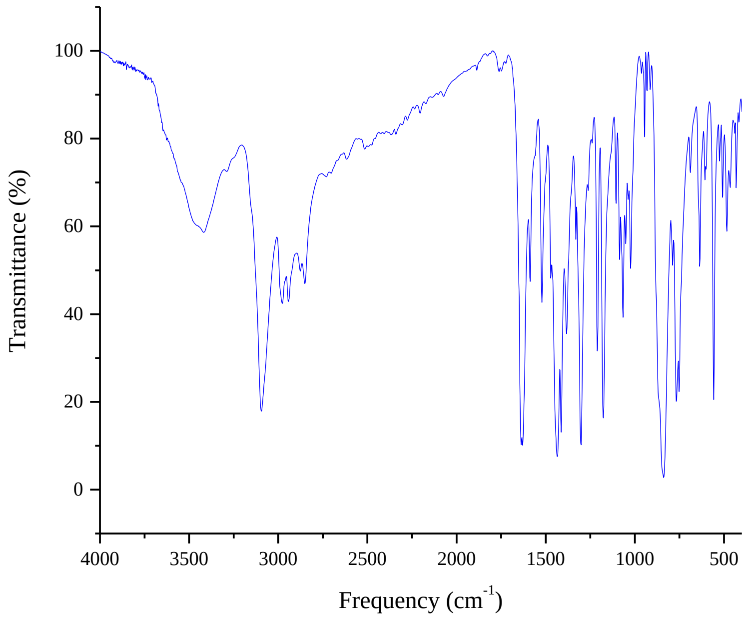

Figure A.8 FTIR spectrum of **C7**.

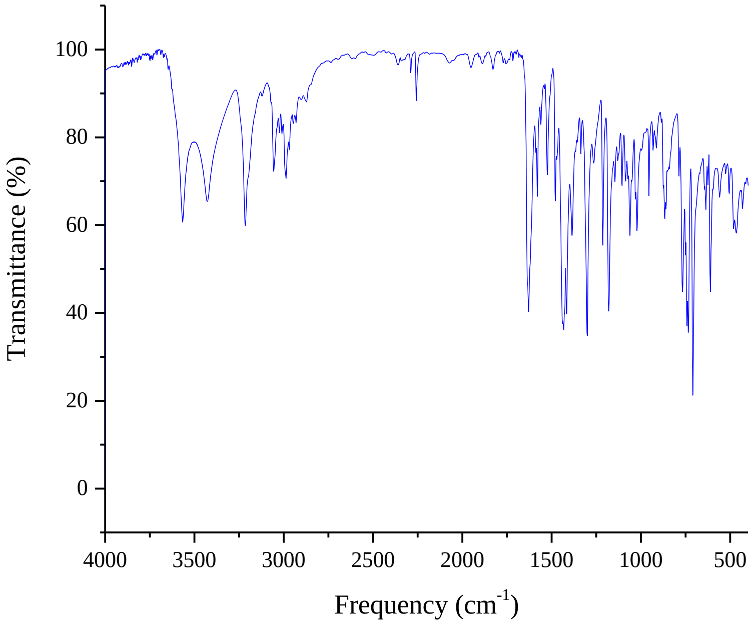

Figure A.9 FTIR spectrum of **C8**.

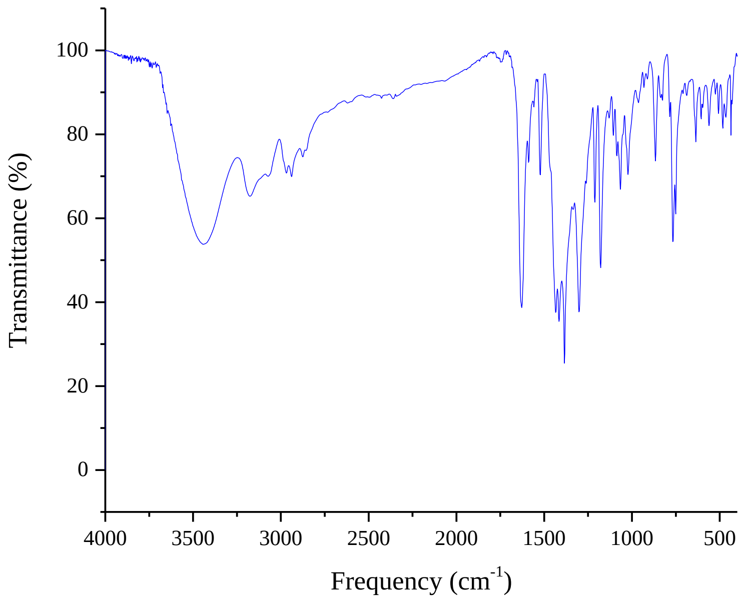

Figure A.10 FTIR spectrum of **C9**.

Table A.1 Crystal data and structure refinement of **C6** and **C8•H$_2$O•CH$_3$CN**.

Complex	**C6**		**C8•H$_2$O•CH$_3$CN**	
Temperature	110(2) K		296(2) K	
Crystal system	Monoclinic		Monoclinic	
Space group	C 2/c		P 21/c	
Unit cell dimensions	a = 21.096(7) Å	α= 90°	a = 17.217(8) Å	α= 90°
	b = 11.355(4) Å	β= 105.974(7)°	b = 15.145(7) Å	β= 104.621(19)°
	c = 26.769(8) Å	γ = 90°	c = 18.999(11) Å	γ = 90°
Volume	6165(3) Å^3		4794(4) Å^3	
Z	8		4	
Goodness-of-fit on F^2	1.026		1.021	
Final R indices [I>2sigma(l)]	R1 = 0.1165	wR2 = 0.2957	R1 = 0.0520	wR2 = 0.0923
R indices (all data)	R1 = 0.2022	wR2 = 0.3396	R1 = 0.1270	wR2 = 0.1065

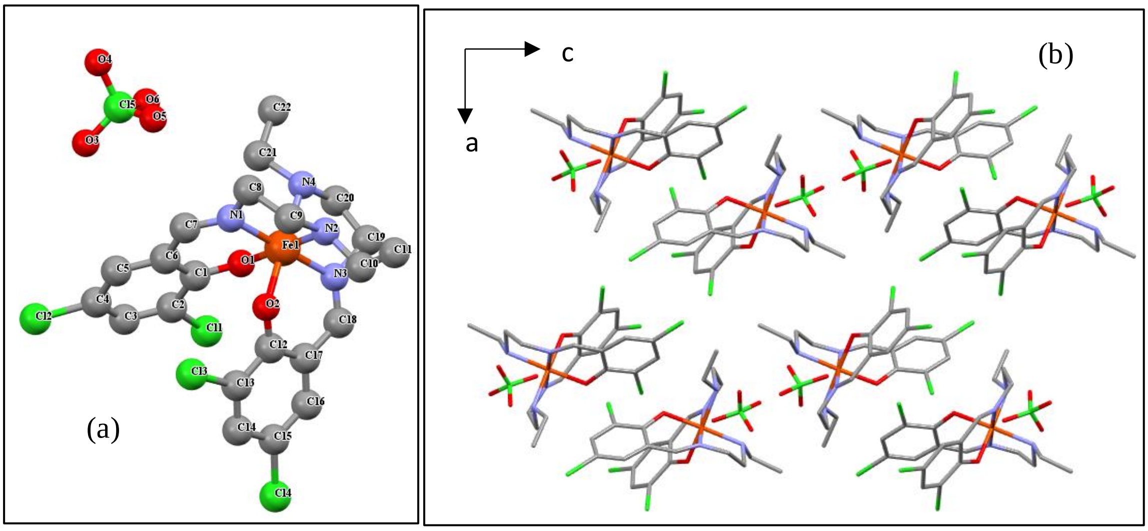

Figure A.11 X-ray crystal structure of **C6**, at 110 K: (a) asymmetric unit; (b) unit cell.

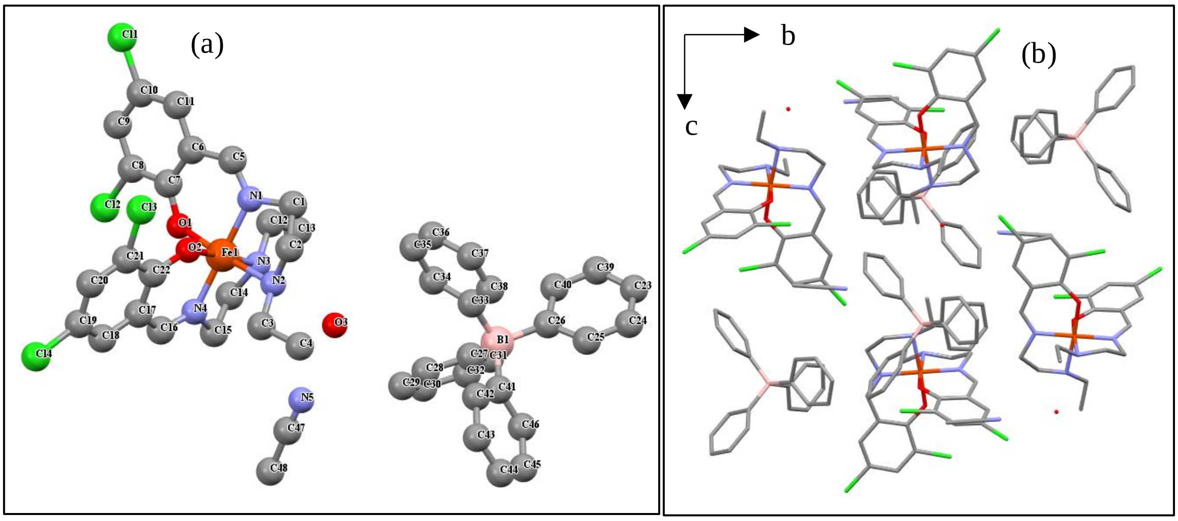

Figure A.12 X-ray crystal structure of **$C8\bullet H_2O\bullet CH_3CN$**, at 296 K: (a) asymmetric unit; (b) unit cell.

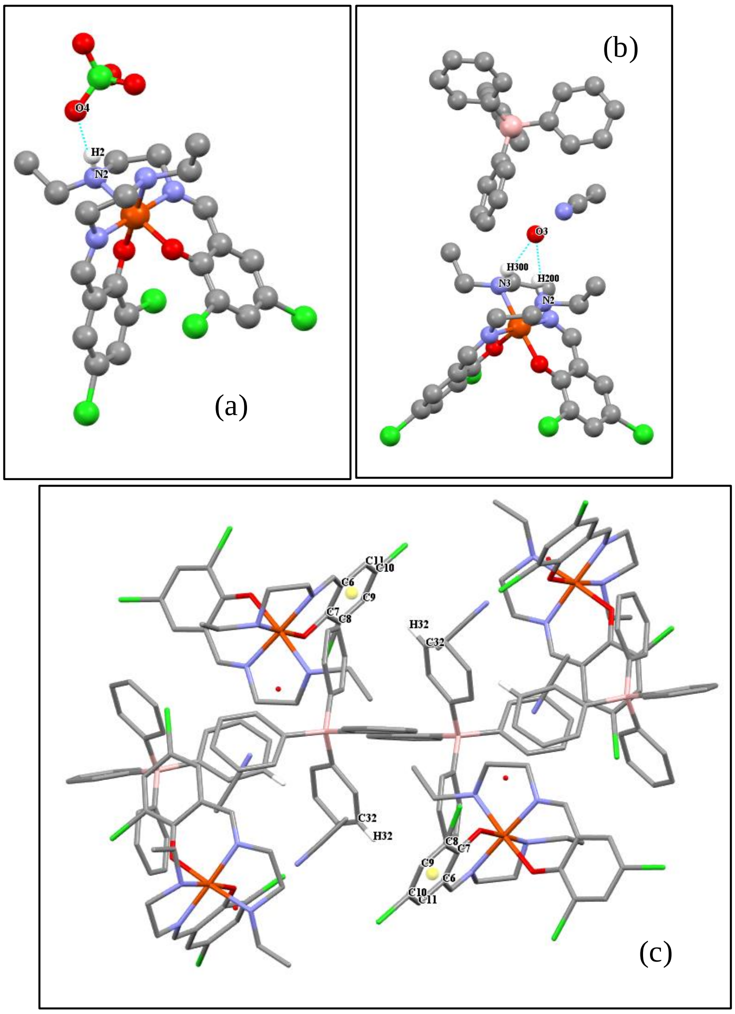

Figure A.13 Hydrogen bonds in the X-ray single crystal structure: (a) **C6** and (b) **$C8\bullet H_2O\bullet CH_3CN$**; C-H···π (c) **C8•H2O•CH3CN**.

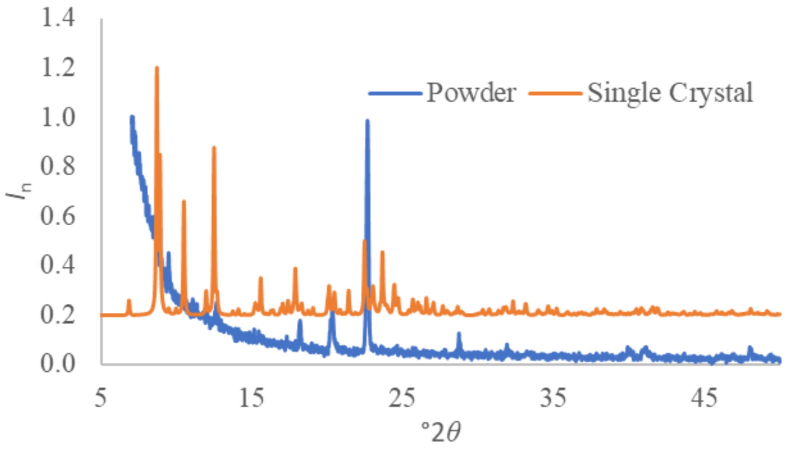

Figure A.14 Single Crystal and powder X-ray diffractogram of **C6**.

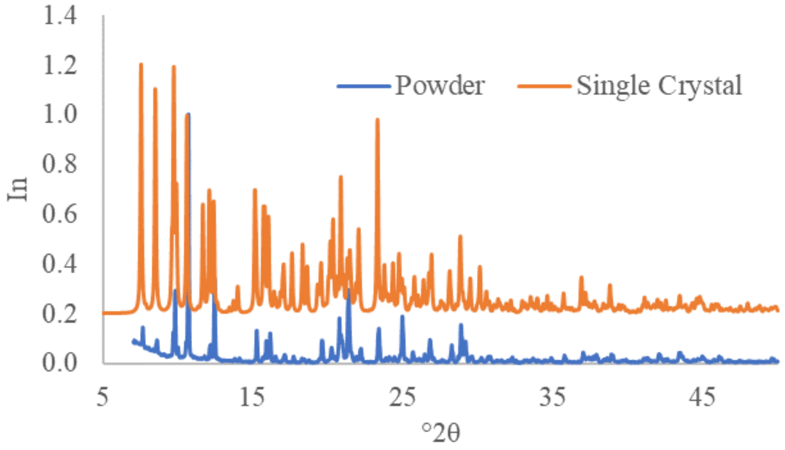

Figure A.15 Single Crystal and powder X-ray diffractogram of **C8•H$_2$O•CH$_3$CN**.

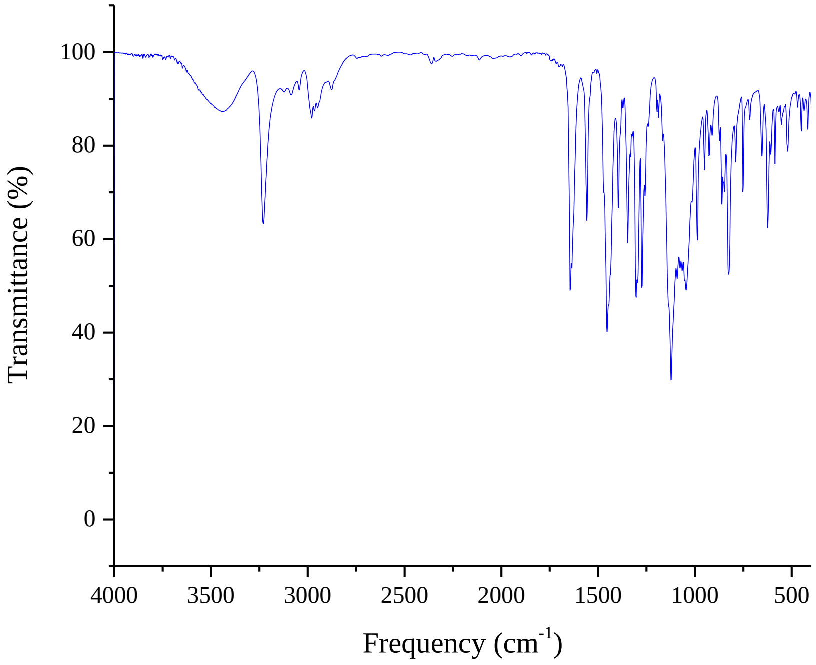

Figure A.16 FTIR spectrum of **C10**.

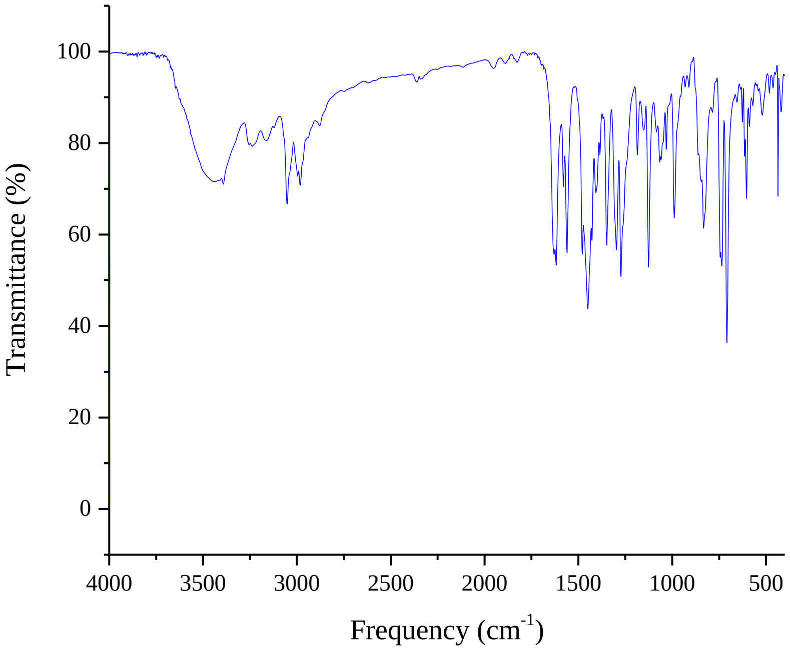

Figure A.17 FTIR spectrum of **C12_1**.

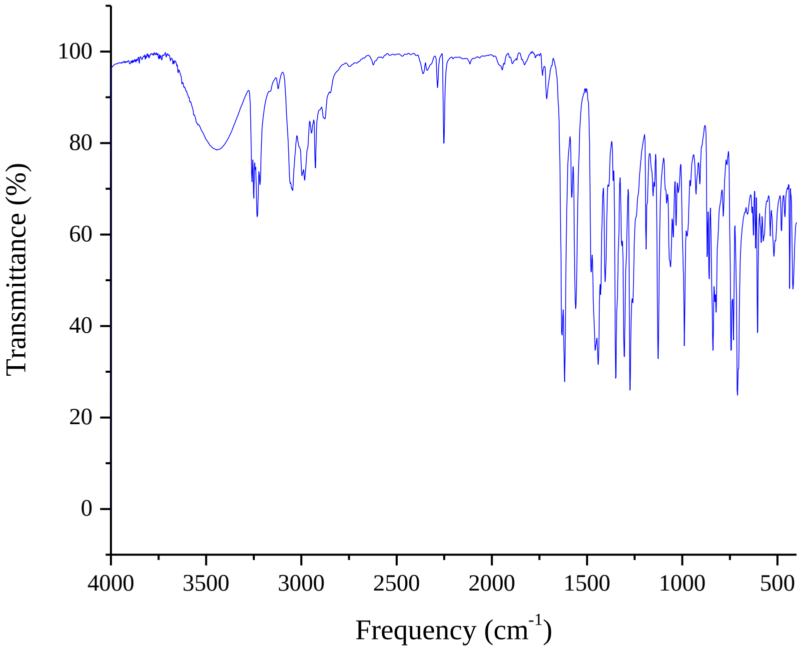

Figure A.18 FTIR spectrum of **C12_2**.

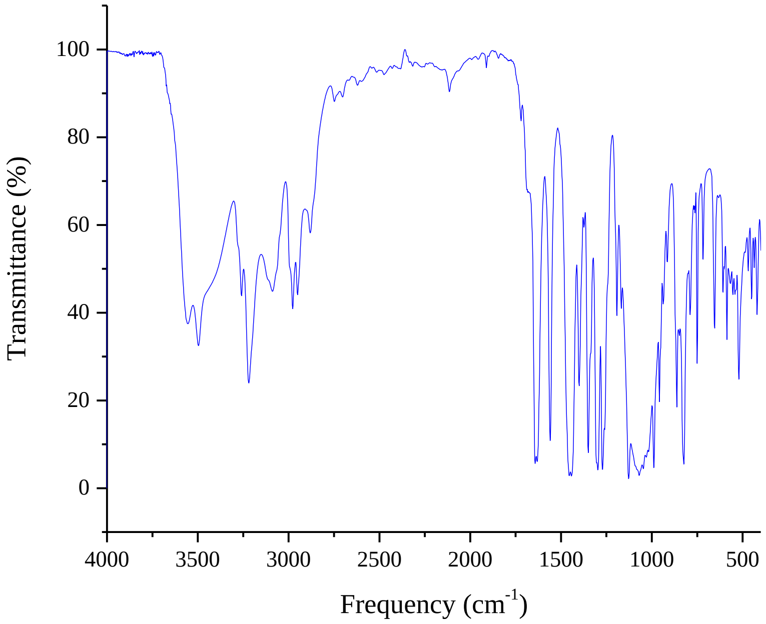

Figure A.19 FTIR spectrum of **C13**.

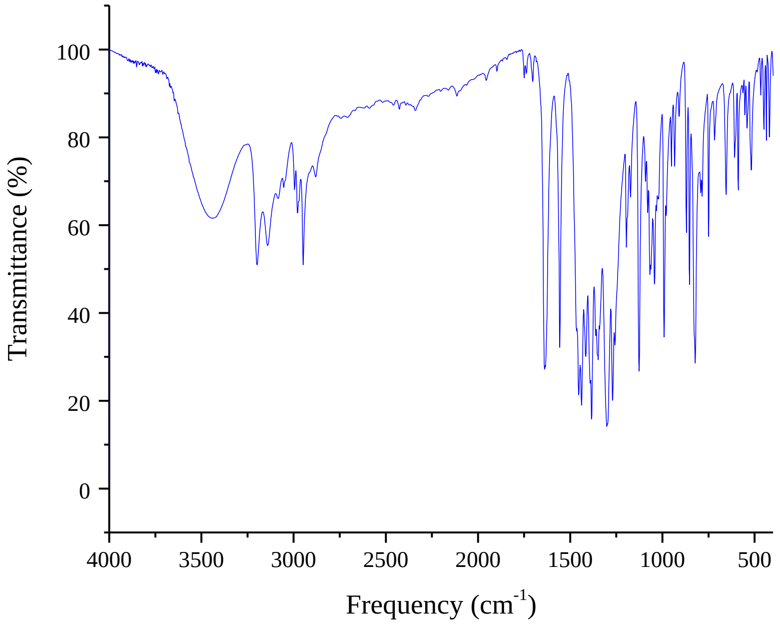

Figure A.20 FTIR spectrum of **C14**

Table A.2 Crystal data and structure refinement of **C10-C12_2•CH_3CN** and **C14**.

Complex	**C10**	**C11**	**C12•H_2O•MeOH**	**C12•CH_3CN**	**C14**
Temperature	196(2) K	296(2) K	296(2) K	296(2) K	296(2) K
Crystal system	Orthorhombic	Orthorhombic	Monoclinic	Orthorhombic	Triclinic
Space group	P b c a	P b c a	P 21/c	P 21 21 21	P -1
Unit cell dimensions	a = 11.2363(11) Å	a = 11.346(5) Å	a = 14.645(2) Å	a = 13.8147(5) Å	a = 9.7951(16) Å
	b = 15.3185(14) Å	b = 15.679(7) Å	b = 19.438(3) Å	b = 15.8096(6) Å	b = 10.3328(16) Å
	c = 30.177(3) Å	c = 30.611(14) Å	c = 16.515(2) Å	c = 20.4276(8) Å	c = 14.223(2) Å
	α= 90°	α= 90°	α= 90°	α= 90°	α= 108.806(4)°
	β= 90°	β= 90°	β= 106.233(5)°	β= 90°	β= 93.183(4)°
	γ = 90°	γ = 90°	γ = 90°	γ = 90°	γ = 112.831 (4)°
Volume	5194.1(8) Å^3	5445(4) Å^3	4513.8(13) Å^3	4461.5(3) Å^3	1228.7(3) Å^3
Z	8	8	4	4	2
Goodness-of-fit on F^2	1.057	1.161	1.103	1.037	1.023
Final R indices [I>2sigma(I)]	R1 = 0.0604	R1 = 0.0974	R1 = 0.0816	R1 = 0.0502	R1 = 0.0912
	wR2 = 0.1877	wR2 = 0.1675	wR2 = 0.2208	wR2 = 0.1088	wR2 = 0.1538
R indices (all data)	R1 = 0.0855	R1 = 0.1390	R1 = 0.1277	R1 = 0.0923	R1 = 0.2060
	wR2 = 0.2022	wR2 = 0.1796	wR2 = 0.2438	wR2 = 0.1209	wR2 = 0.1791

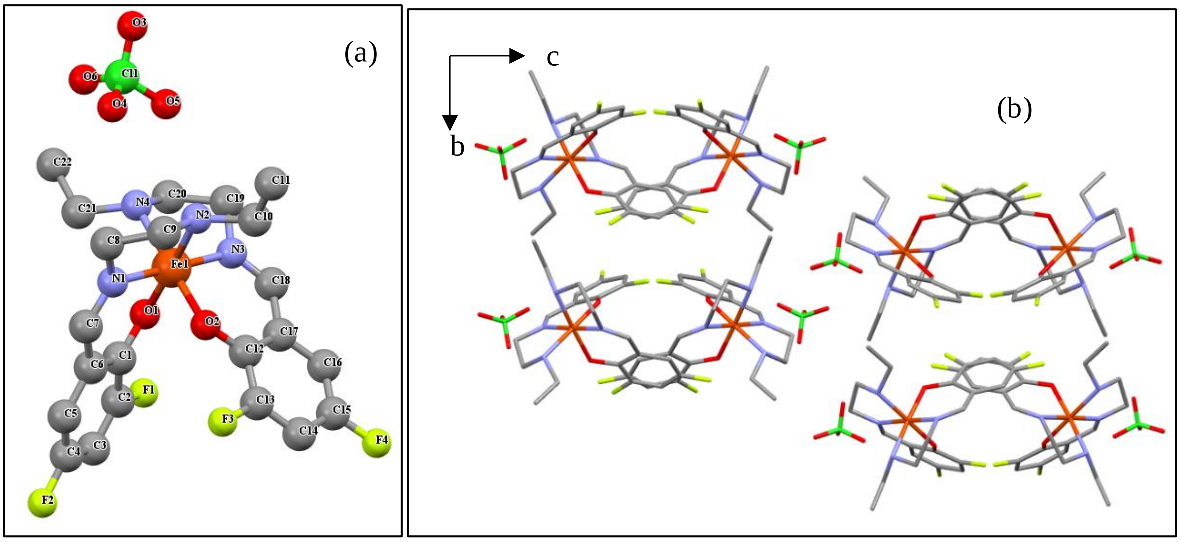

Figure A.21 X-ray crystal structure of **C10**, at 296 K: (a) asymmetric unit; (b) unit cell.

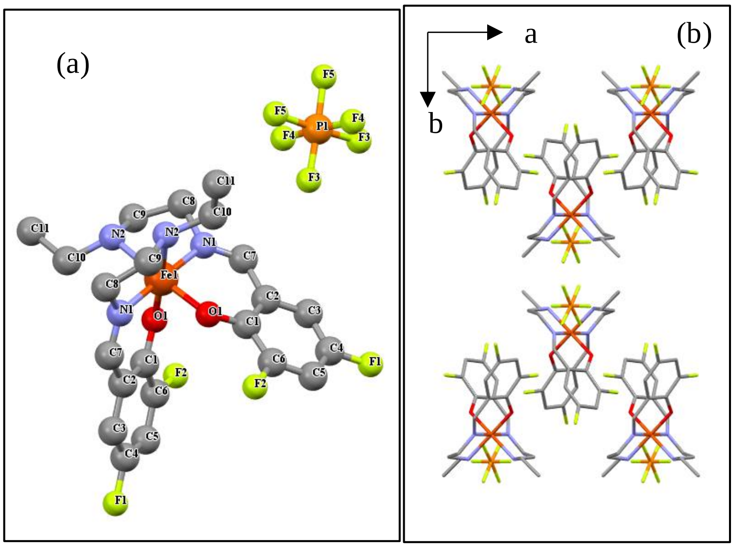

Figure A.22 X-ray crystal structure of **C11**, at 296 K: (a) asymmetric unit; (b) unit cell.

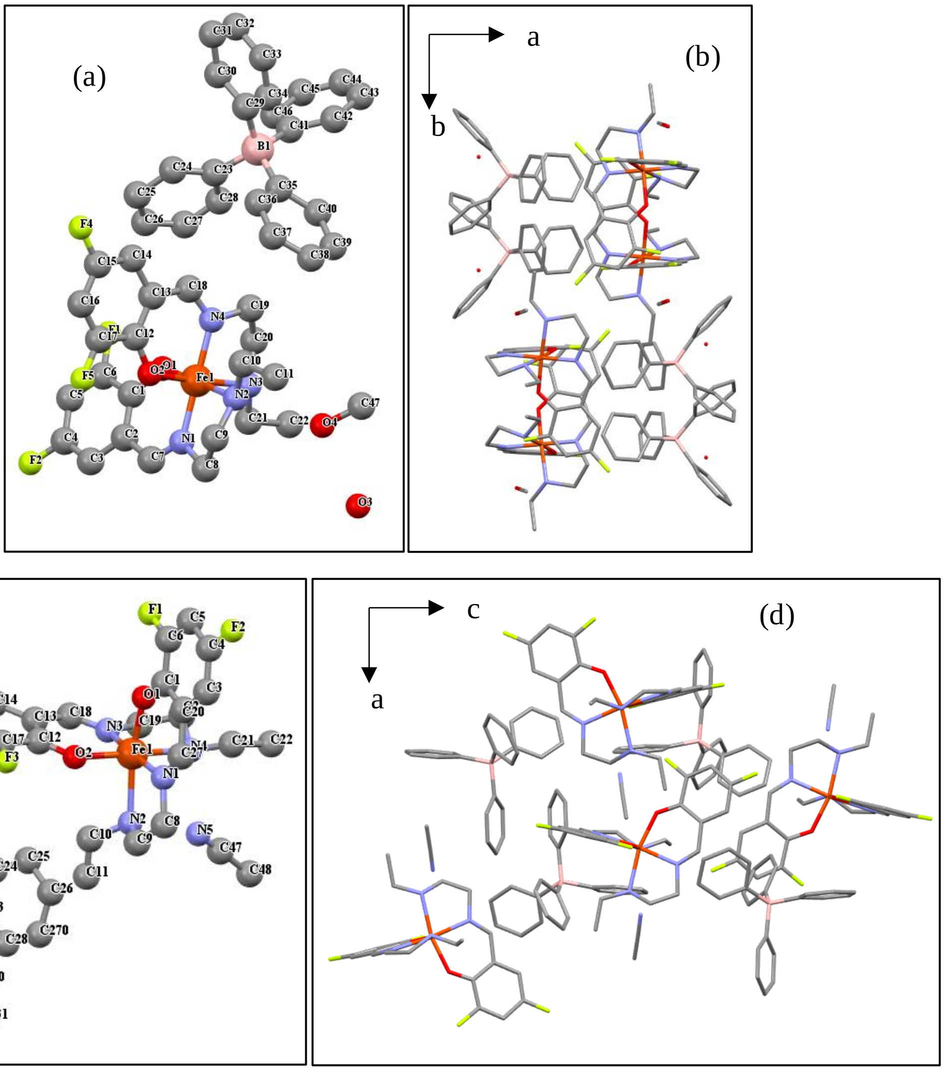

Figure A.23 X-ray crystal structure of **C12_1•H_2O•MeOH** and **C12_2•CH_3CN**, at 296 K: (a) (c) asymmetric unit; (b) (d) unit cell.

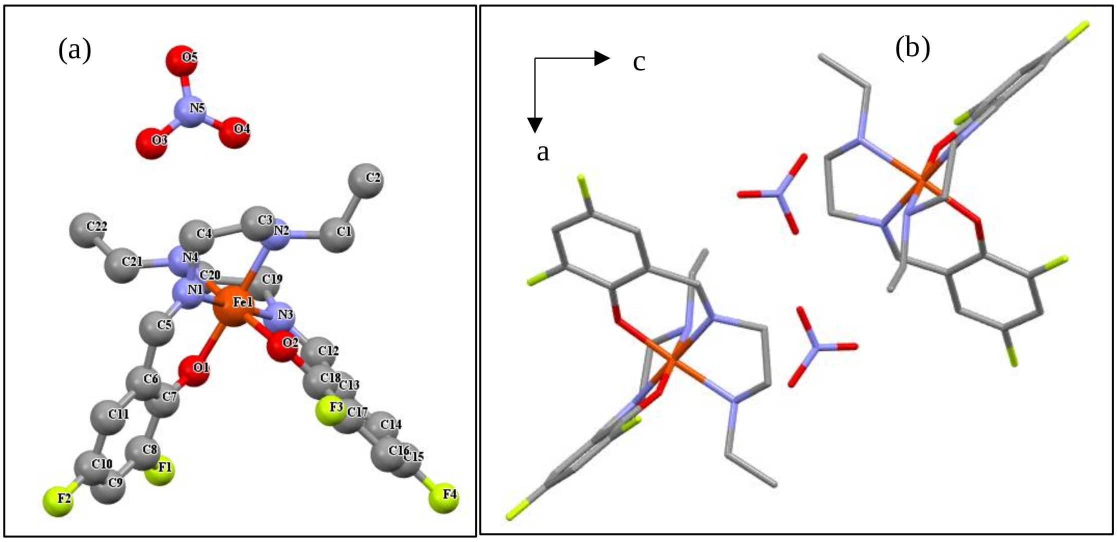

Figure A.24 X-ray crystal structure of **C14**, at 296 K: (a) asymmetric unit; (b) unit cell.

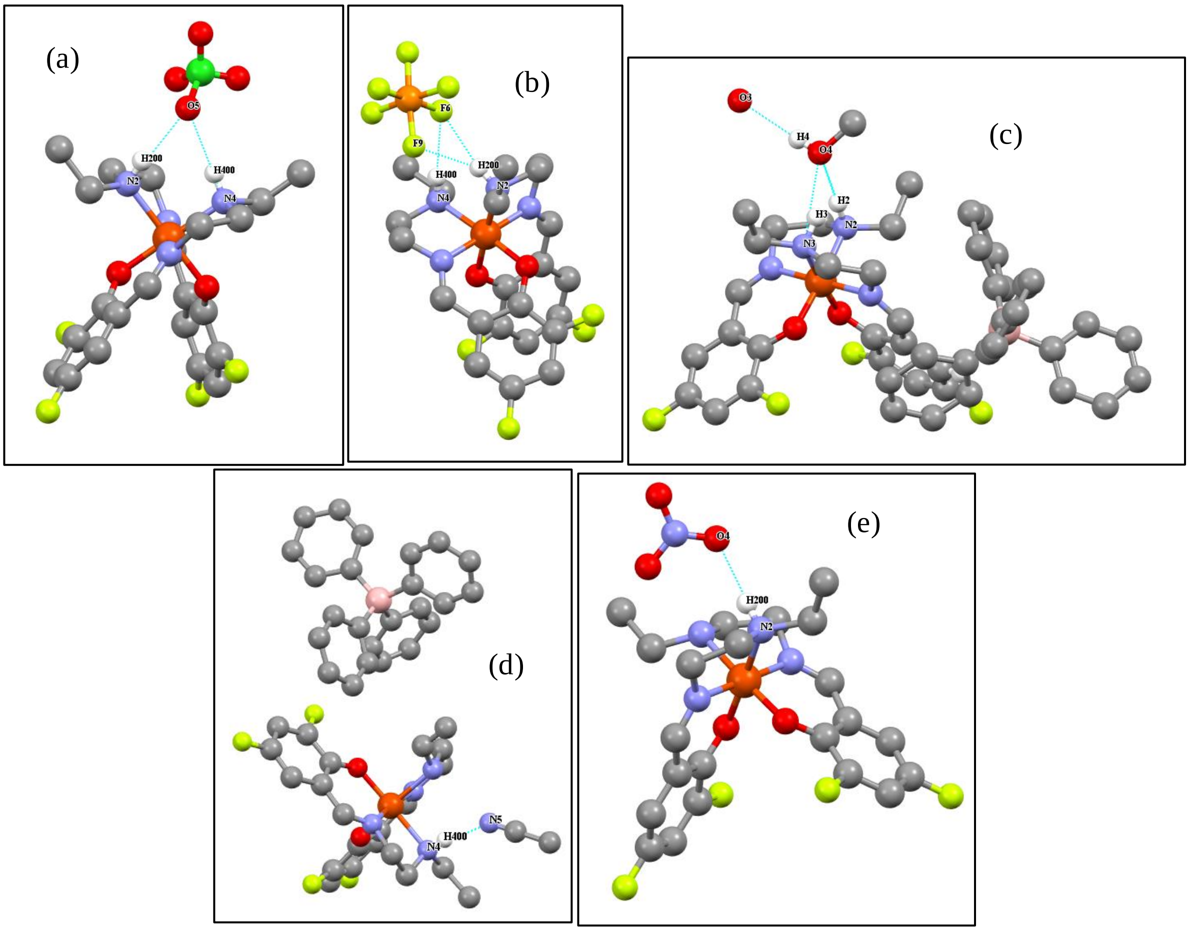

Figure A.25 Hydrogen bonds in the X-ray single crystal structure: (a) **C10;** (b) **C11**; (c) **C12_1•H_2O•MeOH**; (d) **C12_2•CH_3CN** and (e) **C14**.

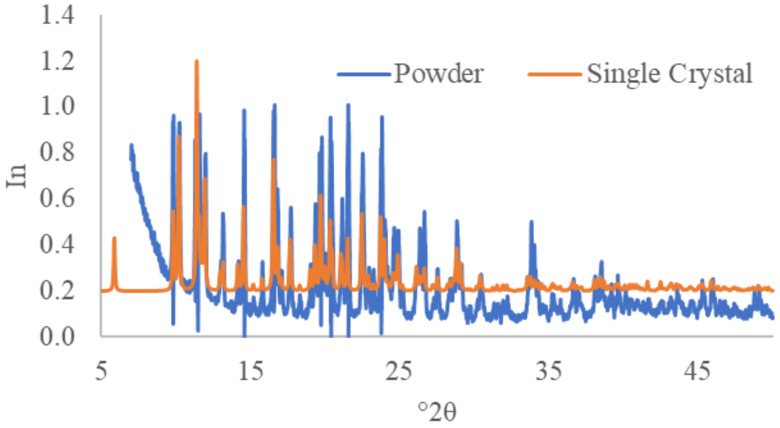

Figure A.26 Single Crystal and powder X-ray diffractogram of **C10.**

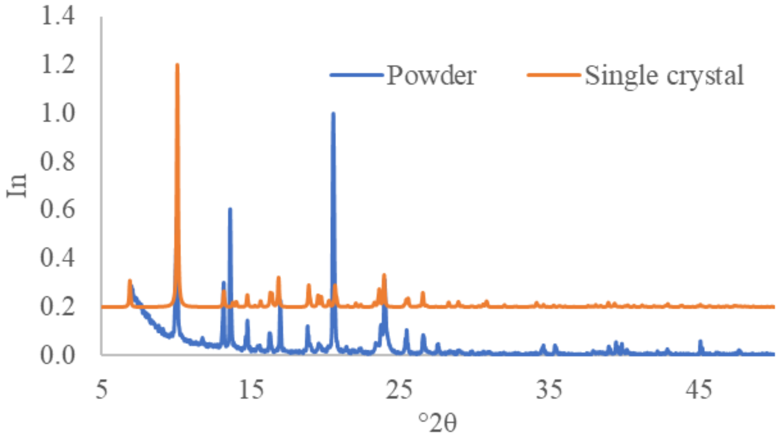

Figure A.27 Single Crystal and powder X-ray diffractogram of **C11.**

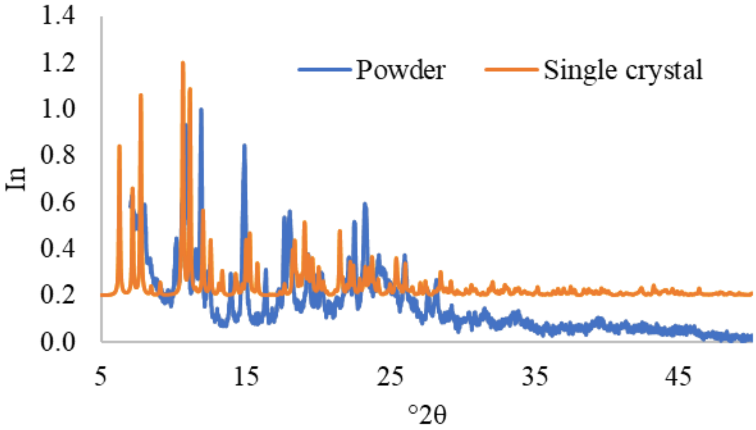

Figure A.28 Single Crystal and powder X-ray diffractogram of **C12_1•H_2O•MeOH.**

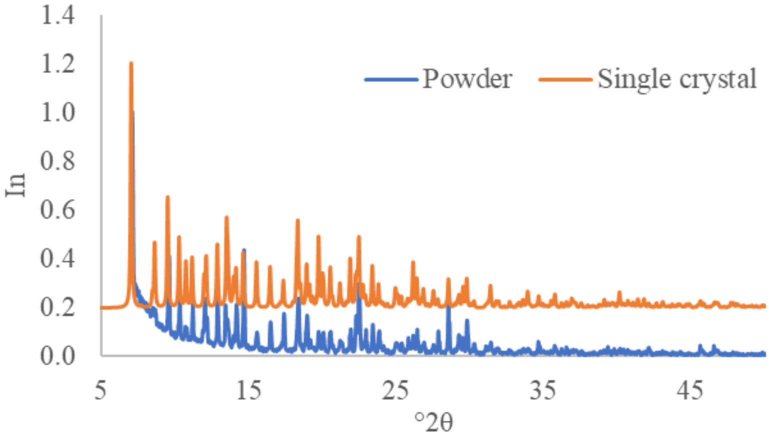

Figure A.29 Single Crystal and powder X-ray diffractogram of **C12_2•CH_3CN.**

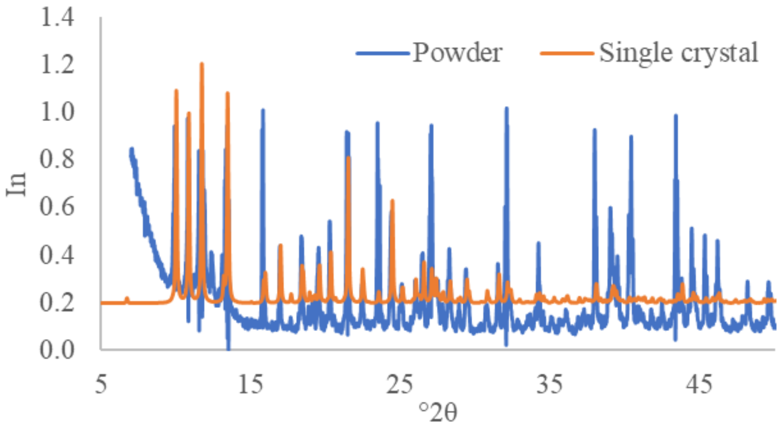

Figure A.30 Single Crystal and powder X-ray diffractogram of **C14.**

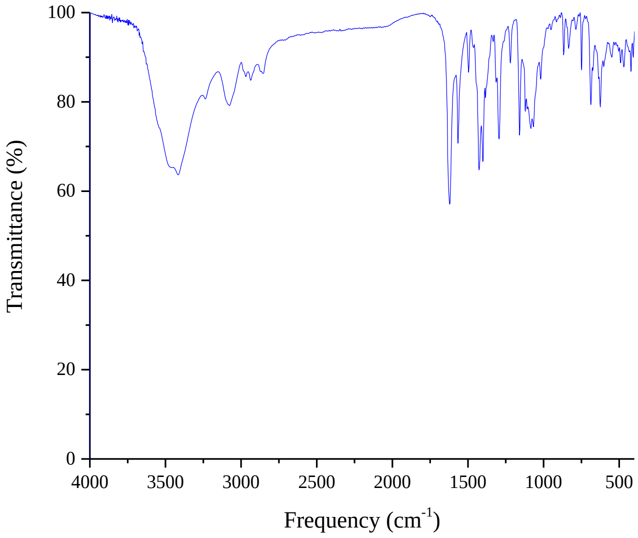

Figure A.31 FTIR spectrum of **C15.**

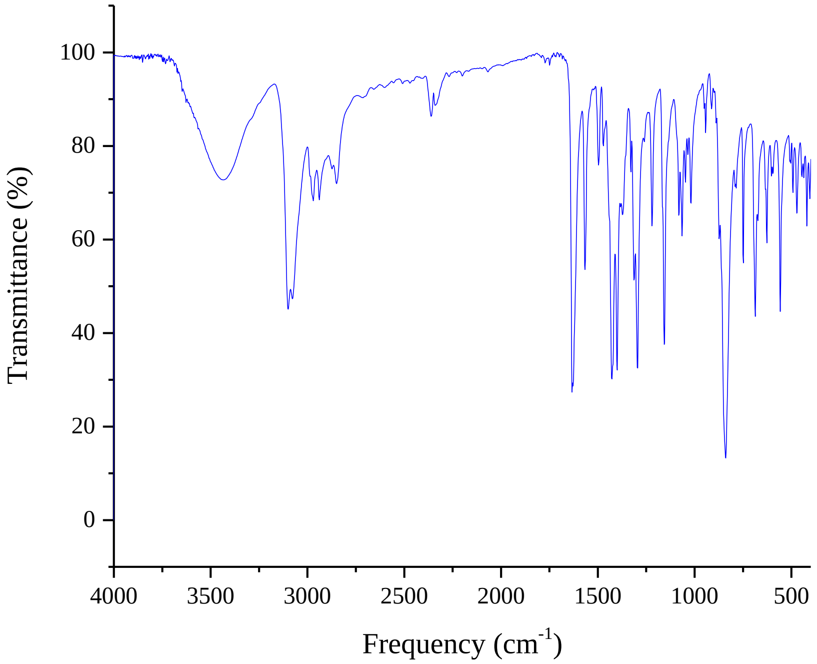

Figure A.32 FTIR spectrum of **C16.**

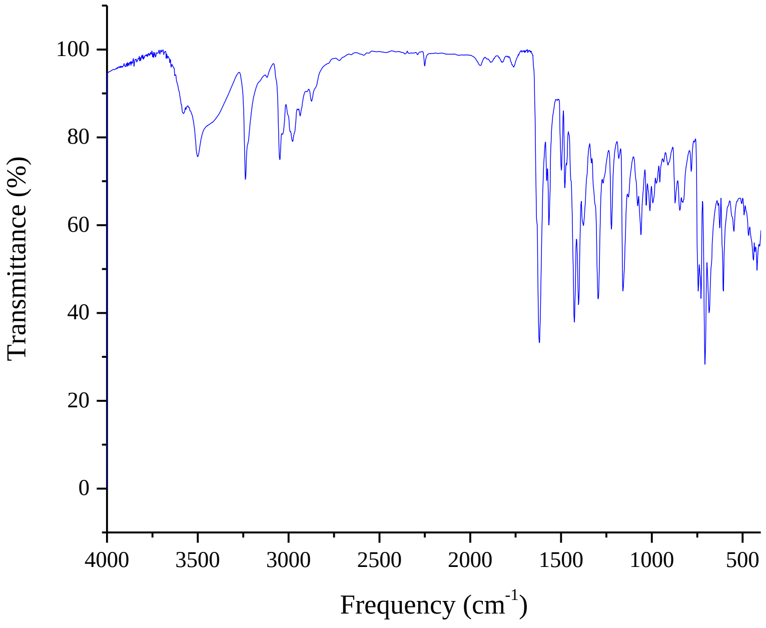

Figure A.33 FTIR spectrum of **C17.**

Table A.3 Crystal data and structure refinement of **C5, C18** and **C19**.

Complex	**C15**	**C18**	**C19**
Temperature	296(2)K	110(2) K	296(2) K
Crystal system	Orthorhombic	Monoclinic	Orthorhombic
Space group	P c a 21	P 21/c	P b c n
Unit cell dimension	a = 27.0029(18) Å	a = 13.953(3) Å	a = 11.0718(12) Å
	b = 11.6164(8) Å	b = 12.681(2) Å	b = 17.8479(18) Å
	c = 22.2296(13) Å	c = 17.083(3) Å	c = 32.042(3) Å
	α = 90°	α = 90°	α = 90°
	β = 90°	β = 93.001(6)°	β = 90°
	γ = 90°	γ = 90°	γ = 90°
Volume	6972.9(8) Å^3	3018.4(10) Å^3	6331.7(12) Å^3
Z	8	4	8
Goodness-of-fit on F^2	1.036	1.041	1.114
Final R indices [I>2sigma(I)]	R1 = 0.0458	R1 = 0.0507	R1 = 0.0542
	wR2 = 0.1068	wR2 = 0.1193	wR2 = 0.1262
R Indices (all data)	R1 = 0.0585	R1 = 0.0833	R1 = 0.0616
	wR2 = 0.1117	wR2 = 0.1329	wR2 = 0.1293

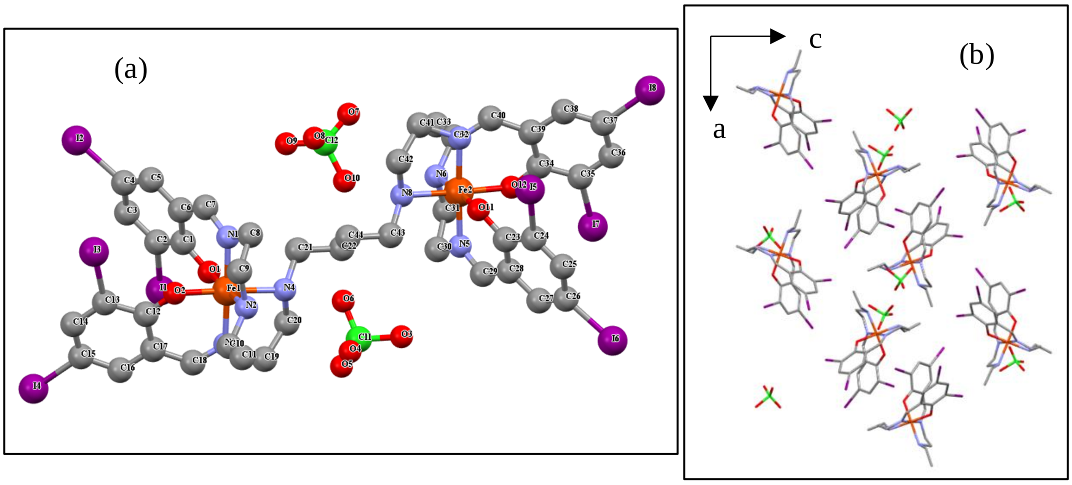

Figure A.34 X-ray crystal structure of **C15**, at 296 K: (a) asymmetric unit; (b) unit cell.

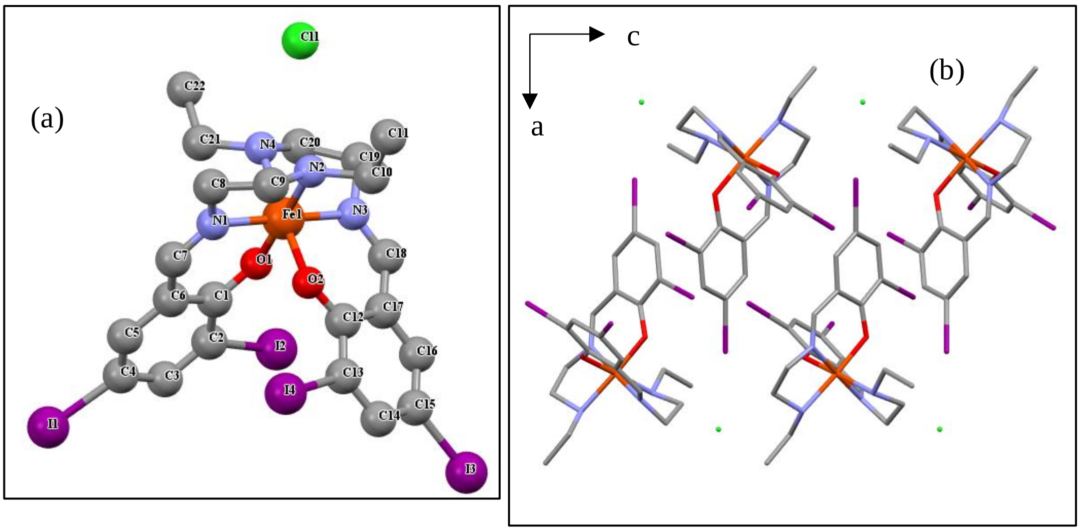

Figure A.35 X-ray crystal structure of **C18**, at 296 K: (a) asymmetric unit; (b) unit cell.

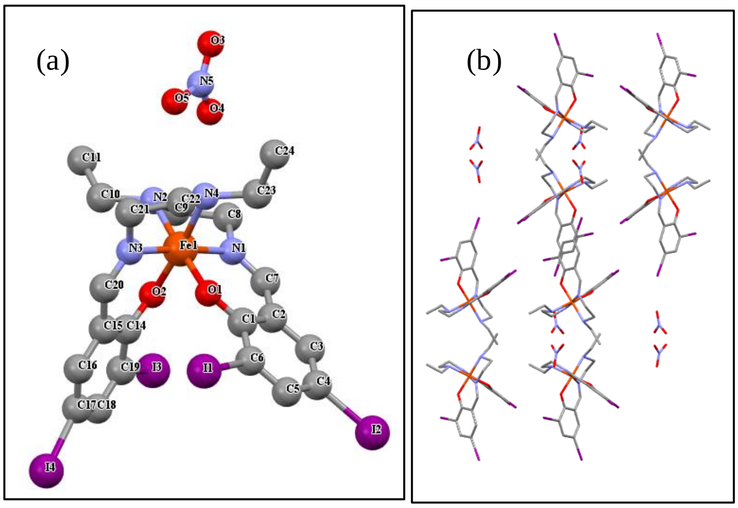

Figure A.36 X-ray crystal structure of **C19**, at 296 K: (a) asymmetric unit; (b) unit cell.

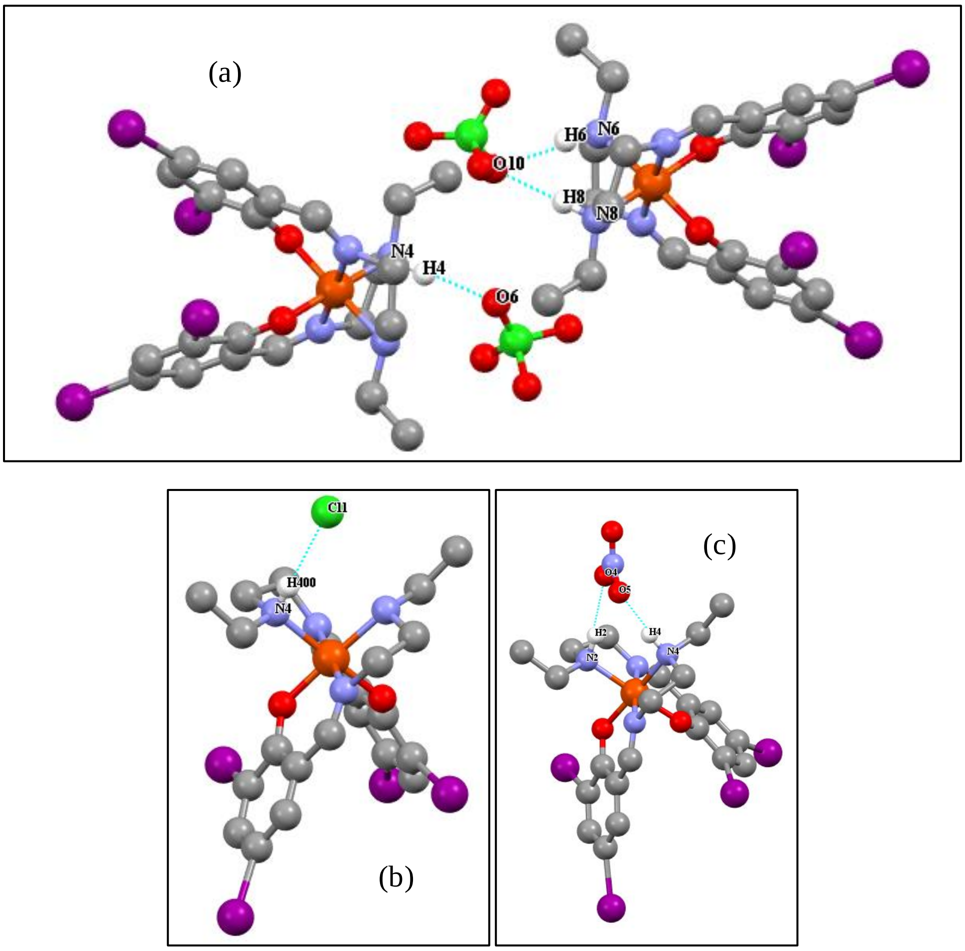

Figure A.37 Hydrogen bonds in the X-ray single crystal structure: (a) **C15;** (b) **C18** and (c) **C19**.

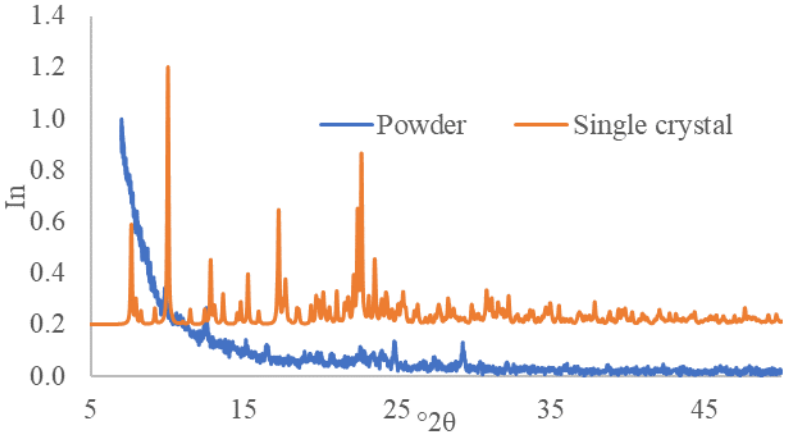

Figure A.38 Single Crystal and powder X-ray diffractogram of **C15**.

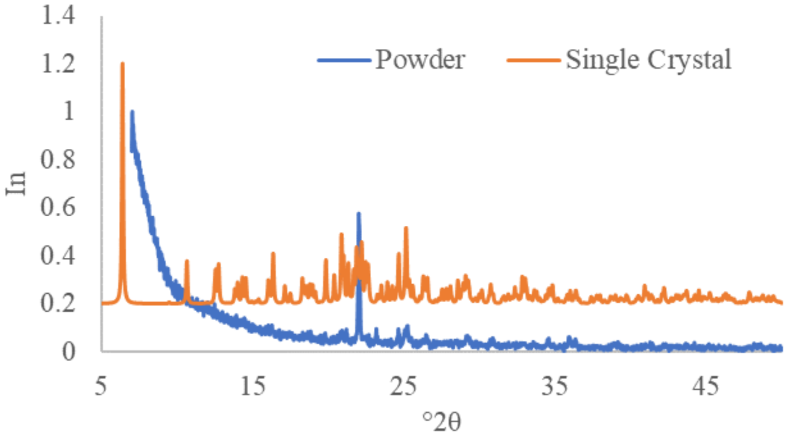

Figure A.39 Single Crystal and powder X-ray diffractogram of **C18.**

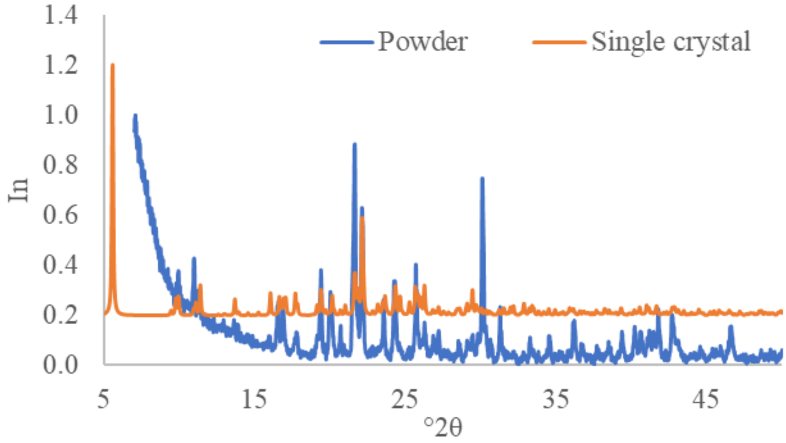

Figure A.40 Single Crystal and powder X-ray diffractogram of **C19.**

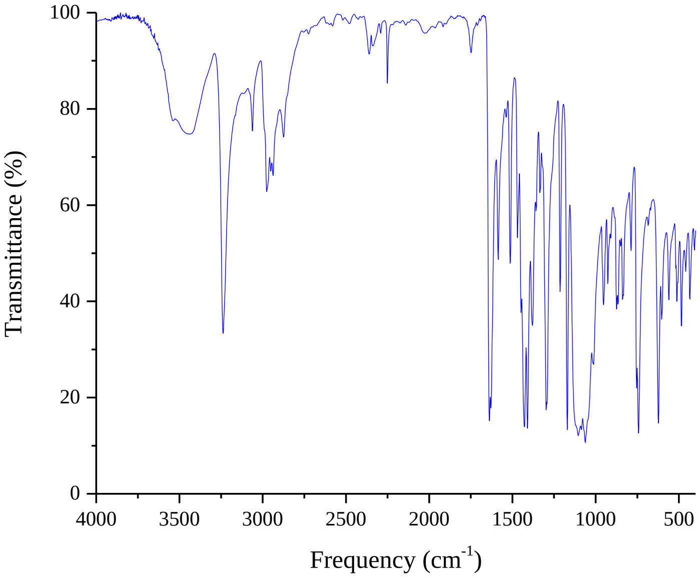

Figure A.41 FTIR spectrum of **C20.**

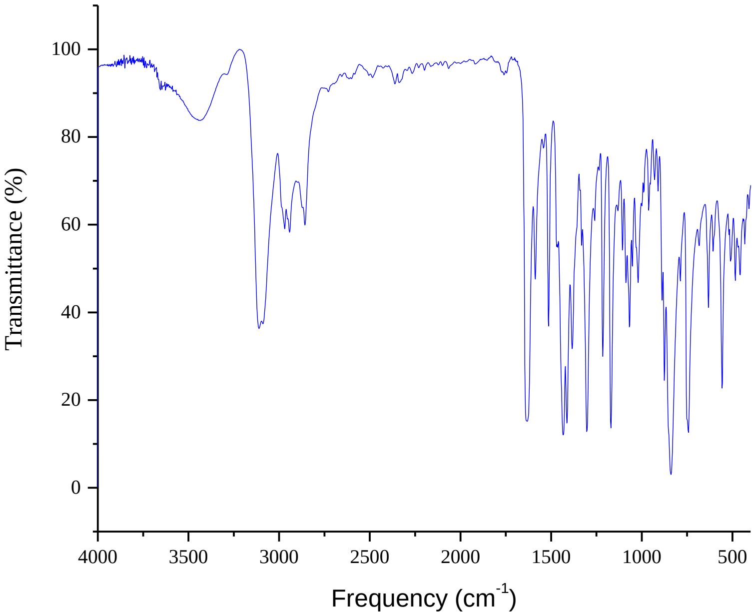

Figure A.42 FTIR spectrum of **C21.**

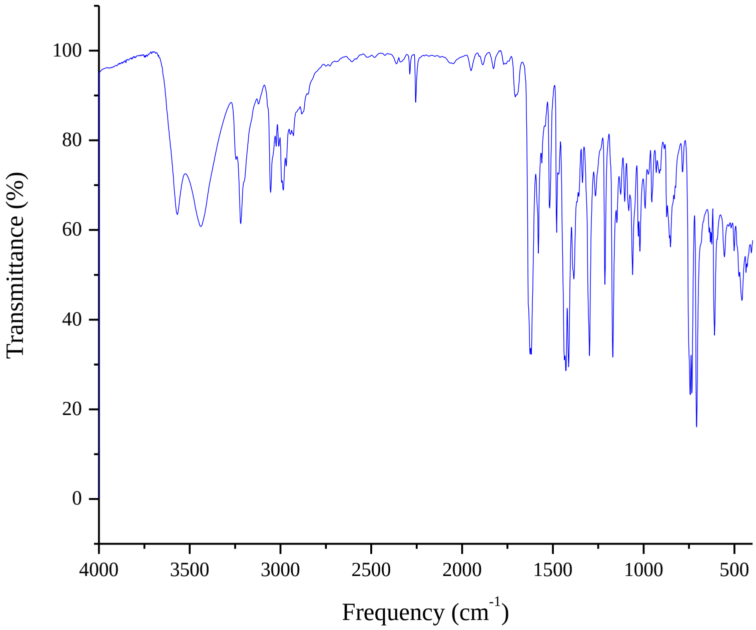

Figure A.43 FTIR spectrum of **C22.**

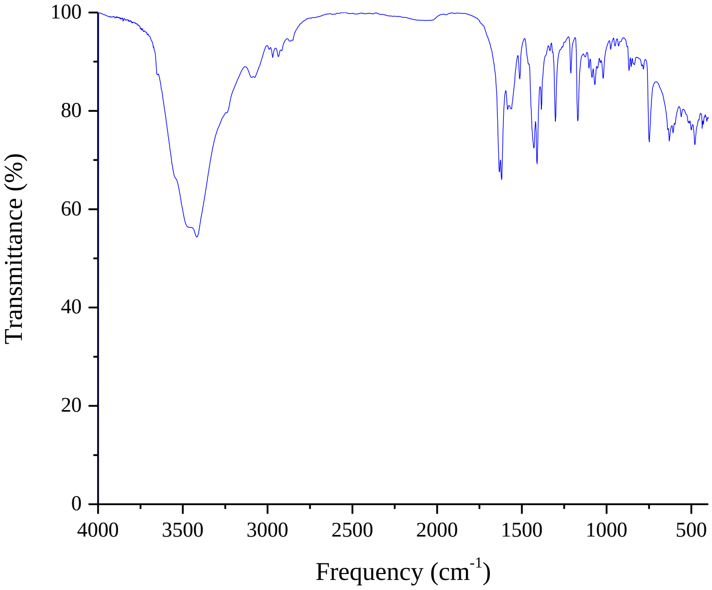

Figure A.44 FTIR spectrum of **C23.**

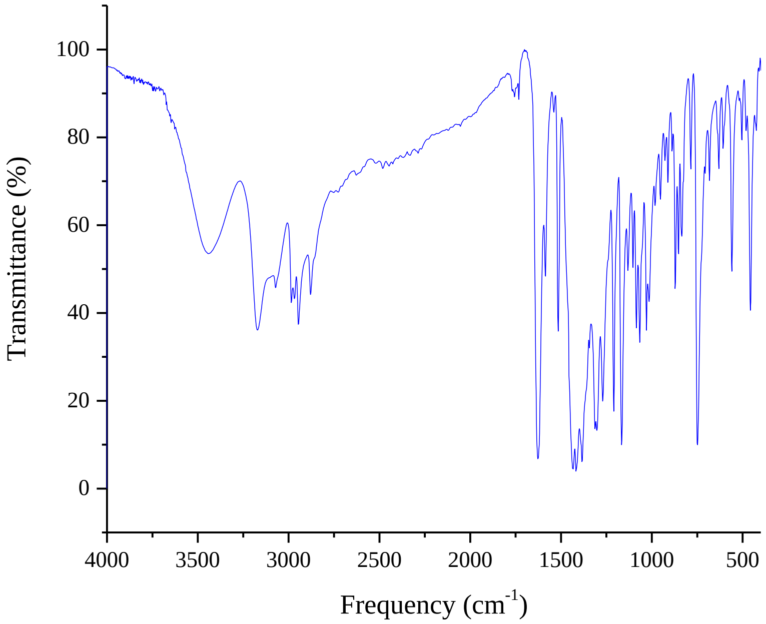

Figure A.45 FTIR spectrum of **C24**

Table A.4 Crystal data and structure refinement of **C20•CH$_3$CN-C22•H$_2$O•CH$_3$CN**.

Complex	**C20•CH$_3$CN**	**C21**	**C22•H$_2$O•CH$_3$CN**
Temperature	296(2) K	296(2) K	296(2) K
Crystal system	Monoclinic	Monoclinic	Monoclinic
Space group	C 2/c	C 2/c	P 21/c
Unit cell dimension	a = 21.109(4) Å	a = 27.208(3) Å	a = 17.284(2) Å
	b = 11.4094(17) Å	b = 25.591(3) Å	b = 15.3131(15) Å
	c = 26.947(5) Å	c = 20.752(2) Å	c = 18.9322(19) Å
	α = 90°	α = 90°	α = 90°
	β = 104.312(6)°	β = 123.516(3)°	β = 103.562(4)°
	γ = 90°	γ = 90°	γ = 90°
Volume	6288.5(18) Å^3	12047(3) Å^3	4871.1(9) Å^3
Z	8	8	4
Goodness-of-fit on F^2	1.046	1.063	1.081
Final R indices [I>2sigma(I)]	R1 = 0.0463	R1 = 0.0758	R1 = 0.1239
	wR2 = 0.1175	wR2 = 0.1358	wR2 = 0.3635
R Indices (all data)	R1 = 0.0663	R1 = 0.1370	R1 = 0.1504
	wR2 = 0.1285	wR2 = 0.1538	wR2 = 0.3724

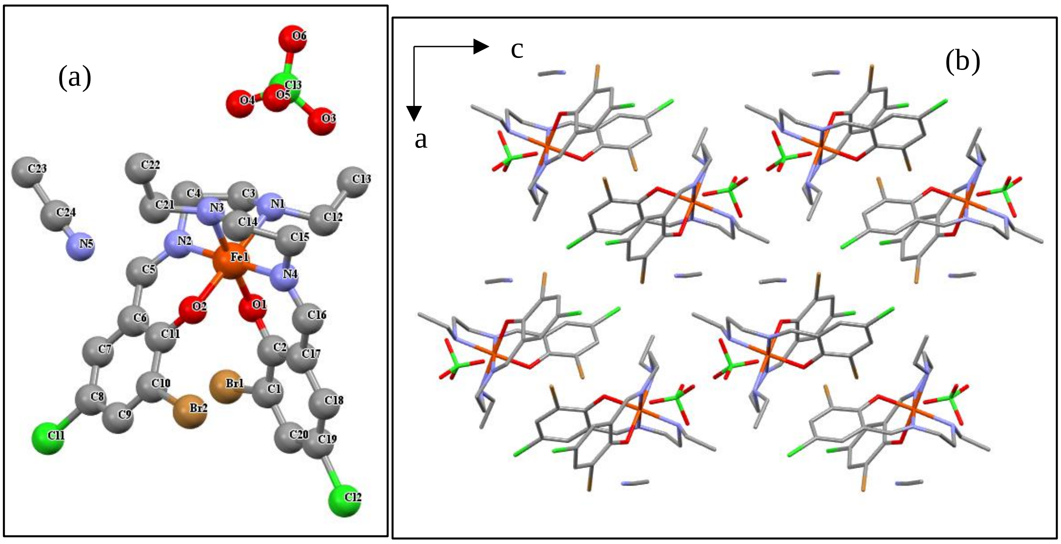

Figure A.46 X-ray crystal structure of **C20•CH$_3$CN**, at 296 K: (a) asymmetric unit; (b) unit cell.

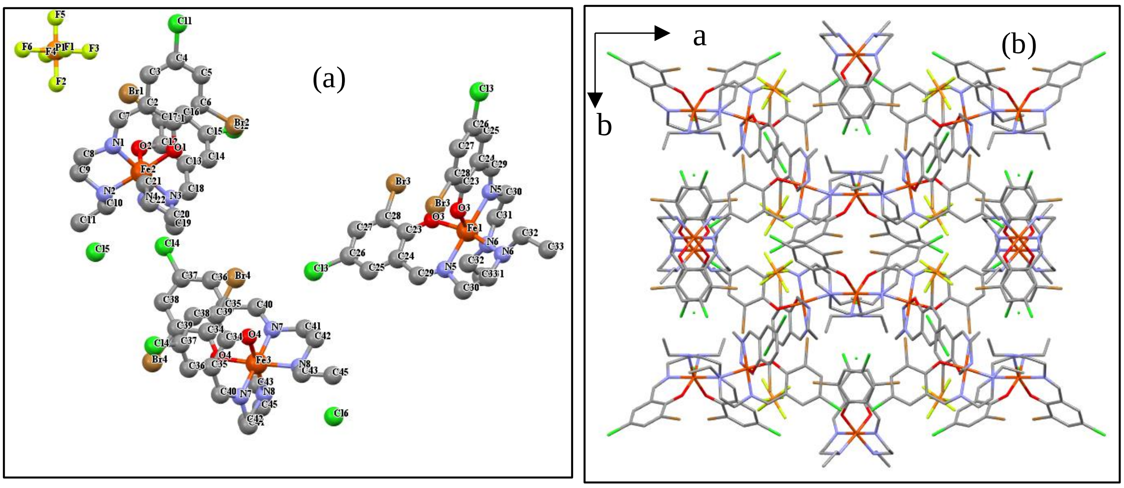

Figure A.47 X-ray crystal structure of **C21**, at 296 K: (a) asymmetric unit; (b) unit cell.

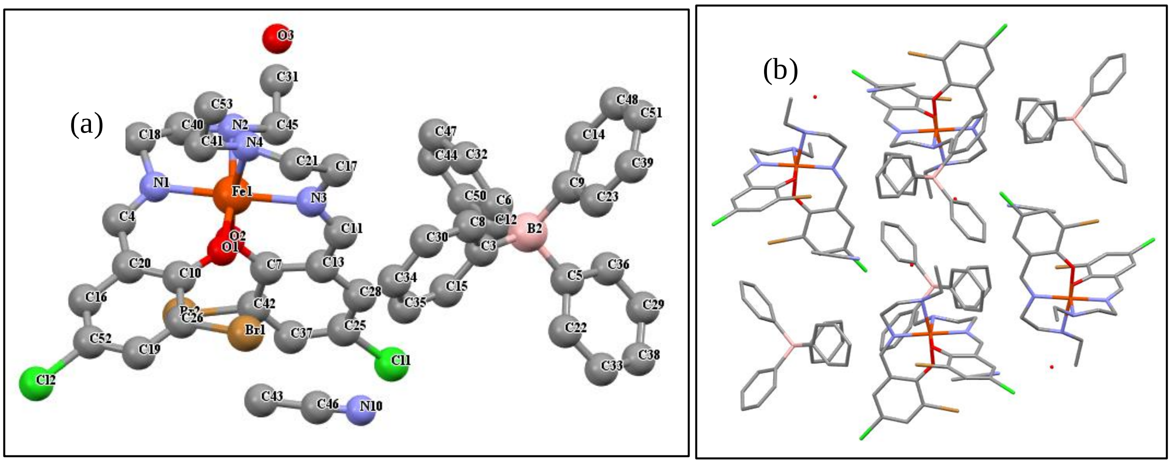

Figure A.48 X-ray crystal structure of **C22•H$_2$O•CH$_3$CN**, at 296 K: (a) asymmetric unit; (b) unit cell.

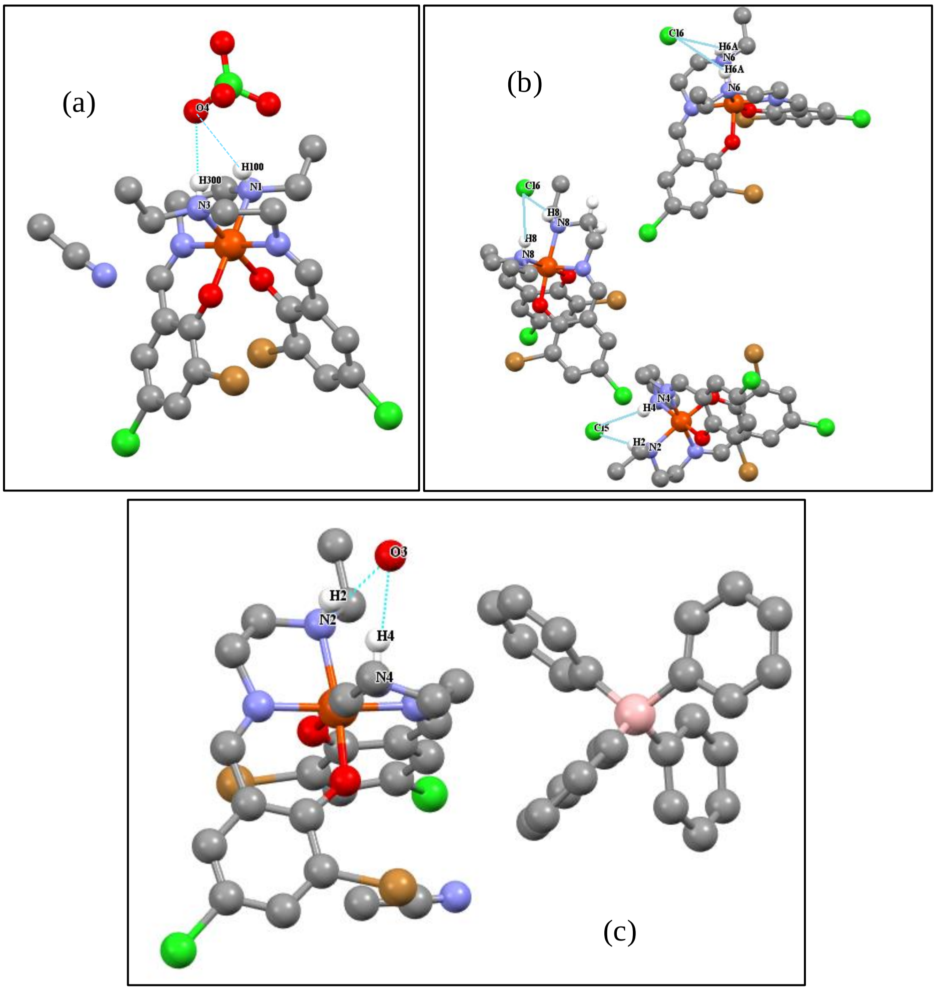

Figure A.49 Hydrogen bonds in the X-ray single crystal structure: (a) **C20•CH$_3$CN;** (b) **C21** and (c) **C22•H$_2$O•CH$_3$CN.**

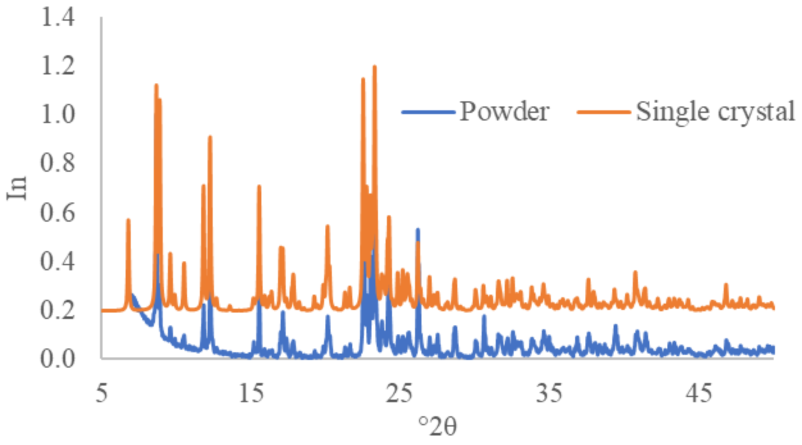

Figure A.50 Single Crystal and powder X-ray diffractogram of **C20•CH$_3$CN.**

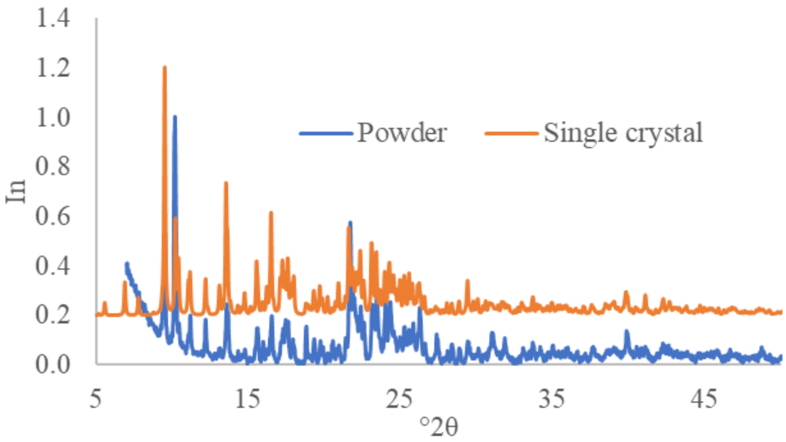

Figure A.51 Single Crystal and powder X-ray diffractogram of **C21.**

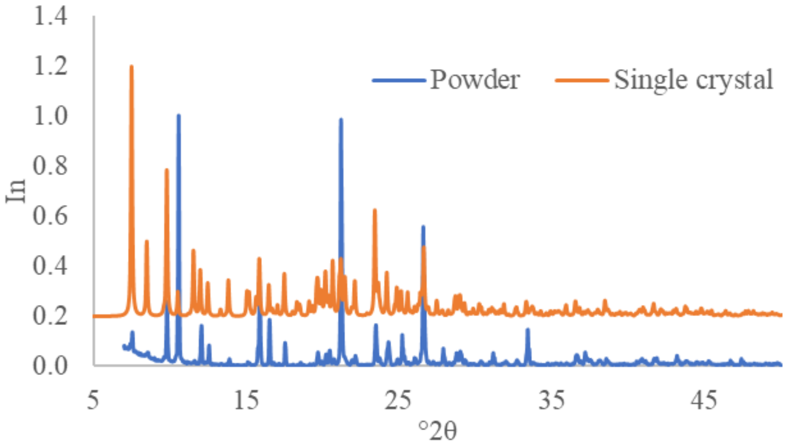

Figure A.52 Single Crystal and powder X-ray diffractogram of **C22•H_2O•CH_3CN.**

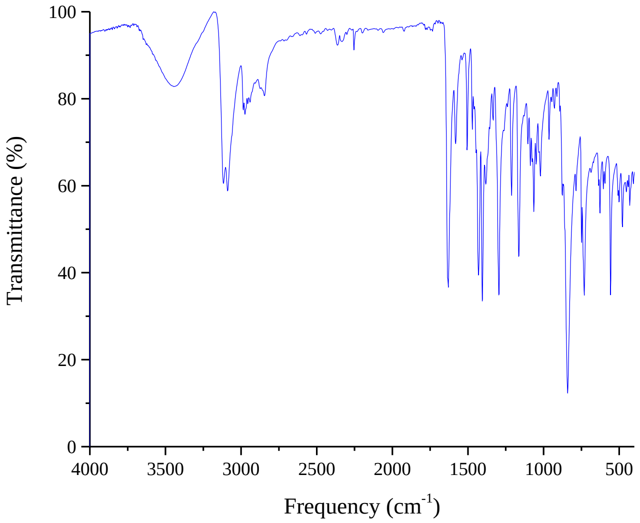

Figure A.53 FTIR spectrum of **C26.**

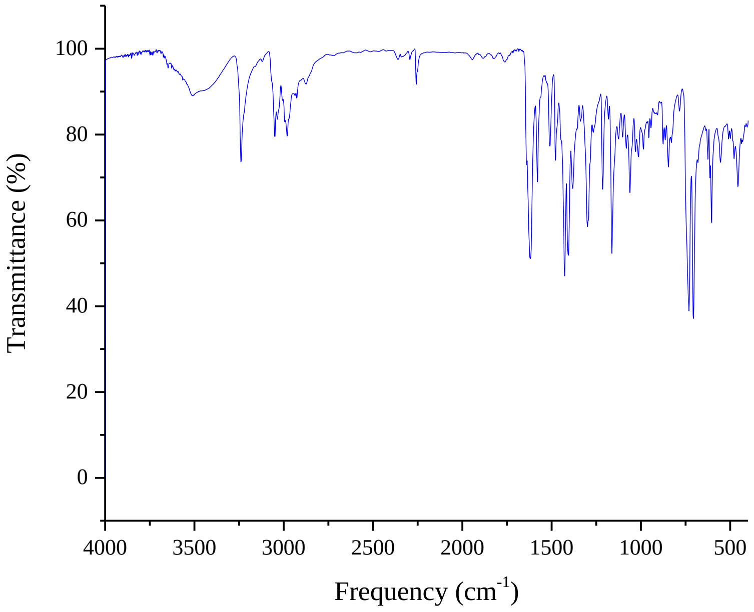

Figure A.54 FTIR spectrum of **C27.**

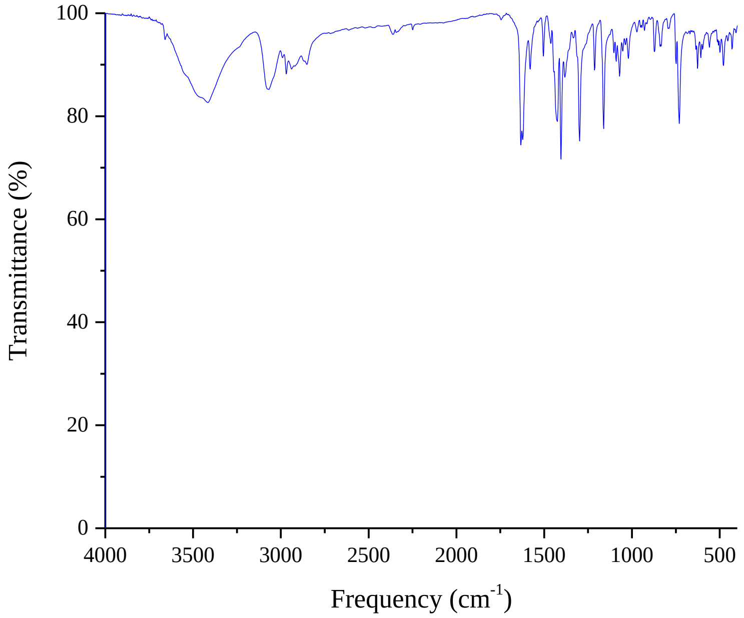

Figure A.55 FTIR spectrum of **C28.**

Table A.5 Crystal data and structure refinement of **C25-C28•2H$_2$O**.

Complex	**C25**	**C26•2H$_2$O•CH$_3$CN**	**C27•H$_2$O•CH$_3$CN**	**C28•2H$_2$O**
Temperature	296(2) K	296(2) K	296(2) K	296(2) K
Crystal system	Monoclinic	Monoclinic	Monoclinic	Orthorhombic
Space group	P 21/c	C 2/c	P 21/c	P b c n
Unit cell dimension	a = 18.664(8) Å	a = 38.627(4) Å	a = 17.2948(17) Å	a = 11.311(3) Å
	b = 9.769(4) Å	b = 11.0267(11) Å	b = 15.4624(15) Å	b = 17.838(6) Å
	c = 16.447(7) Å	c = 16.4593(16) Å	c = 18.968(2) Å	c = 30.275(9) Å
	α = 90°.	α = 90°.	α = 90°.	α = 90°.
	β = 98.863(13)°.	β = 108.968(3)°.	β = 101.891(3)°.	β = 90°.
	γ = 90°.	γ = 90°.	γ = 90°.	γ = 90°.
Volume	2963(2) Å^3	6629.8(11) Å^3	4963.5(9) Å^3	6109(3) Å^3
Z	4	8	4	4
Goodness-of-fit on F^2	1.037	1.045	0.913	1.063
Final R indices [I>2sigma(l)]	R1 = 0.0520	R1 = 0.0477	R1 = 0.0748	R1 = 0.1257
	wR2 = 0.1122	wR2 = 0.1342	wR2 = 0.2011	wR2 = 0.3309
R Indices (all data)	R1 = 0.1151	R1 = 0.0818296(2) K	R1 = 0.1731	R1 = 0.2048
	wR2 = 0.1313	wR2 = 0.1465	wR2 = 0.2429	wR2 = 0.3553

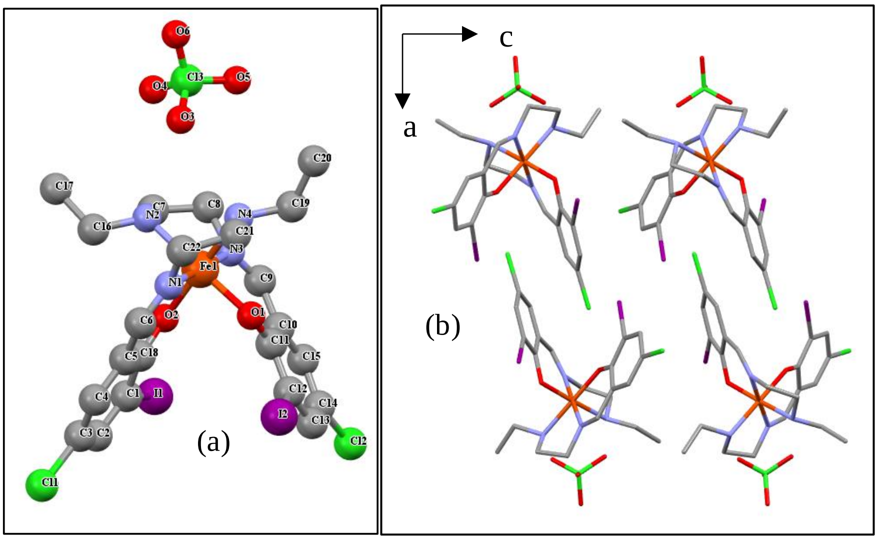

Figure A.56 X-ray crystal structure of **C25**, at 296 K: (a) asymmetric unit; (b) unit cell.

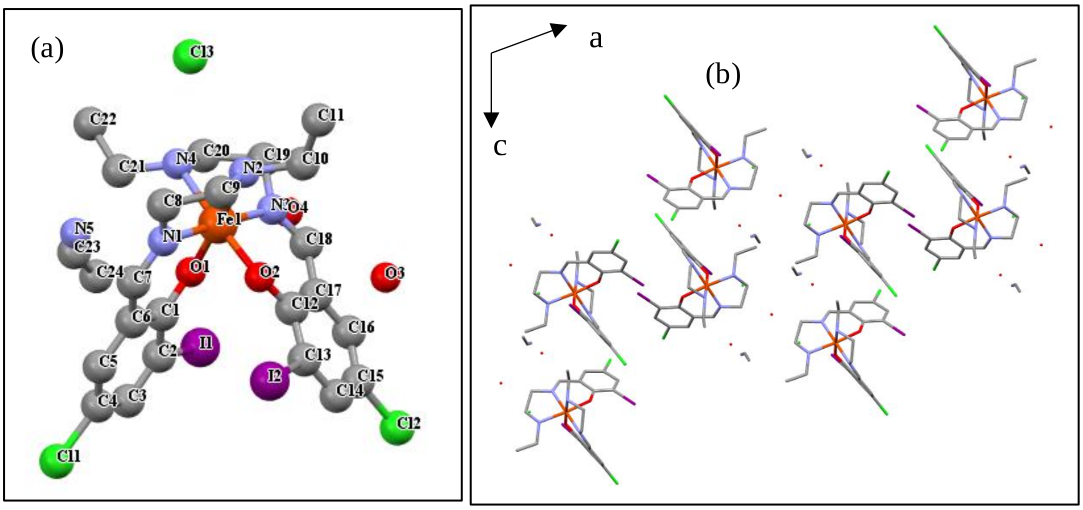

Figure A.57 X-ray crystal structure of **C26•2H$_2$O•CH$_3$CN**, at 296 K: (a) asymmetric unit; (b) unit cell.

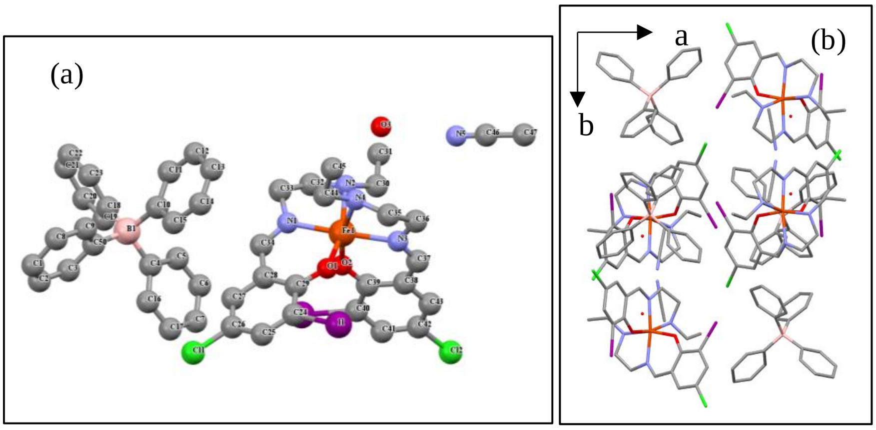

Figure A.58 X-ray crystal structure of **C27•H$_2$O•CH$_3$CN**, at 296 K: (a) asymmetric unit; (b) unit cell.

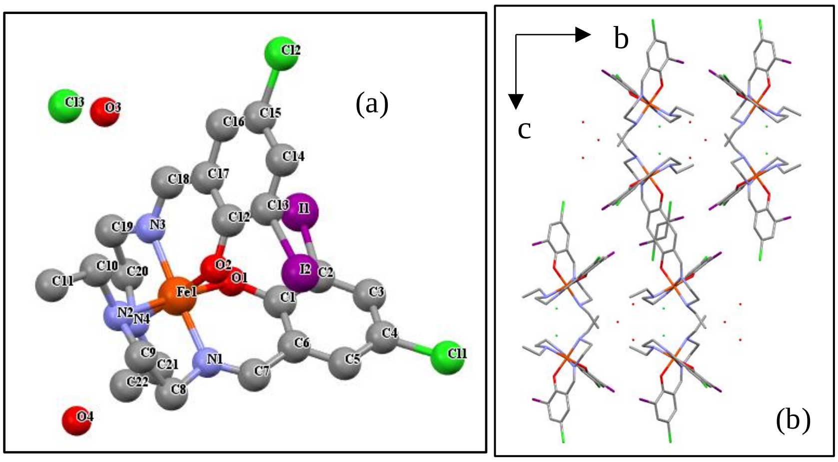

Figure A.59 X-ray crystal structure of **C28•2H$_2$O**, at 296 K: (a) asymmetric unit; (b) unit cell.

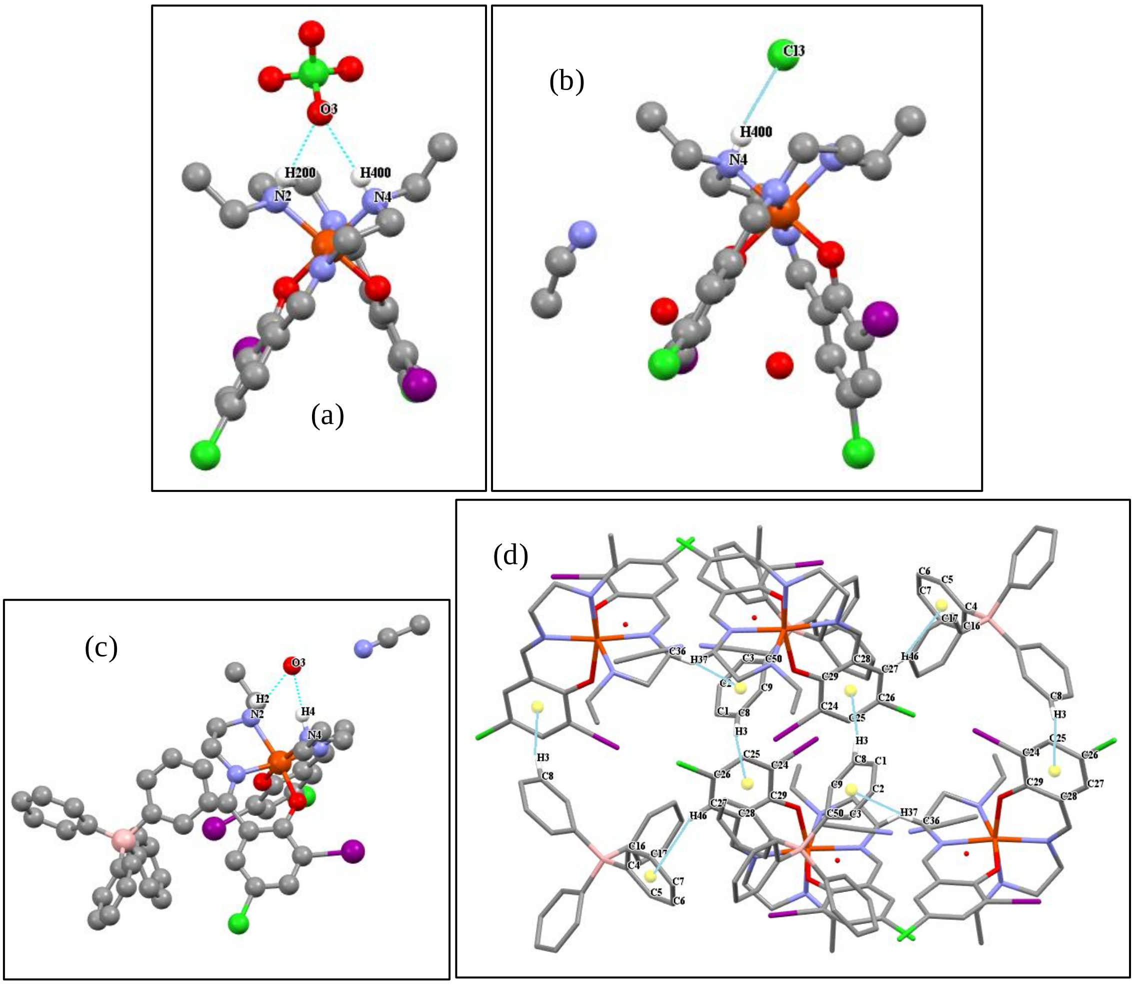

Figure A.60: Hydrogen bonds in the X-ray single crystal structure: (a) **C25;** (b) **C26•$2H_2O$•CH_3CN** and (c) **C27•H_2O•CH_3CN;** C-H···π (d) **C8•H2O•CH3CN.**

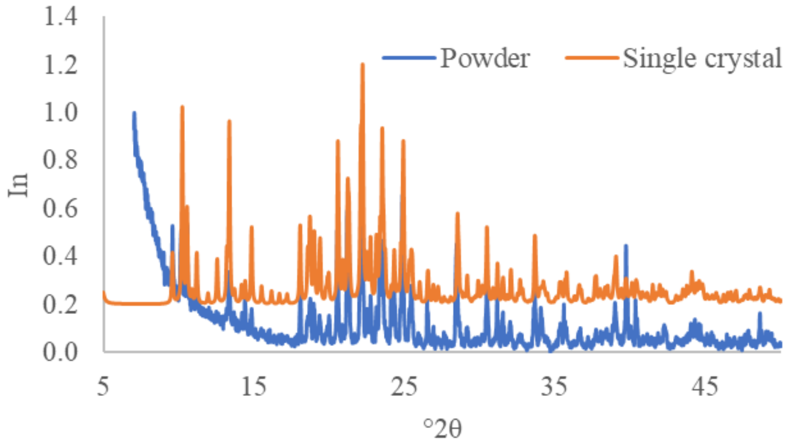

Figure A.61 Single Crystal and powder X-ray diffractogram of **C25.**

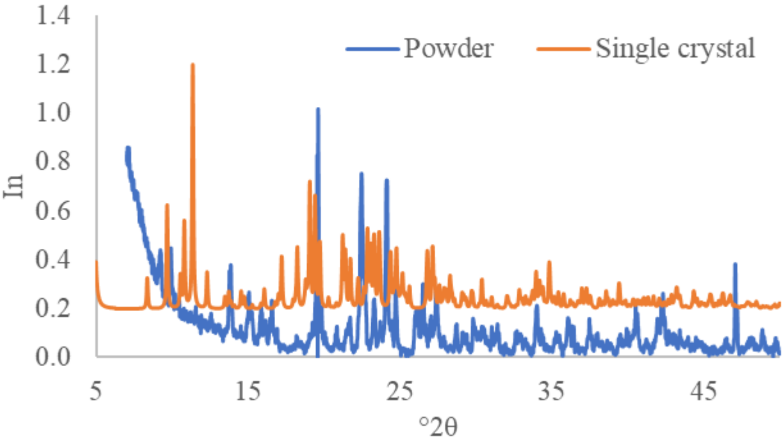

Figure A.62 Single Crystal and powder X-ray diffractogram of **$C26 \bullet 2H_2O \bullet CH_3CN$.**

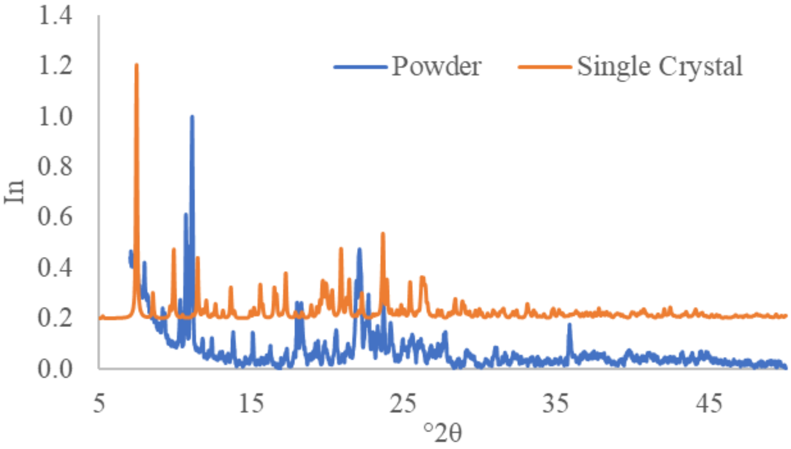

Figure A.63 Single Crystal and powder X-ray diffractogram of **$C27 \bullet H_2O \bullet CH_3CN$.**

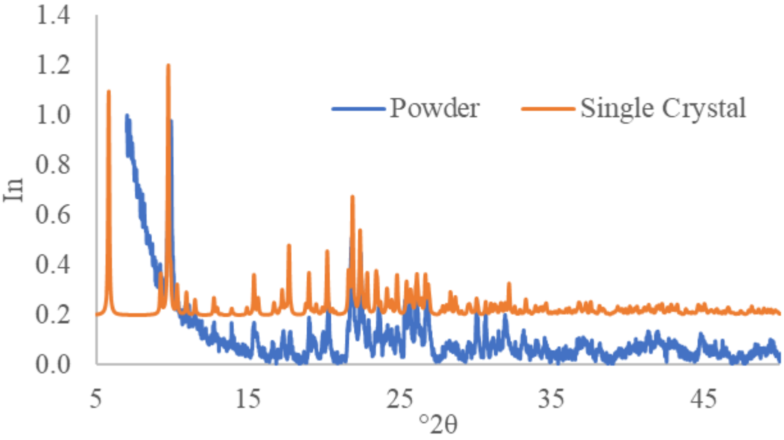

Figure A.64 Single Crystal and powder X-ray diffractogram of **$C28 \bullet 2H_2O$.**

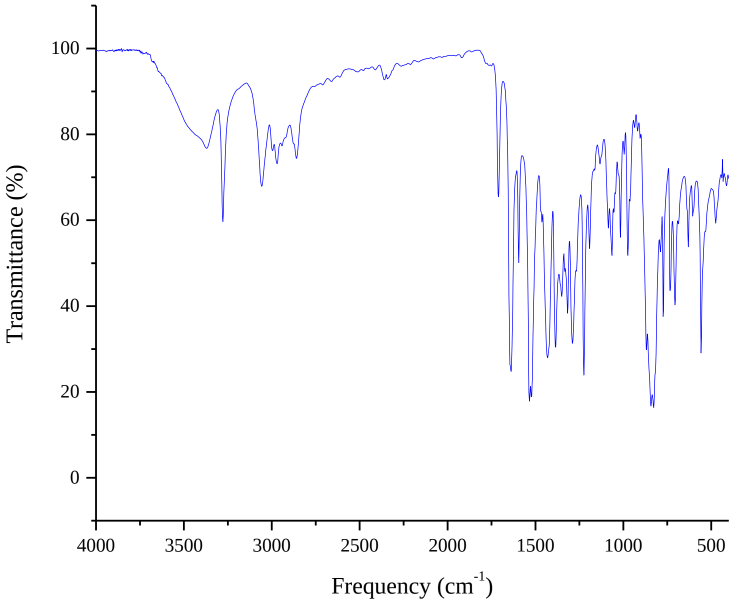

Figure A.65 FTIR spectrum of **C29.**

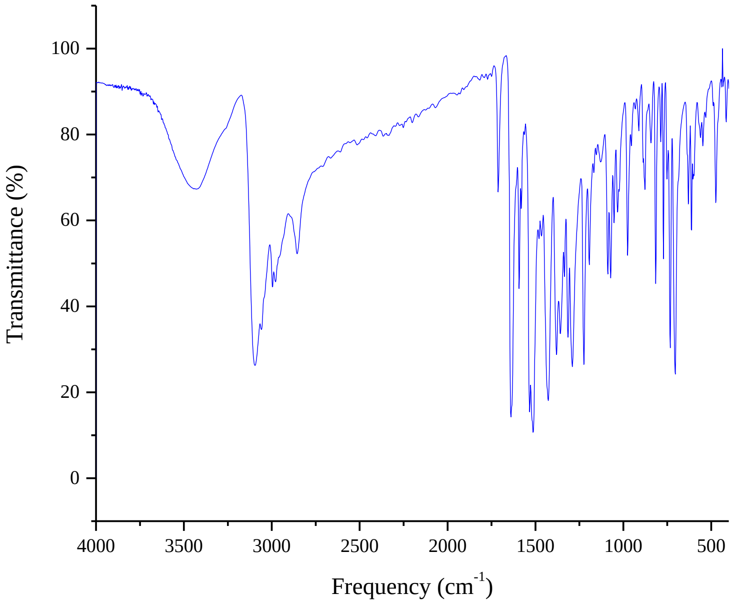

Figure A.66 FTIR spectrum of **C30.**

Table A.6: Crystal data and structure refinement of **C29** and **C30**.

Complex	**C29**		**C30**	
Temperature	296(2) K		296(2) K	
Crystal system	Monoclinic		Monoclinic	
Space group	P 21/c		C 2/c	
Unit cell dimension	a = 17.4605(13) Å	α = 90°	a = 28.700(17) Å	α = 90°
	b = 13.6869(10) Å	β = 92.003(2)°	b = 16.438(7) Å	β = 98.420(16)°
	c = 12.9811(9) Å	γ = 90°	c = 16.283(9) Å	γ = 90°
Volume	3100.3(4) Å^3		7599(7) Å^3	
Z	4		4	
Goodness-of-fit on F^2	1.077		0.996	
Final R indices [I>2sigma(l)]	R1 = 0.0937	wR2 = 0.2477	R1 = 0.0816	wR2 = 0.2257
R Indices (all data)	R1 = 0.1381	wR2 = 0.2671	R1 = 0.1293	wR2 = 0.2422

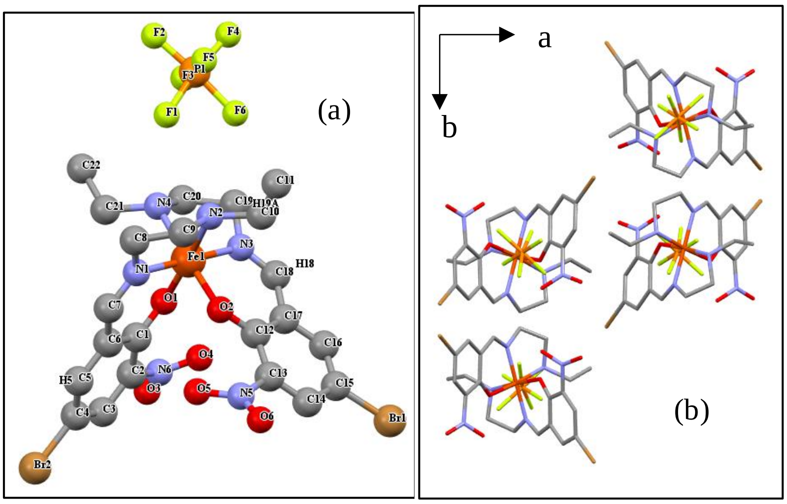

Figure A.67: X-ray crystal structure of **C29**, at 296 K: (a) asymmetric unit; (b) unit cell.

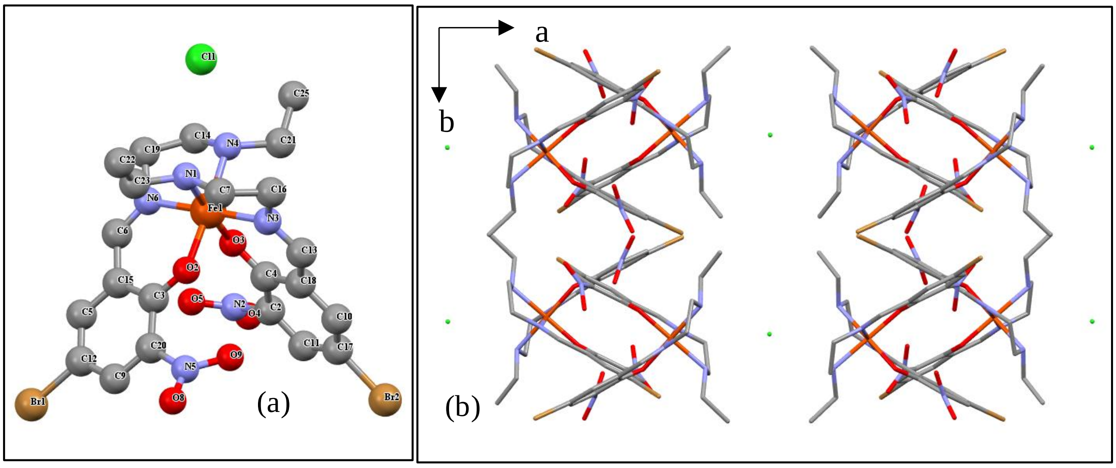

Figure A.68 X-ray crystal structure of **C30**, at 296 K: (a) asymmetric unit; (b) unit cell.

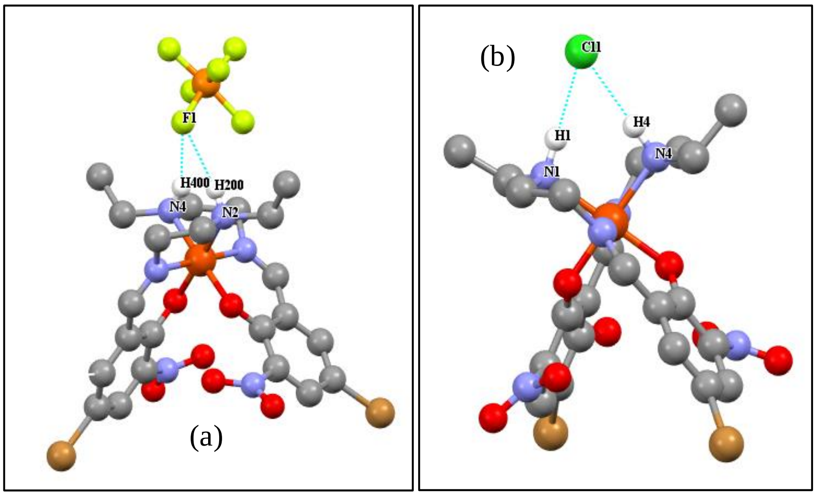

Figure A.69 Hydrogen bonds in the X-ray single crystal structure: (a) **C29** and (b) **C30**.

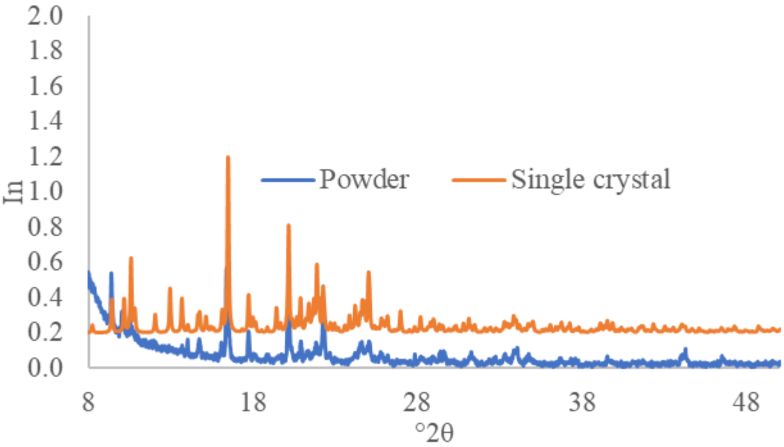

Figure A.70 Single Crystal and powder X-ray diffractogram of **C29.**

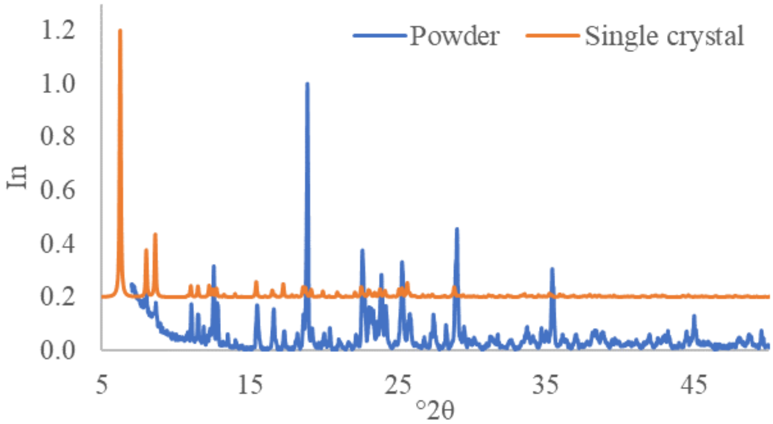

Figure A.71 Single Crystal and powder X-ray diffractogram of **C30.**

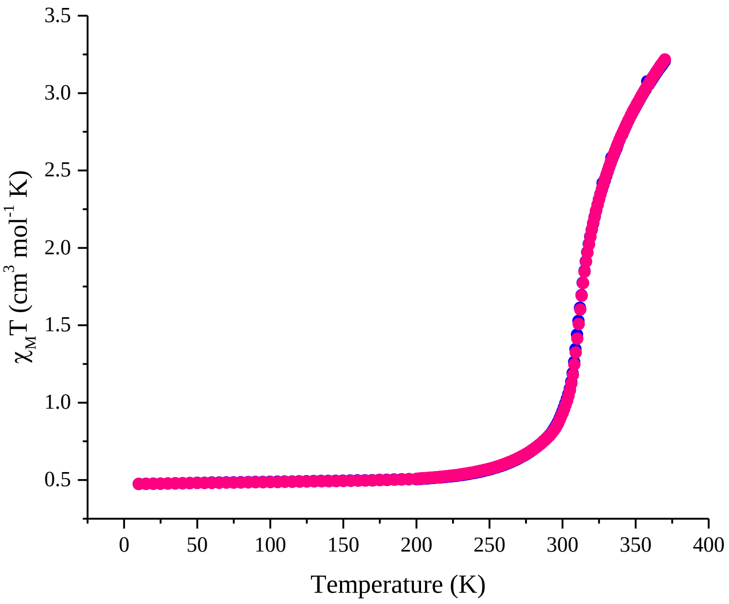

Figure A.72 $\chi_M T$ vs T plot for **C29**, at the rate 1 K min^{-1}.

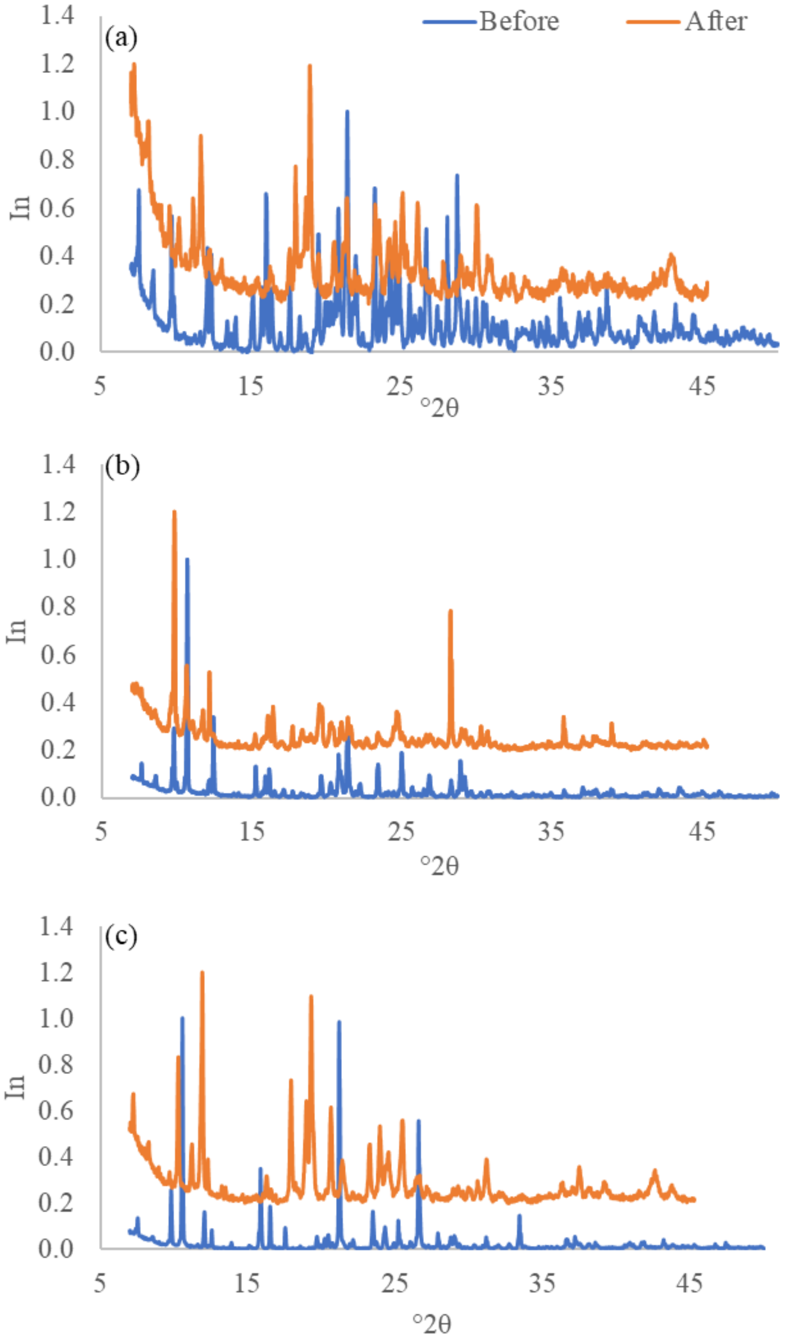

Figure A.73 Powder X-ray diffractogram before and after SQUID of: (a) **C3•H_2O•CH_3CN;** (b) **C8•H_2O•CH_3CN;** (c) **C22•H_2O•CH_3CN.**

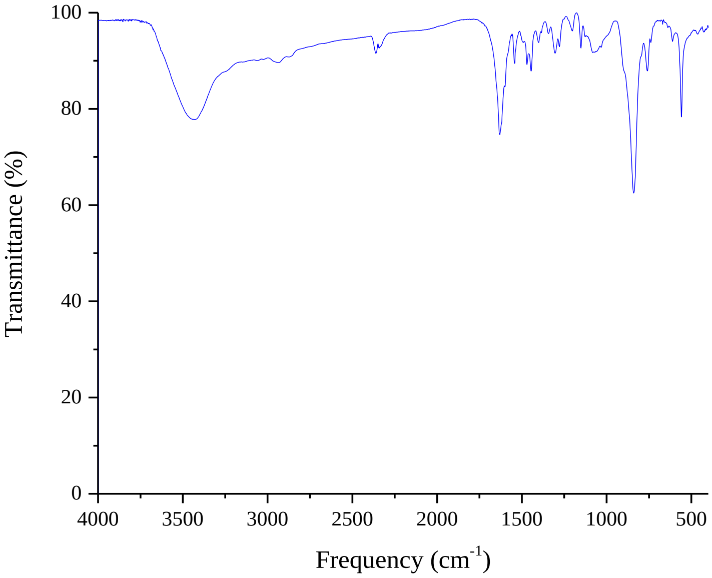

Figure A.74 FTIR spectrum of **C31.**

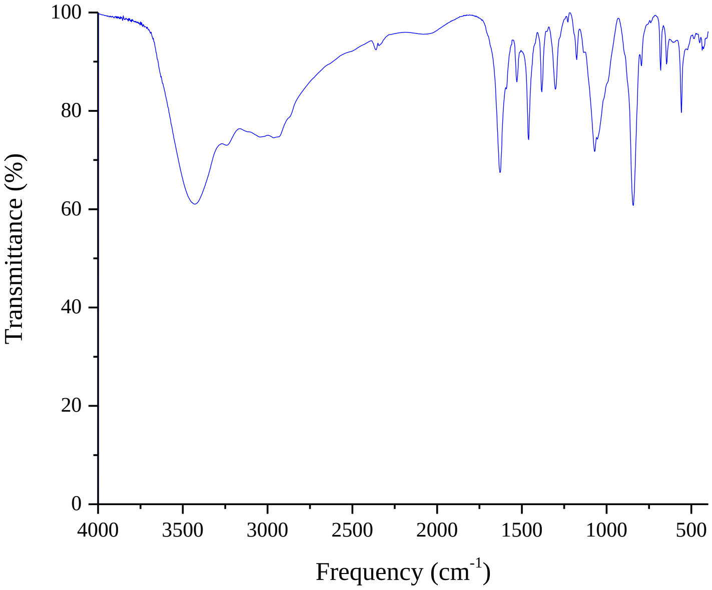

Figure A.75 FTIR spectrum of **C32.**

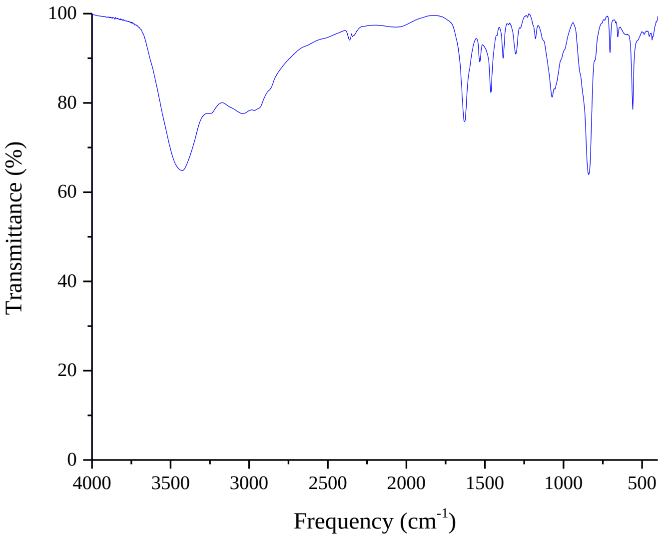

Figure A.76 FTIR spectrum of **C33.**

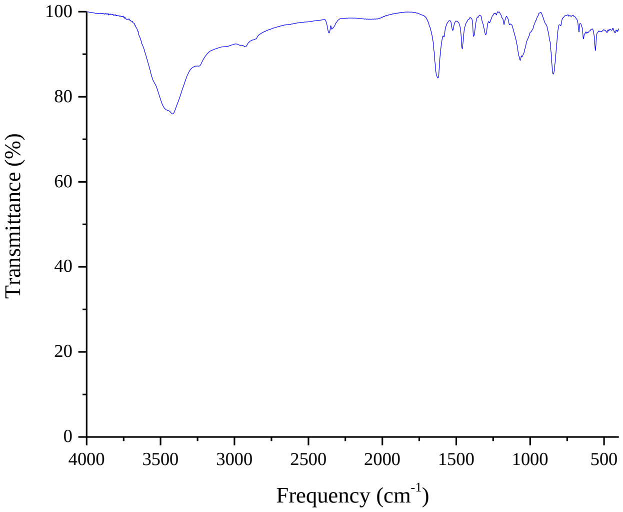

Figure A.77 FTIR spectrum of **C34.**

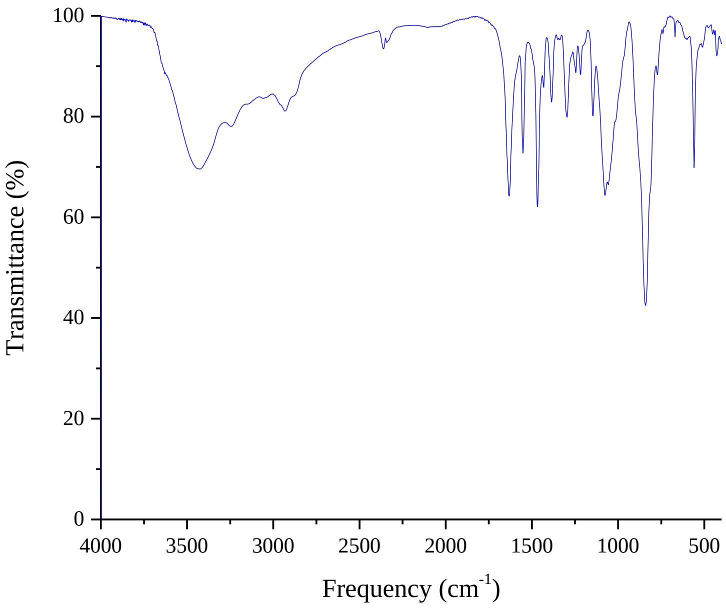

Figure A.78 FTIR spectrum of **C35.**

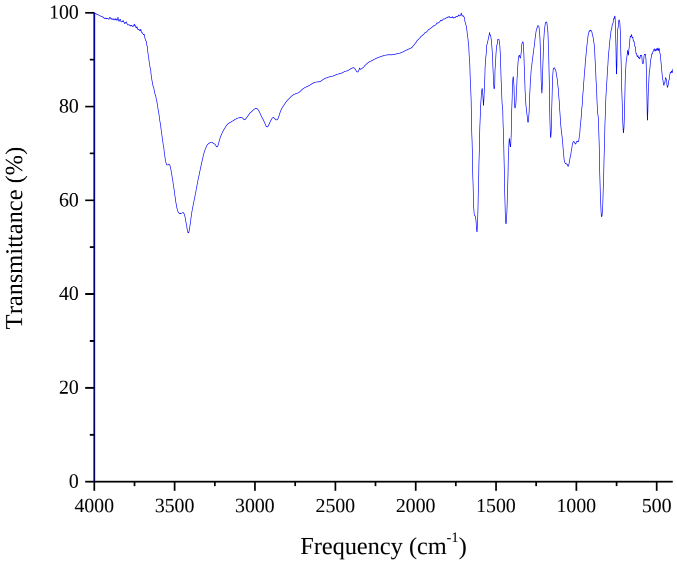

Figure A.79 FTIR spectrum of **C36.**

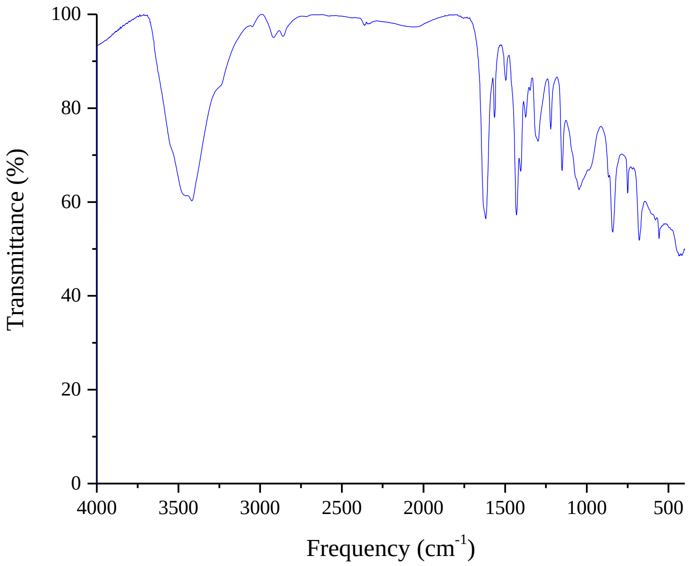

Figure A.80 FTIR spectrum of **C38.**

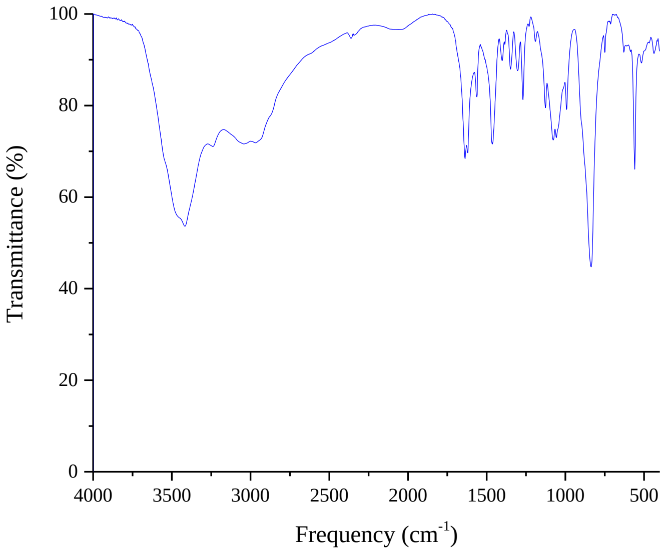

Figure A.81 FTIR spectrum of **C39.**

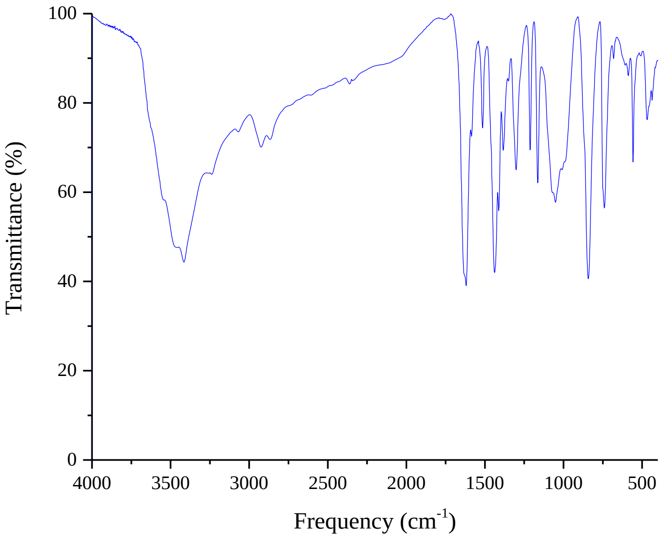

Figure A.82 FTIR spectrum of **C40.**

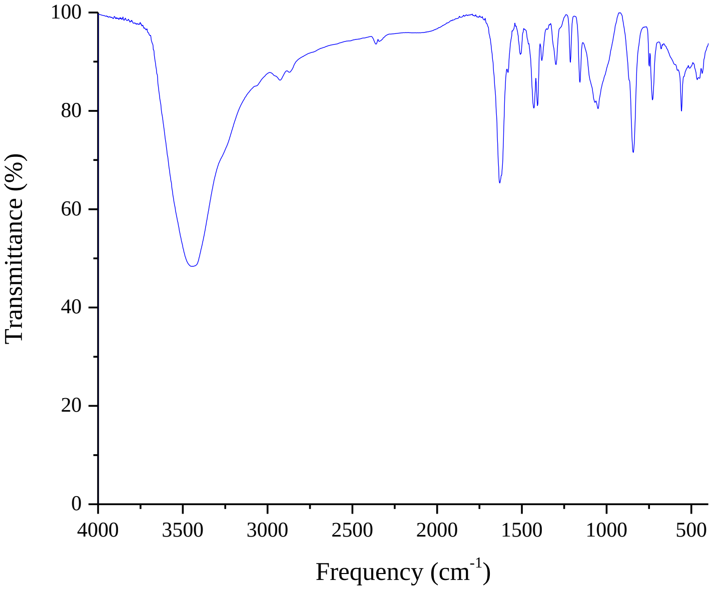

Figure A.83 FTIR spectrum of **C41.**